UC Berkeley
UC Berkeley Electronic Theses and Dissertations

Title

Hydrodesulfurization on Transition Metal Catalysts: Elementary Steps of C-S Bond Activation and Consequences of Bifunctional Synergies

Permalink

https://escholarship.org/uc/item/7ts2s2jq

Author

Yik, Edwin Shyn-Lo

Publication Date

2015

Peer reviewed|Thesis/dissertation

Hydrodesulfurization on Transition Metal Catalysts:
Elementary Steps of C-S Bond Activation and
Consequences of Bifunctional Synergies

by

Edwin Shyn-Lo Yik

A dissertation submitted in partial satisfaction of the

requirements for the degree of

Doctor of Philosophy

in

Chemical Engineering

in the

Graduate Division

of the

University of California, Berkeley

Committee in charge:

Professor Enrique Iglesia, Chair
Professor Alexis T. Bell
Professor Kenneth N. Raymond

Fall 2015

Hydrodesulfurization on Transition Metal Catalysts:
Elementary Steps of C-S Bond Activation and
Consequences of Bifunctional Synergies

© 2015

by

Edwin Shyn-Lo Yik

Abstract

Hydrodesulfurization on Transition Metal Catalysts: Elementary Steps of C-S Bond Activation

and Consequences of Bifunctional Synergies

by

Edwin Shyn-Lo Yik

Doctor of Philosophy in Chemical Engineering

University of California, Berkeley

Professor Enrique Iglesia, Chair

The presence of heteroatoms (e.g. S, N) in crude oil poses formidable challenges in petroleum refining processes as a result of their irreversible binding on catalytically active sites at industrially relevant conditions. Such poisons render these sites inaccessible to reactants, negatively impacting overall process performance, and require replacement and/or regeneration of the catalysts, leading to high material and time costs. With increasing pressures from legislation that continues to lower the permissible levels of sulfur content in fuels, hydrodesulfurization (HDS), the aptly named reaction for removing heteroatoms from organosulfur compounds, has become an essential feedstock pretreatment step to remove deleterious species from affecting downstream processing. Extensive research in the area has identified the paradigm catalysts for desulfurization; MoS_x or WS_x, promoted with Co or Ni metal; however, despite the vast library of both empirical and fundamental studies, a clear understanding of site requirements, the elementary steps of C-S hydrogenolysis, and the properties that govern HDS reactivity and selectivity have been elusive. While such a lack of rigorous assessments has not prevented technological advancements in the field of HDS catalysis, fundamental interpretations can inform rational catalyst and process design, particularly in light of new requirements for "deep" desulfurization and in the absence of significant hydrotreatment catalyst developments in recent decades.

We report HDS rates of thiophene, which belongs to a class of compounds that are most resistant to sulfur removal (i.e. substituted alkyldibenzothiophenes), over a range of industrially relevant temperatures and pressures, measured at differential conditions and therefore revealing their true kinetic origins. These rates, normalized by the number of exposed metal atoms, on various SiO_2-supported, monometallic transition metals (Re, Ru, Pt), range several orders of magnitude. Under relevant HDS conditions, Pt and Ru catalysts form a layer of chemisorbed sulfur on surfaces of a metallic bulk, challenging reports that assume the latter exists as its pyrite sulfide phase during reaction. While convergence to a single phase is expected and predictable from thermodynamics at a given temperature and sulfur chemical potential, metastability of two phases can exist. We demonstrate, through extensive characterization and kinetic evidence, such behaviors exist in Re, where structural disparities between its phases lead to kinetic hurdles that prevent interconversions between layered ReS_x nanostructures and sulfur-covered Re metal

1

clusters. Such features allowed, for the first time, direct comparisons of reaction rates at identical conditions on two disparate phases of the same transition metal identity. Rigorous assessments of kinetic and selectivity data indicated that more universal mechanistic features persist across all catalysts studied, suggesting that differences in their catalytic activity were the result of different densities of HDS sites, which appeared to correlate with their respective metal-sulfur bond energies.

Kinetic responses and product distributions indicated that the consumption of thiophene proceeds by the formation of a partially-hydrogenated surface intermediate, which subsequently produces tetrahydrothiophene (THT) and butene/butane (C_4) via primary routes on similar types of sites. These sites are formed from desorption of weakly-bound sulfur adatoms on sulfur-covered metal surfaces, which can occur when the heat of sulfur adsorption is sufficiently low at high sulfur coverage as a result of increased sulfur-sulfur repulsive interactions. Relative stabilities and differences in the molecularity of the respective transition states that form THT and C_4 dictate product distributions. THT desulfurization to form C_4 occurs via readsorption and subsequent dehydrogenation, evidenced by secondary rates that exhibited negative H_2 dependences. These behaviors suggest that C-S bond activation occurs on a partially (un)saturated intermediate, analogous to behaviors observed in C-C bond scission reactions of linear and cycloalkanes on hydrogen-covered metal surfaces. Our interpretations place HDS in a specific class of more general C-X hydrogenolysis reactions, including hydrodeoxygenation (HDO) that has gained popular appeal in recent biomass conversion processes.

These hydrodearomatization routes, hydrogenolysis and hydrogenation, act as probes for studying hydrogen spillover, a frequently observed phenomenon in bifunctional systems. Indeed, we observe enhancements solely in the rates of thiophene hydrogenation when monofunctional catalysts, which generate equilibrated concentrations of surface H-species, are mixed with materials (e.g. Al_2O_3) that cannot dissociate H_2. Conventional mechanisms that suggest gas phase or surface diffusion of atomic H-species (or H^+-e^- pairs) are implausible across distances along insulating surfaces (i.e. SiO_2, Al_2O_3). We propose, with kinetic-transport models that are consistent with all observed behaviors, that mobility of active H-species occurs through gas phase diffusion of thiophene-derived molecular H-carriers, whose rate of formation on HDS sites can control maximum spillover enhancements. This synergy is disrupted when the ability of thiophene to form these H-carriers is suppressed, leading to an absence of spillover-mediated rates and further challenging any diffusive roles of atomic H-species. Such implications help guide optimal designs of bifunctional cascades to permit the uninhibited access and egress of larger molecules within both catalytic functions.

Dedication

in memory of my maternal grandfather,
a chemical engineer who later devoted his life to civil service,

and

to my parents,
whose advocacy of education and learning has deeply influenced my life.

TABLE OF CONTENTS

ACKNOWLEDGEMENTS

CHAPTER ONE

Introduction to Hydrodesulfurization Catalysis

1.1 Introduction

Hydrodesulfurization (HDS), the reaction by which sulfur is removed from petroleum streams, is a specific category of hydrotreatment processes, a collection of catalytic reactions that saturate bonds (i.e. hydrogenation), remove heteroatoms such as sulfur, nitrogen (i.e. hydrodenitrogenation), and oxygen (i.e. hydrodeoxygenation), and remove metals (i.e. hydrodemetallization) from hydrocarbon feeds. The prevalence of these processes in oil refining is in part a result of their ability to eliminate species that poison reforming and cracking catalysts (e.g. via S and N removal, respectively), minimize catalyst destruction (e.g. via metal removal), and reduce coking (e.g. via double bond saturation) [1]. Furthermore, environmental legislation that restricts the permissible levels of sulfur and aromatic contents continues to challenge the growing need to process heavier, sour crude supplies [2,3]. These trends have increased the demand for hydrotreating to meet both technical and environmental requirements and concurrently shifted focus to reactions (i.e. "deep desulfurization") of polyaromatic sulfur compounds (e.g. substituted dibenzothiophene species), which are among the most recalcitrant toward HDS [4].

Extensive efforts have been made in characterizing the commercial catalysts [5-8], Co- or Ni-promoted MoS_x and WS_x, but rigorous assessment of fundamental HDS mechanisms and developments of accurate structure-function relationships remain absent. Studies that attempt to elucidate the effects of catalyst properties on shaping HDS reactivity, often by measuring rates across a range of supported transition metals at given industrial conditions, have frequently neglected to identify the integrity of catalyst structure and phase under reaction environments. Such ambiguities are further compounded by inaccurate measurements of surface dispersion, particularly in structures exhibiting layered morphologies, via inexact probes [9,10] (e.g. O_2 chemisorption) that depend on the specific sample pretreatments employed. Nevertheless, such negligence has not precluded canonical reports of HDS activity [11] that exhibit volcano-like correlations to "d-electron" character or heat of sulfide formation of the metals, which suggest that optimal catalyst performance is achieved on an intermediate metal-adsorbate binding, purportedly consistent with classic Sabatier principles.

Our approach relies on rigorous studies of thiophene HDS on SiO_2-supported monometallic nanostructures, loaded in tubular packed bed reactors that maintain plug-flow hydrodynamics and avoid axial gradients in concentration. Dilutions of the catalyst bed with inert materials (i.e. SiO_2) serve to eliminate transport artifacts or heat effects that can result from the exothermic nature of these reactions. Extensive characterization of fresh and spent catalysts, coupled with kinetic evidence, reported the surface coverages and bulk phases of the catalyst under relevant HDS conditions and provided insights on the site requirements for reaction. Using thiophene, the monomeric backbone of the most resistant class of organosulfur compounds (i.e. substituted dibenzothiophenes), as a reactant facilitates both the analysis of hydrogen-assisted pathways of dearomatization, namely hydrogenation (to form tetrahydrothiophene) or hydrogenolysis (to form butene or butane and H_2S). The insights gained in these model systems,

which themselves are not well explained in the literature, assist in describing more general features of C-S bond activation, the crucial step of all desulfurization reactions.

Transition metals can undergo bulk transformations to metal sulfides; these transformations are thermodynamically driven and stable phases are determined by (state functions of) temperature and sulfur chemical potential. These phase boundaries are widely established [12] and act as predictive measures of catalyst phase during HDS reaction. Rhenium, in particular, is a transition metal whose phase boundary is within the range of relevant sulfur chemical potentials prevalent at practical HDS operating temperatures. Such properties make Re-based catalysts reasonable candidates in exploring these transitions and their consequences on HDS reactivity. In Chapter Two, we discuss HDS on SiO_2-supported Re and ReS_x catalysts, synthesized from ReO_x precursors. Extensive characterization techniques, such as transmission electron microscopy (TEM), reduction dynamics, and X-ray absorption spectroscopy (XAS), were employed to probe the state of the catalyst under relevant HDS conditions. We conclude, with kinetic evidence, that kinetic barriers prevent the interconversion of Re and ReS_x under conditions (i.e. sulfur chemical potentials, set by H_2S/H_2 ratios in our studies) that should have preferentially stabilized one (or the other) phase. Instead, both catalysts exhibited high (meta)stability and minimal deactivation under continuous operation, indicating a memory of their respective pretreatments and allowing, for the first time, direct comparisons of HDS reactivity between different phases of the same metal at identical reaction conditions.

A similar sequence of elementary steps, derived from measured pressure responses, suggests that thiophene consumption is limited by a first hydrogen addition to thiophene species adsorbed on HDS sites that are partially covered with thiophene (T*) and sulfur adatom (S*) species for both Re and ReS_x. This implies that enhanced rates observed on ReS_x are derived from differences in its surface properties and/or in site accessibility rather than from a change in overall reaction mechanisms. Furthermore, product selectivities to tetrahydrothiophene (THT) and butene/butane (C_4) and their trends with thiophene conversion appear independent of thiophene pressures and H_2S/H_2 ratios, which set relative (equilibrated) surface concentrations of (T*) and (S*), respectively, indicating that all products are formed on similar types of sites. These behaviors avoid the need to attribute selective product pathways to separate hydrogenation or desulfurization sites, as often proposed in the literature [13,14]. Primary THT/C_4 concentration ratios increase with H_2 pressure, reflecting differences in the molecularities of transitions states that lead to their respective formations. Non-zero selectivity to C_4 near zero thiophene conversion suggests primary formation of C_4, without the prerequisite formation of THT. Secondary desulfurization of THT, however, does lead to additional C_4 formation, but their rates exhibit negative dependences on H_2 pressure, indicating that dehydrogenation of THT must occur prior to C-S bond scission. Such behaviors suggest C-S activation occurs on a partially (de)hydrogenated surface intermediate that forms from the most favorable energy balance of weakening the C-S bond, forming C-metal bonds (enthalpic gain), breaking C-H bonds (enthalpic penalty), and forming H_2 molecules (entropic gain). These features share similarities with C-C bond activations, explored extensively in metal-catalyzed n-alkane bond scission [15] and cycloalkane ring opening [16] reactions. Our interpretations, described in fuller detail in Chapter Two, place hydrodesulfurization within the context of more universal hydrogenolysis reactions and challenge former preconceptions of the role of hydrogen in HDS.

As we detail in Chapter Three, similar mechanistic features persist on more noble metals (e.g. Ru and Pt). Previous characterization and kinetic evidence on these systems [17,18] indicated that catalysts formed sulfur-covered, bulk metal clusters under typical HDS conditions [18,19], as predicted by thermodynamics. In contrast to Re catalysts, Pt and Ru exhibited a kinetic ease in phase transformation, likely as a consequence of the existing structural isotropy between the two phases, which is absent between anisotropic layered nanostructures (e.g. ReS_x) and isotropic metal clusters (e.g. Re). Similar functional forms of the rate expression derived for Re-based systems can also describe kinetic data on supported clusters of Ru and Pt; however, slight differences in their kinetic H_2 dependences reflect the equilibrated formation of surface monohydrothiophene species on S-covered noble metal (Ru, Pt) surfaces prior to a kinetically-relevant (second) H-addition step. Despite these differences, C-S bond activation requires the formation of partially-saturated intermediates on all surfaces, but actual primary and secondary product distributions were influenced by metal identity, indicating its role in stabilizing relevant transition states formed on HDS surfaces.

Consistent with other HDS reports [11,20,21], we find absolute turnover rates range over multiple orders of magnitude as a function of metal identity; however, rigorous comparative studies between catalysts require assessments of rate constants or of their ratios. We find that rate differences exhibited on Re, Pt, and Ru are more significantly influenced by their (effective) kinetic rate constants (rather than by differences in the adsorption constants of various abundant surface species). These kinetic rate constants reflect the energy of the transition state referenced to those of gas phase reactants and empty HDS sites, thus, the accuracy of their values depends on accurate counts of these "empty" sites, which becomes nontrivial for reactions that occur on sulfur-covered surfaces. Sulfur adatoms bind strongly to metal sites, but vacant (HDS) sites are formed upon desorption of weakly-bound sulfur adatoms, which can occur as a result of repulsive sulfur-sulfur interactions that lower the heat of sulfur adsorption at sufficiently high sulfur coverages [22,23]. Turnover rates are normalized by the number of exposed metal atoms and not of these steady-state HDS sites; this seemingly subtle distinction significantly affects the rigorous comparison between rates measured on different metal catalysts. Still, correlations between rate (constants) and metal-sulfur bond energy persist, suggesting that the density of vacant sites on exposed metal surfaces is influenced by the intrinsic sulfur affinity of a metal.

We expand on insights gained from these monofunctional systems (discussed fully in Chapter Three) to study their applications in bifunctional cascades, a technique common in the practice of catalysis. Such methods rely on a synergy between two (or more) functions to enhance performance, either by increasing rates or improving selectivity. Of greatest notoriety is the synergy reported for hydrogen spillover phenomenon [24,25], whereby hydrogenation or reduction can be observed on surfaces that cannot themselves generate the active hydrogen species implicated in these reactions. This cascade effect relies on nearby functions to form active hydrogen intermediates that are then transferred beyond atomic distances. Gas phase or surface diffusion of neutral atomic hydrogen species (either in the form of open-shell radicals or proton-electron pairs [25-27]) formed on metal surfaces to non-conducting surfaces (such as SiO_2 or Al_2O_3) is implausible because such mechanisms would require reaction barriers on the order of metal-hydrogen bond strengths. Thus, we propose mechanisms that, instead, involve a molecular H-carrier; the mobility and requirements for such hydrogen carrying species, along with their catalytic consequences, form the subject of discussion in Chapter Four.

Indeed, we unequivocally observe enhancements in thiophene conversion rates upon addition of γ-Al$_2$O$_3$ to SiO$_2$-supported Pt and Ru clusters, consistent with the presence of spillover-mediated pathways. Selective enhancements in the rate of THT formation are consistent with the ability of (weak) acid sites to activate thiophene for H-transfer but not to catalyze bond (e.g. C-S, C-C) scission events. Thus, while hydrogen spillover mechanisms become of limited utility toward any heteroatom removal strategies of thiophene, their potential applicability is relevant in the hydrogenolysis of substituted dibenzothiophene compounds, whose more saturated cyclic derivatives (e.g. tetrahydrodibenzothiophene or hexahydrodibenzothiophene) were observed to undergo more facile desulfurization [28].

Spillover-mediated turnover rates (i.e. measured from the additional rate of THT formation) initially increase with acid-to-metal ratios (β) before reaching asymptotic values. These maximum (asymptotic) limits are consistent with the scavenging of unstable, active H-carrying intermediates, at concentrations below analytical detection, by reaction on acid sites. At (sufficiently) high β values, spillover pathways are limited by H-carrier formation on metal (i.e. Pt or Ru) surfaces, further evidenced by spillover-mediated rates that are similarly inhibited by increasing H$_2$S/H$_2$ ratio (i.e. S* concentration), which affects only the metal function, despite equilibrated H$_2$ dissociation on metal HDS sites at these conditions [18]. Such behaviors challenge the purported participation of atomic hydrogen species, whose equilibrated (i.e. constant) concentrations should have led to similar H-transfer rates at constant H$_2$ pressure over the range of H$_2$S/H$_2$ ratio. We propose and develop a kinetic-transport model that involves a thiophene-derived, molecular H-carrier, which serves as a shuttle that transfers active hydrogen species to activated molecules (i.e. thiophene) adsorbed on acid functions via gas phase diffusion. The diffusive nature of these carriers are further substantiated by lower observed rates with decreasing proximity, systematically probed by increasing domain sizes of both functions and consequently imposing diffusional constraints, at constant β values.

All kinetic evidence implicates an open-shell, monohydrothiophene species as the H-carrier that facilitates bifunctional routes, consistent with spillover-mediated rates that exhibited kinetic half-order H$_2$ dependences on Pt and Ru. In contrast, enhancements were not observed for bifunctional ReS$_x$ system, whose monofunctional rates themselves carry kinetic half-order dependences on H$_2$ pressures, thereby preventing the formation of H-carriers that are independent of the kinetically-relevant step along the monofunctional reaction coordinate of sequential surface hydrogenation (i.e Horiuti-Polanyi mechanism). We can also suppress the formation of these H-carriers by selectively excluding thiophene from accessing metal clusters by exploiting recent synthetic advancements in encapsulated noble metals within zeolite frameworks [29], such as FAU (0.74 nm aperture size) and LTA (0.41 nm aperture size) which permit and prevent the entry of thiophene molecules (0.46 nm kinetic diameter), respectively. The absence of appreciable activity on Pt encapsulated within LTA frameworks even upon the addition of γ-Al$_2$O$_3$, indicate that access of H$_2$ (0.29 nm kinetic diameter) alone is a necessary but *insufficient* condition for spillover-mediated routes. Such consequences inform the optimal designs of bifunctional cascading processes, which must allow the unhindered access of larger hydrocarbon molecules to both active H-generator (i.e. metal) and H-acceptor (i.e. acid) sites.

1.2 References

1. *Catalysis Science and Technology*; H. Topsøe, B. S. C., F.E. Massoth in: J.R. Anderson, M. Boudart Ed.; Springer-Verlag: New York, 1996; Vol. 11.
2. Song, C. S. *Catal Today*. **86** (2003) 211.
3. Stanislaus, A.; Marafi, A.; Rana, M. S. *Catal Today*. **153** (2010) 1.
4. Girgis, M. J.; Gates, B. C. *Ind Eng Chem Res*. **30** (1991) 2021.
5. Prins, R.; De Beer, V. H. J.; Somorjai, G. A. *Catalysis Reviews*. **31** (1989) 1.
6. Besenbacher, F.; Helveg, S.; Lauritsen, J. V.; Laegsgaard, E.; Stensgaard, I.; Norskov, J. K.; Clausen, B. S.; Topsoe, H. *Phys Rev Lett*. **84** (2000) 951.
7. Lauritsen, J. V.; Kibsgaard, J.; Olesen, G. H.; Moses, P. G.; Hinnemann, B.; Helveg, S.; Norskov, J. K.; Clausen, B. S.; Topsoe, H.; Laegsgaard, E., et al. *J Catal*. **249** (2007) 220.
8. Neurock, M.; Vansanten, R. A. *J Am Chem Soc*. **116** (1994) 4427.
9. Hensen, E. J. M.; Kooyman, P. J.; van der Meer, Y.; van der Kraan, A. M.; de Beer, V. H. J.; van Veen, J. A. R.; van Santen, R. A. *J Catal*. **199** (2001) 224.
10. Zmierczak, W.; MuraliDhar, G.; Massoth, F. E. *J. Catal.* **77** (1982) 432.
11. Pecoraro, T. A.; Chianelli, R. R. *J Catal*. **67** (1981) 430.
12. Shatynski, S. *Oxid Met*. **11** (1977) 307.
13. Borgna, A.; Hensen, E. J. M.; van Veen, J. A. R.; Niemantsverdriet, J. W. *J Catal*. **221** (2004) 541.
14. Kasztelan, S.; Guillaume, D. *Ind Eng Chem Res*. **33** (1994) 203.
15. Flaherty, D. W.; Iglesia, E. *J. Am. Chem. Soc*. **135** (2013) 18586.
16. Flaherty, D. W.; Uzun, A.; Iglesia, E. *The Journal of Physical Chemistry C*. **119** (2015) 2597.
17. Wang, H. M.; Iglesia, E. *J Catal*. **273** (2010) 245.
18. Wang, H. M.; Iglesia, E. *Chemcatchem*. **3** (2011) 1166.
19. Wang, H.-M.; Iglesia, E. *J. Catal.* **273** (2010) 245.
20. Hensen, E. J. M.; Brans, H. J. A.; Lardinois, G. M. H. J.; de Beer, V. H. J.; van Veen, J. A. R.; van Santen, R. A. *J Catal*. **192** (2000) 98.
21. Toulhoat, H.; Raybaud, P. *J. Catal.* **216** (2003) 63.
22. McCarty, J. G.; Wise, H. *J. Chem. Phys.* **74** (1981) 5877.
23. McCarty, J. G.; Sancier, K. M.; Wise, H. *J Catal*. **82** (1983) 92.
24. Boudart, M. In *Advances in Catalysis*; D.D. Eley, H. P., Paul, B. W., Eds.; Academic Press: 1969; Vol. Volume 20, p 153.
25. Sermon, P. A.; Bond, G. C. *Catal. Rev.* **8** (1973) 211.
26. Conner, W. C., Jr.; Falconer, J. L. *Chem. Rev. (Washington, D. C.)*. **95** (1995) 759.
27. Roland, U.; Braunschweig, T.; Roessner, F. *J. Mol. Catal. A: Chem.* **127** (1997) 61.
28. Wang, H.; Prins, R. *J. Catal.* **264** (2009) 31.
29. Wu, Z.; Goel, S.; Choi, M.; Iglesia, E. *J Catal*. **311** (2014) 458.

CHAPTER TWO

Mechanism and Site Requirements for Thiophene Hydrodesulfurization on Supported Rhenium Metal and Sulfide Catalysts

Abstract

Supported Re nanostructures, under industrially relevant hydrodesulfurization (HDS) conditions, retained memory of their pretreatment in H_2 or H_2S, which led to the initial formation of metal and sulfide phases, respectively. Total rates were at least 80-fold greater on the latter at all conditions, but both materials were fully described by similar rate expressions, suggesting that HDS reactions proceed through a similar sequence of elementary steps regardless of phase. Thiophene HDS led to tetrahydrothiophene (THT) and butene/butane products occurred, which were formed on similar types of sites from respective transition states that were derived from a pool of partially-hydrogenated, thiophene-derived surface intermediates. Sulfur removal, either of thiophene or of THT (via secondary reactions), requires the formation of a surface intermediate that sufficiently weakens the C-S bond for cleavage, analogous to mechanistic behaviors observed in other hydrogenolysis reactions (i.e. C-C, C-O). These kinetically-accessible vacant sites serve as reaction intermediates, formed from the removal of a reversibly-bound S-atom, which becomes kinetically viable at sufficiently high sulfur coverages as a result of increased S-S repulsions. The relative density of these reactive sites on surfaces can be described by its intrinsic metal-sulfur (M-S) bond energy; weaker M-S bond energies exhibited by ReS_x relative to S-covered Re can lead to a larger fraction of such available sites, which can account for the enhanced rates observed.

2.1   Introduction

Hydrodesulfurization (HDS), the reaction by which sulfur atoms are removed from organosulfur compounds through cleavage of the carbon-sulfur bond, has been studied extensively on transition metal sulfide catalysts [1-3]. The structure and reactivity of Co(Ni)Mo(W) sulfides [3-10], in particular, have garnered the most attention, because of their importance in heteroatom removal from petroleum streams to meet regulations that restrict sulfur levels in marketable fuels [11,12]. Our understanding of HDS mechanisms remains incomplete, at least in part because of the challenges in the structural characterization and active site identification brought forth by the anisotropy and non-uniformity of practical catalysts, which continue to lead to contradictory claims for mechanistic details and site requirements [13]. Monometallic transition metals and their corresponding sulfides are also active for HDS catalysis [1,14-24]; differences in reactivity among these catalysts, often by several orders of magnitude, have been attributed to metal-sulfur (M-S) bond strengths, leading to volcano-type reactivity curves and to maximum rates on surfaces with intermediate M-S bond strengths [9,14,17,23], or to monotonic inverse relationships between rates and M-S bond energies [22]. The anisotropic nature of some metal sulfides, uncertainties in the structure and phase of materials during catalysis, and the ubiquitous gradients in S-chemical potential and surface coverage along the catalyst bed make it difficult to express reactivity as rigorous turnover rates and prevent accurate reactivity comparisons among catalysts and the concomitant development of appropriate reactivity descriptors.

The intrinsic reactivity and mechanism of HDS on well-defined silica-supported Pt and Ru metal clusters were reported previously [18,19]. Here, we extend these findings to Re-based catalysts, motivated by reports of the high HDS reactivity on Re in both metal and sulfide forms [24-31], which, in some instances exceeds that of MoS_2, the purported active phase in $CoMoS_x$ commercial catalyst [24,26,29]. In our earlier studies [18,19], S-covered clusters with a metallic bulk were present during HDS catalysis at practical conditions for both Pt and Ru, irrespective of whether the materials were initially treated to form their sulfide or metallic forms. In contrast, we show here, through extensive characterization, that Re and ReS_2 retain their initial phase during HDS catalysis, thus exhibiting reactivities that depend very sensitively on the initial treatments.

The retention of Re and ReS_2 imposed by initial treatments allows direct comparisons of the reactivity and mechanism for HDS reactions on Re/SiO_2 and on ReS_x/SiO_2, without distracting changes in structure or composition with changes in S-chemical potential. We find that surfaces of ReS_x structures are nearly 100-fold more reactive than those of sulfur-saturated Re metal clusters; such reactivity differences may be even greater because the lamellar ReS_x structures [13] made it difficult to estimate their surface areas, leading us to use the total number of Re atoms (instead of those at surfaces) to normalize HDS rates. The rate equations derived from exhaustive kinetic data obtained over practical pressures of thiophene, H_2, and H_2S were similar for ReS_x and Re surfaces, suggesting the involvement of similar sites and mechanisms, in spite of their different structure, composition, and catalytic reactivity.

The rate equations and their mechanistic analysis indicate that HDS reactions occur via Mars van Krevelen redox cycles ubiquitous in oxidation catalysis [32], in this case the oxidation of H_2 by thiophene. The vacant sites involved as HDS intermediates form via sulfur reactions with the H_2 reductants to produce H_2S. The "vacancy" is then oxidized by thiophene-derived S-atoms, formed via C-S cleavage, thus completing a catalytic turnover. Equilibrated reaction of one half of the cycle, in particular between gaseous H_2 and surface S-atoms, allows S-chemical potential to be set by the ratio of H_2S to H_2 pressure, but absolute fractional S-coverage of the catalyst is determined by thermodynamic equilibrium constants, which depends on both the reaction temperature and the chemical affinity to sulfur of the particular metal catalyst. Available vacant sites form in higher fractions on surfaces exhibiting weaker M-S bond energies, leading to higher observed turnover rates. Lower turnover rates observed on S-covered Re metal relative to its corresponding sulfide is arguably a general result of its higher metal-sulfur (M-S) binding energy [33,34] and concomitant decrease in the availability of required vacancies.

Here, we report thiophene turnover rates and product selectivities on Re metal clusters and sulfide catalysts. Through our analyses, thiophene HDS products (i.e. tetrahydrothiophene (THT) and C_4 products) are derived from a pool of surface intermediates formed by a kinetically-relevant H-addition to adsorbed thiophene species. True desulfurization (i.e. C_4 formation) occurs from transition states involving a degree of unsaturation on S-covered metal or sulfide surfaces that can activate the C-S bond, analogous to requirements involved in C-C bond activation for hydrogenolysis of cyclo-, iso-, and n-alkanes on H-covered metal surfaces [35-38]. Similar kinetic behaviors observed for both Re metal clusters and ReS_x suggest that the same mechanism occurs on both catalysts, irrespective of whether reactions occur on minority empty sites on a nearly S-saturated metal surface or on those acquired from the removal of a lattice S-atom on a bulk sulfide surface

2.2 Methods

2.2.1 Catalyst synthesis

Supported Re catalysts were prepared using SiO_2 (Cabosil, HS-5, 310 m^2 g^{-1}) that was acid-washed and treated in flowing dry air (Praxair, 99.99%, 1.0 cm^3 g^{-1} s^{-1}) at 773 K (0.033 K s^{-1}) for 4 h. Aqueous solutions of NH_4ReO_4 precursors (Aldrich, 99%+), were impregnated onto SiO_2 support by incipient wetness impregnation methods [28-30,39,40]. These samples were kept in vacuum at ambient temperature for >12 h and then treated overnight in flowing dry air (Praxair, 99.99%, 1.0 cm^3 g^{-1} s^{-1}) at 353 K. High Re contents (e.g. 15% wt.) required sequential impregnation cycles because of the limited NH_4ReO_4 solubility, with intervening overnight drying cycles in stagnant air at 353 K [29,40]. The samples were then treated at 573 K in flowing dry air (Praxair, 99.99%, 1.0 cm^3 g^{-1} s^{-1}; 0.033 K s^{-1} ramp rate) for 3 h, except the 1% wt. sample, for which this high temperature air treatment was not carried out.

Re metal catalysts were prepared by treating in flowing H_2 (Praxair, 99.999%, 1.0 cm^3 g^{-1} s^{-1}) at 773 K (0.05 K s^{-1}) for 2 h at ambient pressure and then passivated (Praxair, 0.1% O_2/He, 1.0 cm^3 g^{-1} s^{-1}; ambient temperature) for 2 h. ReS_x catalysts were prepared by exposing air-treated samples to flowing 5% H_2S/balance He at 773 K (0.05 K s^{-1}) and ambient pressure for 2 h (Praxair, certified mixture, 45 cm^3 g^{-1} s^{-1}). Table 2.1 lists the samples referenced in this study and their corresponding structural properties and composition.

2.2.2 Catalyst characterization

Re contents were measured by inductively-coupled plasma optical emission spectroscopy (ICP-OES; Galbraith Laboratories, Inc.). Temperature-programmed reduction (TPR) and X-ray diffraction (XRD; Cu Kα radiation λ = 0.15418 nm, Siemens D500) were carried out after samples were treated in air but before subsequent exposure to H_2 or H_2S/He. The effluent H_2 concentration in TPR experiments was measured by thermal conductivity using a bridge current of 150 mA during exposure of samples to flowing 1% H_2/Ar (Praxair, certified mixture, ~90 cm^3 s^{-1} g^{-1}) at ambient pressure and temperature ramping to 1073 K at 0.17 K s^{-1}. The thermal conductivity detector was calibrated by reduction of a CuO standard. Transmission electron microscopy (TEM), oxygen chemisorption experiments and XRD were used to determine cluster size and metal dispersion. TEM was carried out on fresh samples, treated at 773 K (0.05 K s^{-1}) in flowing H_2 (Praxair, 99.999%) or 5% H_2S/He (Praxair, certified mixture); these samples were then exposed to simulated HDS conditions (573 K, 3.0 MPa H_2, 1.0 kPa H_2S, 5 h) and subsequently cooled in flowing He (Praxair, 99.999%) and passivated with 0.5% O_2/He (Praxair, certified mixture) at ambient conditions. TEM samples (fresh and post-HDS) were prepared by dispersing these collected powders in acetone and placing the suspension onto an ultrathin carbon film supported on a 400 mesh copper grid (Ted Pella, Inc.). The grids were dried at ambient conditions, and micrographs were obtained using a JEOL 1200 EX TEM operated at 80 kV or a Philips 420 TEM operated at 120 kV. Surface-averaged cluster sizes were calculated from measurements on more than 300 Re particles using the equation $\Sigma_i n_i d_i^3 / \Sigma_i n_i d_i^2$, where n_i represents the frequency of clusters exhibiting a diameter of d_i. The dispersity index (DI) was calculated by normalizing the surface-averaged diameter by its number-averaged diameter ($\Sigma_i n_i d_i / \Sigma_i n_i$). Values less than 1.5 are typically considered to reflect uniformly-sized clusters.

Oxygen chemisorption was also used to measure Re dispersion because of the oxophiic nature of Re surfaces. Isotherms were measured on Re/SiO$_2$ samples at 0.1-50 kPa O$_2$ pressure and 298 K, 323 K, and 473 K after treating passivated samples in pure H$_2$ flow (Praxair, 99.999%, 17 cm^3 s^{-1} g^{-1}) at 773 K (0.05 K s^{-1}) for 1 h and then cooling to adsorption temperature in vacuum (Pfeiffer Vacuum IPS 100) for at least 2 h. Uptakes were measured volumetrically. The dispersion was calculated by assuming a 0.4:1 O:Re$_s$ stoichiometry (as discussed in Section 2.3.2). XRD was used to obtain volume-averaged cluster diameters using Rietveld refinement methods (Maud software [41], Section 2.8.1). Such chemisorption techniques were not used for ReS$_x$ materials because of reported difficulty in measuring accurate dispersions of layered structures [25].

TPR experiments were used to measure the S-content in catalyst samples (TPR-S to distinguish it from experiments intended to measure O-removal from air-treated samples). H$_2$ and H$_2$S/He treatments were performed as described in Section 2.2.1; samples were then cooled in flowing He to ambient temperature before exposure to H$_2$ and temperature ramping. Some samples were then cooled to typical HDS temperatures (573 K) and exposed to H$_2$S/H$_2$ mixtures (3.0 MPa H$_2$, 3.0 kPa H$_2$S) for 3 h to simulate the S-chemical potentials present during HDS catalysis. The sample (~0.015 g of fresh or spent catalysts) was then heated at 0.17 K s^{-1} to 873 K or 973 K and held at that temperature for 1 h while flowing a 2% H$_2$ /8% Ar/He mixture (Praxair, certified mixture, 222 cm^3 s^{-1} g^{-1} total flow). The H$_2$S formed was detected by mass spectroscopy (Leybold Inficon, Transpector Series) and quantified using calibrated mixtures of known H$_2$S concentrations to obtain S/Re ratios for each sample.

Fresh and post-HDS samples (prepared using the H$_2$S/H$_2$ mixtures described above for TEM analysis) of 5% nominal wt. samples of ReS$_x$/SiO$_2$ and Re/SiO$_2$ (0.41 dispersion, Table 2.1) were also examined using X-ray absorption spectroscopy (XAS). After cooling to ambient temperatures in He, samples were rapidly transferred in N$_2$ into a XAS cell. The Re L$_{III}$-edge was used to obtain the X-ray absorption near-edge structure (XANES) and extended X-ray absorption fine structure (EXAFS) at the Stanford Synchrotron Research Laboratory (SSRL, beamline 4-1). EXAFS data were extracted from the raw files using the Athena software, and the fitting was achieved with the Artemis software over ranges of 3.5-16.1 Å^{-1} k (photoelectron wave number) and 1.5-5.7 Å R (distance between absorbing and scattering atoms) for the metal sample and of 2.0-15.9 Å^{-1} k and 1.0-3.5 Å R for the sulfide sample following scattering models reported in the literature [42,43].

2.2.3 HDS rate and selectivity measurements

Turnover rates and product selectivities were measured in a packed-bed reactor with plug-flow hydrodynamics, as described in previous studies on Ru and Pt [18,19]. Re metal samples were diluted with SiO$_2$ (Cab-O-Sil, HS-5, 310 m^2 g^{-1}) at 1:1 and 4:1 diluent:catalyst mass ratios whereas ReO$_x$ powders, intended as precursors to ReS$_x$ via *in situ* sulfidation were either diluted at 1:1 or undiluted. The powders were then pressed and sieved to retain 0.125- to 0.180-mm aggregates. The aggregates (diluted or undiluted) were physically mixed with quartz granules of the same size to avoid bed temperature gradients that can corrupt the chemical origins of measured kinetic data. Calculations using Mears' criterion for internal transport artifacts confirmed the absence of such mass or heat transfer limitations (Section 2.8.2).

After *in situ* treatment in pure H_2 (Praxair, 99.999%, 2.9 cm^3 g^{-1} s^{-1}) or 5% H_2S/He (Praxair, certified mixture, 45 cm^3 g^{-1} s^{-1}) to form Re/SiO_2 or ReS_x/SiO_2, respectively (Section 2.2.1), the reactor temperature was decreased to 573 K, and H_2 (Praxair, 99.999%) and H_2S (0.5% H_2S/H_2, Praxair, certified mixture) pressures were set to the desired values. Thiophene (Alfa Aesar, 99%) and decane (Aldrich, 99+%), which was used as the thiophene solvent and as an internal standard, were vaporized into the H_2S/H_2 flow using a high-pressure syringe pump (Isco 500D); the injection point and all transfer lines thereafter were kept above 433 K to avoid condensation.

The speciation and concentrations of all compounds in the effluent stream were measured by on-line gas chromatography (Agilent 6890) using a methyl silicone capillary column (HP-1, Agilent, 25 m × 0.32 mm × 0.52 μm film) connected to a flame ionization detector and a Porapak Q packed column (Supelco, 1.82 m × 3.18 mm, 80-100 mesh) connected to a thermal conductivity detector. Rates are reported as the molar rate of conversion of thiophene normalized per surface g-atom for Re catalyst from TEM and/or oxygen chemisorption and per total Re atom for ReS_x because of their highly dispersed lamellar structure, which prevented accurate dispersion values as methods to quantify the number layered surface sites from TEM images [13,20] remain controversial [20]. Residence times were varied by changing the H_2, H_2S, and thiophene flow rates using electronic controllers (Parker, Series 201) while controlling total pressures using a back pressure regulator (Mity Mite) with a Teflon diaphragm (Freudenberg Oil and Gas). Co-feeding H_2S at the inlet, operating at low conversions (3-15%), and extrapolating reaction rates to zero residence time served to minimize axial gradients in thiophene and H_2S concentrations, thus ensuring differential conditions. Kinetic responses were collected over a wide range of practical H_2 (1-3 MPa), H_2S (0.2-3.0 kPa), and thiophene (1-10 kPa) pressures.

2.3   Results and Discussions

2.3.1   *Structure of Re catalysts and the effect of pretreatment*

Two distinct kinetically-stable phases of Re could be formed from ReO_x precursors, initially prepared by thermal treatment in air. Re metal clusters formed in Re/SiO_2 after treatment in H_2 and Re sulfide lamellar structures in ReS_x/SiO_2 after exposure to H_2S. X-Ray diffractograms showed that thermal treatment in air at 573 K formed Re(VII) oxide (Section 2.8.3), consistent with reported Re-O phase diagrams [44]. The reduction profiles of ReO_x in H_2 showed sharp features, characteristic of autocatalytic reduction processes often observed in the reduction of metal oxides [40,45,46]; these profiles showed features below 773 K (Section 2.8.4), consistent with full reduction of Re(VII) to Re^0, as also shown by H_2/Re consumption ratios of 3.45-3.55. TEM images showed quasi-spherical Re clusters (Fig. 2.2.1a) after H_2 treatment at 773 K and lamellar structures (Fig. 2.2.1c), typical of ReS_2 phases, after exposure of Re_2O_7 to H_2S at 773 K. The EXAFS spectrum (Fig. 2.2a) for Re clusters (5% nominal wt. sample) formed after H_2 treatment at 773 K appears consistent with our measurements on standard Re foil (not shown) and those reported for metal Re nanoparticles in the literature [43]. The formation of ReS_x is apparent from the lamellar structure in micrographs (Fig. 2.2.1c), S/Re ratios of 2.05 (from TPR-S), and from an EXAFS spectrum (Fig. 2.2b) that resembles that of ReS_2 [42].

The stability of Re metal and ReS$_2$ phases, detected after treating Re$_2$O$_7$ precursors in H$_2$ or H$_2$S, were probed by structural analysis upon their exposure to streams with S-chemical potentials similar to those present during HDS catalysis. TEM analysis indicates that the structure of Re metal and ReS$_x$ remains unchanged during catalysis (Figs. 2.1b and 2.1c), even though some sulfur has been removed from ReS$_2$ (S/Re=1.32) (Fig. 2.3b) as a result of partial reduction [47,48] and some chemisorbed sulfur is present in Re metal samples (S/Re=0.10), occupying more than half of exposed Re atoms (dispersion=0.17, Table 2.1). Surface-averaged diameters were similar for Re/SiO$_2$ before (6.6 nm) and after (5.6 nm) exposure to S-chemical potentials prevalent during HDS. S/Re ratios in the spent Re metal sample (i.e. exposed to H$_2$S/H$_2$ ratios) were below unity (Fig. 2.3), consistent with near monolayer S-coverages (S/Re$_s$=0.6) depending on S-coordination. Incipient evolution of H$_2$S appears to occur at similar temperatures (873K, Fig. 2.3), suggesting similar reducibility of both S-covered Re metal surfaces and ReS$_x$ nanostructures.

Radial distribution functions resulting from Fourier transforms of processed EXAFS spectra for Re$_2$O$_7$ precursors treated in either H$_2$ or H$_2$S differ significantly, but exhibit similar features before and after exposure to the S-chemical potentials prevalent during HDS catalysis (Fig. 2.2). Raw XAS data, which include transmitted and incident X-ray intensities (I$_t$ and I$_0$, respectively), were averaged for a given sample and processed to acquire adsorption coefficient (μ) as function of energy, based on I$_t$=I$_0$e$^{-\mu x}$ (sample thickness, x). Background subtraction and normalization of μ at the EXAFS region lead to χ(E), which can be regressed to the EXAFS equation; the EXAFS equation is a summation of constructive and destructive interferences resulting from photoelectron scatterings, fitted by single and multiple scattering pathway models. Regression of our data, facilitated by inputting crystallographic information [42,43], gave coordination numbers and bond lengths (Re-Re, Re-S) consistent with EXAFS reports [42,43], which were evaluated through the first and third coordination shells for ReS$_x$ and Re, respectively. A L$_{III}$ Re-S first shell, single scattering path was included (Fig. 2.2c) in the fitting of the spent Re/SiO$_2$ sample (that was exposed to relevant S-chemical potentials), resulting in a Re-S length shorter than that in ReS$_x$. The Re-Re scattering features overlap with the Re-S coordination feature, however, making regressed fine structure spectra equally well described with and without a Re-S scattering path; thus S-contents from TPR-S remain the definitive evidence for the presence of chemisorbed sulfur (i.e. S/Re ratios) after HDS catalysis (Fig. 2.3c). The fine structure of ReS$_x$ samples before and after HDS catalysis are similar, even though their S-contents differ (S/Re=2.05 and 1.32, from TPR-S, respectively). As in the case of MoS$_x$ and RuS$_x$, these data may reflect the absence of structural ReS$_x$ transformations even upon removal of nearly half of the S-atom [47]. We conclude from these XAS spectra and their analysis that changes in the S-content is restricted to the near-surface regions of ReS$_x$.

The white line features at the Re L$_{III}$ edge become less intense (i.e. peak areas, μ(E)·dE) after Re metal clusters are exposed to the S-chemical potentials prevalent during HDS catalysis. This trend would indicate that Re atoms become more reduced as a layer of chemisorbed sulfur forms, directionally inconsistent if sulfur were to "oxidize" the metal (i.e. decreasing the occupancy of d-states). Instead, the decrease in white line intensity may be a result of a more covalent interaction between the metal and S-atom [49], resulting in electron donation from sulfur to Re metal d-bands (i.e. increasing the occupancy of d-states) upon adsorption. An increase in the white line intensity was observed after ReS$_x$ was exposed to S-chemical potentials

prevalent during HDS; the removal of sulfur as a result of this treatment, as evidenced by lower S-content (via TPR-S), may serve to decrease the electron density around the Re center, in this case, leading to lower occupancy of Re d-states. Comparisons of the white line intensities between different materials is quantified by the difference in their adsorption coefficients ($\Delta\mu$, Fig. 2.4, inset), near the edge energy (XANES region), which further emphasize the distinct chemical nature of samples before and after exposure to S-chemical potentials prevalent in HDS for both Re/SiO$_2$ (Fig. 2.4, inset, (i)) and ReS$_x$/SiO$_2$ (Fig. 2.4, inset, (ii)). Significant discrepancies in XANES features between the two spent phases (Fig. 2.4, inset, (iii)) highlight the absence of phase interconversion despite prolonged exposure of the samples to the same S-chemical potentials.

Exposure of these two materials to identical HDS reaction conditions (3 MPa H$_2$, 2.5 kPa thiophene, 573 K) did not result in any changes in HDS rates or selectivities over extended periods of time (~100 h) (Fig. 2.5). ReS$_x$/SiO$_2$ gave turnover rates nearly 100-fold higher than Re/SiO$_2$, even when rates were normalized by the total number of Re atoms, thus representing a lower bound for its turnover rates. The H$_2$S/H$_2$ ratios used in this study would have caused phase transitions between Re and ReS$_2$, according to the reported thermodynamics of the bulk compounds [50]; yet, the two materials differed markedly in turnover rates and remained different throughout the course of HDS reactions, indicating that they preserved the metastable phase imposed by their respective initial treatments in H$_2$ or H$_2$S.

The metastable nature of ReS$_x$/SiO$_2$ was confirmed by their treatment in H$_2$ at the same conditions (Section 2.2.1) as Re$_2$O$_7$/SiO$_2$ samples. HDS turnover rates (normalized by total Re atoms) decreased 5-10 fold after such treatments and did not change with time. The subsequent treatment of this sample in H$_2$S (5 kPa, 773 K, 2 h) did not restore the reactivity observed on ReS$_x$/SiO$_2$ samples that were prepared via direct H$_2$S treatment of Re$_2$O$_7$/SiO$_2$ sample (Section 2.8.5). These data, taken together with the S-contents, X-ray diffractograms, and X-ray adsorption spectra of samples exposed to S-chemical potentials prevalent during HDS catalysis, show that the nucleation of ReS$_2$ from Re metal clusters is not possible, even at S-chemical potentials much larger than those predicted by thermodynamics. Such kinetic hurdles seem to reflect the barriers imposed by extensive structural changes from isotropic metal phases to lamellar sulfides, which is also observed in the facile formation of carbides and nitrides from oxides, but not from metals [51-53]. Lower relative physical densities of oxide and sulfide phases and requirements for heteroatom diffusion may inhibit dense metal particles from undergoing phase transformations. Thus, while bulk thermodynamics predict stable metal phases at low S-chemical potentials, nanostructures of ReS$_x$ may be thermodynamically stable at such conditions as a result of its size [54] implicating metal Re clusters as the kinetically-trapped, metastable structures during catalysis.

2.3.2 *Surface dispersion of rhenium metal and sulfide catalysts*

Our previous characterization of Ru and Pt HDS catalysts by TEM and H$_2$ uptakes gave consistent metal dispersions [18,19]. The activated nature of H$_2$ dissociation on Re has led, however, to ambiguous H:Re adsorption stoichiometries [39,55-58], rendering such methods unreliable. Similar discrepancies have been reported for CO:Re$_s$ and O:Re$_s$ values [56]. Also, CO can bind in linear or bridged forms and O$_2$ often forms subsurface oxides [59]. Yet, the oxophilic

nature of Re metal makes O_2 chemisorption uptakes the more appropriate choice, as long as O-atom diffusion can be minimized by the choice of conditions.

The number of O-atoms adsorbed would give Re dispersions for 1:1 $O:Re_s$ stoichiometries (Section 2.8.6) but previous studies report values ranging from 0.5:1 to 1:1 [56,59,60]. Therefore, we determined its value by comparing diameters calculated from chemisorptions uptakes (with the assumption of quasi-spherical clusters) with TEM-derived surface-averaged diameters. TEM-derived size distributions are unimodal (e.g. 5% wt. and 15% nominal wt. loadings of Re/SiO_2; Fig. 2.6) and narrow (1.2-1.3 dispersity index); their surface-averaged diameters are 2.4 nm and 6.9 nm, respectively, corresponding to Re dispersions of 47% and 17%. When compared with the diameters obtained from O_2 uptakes, TEM-derived diameters give $O:Re_S$ stoichiometry of 0.34:1 and 0.41:1 respectively, indicative of binding at bridging two-fold and three-fold sites. Decreases in $O:Re_s$ stoichiometry in smaller particles may reflect preferential three-fold O-coordination, perhaps as a result increased O-Re bond energies. Adsorption isotherms were measured at 298 K, 323 K, and 373 K (Section 2.8.6) with the same saturation uptakes achieved at 298 K and 323 K, avoiding increased O/Re ratios observed at 373 K presumably from subsurface oxidation. TEM was unable to give accurate cluster size distributions for 1% wt. Re/SiO_2, because of the small number and size of Re clusters; therefore, its dispersion (95%) was measured from O_2 uptakes with $O:Re_s$ stoichiometry of 0.4:1, as the mean value of the two samples with higher Re contents.

Rietveld refinement of X-ray diffractograms were also used to estimate Re diameters. The volume-averaged diameter was 13 nm for the 15% wt. Re/SiO_2 (diffractogram and fitting shown in Section 2.8.1) and was larger than TEM-derived surface-averaged values. XRD is a bulk technique, therefore its particle size estimate was compared to the volume-averaged diameter of the size distribution measured from TEM (7.3 nm). The different values may reflect inaccuracies in accounting for the contributions of a few large particles (not observed in TEM) toward narrowing crystallographic peaks, despite efforts in refining the data.

A quantitative determination of the dispersion of lamellar ReS_x is not feasible from TEM or uptake data. Even the protocols proposed to estimate their size and numbers of layers (e.g. to obtain the number of edge sites) require assumptions about symmetry and orientation and the transformation of a two-dimensional projected image into its full three-dimensional features [20]. O_2 uptakes, often used to titrate surface sites in HDS catalysts [14], merely report the number of vacancies formed upon a given H_2 treatment, thus combining a measure of surface area with the lability of M-S bonds [61]. Such inaccuracies and uncertainties lead us to report turnover rates on ReS_x on the basis of the total number of Re atoms, even though not all of them reside at surfaces, to obtain a reasonable and reproducible lower bound for the reactivity of exposed ReS_x surfaces.

2.3.3   *Thiophene hydrodesulfurization turnover rates on Re/SiO₂ and ReSₓ/SiO₂ catalysts*

The depletion of thiophene reactants and the formation of inhibiting H_2S products lead to the observed decrease in turnover rates with increasing residence time for H_2/thiophene reactant mixtures (Fig. 2.7). The presence of added H_2S minimizes S-chemical potential gradients along the bed and, together with relative low thiophene conversions (5-10%), impose nearly

13

differential conditions that permit accurate rate measurements, with modest (if any) required extrapolations to zero residence times.

Thiophene HDS leads to the formation of organosulfur compounds (tetrahydrothiophene) and acyclic alkanes and alkenes (1-butene, *cis*-2-butene, *trans*-2-butene, *n*-butane) (Fig. 2.8). In contrast with our previous findings on Ru and Pt catalysts [18,19], butadiene and dihydrothiophene were not detected as products on Re/SiO_2 while low concentrations of dihydrothiophene was detected on ReS_x/SiO_2, suggesting their facile hydrogenation before desorption or via readsorption along the catalyst bed, consistent with faster rates of butene readsorption and secondary hydrogenation observed. No products of n-decane hydrogenolysis were detected, and all butene isomers were equilibrated, therefore, we report selectivity to alkenes as a lumped species.

Secondary reactions of THT primary products lead to n-butenes (and n-butane) on both Re and ReS_x at all H_2 pressures (1-3 MPa); these reactions decrease THT selectivity and increase butene/butane (C_4) selectivity as thiophene conversion increases with increasing residence time (Fig. 2.8), consistent with the reaction network depicted in Scheme 2.1. The selectivity to primary products, those formed in a single sojourn, cannot be determined unequivocally without the form of the equation required to extrapolate selectivities to zero conversion, thus requiring the rigorous kinetic analysis shown in Section 2.3.5. Thiophene conversion rates were strongly influenced by thiophene pressures and H_2S/H_2 ratios (Figs. 2.9a and 2.9c), but product selectivity values and their trends with residence time were unaffected.

The inhibition of HDS reactions by H_2S is evident from previous studies [2,4,5,62]; some studies [18,63,64] have inferred that H_2S leads to higher THT selectivities, an effect attributed to H_2S dissociation on metal-sulfur (*—*S) site pairs to form (*$S^{\delta-}H^{\delta+}$—*$S^{\delta-}H^{\delta+}$) pairs [65,66], with purported, charged character ($\delta+/\delta-$). These resulting $H^{\delta+}$ species have been implicated in THT formation, even though cationic H-species are unlikely to effect hydrogenations. We show here that the attribution of these effects of H_2S to these types of H-species is unnecessary because selectivity values and their trends with residence time are, in fact, not influenced by ten-fold differences in H_2S/H_2 ratios (Fig. 2.8). We surmise that previously reported effects of H_2S on THT selectivity reflect, instead, selectivity data obtained at very different conversions because of the strong effects of H_2S on HDS rates and their non-rigorous extrapolation to zero conversions to obtain primary selectivities, as we discuss in further detail in Chapter Three.

2.3.4   Elementary steps of thiophene HDS on Re and ReS_x

The total consumption of thiophene increased with increasing thiophene and H_2 pressures (Figs. 2.9a and 2.9b), but decreased with increasing H_2S/H_2 ratios (Fig. 2.9c). The strong inhibitory effect of H_2S/H_2 on HDS rates is consistent with S-species as the predominant surface species and with active surfaces on which labile S-species are able to form and desorb as H_2S during each catalytic turnover,

$$M\,(s) + H_2S\,(g) \leftrightarrow M - S(surface) + H_2(g), \Delta G^0_{ads} = RT\ln(P_{H_2S}/P_{H_2}) \qquad (2.1)$$

14
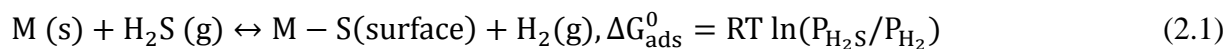
A Langmuirian treatment of S-saturated surfaces would cause rates to depend inversely on H_2S/H_2 ratios, which should lead to rates that exhibit reactant pressure dependences (i.e. thiophene, H_2) that are unattenuated by any reactant-derived surface terms. Instead, the expected first-order rate dependence on thiophene (from its molecular adsorption) is not observed; instead, rates increase sublinearly with thiophene pressure (1-10 kPa), indicative of kinetically-relevant coverages of thiophene-derived species. These observations are not consistent with a Langmuirian surface saturated with S-adatoms formed via H_2S-H_2 equilibration and must be reconciled by considering S-binding energies that change abruptly with S-coverage, leading to strongly-bound adsorbed structures with intervening "patches" of more weakly-bound and consequently more reactive, S-adatoms involved as intermediates in catalytic turnovers.

The ubiquitous poisoning of catalytic metals by sulfur has motivated extensive studies of M-S binding. The presence of sulfur in trace amounts (generally <100 ppm H_2S [33]) at temperatures relevant to catalysis (>300 K) renders surfaces unreactive for a wide range of industrially important reactions (e.g. hydrogenation/dehydrogenation and hydrogenolysis of hydrocarbons [49], Fischer-Tropsch synthesis [67], reforming [33]), apparently through the formation of dense S-monolayers. S-overlayers on single crystals of transition metals (e.g. Ni, Pt, Re [68-70]) reorganize into ordered structures with increasing coverage to form arrangements that lower overall surface energies [69,70]. These surfaces "saturate" at 0.5-0.6 S/M_s stoichimetries upon exposures to H_2S or S_2, typically at temperatures below 500 K, apparently because of steric repulsions at even higher coverages. Indeed, heats of S-adsorption, measured from isosteres from H_2S adsorption and dissociation, decrease with increasing S-coverage on Al_2O_3-supported metals (e.g. Ni, Ru, Fe, Co, Pt, Ir) [71-75], sometimes exhibiting a sharp drop at coverages above 0.8 S/M_s. Such observations and the mechanistic analysis in this study indicate that a large fraction of metal surfaces contains irreversibly-bound S-atoms, with high heats of adsorption, that are responsible for the irreversible poisoining of catalytic reactions; thiophene reactions then occur on sites that contain less strongly-bound S-atoms, which form from thiophene when such sites are uncovered, and are then removed in equilibrated reactions with H_2. It is such sites, with kinetically-removable S-atoms, that account for the ability of highly-covered surfaces to behave as Langmuirian surfaces, containing identical sites, composing a fraction of the surface with reactive sulfur amidst structures consisting of strongly-bound unreactive S-atoms. Such surfaces contain vacancies (*), sulfur and hydrogen atoms (S*, H*) and thiophene-derived species (T*) in quasi-equilibrium with their respective gaseous precursors, thus accounting for the reversible effects of H_2S/H_2 ratios on HDS rates. Similar H_2, thiophene, and H_2S/H_2 dependences persist on ReS_x/SiO_2 (Fig. 2.9), suggesting that thiophene reactions also occur on kinetically-accessible sites on the surface of sulfided materials during catalysis, consistent with the presence of S-vacancies widely adopted as the "active site" of HDS for lamellar MoS_x and WS_x catalysts [76].

The effects of reactant concentrations and H_2S/H_2 ratios on rates can be described by a sequence of elementary steps (Scheme 2.2) mediated via vacancy pairs as the kinetically-relevant sites residing on Langmuirian surfaces (*—*); these steps include reactions of bound thiophene (T*) and H-atoms (H*) at such sites. Even though such sites exhibit detectable (T*) and (S*) coverages, THT and C_4 selectivities (Fig. 2.8) are not sensitive to thiophene pressures and H_2S/H_2 ratios, suggesting that they form on the same surfaces of Re-based catalysts. We considered total thiophene consumption rates (to form both THT and C_4), thus avoiding any

15

inherent inaccuracies in extrapolating selectivities to zero conversions required to report their respective primary rates; in doing so, we observe that (total) rates are accurately described by a rate expression (derived from the steps in Scheme 2.2) that assumes quasi-equilibrated adsorption of reactants (to form T* and H*) and of products (i.e. H$_2$S*, HS*, S*) and the (first) H-addition step to T* as the kinetically-relevant step,

$$\frac{r}{[L]} = \frac{\alpha(H_2)^{0.5}(T)}{\left(\underset{(*)}{1} + \underset{(T*)}{\beta(T)} + \underset{(H*)}{\gamma(H_2)^{0.5}} + \underset{(H_2S*)}{\delta(H_2S)} + \underset{(HS*)}{\epsilon\frac{(H_2S)}{(H_2)^{0.5}}} + \underset{(S*)}{\eta\frac{(H_2S)}{(H_2)}}\right)^2} \tag{2.2}$$

The denominator terms reflect site occupancy through the balance equation,

$$[L] = (*) + (T*) + (H*) + (HS*) + (S*) = (*)\cdot\left(1 + \beta(T) + \gamma(H_2)^{0.5} + \delta(H_2S) + \epsilon\frac{(H_2S)}{(H_2)^{0.5}} + \eta\frac{(H_2S)}{(H_2)}\right) \tag{2.3}$$

, with parameters in the previous two equations defined as,

$$\alpha = k_0 K_{H_2}^{0.5}K_T, \beta=K_T, \gamma=K_{H_2}^{0.5}, \delta = K_{H_2S}, \epsilon = \frac{K_{H_2S}K_{HS}}{K_{H_2}^{0.5}}, \eta = \frac{K_S K_{H_2S}K_{HS}}{K_{H_2}}$$

Thiophene rates are limited by the formation of singly-hydrogenated adsorbed thiophene species (I*), while the ratio of products formed reflects the relative stability of two transition states that occur after this kinetically-relevant step, thus making it impossible to discern the specific mechanistic route that leads to THT and C$_4$ products.

Equation 2.2 accurately describes the observed effects of H$_2$, H$_2$S, and thiophene concentrations on thiophene for both Re and ReS$_x$ catalysts. This equation retains denominator terms for the various H$_2$S-derived species, assumed to reflect their thermodynamics, as found from H$_2$-D$_2$ and H$_2$S-D$_2$S isotopic exchange data on Pt and Ru catalysts with kinetic behaviors [18,19] similar to those reported here for Re-based catalysts. Thus, the relative coverages of these H$_2$S-derived species are given by the thermodynamics of,

$$H_2S\,(g) + * \rightleftharpoons H_2S* \tag{2.4}$$

$$H_2S\,(g) + * \rightleftharpoons HS* + \frac{1}{2}H_2\,(g) \tag{2.5}$$

$$H_2S\,(g) + * \rightleftharpoons S* + H_2\,(g) \tag{2.6}$$

Intact H$_2$S adsorbs weakly on metals and has been detected only at subambient temperatures (<200 K), [77]) and dissociates readily to form S* at higher temperatures. DFT treatments show that H$_2$S* dissociates on low-index metal surfaces (Ir, Ni, Pd, Pt) to form HS* and S* in exothermic reactions [77,78]. These S* species, however, are bound to sparsely-covered surfaces instead of interacting with minority vacant sites on highly-covered surfaces prevalent during HDS catalysis; unfortunately, their abundant concentrations on surfaces preclude spectroscopic elucidation of the surface coverage of dilute HDS sites. Entropy would favor dissociation to S*, because of gains upon formation of H$_2$ (g) (Eq. 2.6) over H$_2$S* and HS* formations (Eqs. 2.4 and

2.5, respectively). Thus, we propose that S* prevails over HS* and H_2S^*, consistent with the ability of Equation 2.2 with zero values of δ and ε to describe all rate data. Sensitivity analysis (described in 2.8.7) allowed for further parameter discrimination, probed by evaluating changes in the overall sum of (squared) residuals caused by a fractional change (±20%) in the value of the fitted parameter,

$$Relative\ SSR = \frac{\partial(SSR)}{\delta(k_j)}$$
(2.7)

, where SSR (sum of squared residuals) $=\sum_i(r_{i,predicted} - r_{i,measured})^2$ and k_j is the rate constant of interest (e.g. α, β, γ, etc.).

Values of relative SSR below a set threshold value (e.g. 5%) indicate inconsequential contributions of k_j toward describing reaction rates. We found, here, that rates were insensitive to the value of γ suggesting that H* species were not abundant on HDS surfaces during reaction (i.e. γ=0, Eq. 2.2).

Turnover rates on Re and ReS_x depend similarly on H_2, H_2S, and thiophene and are described by the form Equation 2.2 identified by regressing all rate data and performing the sensitivity analysis described above,

$$\frac{r}{[L]} = \frac{\alpha(H_2)^{0.5}(T)}{\left(\underset{(*)}{1} + \underset{(T^*)}{\beta(T)} + \underset{(S^*)}{\eta\frac{(H_2S)}{(H_2)}}\right)^2}$$
(2.8)

, in spite of their 100-fold differences in turnover rates (Fig. 2.5). The functional form of Equation 2.8 accurately describes rates on Re and ReS_x over a very broad range of practical reaction conditions (1-3 MPa H_2, 1-10 kPa thiophene, 7-100 x 10^{-5} H_2S/H_2 ratios) (Fig. 2.10). Thus, the large differences in turnover rates for Re and ReS_x (Fig. 2.5) reflect their very different values of the kinetic and thermodynamic constants in Equation 2.8 instead of a different sequence of elementary steps. These kinetic and thermodynamic parameters (α, β, η) are shown in Table 2.2 for (15% nominal wt. samples of) Re and ReS_x. Their relative values will be discussed in Section 2.3.6 in the context of how M-S bond energies influence thiophene conversion turnover rates.

2.3.5 Primary and secondary reactions during thiophene conversion on Re and ReS_x

Thiophene conversion turnover rates, by themselves, do not contain information about the factors that determine selectivity (Fig. 2.8) because the branching steps that ultimately form THT and C_4 products occur after the kinetically-relevant step for thiophene consumption. The (THT/C_4) ratios and their trends with thiophene conversion do not depend on thiophene pressure or H_2S/H_2 ratio (Section 2.3.3), but they do depend on H_2 pressure (Figs. 2.8a and 2.8b), even though the steps that form such products occur on the same surface and one that does not contain detectable H* coverage (Eq. 2.8). These H_2 effects must, therefore, reflect a different number of H-atoms in the transition states for the kinetically-relevant steps that form THT and C_4, which

17

can be probed by writing a sequence of steps necessary to form the kinetically-relevant intermediate I* via steps in Scheme 2.2 and consumes it via subsequent steps as depicted in Scheme 2.1. These subsequent steps can be described by pseudo-first-order reactions of thiophene-derived species (I*, THT),

$$r_1 = k_1'(I*) \tag{2.9}$$

$$r_2 = k_2'(I*) \tag{2.10}$$

$$r_3 = k_3'(THT) \tag{2.11}$$

These three reactions occur on surfaces covered in (S*) and (T*), and thus, the rate "constants" in Equations 2.9-2.11 contain the same denominator dependences described in Equation 2.8 but are nearly fixed in their values at a given thiophene pressure and H_2S/H_2 ratio and at low (differential) conversions. The concentration of I* (in Eqs. 2.9 and 2.10) can be described, based on pseudo-steady state assumptions on the consumption of I*,

$$\frac{d(I*)}{d\tau} = \frac{r}{[L]} - (k_1' + k_2')(I*) = 0 \tag{2.12}$$

These reaction steps (Eq. 2.9-2.11) allow us to describe the rates of THT and C_4 formation (as two interdependent differential equations),

$$\frac{d(THT)}{d\tau} = k_1'(I*) - k_3'(THT) \tag{2.13}$$

$$\frac{d(C_4)}{d\tau} = k_2'(I*) + k_3'(THT) \tag{2.14}$$

We measure product selectivity as a function of thiophene conversion (moles converted/moles fed), X, which is related to residence time by the following definition,

$$(1 - X) = e^{-k_0'\tau} \tag{2.15}$$

, where $k_0' = \dfrac{\alpha(H_2)^{0.5}}{\left(1 + \beta(T) + \eta\frac{(H_2S)}{(H_2)}\right)^2} \tag{2.16}$

We define THT selectivity as the ratio of THT formed to thiophene converted,

$$S_{THT} = \frac{(THT)}{T_0(X)} \tag{2.17}$$

, where T_0 is the initial concentration of thiophene.

Solving for THT selectivity as a function of X (Eqs. 2.12-2.17) gives,

$$S_{THT} = \frac{k_1'}{k_1' + k_2'} \cdot \left(1 - \frac{k_3'}{k_0'}\right)^{-1} \cdot \frac{\left\{(1-X) - (1-X)^{\frac{k_3'}{k_0'}}\right\}}{X} \tag{2.18}$$

Regression of selectivity data (Fig. 2.8) to the functional form of Equation 2.18 allow us to extract k_1'/k_2', which reflect the ratio of primary formation rates of THT to those of C_4 (Eqs. 2.9 and 2.10). We can probe H_2 effects on primary selectivity by extracting these ratios at different H_2 pressures,

$$\frac{r_1}{r_2} = \frac{k_1'}{k_2'} \sim (H_2)^\lambda \tag{2.19}$$

Regressed values for the ratios of k_1'/k_2' on both Re and ReS_x exhibit similar H_2 dependences ($\lambda \sim 0.5$) and magnitudes ($k_1/k_2 = 0.023 \pm 0.002$ kPa$^{-0.5}$) (Fig. 2.11a). This half-order dependence in H_2 suggests a difference of one H-atom between the (two) transition states that lead to their respective products; specifically, THT formation appears to require activation from a more hydrogenated surface intermediate relative to that which undergoes C-S bond scission.

We can also probe any effects of H_2 on secondary THT conversions to C_4 by examining k_3'/k_0', which reflects the ratio of secondary (THT desulfurization, Eq. 2.11) to primary (thiophene consumption, Eq. 2.8) rates,

$$\frac{r_3}{r_0} = \frac{k_3'}{k_0'} = \frac{k_3}{k_0} \cdot (H_2)^\delta \tag{2.20}$$

We find that this ratio (Fig. 2.11b) exhibits a negative H_2 dependence ($\delta \sim -1.0$), which, when compared to the forward rates of thiophene consumption (Eq. 2.8), suggests that dehydrogenation of THT must occur before C-S cleavage. We isolate the H_2 dependence of THT desulfurization rates (i.e. of k_3') because kinetic probes have elucidated (Section 2.3.4) the H_2 order of k_0' (i.e. $(H_2)^{0.5}$, Eq. 2.16). Thus, taking Equations 2.16 and 2.20 together, THT desulfurization rates exhibit a negative half-order dependence on H_2, suggesting that trihydrothiophene (TrHT) formation is equilibrated on the surface prior to the kinetically-relevant step (of THT secondary consumption). Such behaviors suggest kinetic barriers between TrHT and dihydrothiophene (DHT) species must exist along the sequential dehydrogenation (and subsequent desulfurization) reaction coordinate and implies that C-S bond activation occurs on either monohydrothiophene (MHT) or DHT surface intermediates.

Primary branching ratios (i.e. r_1/r_2, Eq. 2.19) indicate that the transition state that forms THT (from thiophene) involves one more H-species than that that undergoes C-S bond scission to form C_4 products. We propose DHT as this surface species, which activates the C-S bond (Scheme 2.3), because the barrier that exists between DHT and TrHT during THT desulfurization is also crossed from the other direction (i.e. from thiophene primary conversion) to form THT; such proposals also appeal to the possibility that these surface hydrogenation/dehydrogenation steps are the microscopic reverse of one another. We conclude that the primary formation of both C_4 and THT indicates that the latter formation is not a

prerequisite for C-S bond activation, nor does it make C-S bond cleavage more facile, but rather that it occurs as an "overhydrogenation mistake," corrected upon THT readsorption (and subsequent dehydrogenation). Indeed, the requisite formation of partially (de)hydrogenated surface intermediates prior to bond cleavage appears analogous to mechanisms developed for metal-catalyzed C-C hydrogenolysis for bond scission and ring opening of linear and cycloalkanes [37,38], wherein C-C bonds are activated by first breaking C-H bonds and forming additional C-metal bonds; such features rely on bond-order conservation arguments that strong C-metal bonds can weaken C-X bonds (X = C, S, O). The surface intermediate that undergoes the kinetically-relevant scission reflects a favorable enthalpic and entropic balance of C-H bond cleavage, C-metal bond formation, and H_2 formation. In our HDS study, this intermediate was approached from both directions, starting either from an aromatic (i.e. thiophene, reactant) or a saturated (i.e. THT, primary product) heterocycle, shedding insights on the role of metal surfaces in activating molecular bonds.

2.3.6   *Consequences of M-S bond energy on HDS catalytic rates*

Differences in HDS reactivity on different transition metals have often been attributed to catalyst M-S bond strengths, inferred from their heats of metal sulfide formation or energies of S-binding [14,22,23]. We can similarly examine whether differences in the catalyst S-affinity can play a role in explaining the 100-fold difference in turnover rates on Re and ReS_x by specifically comparing equilibrium S-adsorption constants measured on HDS sites through regression of kinetic data to the rate expression (Eq. 2.8, η),

$$\frac{(S*)}{(*)} = K'_S \frac{(H_2S)}{(H_2)} \tag{2.21}$$

, where $K'_S = K_S K_{H2S} K_{HS} K_{H2}^{-1} (= \eta)$

Regressed values of K'_S (Table 2.2), which is a surrogate of S-binding energy on HDS sites, are higher for Re ($6.3 \pm 1.9 \times 10^2$) than for ReS_x ($3.2 \pm 3.2 \times 10^2$), but parameter uncertainties could lower the statistical significance of their perceived difference. We find, instead, that much of the discrepancies in their HDS rates are accounted for by differences in their regressed numerator constant (Eq. 2.8, α), $k_0 K_{H2}^{0.5} K_T$, which does not involve parameters directly associated with S-atom binding, suggesting that significant differences in their respective reaction barriers must exist; this constant reflects the energy difference between the transition state with respect to two empty sites (*) and gas phase reactants (thiophene and H_2),

$$\Delta G_{eff}^{\ddagger} = G^{\ddagger} - \left(2 G_* + \frac{1}{2} G_{H_2} + G_T\right) = -RT\ln\left(k_0 K_{H_2}^{0.5} K_T\right) \tag{2.22}$$

Rigorous comparisons of these energies require accurate counts of total HDS sites (L), which cannot be determined from measurements of surface dispersion because strongly bound S-atoms cover different fractions of surfaces on different catalysts during catalysis. Regressed values of $k_0 K_{H2}^{0.5} K_T$ become direct functions of our (in)accurate estimates of HDS site densities, affecting our ability to rigorously assess the degree to which transition state stabilizations (i.e. $G^{\ddagger}$) on Re and ReS_x truly influence their respective overall rates.

M-S binding strengths are reportedly greater between chemisorbed sulfur and surface metal atoms than between lattice sulfur and metal atoms in sulfides [33,34], consistent with bond-order conservation, which argue that electron density is less localized (and interactions therefore weaker) between metal and sulfur atoms when the metal must share bonds with multiple S-atoms (as in the case of MS_x materials) compared to when it only bonds to one S-atom (as in the case of chemisorbed S-layers). Thus, weaker S-affinities expected in ReS_x relative to Re should have led to greater destabilization of thiophene-derived transition states, inconsistent with the lower value of $G^{\ddagger}$ (Eq. 2.22) measured on ReS_x. Such apparent contradictions are reconciled if, instead, weaker M-S bonds increase the density of HDS sites available for catalysis as a result of promoting the lability of bound S-atoms, leading to a greater number of HDS sites on ReS_x relative to Re, which can consequently yield more turnovers if the intrinsic reactivity of Re sites is not significantly greater than those of ReS_x.

The limitations of accurate HDS site counts are avoided when we consider ratio of rates (e.g. r_1/r_2 and r_3/r_0, Eqs. 2.18 and 2.19) because all reactions occur on similar types of sites. These rate ratios exhibit similar values and responses to H_2 pressure on both Re and ReS_x (Fig. 2.11), suggesting that reactive centers are of similar chemical nature, irrespective of phase. Such results are surprising given the differences in both the global morphology (i.e. bulk phase) and local (surface) coordination environments between S-covered Re and ReS_x, and challenge whether our rates are measured on distinct sites whose nature truly reflects the properties of these disparate phases. While characterization probes have suggested that the bulk properties of the two phases remain intact during reaction, it remains possible that Re/SiO_2 can form low concentrations (e.g. 1/100 of the surface, undetectable by TEM) of a reactive phase (i.e. ReS_2) upon exposure to moderate S-chemical potentials. Rates on S-covered Re were arguably more inhibited by H_2S/H_2 ratio (Fig. 2.9c) than those on ReS_x, however, suggesting that reactive sites on ReS_x and Re do exhibit dissimilar sensitivities toward S-chemical potential. In fact, increasing H_2S/H_2 ratios should have encouraged the additional formation of ReS_x "patches" on Re metal surfaces, which would have led to a weaker (not stronger) effect of H_2S/H_2 on the rates for Re/SiO_2 had S-inhibition competed with the formation of a markedly more active phase (in the absence of any kinetic hurdles against such formations). Differences in their thiophene dependences are also apparent from turnover rates that reach zero-order regimes (at 5 kPa thiophene) on ReS_x but that continue to increase monotonically (but sublinearly) on Re, leading to a greater value of K_T on ReS_x (Table 2.2); while stronger thiophene adsorption in ReS_x seems inconsistent with the weaker S-affinity expected in ReS_x, these behaviors could reflect the increased ability of thiophene (T*) to compete against (S*) on surfaces that exhibit weaker S-affinity.

We conclude that M-S bond energy plays a prevailing role in determining the density of reactive HDS sites on catalytic surfaces. We can extend this concept through probing the effects that metal cluster size, which can affect average coordination of exposed metal sites when particles are <10 nm, may have on reaction rates [79]; as clusters decrease in size, increased coordinative unsaturation can lead to stronger S-binding and lower the densities of HDS sites. We find, instead, that turnover rates on Re metal clusters appear insensitive to such structural changes (Fig. 2.12) over a range of particle sizes (1-7 nm). Such behaviors suggest the presence of compensation effects, possibly via surface adsorbate restructuring to minimize surface energy [80], that lead to similar fractions of kinetically-accessible sites exhibiting similar reactivity and

yielding nearly constant thiophene conversion turnover rates when normalized by the number of exposed metal atoms. While such a perfect balance in compensating variables seems pathological, the lack of particle size effects on adsorbate-covered surfaces is not unprecedented, most notably in CO oxidation on CO-covered Pt, where both turnover rates and heats of CO adsorption remained constant over a range of cluster sizes for which significant changes in average metal surface coordination also occurred [81]. Significant changes in HDS turnover rates appear to require greater differences in surface binding properties, attainable when different metal (e.g. Pt, Ru) catalysts, whose chemical nature can shape both intrinsic reactivity and HDS site densities, are used, as we will discuss in greater detail in the next chapter.

2.4   Conclusions

This study extends our previous mechanistic studies of well-defined isotropic sulfur-covered metal catalysts to lamellar nanostructures, similar in morphology to $Mo(W)S_x$ HDS catalysts. From their kinetic responses, we conclude common mechanistic features persist, irrespective of catalyst morphology. Re and ReS_x stabilities during HDS reaction afforded the ability to study the reaction on both phases, at identical conditions, because kinetic hurdles prevented interconversions to a single thermodynamically-favored Re phase. While thiophene consumption was more facile on ReS_x relative to S-covered Re metal, we universally find that the activation of C-S bonds requires the formation of a partially-saturated thiophene-derived surface species that sufficiently lowers barriers for bond scission. Such conclusions were derived from rigorous analysis of product selectivities because primary branching of hydrogenation and desulfurization paths occurred along the part of the reaction coordinate that is kinetically-silent. These behaviors appear analogous to those observed in C-C and C-O bond activations required for alkane and alkanol hydrogenolysis on H-covered metal surfaces, respectively, placing HDS as a specific class of more general C-X hydrogenolysis (X = C, O, S) reactions.

2.5   Acknowledgements

2.6 Tables, Figures, and Schemes

2.6.1 Tables

Table 2.1: Catalyst dispersion and diameter of Re/SiO$_2$ and ReS$_x$/SiO$_2$ catalysts.

Nominal/actual weight loading (% wt. Re)	Phase	Re dispersion[b]	Cluster diameter (nm)	Dispersity Index (DI)[f]
15 / 13.5[a]	Re^0	0.17	6.9[d] / 6.9[e]	1.3
15 / --	ReS$_x$	1.00[c]	--	--
5 / 4.3[a]	Re^0	0.41	2.9[d] / 2.4[e]	1.2
5 / --	ReS$_x$	1.00[c]	N/A	--
1 / 0.97[a]	Re^0	0.95	1.2[d] / --	--

[a] Measured from ICP-OES elemental analysis (Galbraith Laboratories, Inc.).
[b] Calculated from Re dispersion assuming spherical clusters and bulk diameter of Re metal. diameter (nm) = 1.18/(fractional dispersion)
[c] Sulfide phases are assumed to be fully-dispersed.
[d] Based on O$_2$-chemisorption assuming a O:Res stoichiometry of 0.4:1 (see Section 2.3.1).
[e] Surface-averaged diameter from cluster size distributions measured via TEM.
[f] Calculated from the ratio of surface-averaged to linear-averaged cluster sizes.

Table 2.2: Kinetic parameters for thiophene HDS on 15% nominal wt. samples of Re/SiO$_2$ and ReS$_x$/SiO$_2$ based on regression of kinetic data to the functional form of the rate expression (Eq. 2.8) at 573 K.

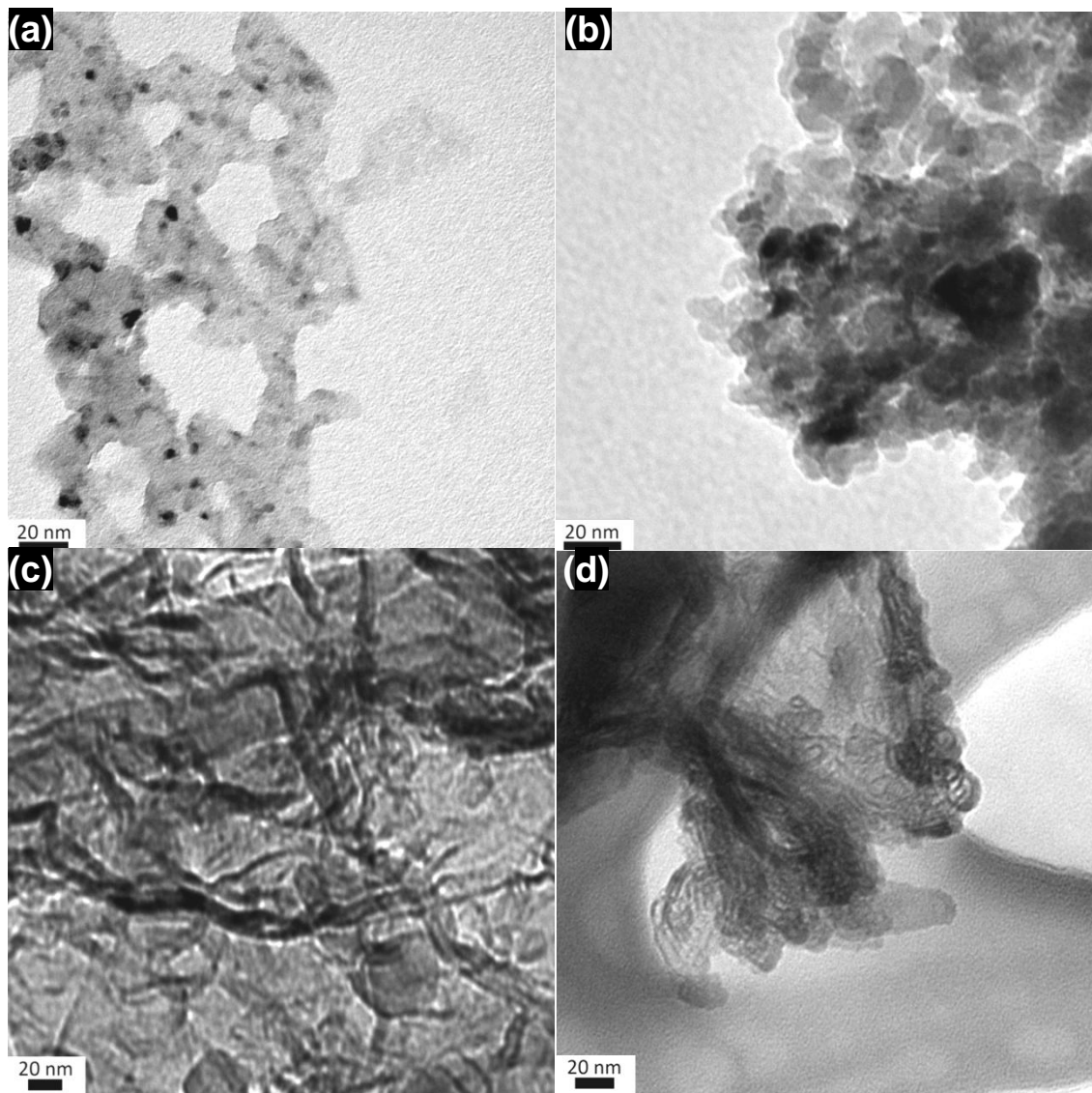| Thermodynamic/Kinetic Parameter	Re	ReS$_x$
$k_0 K_{H2}^{0.5} K_T$ (mol mol^{-1} s^{-1} kPa$^{-1.5}$)	2.2 ($\pm$0.4) x 10^{-6}	2.6 ($\pm$0.7) x 10^{-4}
K_T (kPa^{-1})	6.8 ($\pm$1.2) x 10^{-2}	1.6 ($\pm$0.3) x 10^{-1}
$K_S K_{H2S} K_{HS} K_{H2}^{-1}$	6.3 ($\pm$1.9) x 10^{2}	3.2 ($\pm$3.2) x 10^{2}

Figure 2.1: TEM images of (15% nominal wt. samples of) Re/SiO$_2$ after H$_2$ treatment of ReO$_x$ at 773 K (a) and after exposure to simulated HDS conditions at 3MPa H$_2$, 1 kPa H$_2$S and 573 K (b) and of ReS$_x$/SiO$_2$ after H$_2$S/He treatment of ReO$_x$ at 773 K (c) and after exposure to simulated HDS conditions at 3 MPa H$_2$, 1 kPa H$_2$S, and 573 K (d).
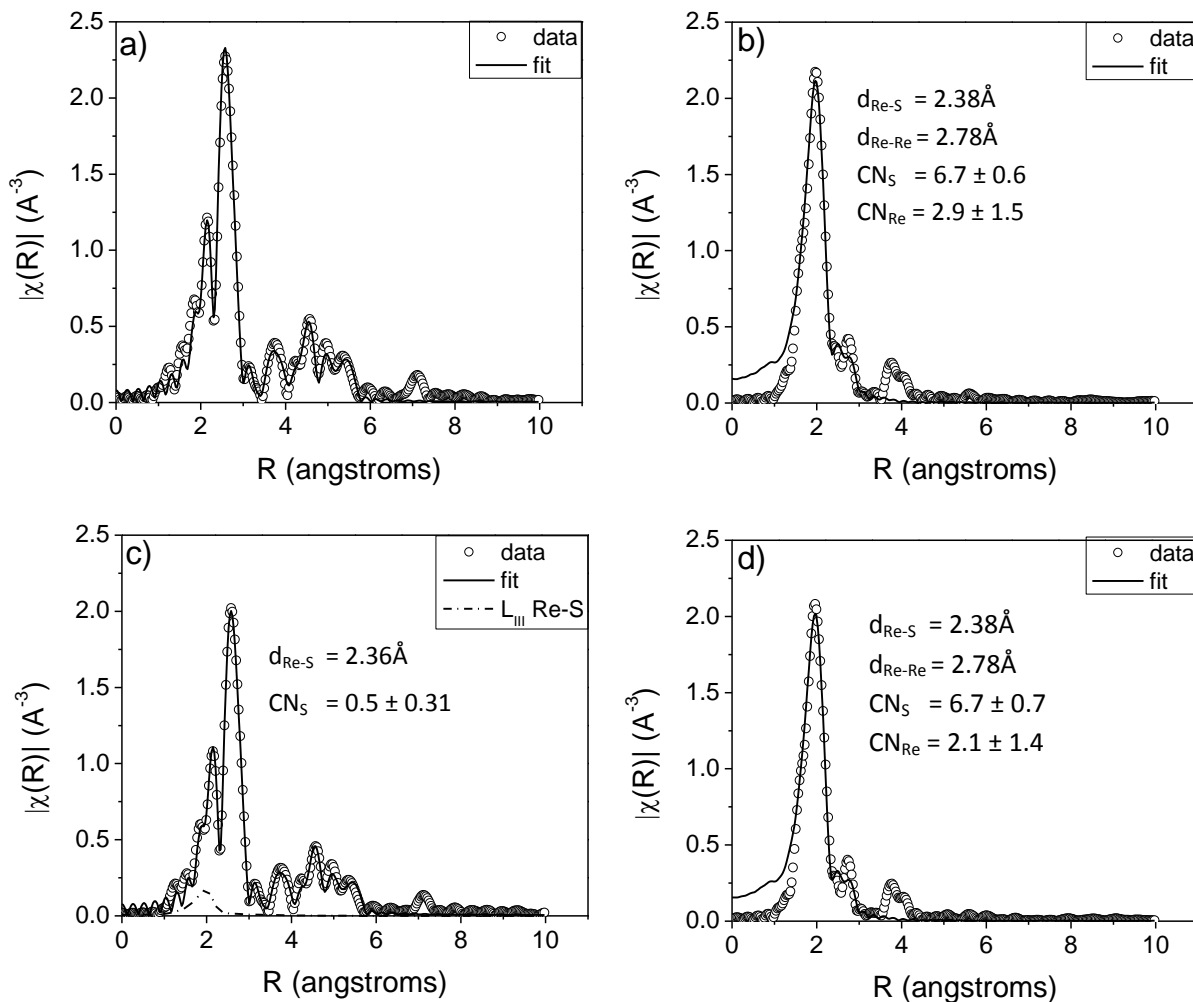
Figure 2.2: Fourier transforms of the EXAFS spectra of (5% nominal wt. samples of) fresh Re/SiO_2 (a) and fresh ReS_x/SiO_2 (b) synthesized from ReO_x and spent Re/SiO_2 (c) and spent ReS_x/SiO_2 (d) after exposure to simulated HDS conditions (3.0 MPa H_2, 1 kPa H_2S, 573 K). Spectra fittings were based on EXAFS equation, $\chi(R)$, over range of k (photoelectron wave number) and R (distance between absorbing and scattering atoms) of 3.5-16.1 Å^{-1} and 1.5-5.7 Å, respectively, for Re/SiO_2 and of 2.0-15.9 Å^{-1} and 1.0-3.5 Å, respectively, for ReS_x/SiO_2. Multiple and single photoelectron scattering pathway models are used to fit (—) actual data (○). Regression marked by a dotted line (--) represents the inclusion of an additional Re-S pathway for the spent Re/SiO_2 (c). The distances (d_{Re-Re}, d_{Re-S}) reflect the bond length of the absorber-scatterer pair and CN_i denotes the number of nearest i neighbors (coordination number) in the first shell.
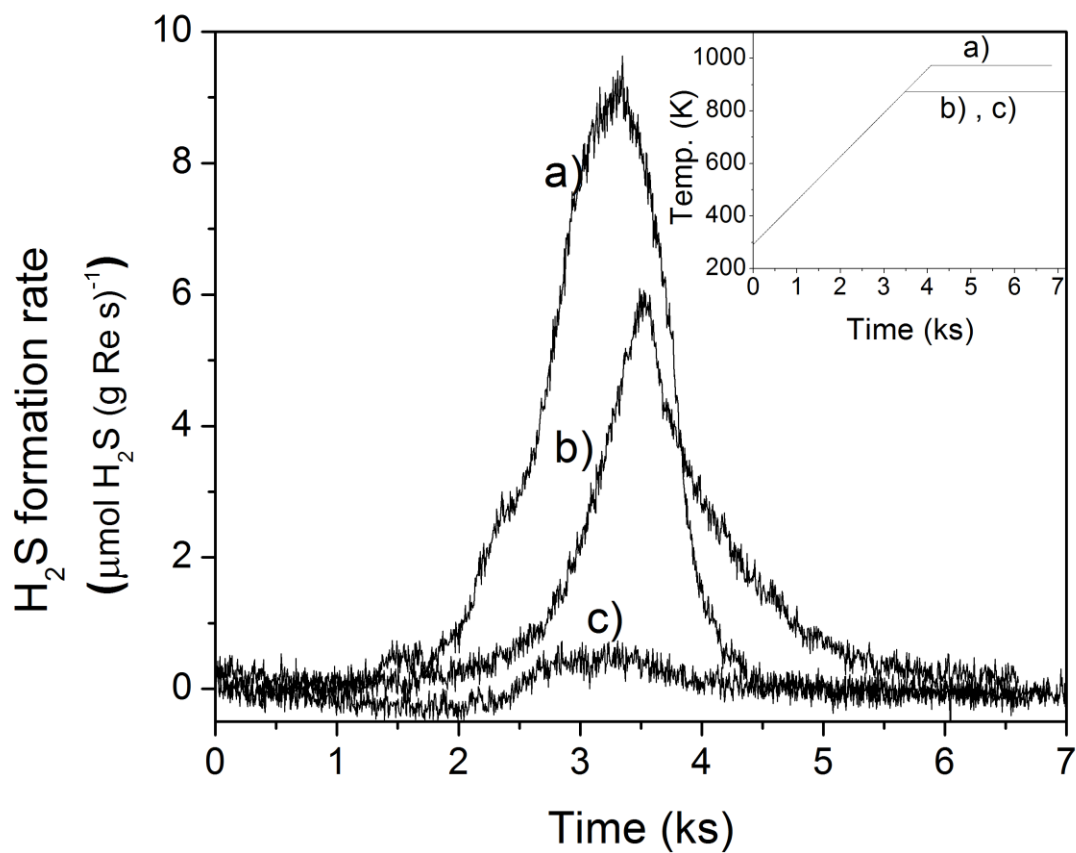
Figure 2.3: Temperature programmed reduction (TPR) of S-content in (15% nominal wt. samples of) of fresh ReS_x/SiO_2 (a) and of ReS_x/SiO_2 (b) freshly synthesized from ReO_x and of Re/SiO_2 (c) after exposure to simulated HDS conditions at 3MPa H_2, 3 kPa H_2S and 573 K. Inset: temperature ramp for the TPR of samples (a), (b), and (c).
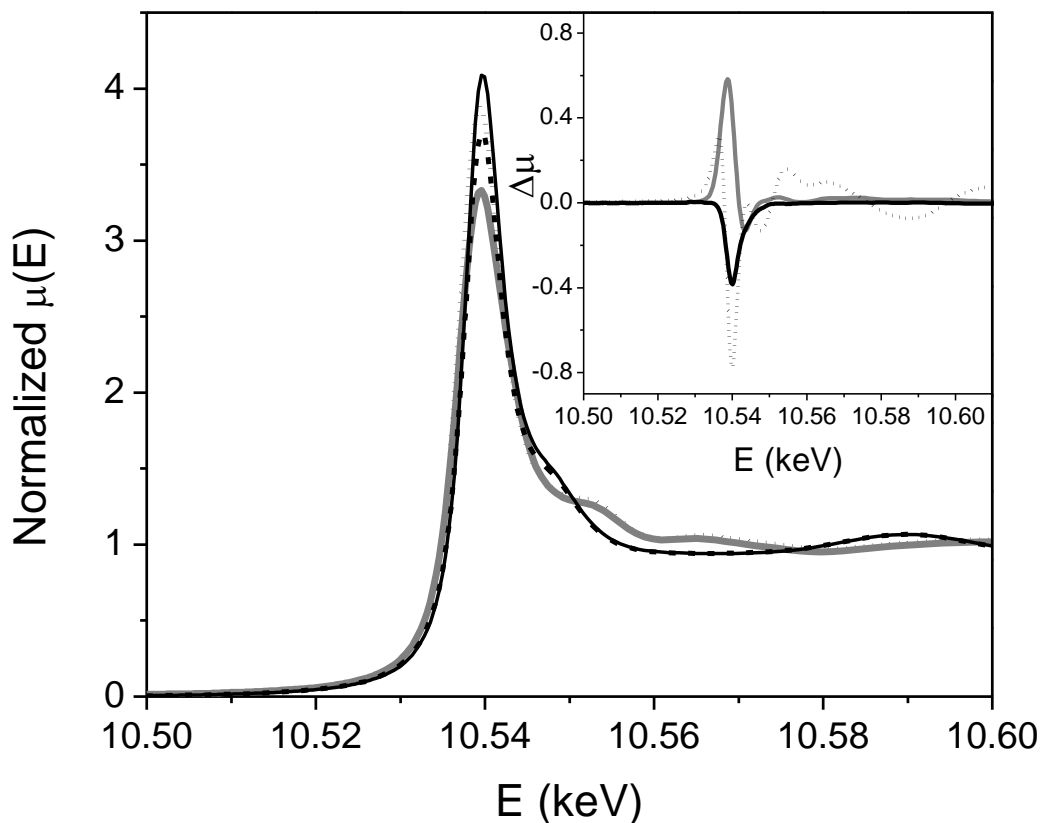
Figure 2.4: Normalized XAS absorption coefficient (μ), measured from energy differences of incident (I_o) and transmitted (I_0) X-ray intensities ($I_t = I_0 e^{-\mu x}$, x is sample thickness) as a function of energy, E, of 5% nominal wt. samples of Re/SiO$_2$ after H$_2$ treatment of ReO$_x$ at 773 K ($\cdots$, fresh) and after exposure to simulated HDS conditions at 3MPa H$_2$, 1 kPa H$_2$S and 573 K (—, spent) and of ReS$_x$/SiO$_2$ after H$_2$S/He treatment ReO$_x$ at 773 K (---, fresh) and after exposure to simulated HDS conditions at 3 MPa H$_2$, 1 kPa H$_2$S, and 573 K (—, spent). Inset: differences in μ near the L$_{III}$ edge (~10.54 keV) of (i) $\mu_{fresh\ Re} - \mu_{spent\ Re}$ (—), (ii) $\mu_{fresh\ ReSx} - \mu_{spent\ ReSx}$ (—), and (iii) $\mu_{post\text{-}HDS\ Re} - \mu_{spent\ ReSx}$ ($\cdots$).
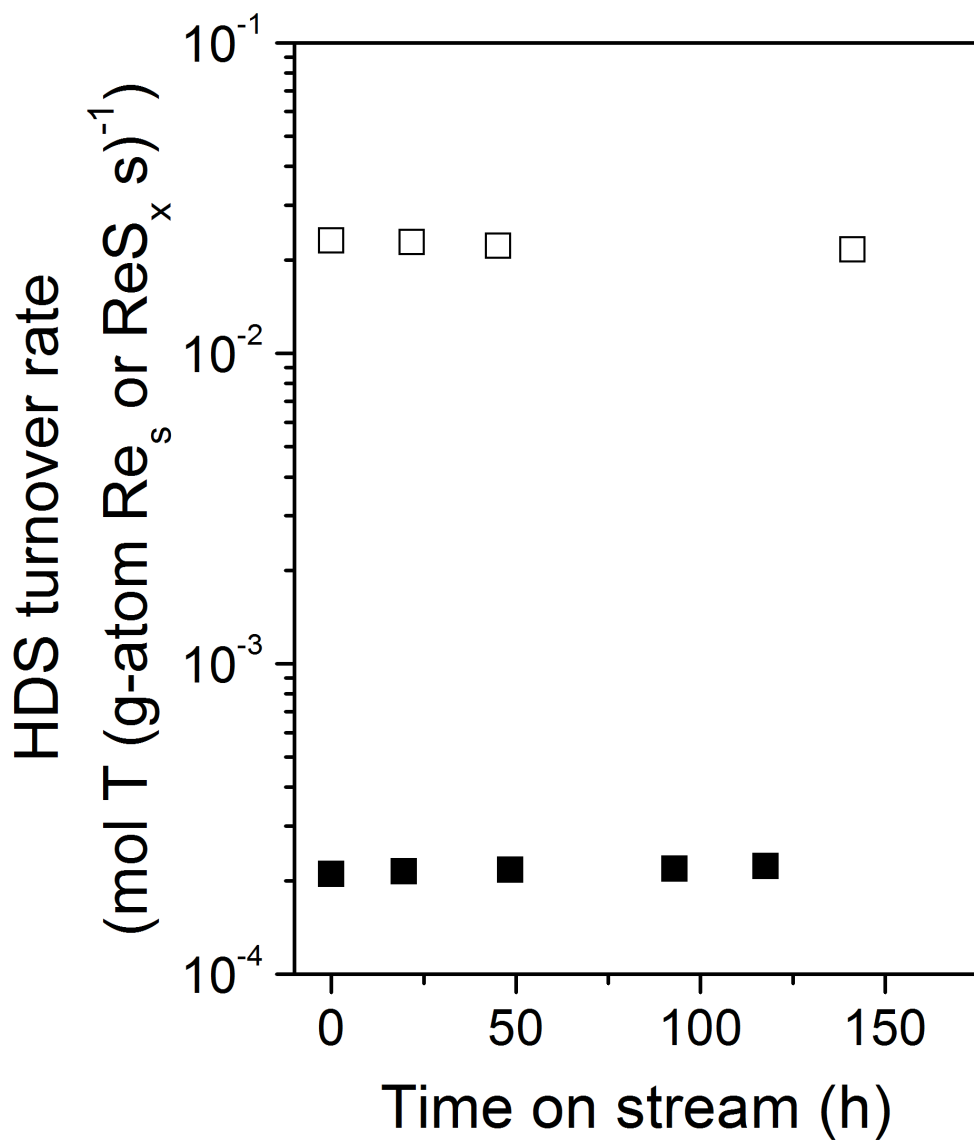
Figure 2.5: HDS turnover rates of thiophene (T) consumption on 15% nominal wt. samples of Re/SiO$_2$ (■) and ReS$_x$/SiO$_2$ (□) normalized by surface and total moles of Re, respectively, as a function of time on stream (3.0 MPa H$_2$, 2.5 kPa thiophene, 573 K).
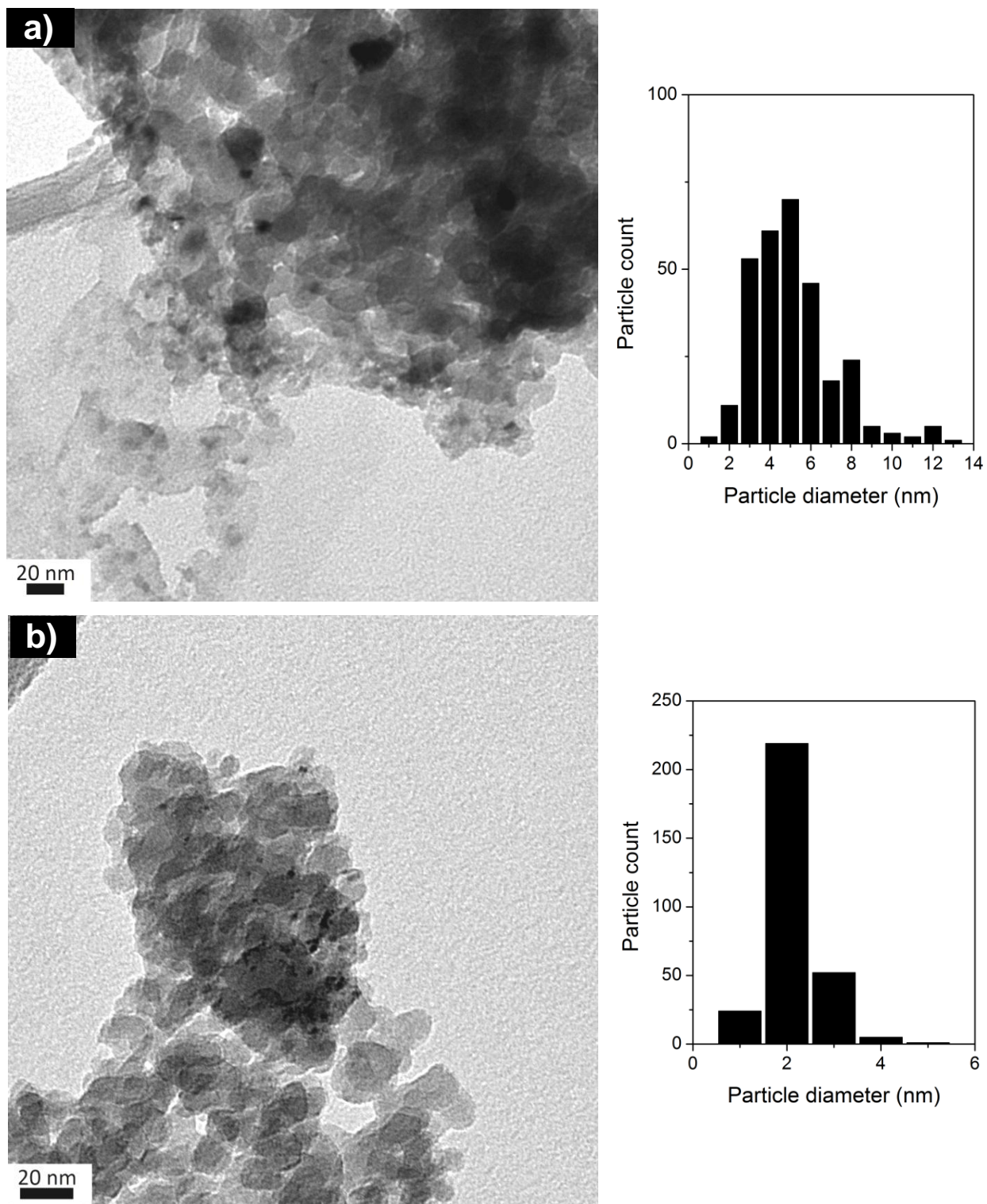
Figure 2.6: Transmission electron micrographs and measured particle diameter distribution for a) 5% nominal wt. and b) 15% nominal wt. Re/SiO_2, after H_2 treatment of ReO_x at 773 K.
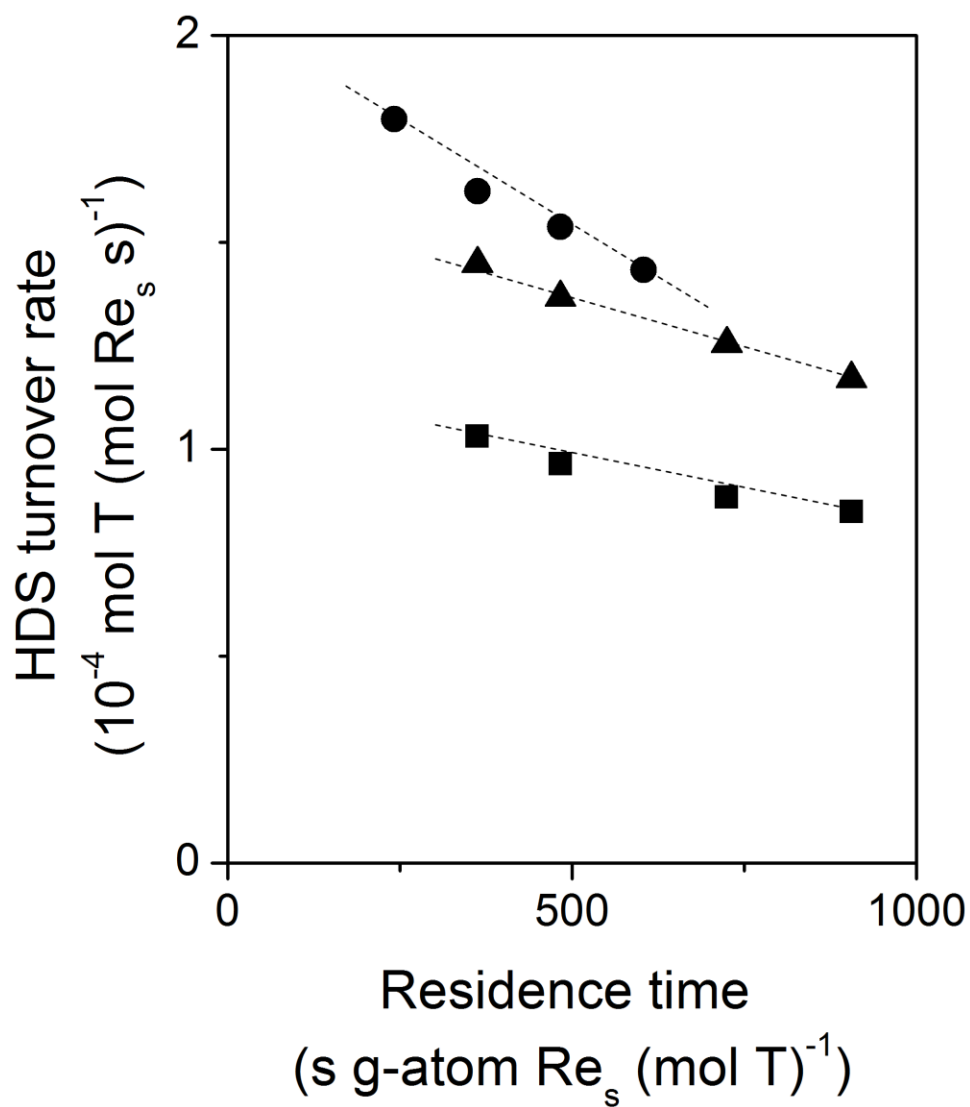
Figure 2.7: HDS turnover rates of thiophene (T) consumption as a function of residence time for different H_2S/H_2 ratios ($1.7x10^{-4}(\bullet)$, $3.0x10^{-4}(\blacktriangle)$,$1.0x10^{-3}(\blacksquare)$)) on 15% nominal wt. Re/SiO_2 at 3.0 MPa H_2, 2.5 kPa thiophene, 573 K.
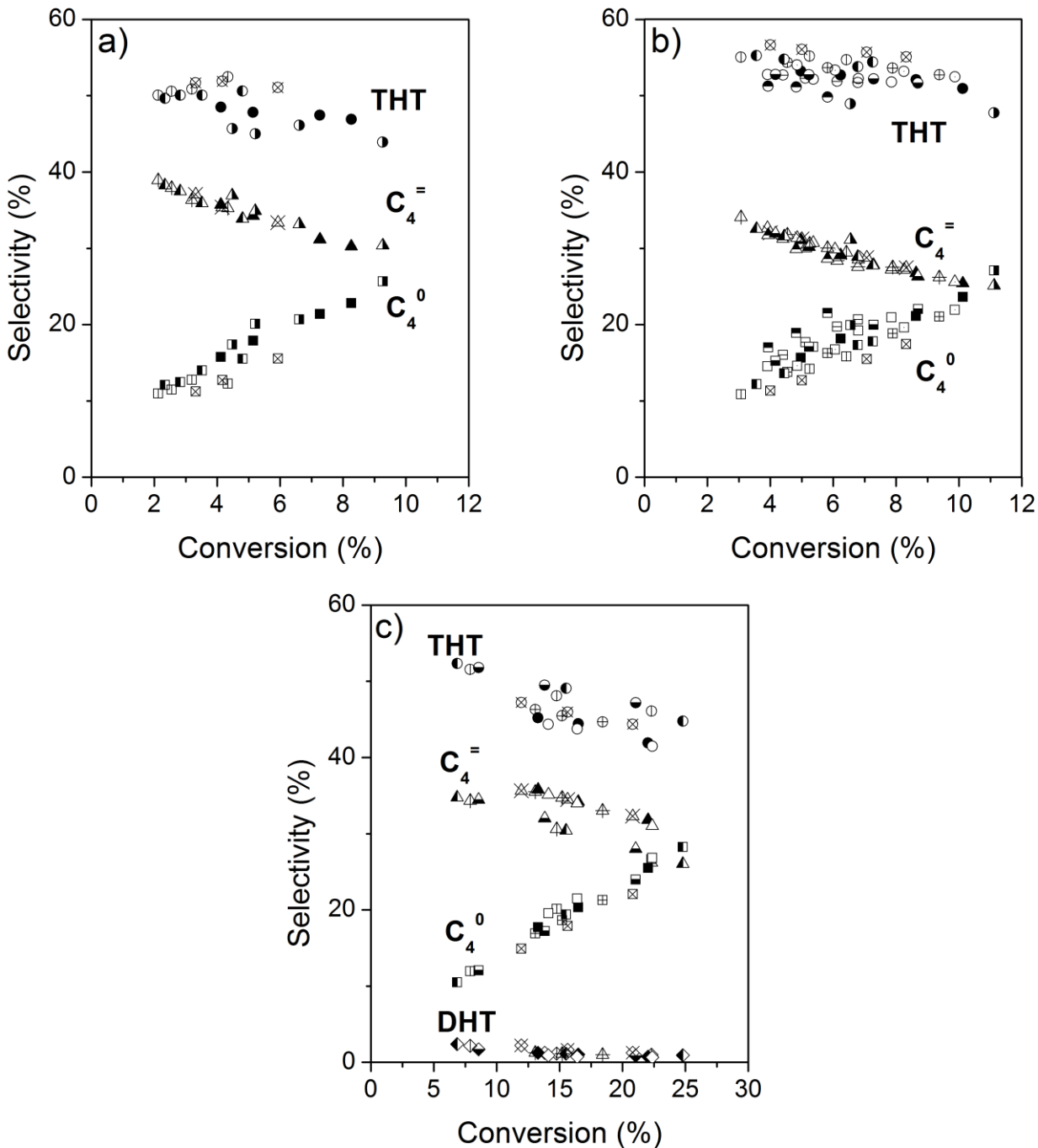
Figure 2.8: Selectivity towards tetrahydrothiophene, THT (circle), butenes, $C_4^=$ (triangle), butane, C_4^0 (square), dihydrothiophene , DHT (diamond) as a function of conversion on 15% nominal wt. samples of Re/SiO$_2$ at (a) 2.0 MPa H$_2$, (b) 3.0 MPa H$_2$ and of ReS$_x$ at (c) 3.0 MPa H$_2$ at 573 K and 1.0 kPa thiophene, 0.0003 H$_2$S/H$_2$ (◑); 2.5 kPa thiophene, 0.0003 H$_2$S/H$_2$ (●); 5.0 kPa thiophene, 0.0003 H$_2$S/H$_2$ (◓); 7.5 kPa thiophene, 0.0003 H$_2$S/H$_2$ (◐); 10.0 kPa thiophene, 0.0003 H$_2$S/H$_2$ (◌); 2.5 kPa thiophene, 0.000067 H$_2$S/H$_2$ (◒); 2.5 kPa thiophene, 0.0001 H$_2$S/H$_2$ (⊖); 2.5 kPa thiophene, 0.00017 H$_2$S/H$_2$ (○); 2.5 kPa thiophene, 0.00027 H$_2$S/H$_2$ (⊙); 2.5 kPa thiophene, 0.00033 H$_2$S/H$_2$ (⊕); 2.5 kPa thiophene, 0.0005 H$_2$S/H$_2$ (⊗).
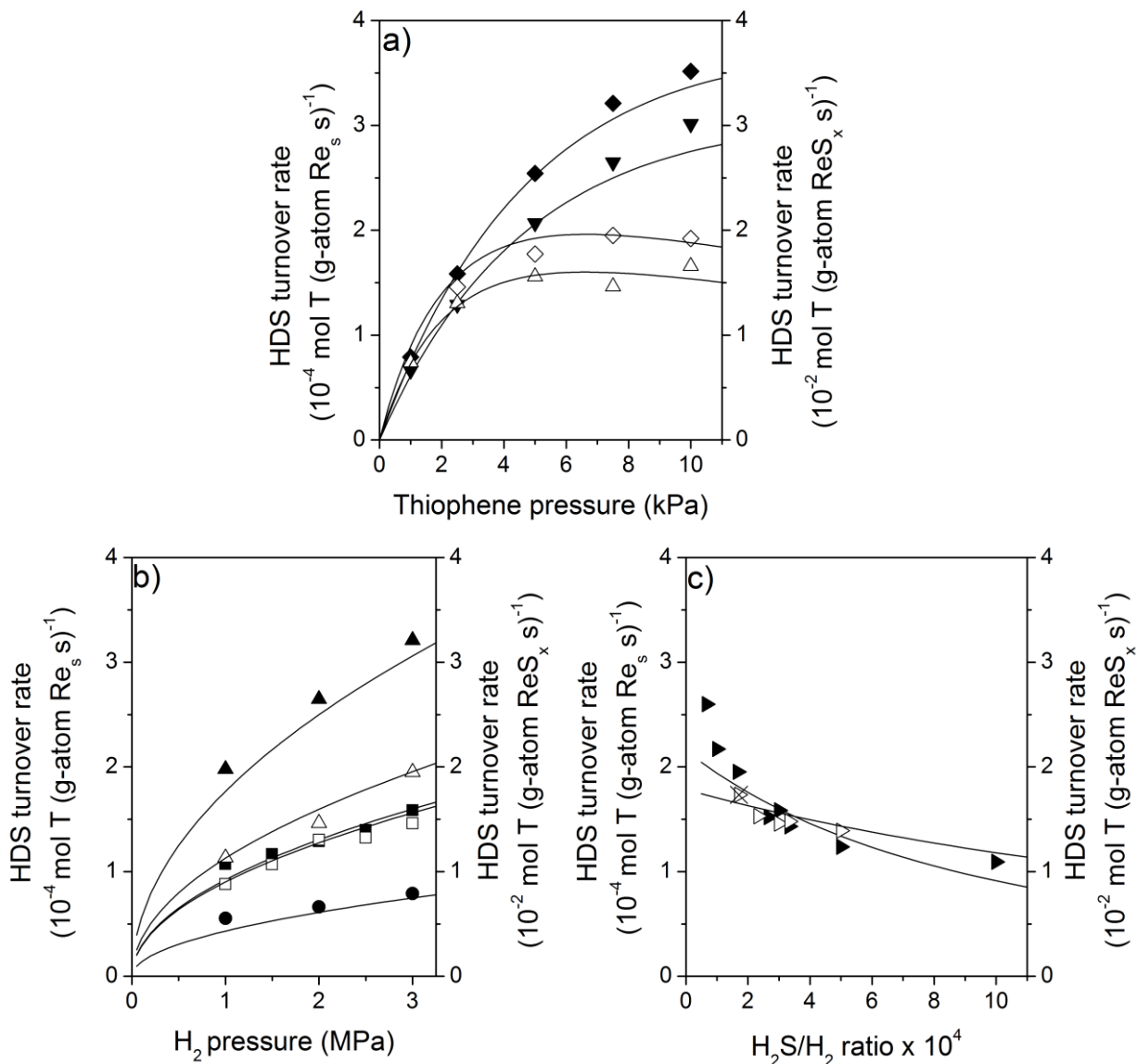
Figure 2.9: HDS turnover rates of thiophene (T) consumption on 15% nominal wt. samples of Re/SiO$_2$ (closed symbols, left axis) and of ReS$_x$/SiO$_2$ (open symbols, right axis) as a function of a) thiophene pressure at 2.0 MPa (▼) and 3.0 MPa (◆) H$_2$, 0.0003 H$_2$S/H$_2$ ratio, b) H$_2$ pressure at 1.0 kPa (●), 2.5 kPa (■), and 7.5 kPa (▲) thiophene, 0.0003 H$_2$S/H$_2$ ratio, and c) H$_2$S/H$_2$ ratio at 3.0 MPa H$_2$, 2.5 kPa thiophene (▶) at 573 K. Curves reflect regression of all measured data to the rate expression (Eq. 2.8). The data point for ReS$_x$ marked by ✖ was measured by calculating an average H$_2$S/H$_2$ ratio at a particular space velocity without inlet H$_2$S feed and thus not included in the fit.
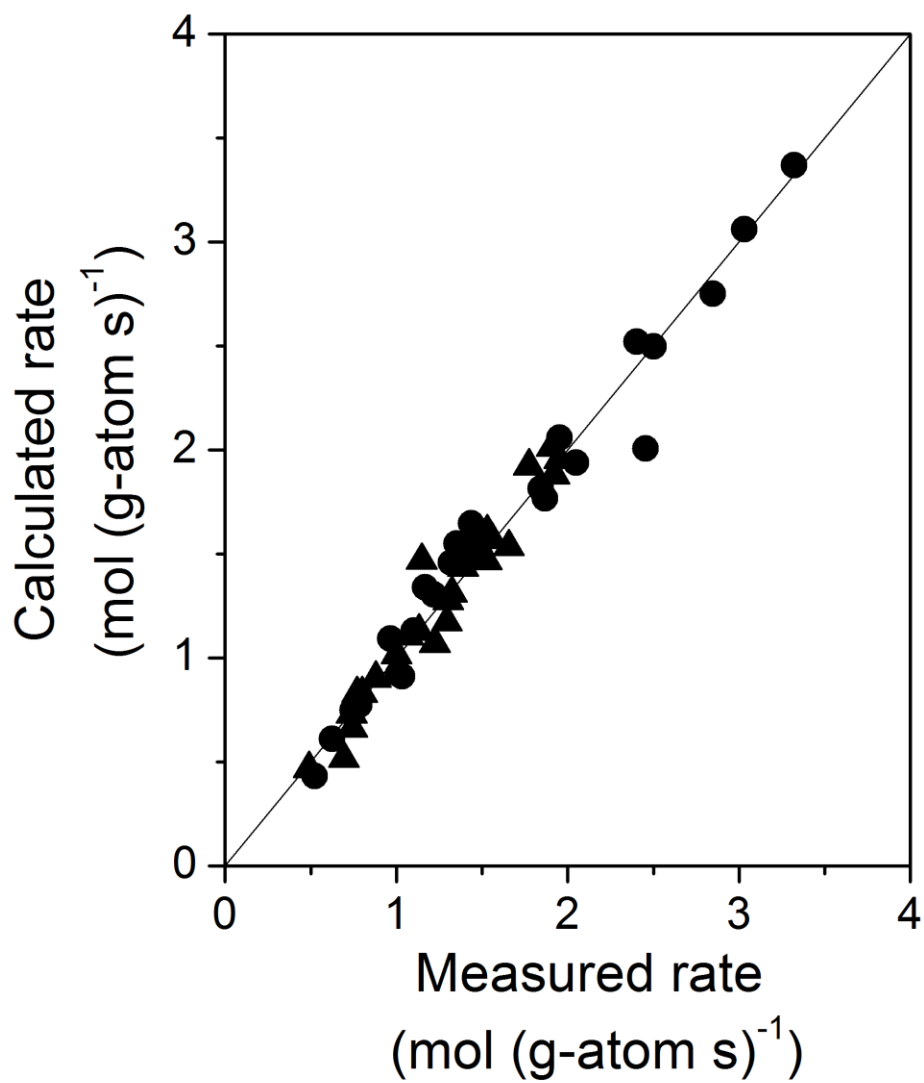
Figure 2.10: Parity plot of measured and calculated HDS rates from data regressed to the functional form of Equation 2.8 on 15% nominal wt. samples of (a) Re/SiO$_2$ x 10^4 (●) and (b) ReS$_x$/SiO$_2$ x 10^2 (▲) at 573 K.
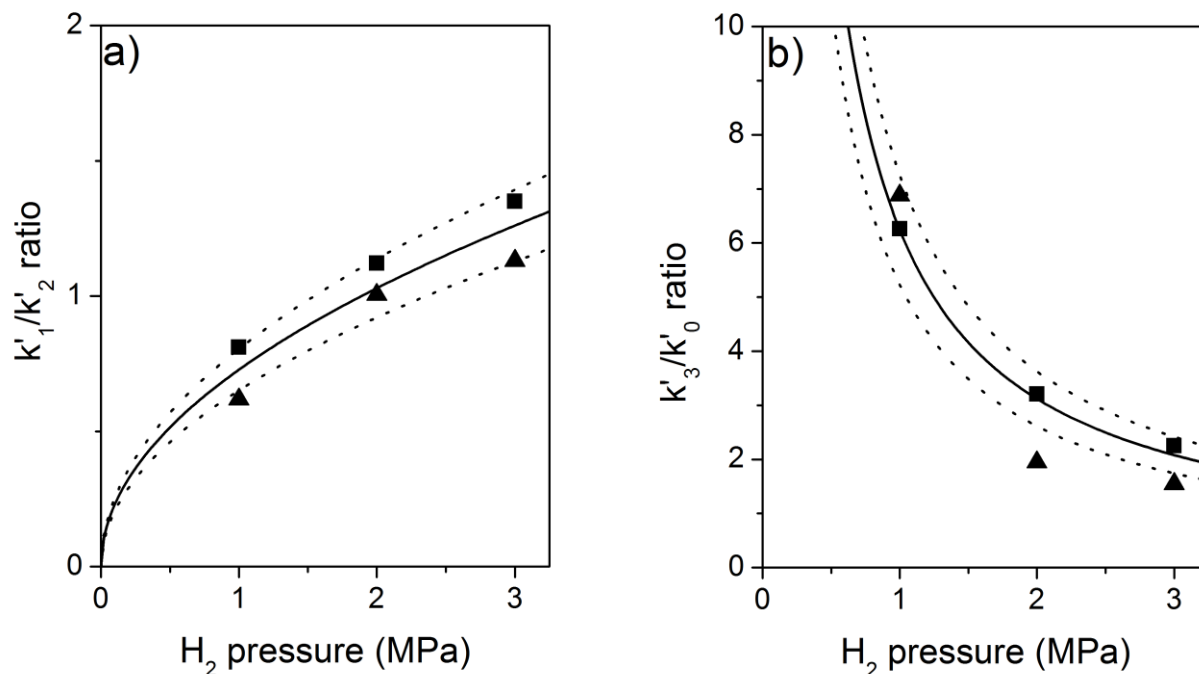
Figure 2.11: Calculated ratio of rate constants, a) k'_1 to k'_2 and b) k'_3 to k'_0 (from Scheme 2.1), acquired from regressed fittings (to Eq. 2.18) of THT selectivity to the functional forms of Equations 2.19 and 2.20, which are based on the assumptions of pseudo-first-order thiophene primary and THT secondary reactions for (15% nominal wt. samples of) Re/SiO$_2$ metal (■) and of ReS$_x$/SiO$_2$ (▲) at 573 K. Solid curves (—) indicate the best fit of the data to the equations $k'_1/k'_2 \sim (H_2)^{0.5}$ or $k'_3/k'_0 \sim (H_2)^{-1.0}$ for combined values measured on both catalysts. Dotted curves (⋯) indicate upper and lower 95% confidence intervals from regression of k'_1/k'_2 and k'_3/k'_0 to $\sim(H_2)^{0.5}$ and $\sim(H_2)^{-1.0}$, respectively.
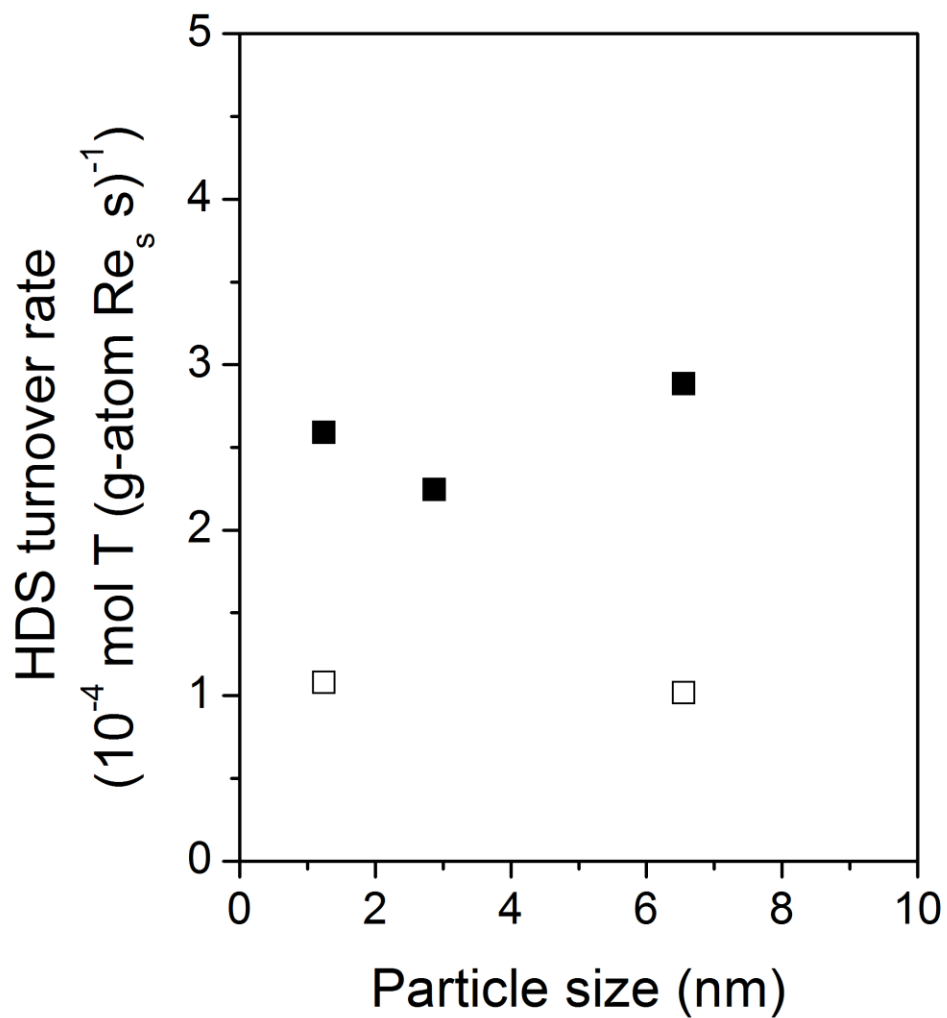
Figure 2.12: HDS turnover rates of total thiophene (T) conversion as a function of Re particle size (calculated from Re dispersion) of 15% nominal wt. Re/SiO$_2$ at 573 K, 3.0 MPa H$_2$, 2.5 kPa thiophene, with 0 kPa (■) and 1.0 kPa (□) H$_2$S co-feed at the inlet.
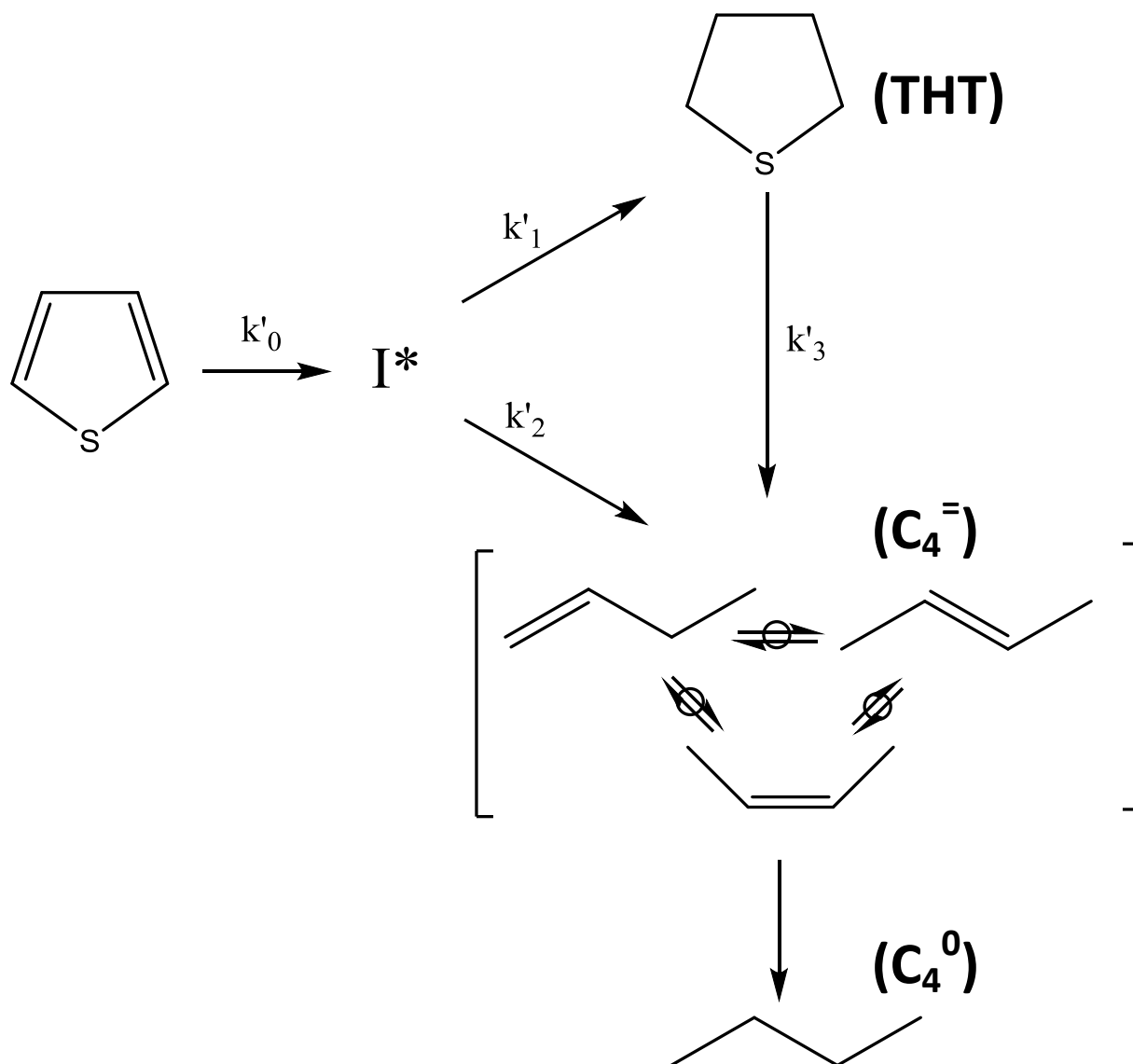
Scheme 2.1: Proposed reaction network for thiophene reaction on vacant sites of Re and ReS_x. Kinetic constants, k'_i, represent pseudo-rate constants, containing a product of relevant thermodynamic and kinetic rate constants (and terms associated to pressures associated to surface species and H_2 pressure, see Section 2.3.5). All steps occur on similar types of surface sites and the isomers of C_4 olefins are experimentally detected to form in an equilibrated mixture, as represented by ⇌.

H_2	+	2*	$\xrightleftharpoons{K_{H2}}$	2 (H*)	(i)
H_2S	+	*	$\xrightleftharpoons{K_{H2S}}$	H_2S^*	(ii)
H_2S^*	+	*	$\xrightleftharpoons{K_{HS}}$	H* + HS*	(iii)
HS*	+	*	$\xrightleftharpoons{K_S}$	H* + S*	(iv)
T	+	*	$\xrightleftharpoons{K_T}$	T*	(v)
T*	+	H*	$\xrightarrow{k_0}$	I*	(vi)
I*	+	nH*	$\xrightarrow{k_1}$	THT*	(vii)
I*	+	(n-1)H	$\xrightarrow{k_2}$	C_4^*	(viii)
C_4^*			$\xrightleftharpoons{K_{C4}^{-1}}$	C_4 + *	(ix)
THT*			$\xrightleftharpoons{K_{THT}^{-1}}$	THT + *	(x)
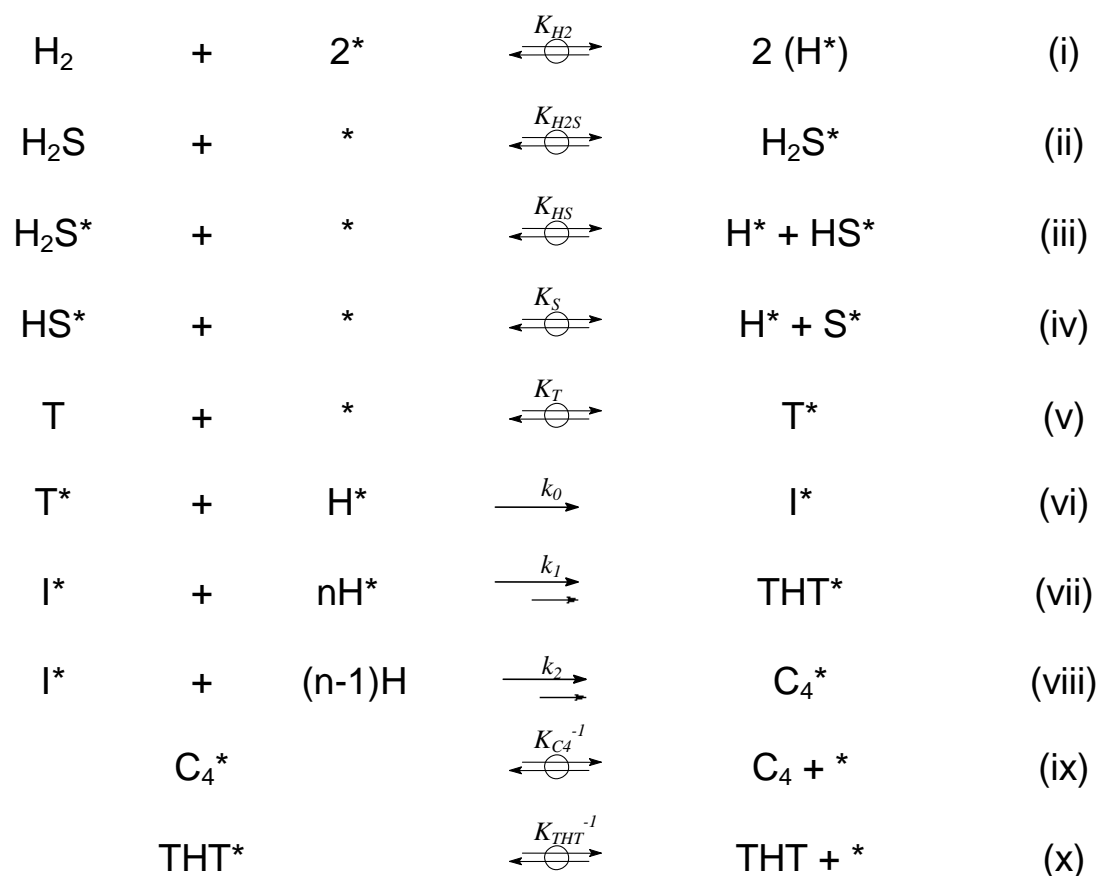
Scheme 2.2: Elementary steps for thiophene HDS and DS/HYD pathways. * is a vacant site; H*, H2S*, HS*, S*, T*, and I* are hydrogen, hydrogen sulfide, sulfhydryl, sulfur, thiophene, and monohydrothiophene surface species; $\xrightleftharpoons{}$ indicates a quasi-equilibrated step and $\xrightarrow{}$ represents the kinetically-relevant step followed by subsequent fast steps to form the products; T, THT, and C_4 represent thiophene, tetrahydrothiophene and butenes/butane gas phase species respectively.
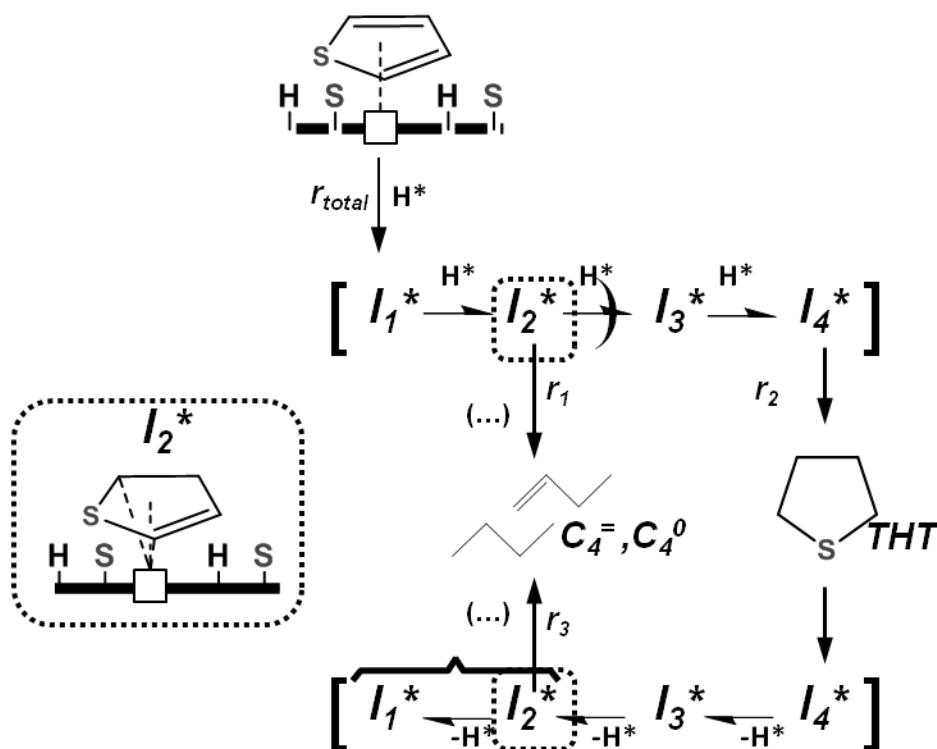
Scheme 2.3: Representation of the proposed set of elementary steps, described in Scheme 2.2. Molecularly adsorbed thiophene undergoes a kinetically-relevant hydrogen addition to enter a pool of partially-hydrogenated thiophene-derived surface intermediates, denoted as I_n^*, where n indicates the number of hydrogens added to an adsorbed thiophene species. THT is formed from desorption of I_4^*, but its rate (r_2) is determined by the barrier of the third H* addition, denoted by the counter,). Analysis of primary and secondary selectivity and reactions suggest that the dihydrothiophene species, I_2^*, undergoes C-S bond activation leading to C_4 products in both directions (i.e. from thiophene or from THT).

2.7   References

1.   *Catalysis Science and Technology*; H. Topsøe, B. S. C., F.E. Massoth in: J.R. Anderson, M. Boudart Ed.; Springer-Verlag: New York, 1996; Vol. 11.
2.   Girgis, M. J.; Gates, B. C. *Ind Eng Chem Res*. **30** (1991) 2021.
3.   Prins, R.; Debeer, V. H. J.; Somorjai, G. A. *Catal Rev*. **31** (1989) 1.
4.   Kasztelan, S.; Guillaume, D. *Ind Eng Chem Res*. **33** (1994) 203.
5.   Borgna, A.; Hensen, E. J. M.; van Veen, J. A. R.; Niemantsverdriet, J. W. *J Catal*. **221** (2004) 541.
6.   Besenbacher, F.; Helveg, S.; Lauritsen, J. V.; Laegsgaard, E.; Stensgaard, I.; Norskov, J. K.; Clausen, B. S.; Topsoe, H. *Phys Rev Lett*. **84** (2000) 951.
7.   Lauritsen, J. V.; Kibsgaard, J.; Olesen, G. H.; Moses, P. G.; Hinnemann, B.; Helveg, S.; Norskov, J. K.; Clausen, B. S.; Topsoe, H.; Laegsgaard, E., et al. *J Catal*. **249** (2007) 220.
8.   Neurock, M.; Vansanten, R. A. *J Am Chem Soc*. **116** (1994) 4427.
9.   Brunet, S.; Daudin, A.; Perot, G.; Raybaud, P.; Bouchy, C. *J Catal*. **248** (2007) 111.
10.   Cesano, F.; Bertarione, S.; Piovano, A.; Agostini, G.; Rahman, M. M.; Groppo, E.; Bonino, F.; Scarano, D.; Lamberti, C.; Bordiga, S., et al. *Catal. Sci. Technol.* **1** (2011) 123.
11.   Song, C. S. *Catal Today*. **86** (2003) 211.
12.   Stanislaus, A.; Marafi, A.; Rana, M. S. *Catal Today*. **153** (2010) 1.
13.   Hensen, E. J. M.; Kooyman, P. J.; van der Meer, Y.; van der Kraan, A. M.; de Beer, V. H. J.; van Veen, J. A. R.; van Santen, R. A. *J Catal*. **199** (2001) 224.
14.   Pecoraro, T. A.; Chianelli, R. R. *J Catal*. **67** (1981) 430.
15.   Lacroix, M.; Boutarfa, N.; Guillard, C.; Vrinat, M.; Breysse, M. *J Catal*. **120** (1989) 473.
16.   Niquille-Röthlisberger, A.; Prins, R. *J Catal*. **242** (2006) 207.
17.   Hensen, E. J. M.; Brans, H. J. A.; Lardinois, G. M. H. J.; de Beer, V. H. J.; van Veen, J. A. R.; van Santen, R. A. *J Catal*. **192** (2000) 98.
18.   Wang, H.; Iglesia, E. *J Catal*. **273** (2010) 245.
19.   Wang, H.-M.; Iglesia, E. *ChemCatChem*. **3** (2011) 1166.
20.   Quartararo, J.; Mignard, S.; Kasztelan, S. *J. Catal.* **192** (2000) 307.
21.   Ishihara, A.; Dumeignil, F.; Lee, J.; Mitsuhashi, K.; Qian, E. W.; Kabe, T. *Appl. Catal., A*. **289** (2005) 163.
22.   Noerskov, J. K.; Clausen, B. S.; Topsoe, H. *Catal. Lett.* **13** (1992) 1.
23.   Toulhoat, H.; Raybaud, P. *J. Catal.* **216** (2003) 63.
24.   Jacobsen, C. J. H.; Tornqvist, E.; Topsoe, H. *Catal. Lett.* **63** (1999) 179.
25.   Bussell, M. E.; Somorjai, G. A. *J. Phys. Chem.* **93** (1989) 2009.
26.   Kelly, D. G.; Odriozola, J. A.; Somorjai, G. A. *J. Phys. Chem.* **91** (1987) 5695.
27.   Escalona, N.; Gil, L. F. J.; Vrinat, M.; Nguyen, T. S.; Laurenti, D.; Lopez, A. A. *Catal. Commun.* **8** (2007) 285.
28.   Arnoldy, P.; Van, d. H. J. A. M.; De, B. V. H. J.; Moulijn, J. A. *Appl. Catal.* **23** (1986) 81.
29.   Arnoldy, P.; Van, O. E. M.; De, B. V. H. J.; Moulijn, J. A.; Prins, R. *Appl. Catal.* **48** (1989) 241.

30. Sepulveda, C.; Belliere, V.; Laurenti, D.; Escalona, N.; Garcia, R.; Geantet, C.; Vrinat, M. *Appl. Catal., A*. **393** (2011) 288.
31. Ho, T. C.; Shen, Q.; McConnachie, J. M.; Kliewer, C. E. *J. Catal.* **276** (2010) 114.
32. Mars, P.; van Krevelen, D. W. *Chem. Eng. Sci.* **3** (1954) 41.
33. Bartholomew, C. H.; Agrawal, P. K.; Katzer, J. R. *Adv. Catal.* **31** (1982) 135.
34. Benard, J.; Oudar, J.; Barbouth, N.; Margot, E.; Berthier, Y. *Surf. Sci.* **88** (1979) L35.
35. Flaherty, D. W.; Iglesia, E. *J. Am. Chem. Soc.* **135** (2013) 18586.
36. Flaherty, D. W.; Hibbitts, D. D.; Gürbüz, E. I.; Iglesia, E. *J Catal*. **311** (2014) 350.
37. Flaherty, D. W.; Hibbitts, D. D.; Iglesia, E. *J Am Chem Soc*. **136** (2014) 9664.
38. Flaherty, D. W.; Uzun, A.; Iglesia, E. *The Journal of Physical Chemistry C*. **119** (2015) 2597.
39. Yates, D. J. C.; Sinfelt, J. H. *J. Catal.* **14** (1969) 182.
40. Arnoldy, P.; Van, O. E. M.; Bruinsma, O. S. L.; De, B. V. H. J.; Moulijn, J. A. *J. Catal.* **93** (1985) 231.
41. Lutterotti, L.; Bortolotti, M.; Ischia, G.; Lonardelli, I.; Wenk, H. R. *Zeitschrift für Kristallographie Supplements*. **2007** (2007) 125.
42. Murray, H. H.; Kelty, S. P.; Chianelli, R. R.; Day, C. S. *Inorganic Chemistry*. **33** (1994) 4418.
43. Yang, N.; Mickelson, G. E.; Greenlay, N.; Kelly, S. D.; Vila, F. D.; Kas, J.; Rehr, J. J.; Bare, S. R. *AIP Conference Proceedings*. **882** (2007) 591.
44. Bai, M.; Liu, Z.-h.; Zhou, L.-j.; Liu, Z.-y.; Zhang, C.-f. *Trans. Nonferrous Met. Soc. China*. **23** (2013) 538.
45. Tysoe, W. T.; Zaera, F.; Somorjai, G. A. *Surface Science*. **200** (1988) 1.
46. Mitra, B.; Gao, X.; Wachs, I. E.; Hirt, A. M.; Deo, G. *Physical Chemistry Chemical Physics*. **3** (2001) 1144.
47. Breysse, M.; Furimsky, E.; Kasztelan, S.; Lacroix, M.; Perot, G. *Catalysis Reviews*. **44** (2002) 651.
48. Mangnus, P. J.; Riezebos, A.; Vanlangeveld, A. D.; Moulijn, J. A. *J Catal*. **151** (1995) 178.
49. Maxted, E. B. *Adv. Catal.* **2** (1951) 129.
50. Shatynski, S. *Oxid Met*. **11** (1977) 307.
51. Oyama, S. T. *Catal Today*. **15** (1992) 179.
52. Volpe, L.; Boudart, M. *Journal of Solid State Chemistry*. **59** (1985) 332.
53. Volpe, L.; Boudart, M. *Journal of Solid State Chemistry*. **59** (1985) 348.
54. Proykova, A.; Berry, R. S. *Journal of Physics B: Atomic, Molecular and Optical Physics*. **39** (2006) R167.
55. Kubicka, H. *J. Catal.* **12** (1968) 223.
56. Yao, H. C.; Shelef, M. *J. Catal.* **44** (1976) 392.
57. Isaacs, B. H.; Petersen, E. E. *J. Catal.* **85** (1984) 1.
58. Chadzynski, G. W.; Kubicka, H. *Thermochim. Acta*. **158** (1990) 353.
59. Chądzyński, G. W.; Kubicka, H. *Thermochimica Acta*. **158** (1990) 369.
60. Okal, J.; Tylus, W.; Kepinski, L. *J. Catal.* **225** (2004) 498.
61. Zmierczak, W.; MuraliDhar, G.; Massoth, F. E. *J. Catal.* **77** (1982) 432.

62.   Niquille-Roethlisberger, A.; Prins, R. *Catal. Today*. **123** (2007) 198.
63.   Topsoe, N. Y.; Topsoe, H. *J Catal*. **139** (1993) 641.
64.   Korányi, T. I.; Moreau, F.; Rozanov, V. V.; Rozanova, E. A. *Journal of Molecular Structure*. **410–411** (1997) 103.
65.   Berhault, G.; Lacroix, M.; Breysse, M.; Mauge, F.; Lavalley, J.-C.; Qu, L. *J. Catal.* **170** (1997) 37.
66.   Berhault, G.; Lacroix, M.; Breysse, M.; Mauge, F.; Lavalley, J.-C.; Nie, H.; Qu, L. *J. Catal.* **178** (1998) 555.
67.   Madon, R. J.; Shaw, H. *Catal. Rev. - Sci. Eng.* **15** (1977) 69.
68.   Oudar, J. *Catal. Rev. - Sci. Eng.* **22** (1980) 171.
69.   Yoon, H. A.; Materer, N.; Salmeron, M.; Van Hove, M. A.; Somorjai, G. A. *Surface Science*. **376** (1997) 254.
70.   Kelly, D. G.; Gellman, A. J.; Salmeron, M.; Somorjai, G. A.; Maurice, V.; Huber, M.; Oudar, J. *Surf. Sci.* **204** (1988) 1.
71.   McCarty, J. G.; Wise, H. *The Journal of Chemical Physics*. **72** (1980) 6332.
72.   McCarty, J. G.; Wise, H. *J. Chem. Phys.* **74** (1981) 5877.
73.   McCarty, J. G.; Wise, H. *The Journal of Chemical Physics*. **76** (1982) 1162.
74.   McCarty, J. G.; Sancier, K. M.; Wise, H. *J Catal*. **82** (1983) 92.
75.   McCarty, J. G.; Wise, H. *J Catal*. **94** (1985) 543.
76.   Topsoe, H.; Clausen, B. S. *Appl. Catal.* **25** (1986) 273.
77.   Alfonso, D. R. *Surf. Sci.* **602** (2008) 2758.
78.   Alfonso, D. R. *The Journal of Physical Chemistry C*. **115** (2011) 17077.
79.   Boudart, M. *Adv. Catal*. **20** (1969) 153.
80.   Somorjai, G. A.; Li, Y. *Introduction to surface chemistry and catalysis*; John Wiley & Sons, 2010.
81.   Allian, A. D.; Takanabe, K.; Fujdala, K. L.; Hao, X.; Truex, T. J.; Cai, J.; Buda, C.; Neurock, M.; Iglesia, E. *J. Am. Chem. Soc.* **133** (2011) 4498.

2.8   Supporting Information

2.8.1   *X-ray diffractogram and Rietveld refinement of Re/SiO₂*

X-ray diffraction patterns were measured on Re/SiO$_2$, treated in flowing H$_2$ at 773 K, 2 h, cooled and passivated with 0.1% O$_2$/He for 2 h under ambient conditions. Samples were uniformly spread on a glass slide with Vaseline, loaded into a diffractometer (Siemens D500). Using Cu Kα radiation (λ = 0.15418 nm), analysis was performed over a range of 2θ angles = 5-55° at 0.05° intervals. The resulting patterns (Figure 2.S1) were then fitted via Rietveld refinement using Materials Analysis Using Diffraction (MAUD) software (University of Trento) after inputting known crystallographic information, corresponding to Re metal, listed below,

Rhenium crystallographic information
(source: Wycoff, R. W. G, *Crystal Structures 1*, 7-83. Interscience Publishers (1963), New York)
Space group: P6$_3$/mmc (hcp)
Cell parameters (a,b,c); (α,β,γ): (2.7608 Å, 2.7608 Å, 4.4582 Å); (90°, 90°, 120°)
Atom distances (x,y,z): (1/3, 2/3, 1/4)

Both isotropic and anistropic models were considered in the fittings. Strain models, based on Popa and Balzar (*J. Appl. Cryst.* **41** (2008) 615.), were employed in the software to account for anisotropy. Estimated particle size was reported by the software, assuming negligible instrument broadening, which provided a lower limit estimate of 13 nm. While this value is less than that predicted from the Scherrer equation, after regression of peaks to Gaussian distributions in order to acquire half-width full maximum (HWFM), they are still larger than surface-averaged particle sizes measured by transmission electron microscopy (TEM). We conclude that we remained unsuccessful in fully accounting for the heterogeneity that can lead to XRD peak broadening despite attempts at refining the patterns.
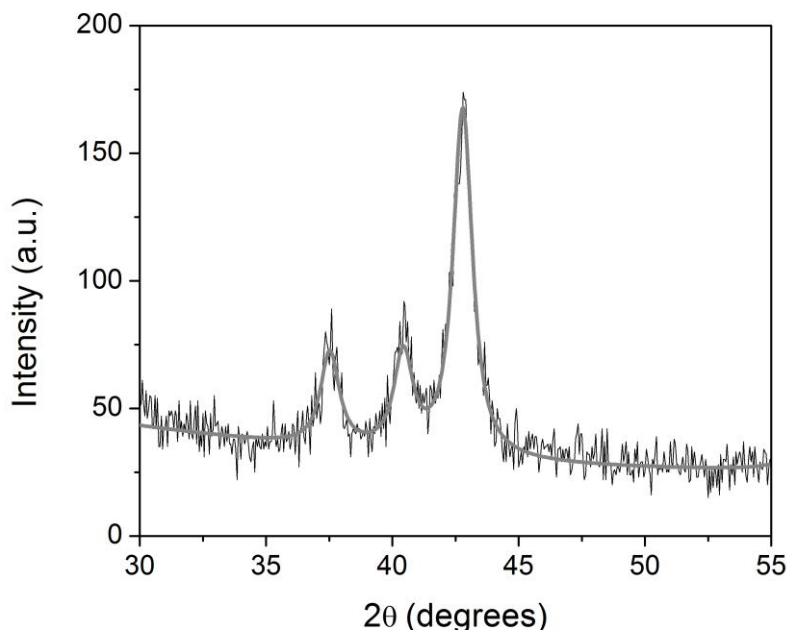
Figure 2.S1: XRD pattern for Re/SiO$_2$ (after H$_2$ treatment at 773 K). Solid curve reflects the Rietveld refinement fit of pattern using MAUD software.
Signature 2θ values reported for Re$_2$O$_7$: 24.8°, 40.5°, 42.9°
(source: Wycoff, R. W. G, *Crystal Structures 1*, 7-83. Interscience Publishers (1963), New York)
.

2.8.2 *Mears' criterion for neglecting internal mass transport effects*

Mears' criterion for neglecting internal mass transport effects can be calculated to ensure that measured rates absent of any transport artifacts. The criterion is defined as follows,

$$M_M = \frac{-r_A'' \cdot \rho_p \left(\frac{4}{3}\pi r_p^3\right)}{\frac{D}{L} \cdot C_A 4\pi r_p^2} \ll 1.0 \tag{2.S1}$$

, where L is the characteristic length (radius of the pellet), C$_A$ is the concentration of thiophene in the reactant stream and r$_A''$ is the reaction rate per mass of catalyst, ρ$_p$ is the mass of Re per volume of catalyst,

$$\rho_p = \frac{grams\ of\ Re}{volume\ of\ pellet} \tag{2.S2}$$

For the diffusion term, D, we considered both molecular and Knudsen diffusion regimes.

$$D_{bA} = \frac{\lambda v}{3} \qquad \text{(molecular diffusivity)} \tag{2.S3}$$
, where
$$\lambda = \frac{RT}{\sqrt{2}\pi d^2 NP} \tag{2.S4}$$

, where d is the diameter of the molecule (4.6Å for thiophene), N is Avogadro's number, and P is the reactant gas (thiophene) pressure.

$$D_K = \frac{2}{3}<r>v \qquad \text{(Knudsen diffusivity)} \tag{2.S5}$$

, where

$$r = \frac{2V}{S} \cdot \frac{\phi}{1-\phi} \tag{2.S6}$$

, where V is the volume and S is the surface area of the sphere and ϕ is the void fraction/porosity.
(source: Tremitchell Wright, Douglas M. Smith, Dorothy L. Stermer, *Ind. Eng. Chem. Res.*, 1987, 26 (6))

Composite diffusivity is used,

$$D_e = \left(\frac{1}{D_{bA}} + \frac{1}{D_K}\right)^{-1} \tag{2.S7}$$

to calculate an effective diffusivity,

$$D_{eff} = \frac{\phi D_e}{\tau} = \phi^2 D_e \tag{2.S8}$$

Table 2.S1 reflects calculated representative values of M_M at typical reaction conditions.

Table 2.S1: Mears' criterion for 1:1 SiO_2/catalyst dilution ratios at different HDS conditions.

HDS conditions[a] H_2 (MPa) / H_2S (kPa)	Measured turnover rate (mol thiophene (g-atom Re_s s)$^{-1}$)	M_M
1 / 0.5	0.026	0.0009
2 / 0.6	0.040	0.0028

[a] At 2.5 kPa thiophene, 573 K.

Since values of M_M are <<1, we confirm the absence of artifacts due to mass transport at the lowest catalyst dilution level for Re/SiO_2.

2.8.3 X-ray diffraction of ReO$_x$

X-ray diffraction was performed on ReO$_x$/SiO$_2$ (after 573 K treatment of impregnated samples in dry air) by loading the powdered samples, prepared as described in Section 2.8.1 for Re/SiO$_2$ samples, into a diffractometer (Siemens D500). Analysis was performed with Cu Kα radiation (λ = 0.15418 nm) over a range of 2θ angles = 5-150° at 0.02° intervals. No features were observed at 2θ angles >40°, indicative of an absence of a crystalline metal phase. Broad features observed at 2θ <30° are attributed to the SiO$_2$ support. The lack of peaks associated with Re$_2$O$_7$ (the expected oxidation state), ReO$_3$, and ReO$_2$ suggest either an absence of an oxide phase or the formation of well-dispersed materials. ICP-OES elemental analysis has confirmed high concentrations of Re content (11.7 % wt.) in this material and sharp features associated to Re metal are formed upon H$_2$ treatment (at 773 K) of this material (Figure 2.S1); thus, we conclude the absence of ReO$_x$ peaks reflect the formation of highly dispersed, non-crystalline Re(+7) oxide phases (oxidation state predicted by phase diagrams) as a result of high temperature treatments in dry air.
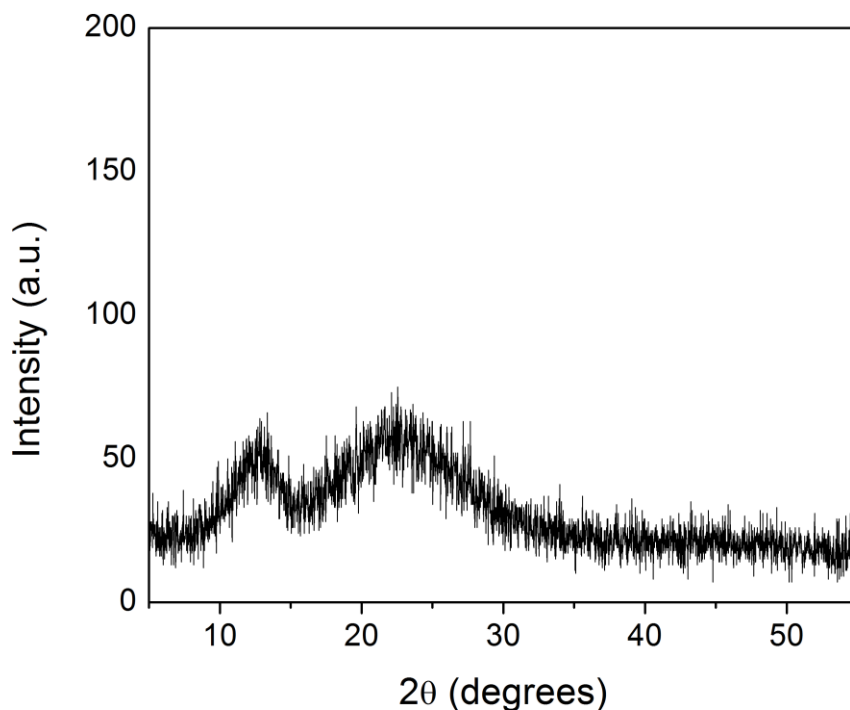
Figure 2.S2: XRD pattern for pre-reduced catalyst.
Signature 2θ values for Re$_2$O$_7$: 22.4°, 35.3°, 47.7°.

2.8.4 Temperature programmed reduction of ReO$_x$ precursors

Temperature programmed reduction (TPR) was performed on ReO$_x$, following protocols reported in Section 2.3.2. A shoulder peak at lower temperatures was observed in samples of higher wt. Re loadings (Figure 2.S3(ii), 2.S3(iii)), indicating multiple species of either different oxidation state or chemical nature. While water evolution was not monitored during these

experiments, previous studies on ReO_x grafted on zeolitic materials have suggested that the lower temperature reduction peak corresponds to a step that breaks the bond between Re and oxygen in SiO_2 (i.e. absence of H_2O evolution). A minority of total oxide species were grafted onto SiO_2 at the highest loading (Figure 2.S3(iii)) while a complete absence of grafting was observed in the catalyst with the lowest loading (Figure 2.S3(i)), consistent with protocols that avoided treatments in air at 573 K for its synthesis. A shift of the maximum peak towards lower temperatures could suggest that lower wt. loadings and, consequently, smaller particle size (Table 2.1) lead to greater reducibility; another possibility is that it facilitates H_2 dissociation because of the higher abundance of more coordinatively unsaturated Re metal atoms, which enhances the autocatalytic nature of ReO_x reduction.
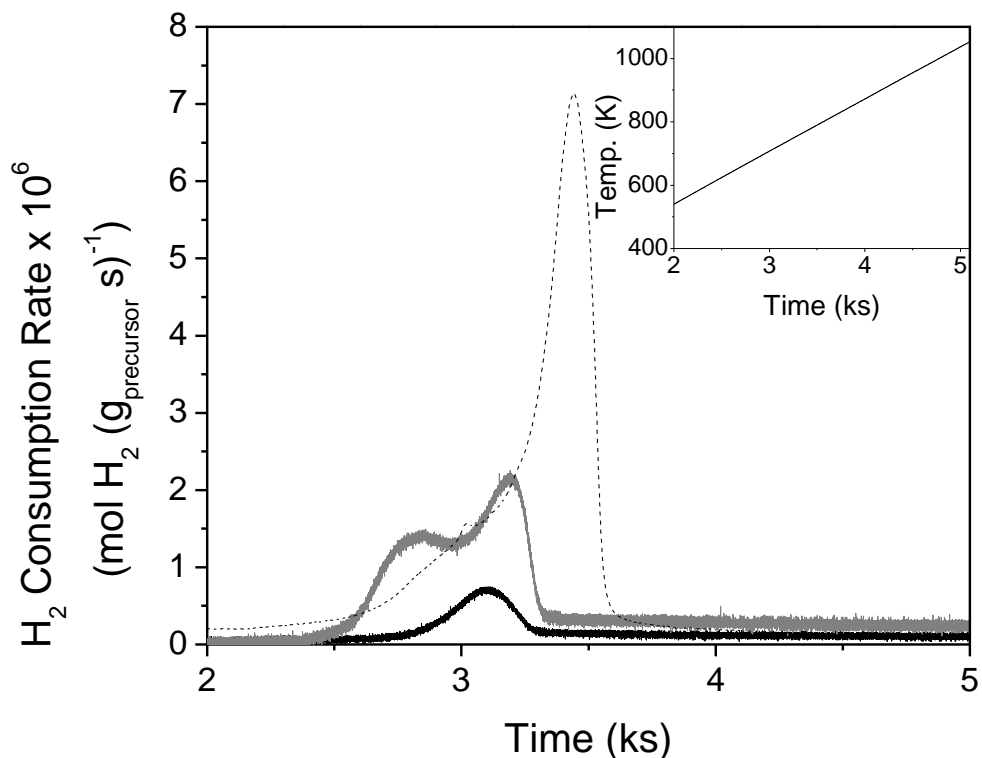
Figure 2.S3: Temperature programmed reduction of ReO_x (or NH_4ReO_4) precursors for (i) 1% (—), (ii) 5% (—), and (iii) 15% (···) wt. Re loadings. Inset: temperature ramp.

2.8.5 Resulfidation of pre-reduced Re clusters

The effects of treatments cycles were performed on Re to probe the metastable nature of phase stability. Kinetic measurements were made at reaction conditions (3.0 MPa H_2, 2.5 kPa thiophene, H_2S/H_2 ratio 3.3×10^{-4}, 623 K) after each treatment (at atmospheric pressure). The initial and intermittent pretreatments included:

(1) Pretreatment of the ReO_x at 773 K, 2h, in 5% H_2S/He (Praxair, certified mixture)
(2) Subsequent treatment at 673 K overnight in H_2 (Praxair, 99.999%)
(3) Subsequent treatment at 773 K, 2h, in 5% H_2S/He (Praxair, certified mixture)
(4) Subsequent treatment at 773 K, 2h, in H_2 (Praxair, 99.999%)
(5) Subsequent treatment at 773 K, 2h, in 5% H_2S/He (Praxair, certified mixture)

Figure 2.S4 shows measured HDS rates after each treatment (1)-(5). Note that catalytic stability of more than 100 h has been demonstrated (Figure 2.5), thus, the reduction in rates is not a result of catalyst deactivation but as a result of structural changes induced by exposing the catalyst to intervening reducing and sulfiding conditions.
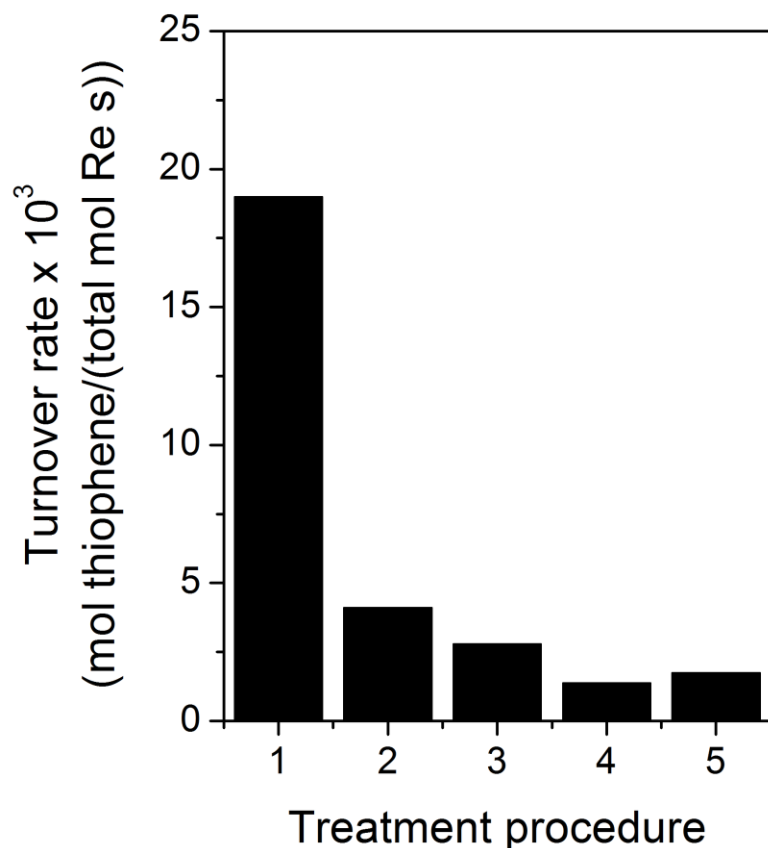
Figure 2.S4: HDS turnover rates (normalized by total Re content) measured after *in-situ* reducing or sulfiding treatments (1-5).

2.8.6 *Oxygen chemisorption on Re metal samples*

Figure 2.S5 shows various isotherms collected from oxygen chemisorption experiments (described in Section 2.3.2) as a function of O_2 pressure at 298, 323, and 373 K on a 15% nominal wt. Re/SiO_2 sample, previously treated at 773 K in H_2. At 298 K and 323 K, saturation of the surface occurred around 250 torr, which is unexpectedly high for strongly oxophilic materials. The lower initial uptake of oxygen (<100 torr) at 323 K compared to that at 298 K resembles behaviors expected for weakly interacting adsorbates. The slow uptake of oxygen on supported Re nanoparticles at temperatures lower than 373 K, however, is not unprecedented [59], and we propose that this effect may be the result of hindered O_2 dissociation on a partially O-covered surface exhibiting minimal adatom surface mobility, thereby lowering the probability of forming two adjacent empty metal sites required for diatomic dissociation. This hindered process is overcome at higher O-chemical potentials, eventually resulting in monolayer coverages. Sub-surface oxidation becomes a concern only at elevated temperatures, as reflected by an increased consumption of O_2 at 373 K, while uptakes observed at temperatures at or below 323 K are assumed to be surface limited due to convergence, at high O_2 pressures, to similar values of O/Re ratio much lower than the stoichiometry expected for the lowest valent stable bulk oxide, ReO_2.

O_2 chemisorption isotherms for various loadings of Re/SiO_2 are shown in Figure 2.S6. These values of oxygen uptake per total Re atoms are proportional to catalyst dispersion, which appears to be a function of Re wt. loading, with samples containing higher total Re content exhibiting lower dispersion. Cleanliness of metal surfaces before starting chemisorption experiments was probed by subjecting the 1% nominal wt. Re/SiO_2 sample to different evacuation procedures after *in-situ* H_2 treatment at 773 K. In case (i), the system was evacuated to 10^{-5}-10^{-4} torr at 773 K for 1 h, followed by continued evacuation as the sample cooled to the analysis temperature (323 K) over 3 h prior to measurements, whereas in case (ii), the sample was cooled first to 323 K under H_2 flow, after which the system was evacuated under vacuum for 0.5 h prior to measurements. The resulting isotherms from both procedures are indistinguishable, and their reproducibility supports an absence of contamination from the reduction procedure or from pumping duration and/or evacuation temperature. The 1% wt. loading sample exhibited a shift to lower saturation pressure (150 torr) compared to that in the case of the 15% wt. sample (250 torr), reflecting a lower kinetic barrier towards surface saturation.
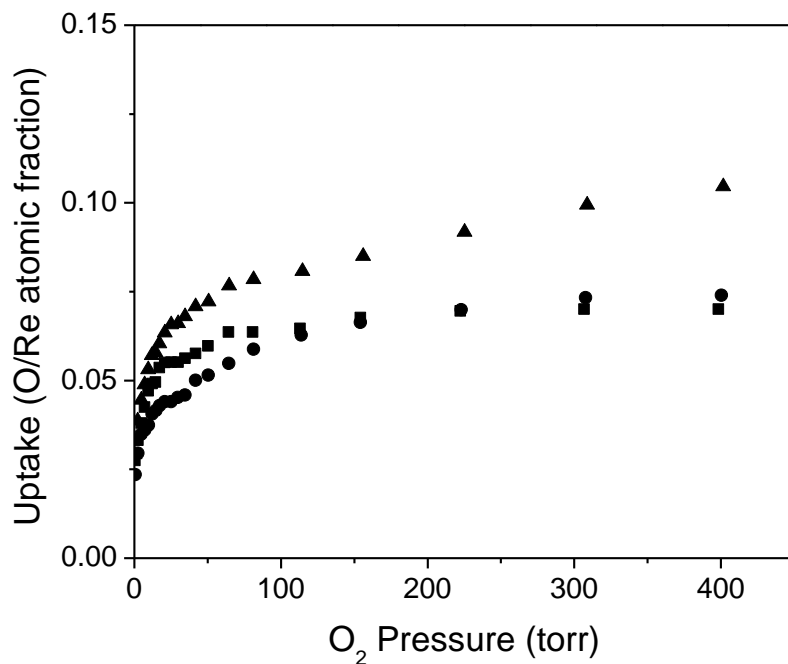
Figure 2.S5: Oxygen adsorption isotherms as a function of O_2 pressure exposed to the 15% nominal wt. Re/SiO_2 sample at 373 K (▲), 323 K (●), and 298 K (■).
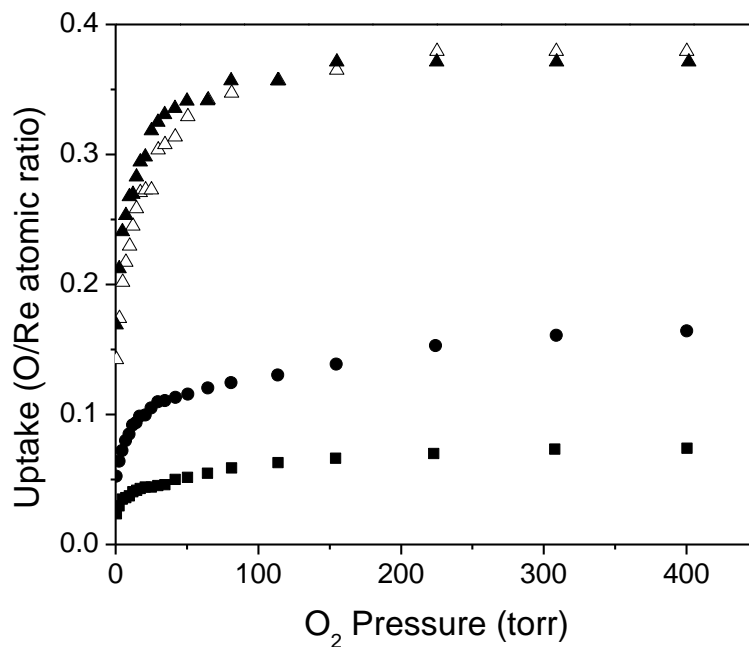
Figure 2.S6: Oxygen adsorption isotherms as a function of oxygen pressure at 323 K for 15% wt. (■), 5% wt. (●), and 1% nominal wt. Re/SiO_2 following pretreatment/evacuation procedures described by case (i) (Δ) and case (ii)(▲), as described in Section 2.8.6.

2.8.7 Sensitivity analysis of fitted parameters

Regression of kinetic data to the derived rate laws requires a balance between goodness of fit and sensitivity of the fitted parameters. More degrees of freedom will unequivocally provide better fits; however, whether a degree is important can be probed by how sensitively it affects the overall sum of residuals. Through statistical treatments, we have identified a simplified form of a rate expression that can describe all kinetic data on Re/SiO$_2$ and ReS$_x$/SiO$_2$,

$$\frac{r}{[L]} = \frac{\alpha (H_2)^{0.5}(T)}{\left(1+\beta(T)+\eta\frac{(H_2S)}{(H_2)}\right)^2} \tag{2.S9}$$

, without any sacrifice in its ability to accurately predict measured rates as evidenced by corresponding parity plots (Figure 2.10).

The numerator H$_2$ order is unequivocally 0.5, as attempts to maximize x (upper bound), by fitting data to the rate expression below led to values of x <1.

$$\frac{r_{\max x}}{[L]} = \frac{\alpha (H_2)^x (T)}{(1+\beta(T)+\gamma(H_2)^{0.5}+\eta(H_2S))^2} \tag{2.S10}$$

The sum of squares of residuals (SSR),

$$SSR = \sum_i \left(r_{i,predicted} - r_{i,measured} \right)^2 \tag{2.S11}$$

, is minimized during non-linear regression of rate parameters. We can probe how strongly the estimated rates depend on these best fit parameter values by analyzing their sensitivity to parameter value changes. The sensitivity of these parameters is quantified by the change in SSR as a response to a change (e.g. ±20%) to the best fit parameter value, described as,

$$Relative\ SSR = \frac{(SSR)_{new\ parameter\ value}}{(SSR)_{regressed\ parameter\ value}} \tag{2.S12}$$

Relative SSR values ranged between 1.3-10 (Figs. 2.S7 and 2.S8), indicating that calculated rates depend sensitively on the best fit values of the regressed constants used to describe measured rates.

Figure 2.S7: Relative sum of squares of residuals as a function of changes in the fitted rate parameter of α (■), β (▲), and η (●) on Re/SiO$_2$.

Figure 2.S8: Relative sum of squares of residuals as a function of changes in the fitted rate parameter of α (■), β (▲), and η (●) on ReS$_x$/SiO$_2$.

CHAPTER THREE

C-S Bond Activation in Thiophene Hydrodesulfurization
on Sulfur-Covered Transition Metal Catalysts

Abstract

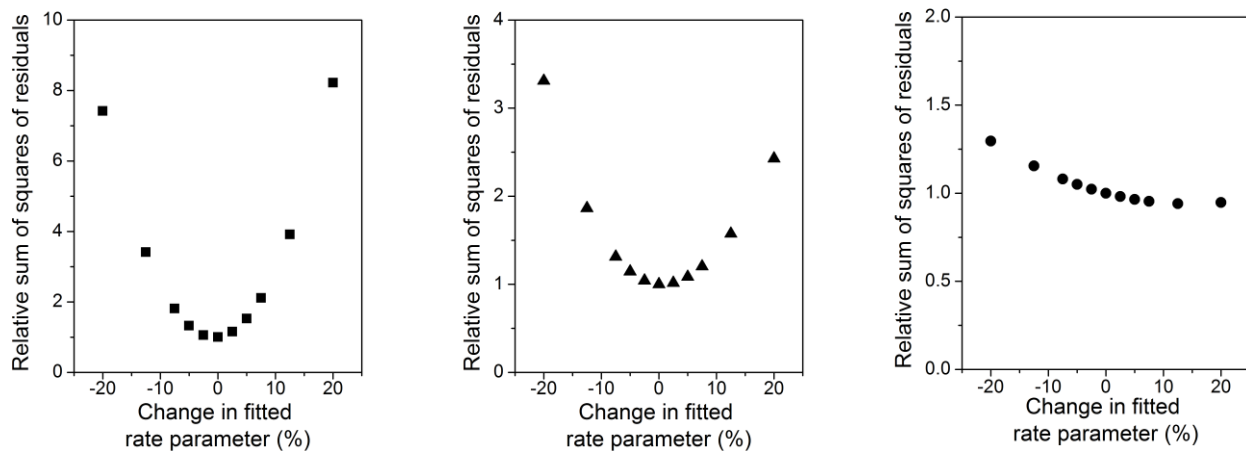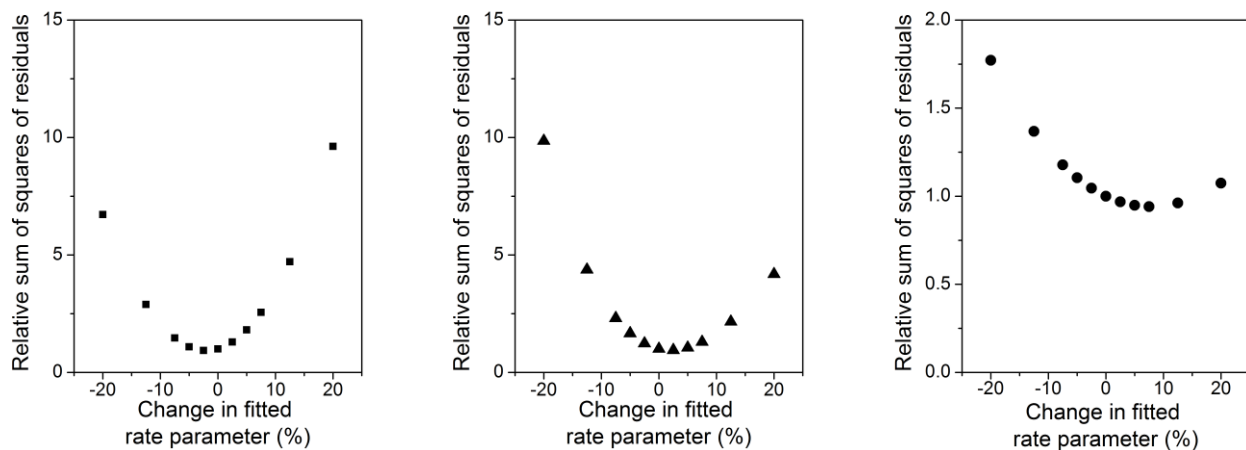Rigorous studies of hydrodesulfurization (HDS) reactions are facilitated by well-defined catalysts, strict reactor operating conditions, and careful kinetic assessments. The formation of H_2S as a product of thiophene conversion inhibits the reaction, challenging accurate rate measurements because of non-uniform inhibition across the catalyst bed as a result of concentration gradient along the axial direction of the reactor. Differential regimes may be maintained by co-feeding H_2S at the inlet, avoiding gradients in sulfur chemical potential set by the H_2S/H_2 ratio as a result of equilibrated adsorptions of H_2S and H_2 under relevant HDS conditions. An understanding of primary and secondary reaction pathways must accompany these rigorous rate measurements because, while measured thiophene consumption rates may be kinetic in origin, interpretations of product formation rates may be affected by fast secondary reactions that render linear extrapolations of selectivity (to zero conversion) non-rigorous over a range of reactant conversions that otherwise maintain near-differential conditions. Kinetic models can describe primary reactions (to form tetrahydrothiophene (THT) and butene/butane products (C_4)) and the secondary reactions (to form C_4 from THT) that occur on similar types of surfaces, shedding insights on the mechanistic details of HDS on various transition metals (e.g. Pt, Ru, Re). The resulting conclusions are similar for these catalysts; C-S bond activation requires the formation of partially-saturated thiophene surface species on kinetically-accessible HDS sites. These minority HDS sites form upon the removal of reversibly-bound sulfur adatoms, which requires a (high) sulfur coverage that sufficiently lowers the heat of sulfur adsorption on metal surfaces. The mechanistic features observed here mirror those observed in C-C hydrogenolysis on hydrogen-covered metal surfaces, wherein both paraffin bond scission and cycloalkane ring opening activation steps occur on partially-dehydrogenated surface intermediates. These understandings preface and permit comparative studies of HDS on sulfur-covered Ru, Pt, and Re clusters. Metal-sulfur (M-S) bond energies, frequently used in the literature to correlate trends in observed HDS activity, play a role in influencing the density of accessible HDS sites, with surfaces exhibiting weaker M-S bond strengths leading to larger fractions of HDS sites and consequently higher turnover rates, normalized by the number of *exposed* metal sites. We find that M-S bond strength, calculated using density functional theory, can predict primary product distributions, reflecting a direct effect of catalyst properties on the relative stabilization of transition states (that lead to C_4 or THT products), which are formed on similar types of sites. Surfaces that exhibit stronger M-S bonds led to preferential primary formation of C_4 products, indicating their greater ability in stabilizing the respective desulfurization transition state, likely because stronger M-S interactions can weaken the C-S bond within the molecule, as predicted by bond-order conservation.

3.1   Introduction

The presence of organosulfur compounds in reactant streams can pose challenges for heterogeneously-catalyzed reactions as a result of their strong binding to catalytic sites, which

52

prevent adsorption and subsequent reaction of desired reactant molecules. Development in the field hydrotreating catalysts to remove these detrimental species has motivated extensive studies of the commercial catalysts, Co(Ni)Mo(W) sulfides, in the last several decades [1-4]. Characterization and theoretical modeling of their anisotropic, lamellar structures and corresponding metal promoters have led to proposals of the HDS active site identity and of the origins of metal promotion. The desire to develop structure-function relationships have also led to comparative studies of HDS reactivity on a range of (non-commercial) transition metal catalysts; however, these comparisons often assume catalysts persist as sulfide phases under the sulfur chemical potentials prevalent at industrially relevant conditions. Quantifying intrinsic HDS activity is often nontrivial, as the number of "active sites" on both metal sulfides and sulfur-covered metal surfaces are difficult to estimate. Despite these ambiguities, structure-function correlations are widely reported in the literature, with many reporting a volcano curve relationship between rates and the metal-sulfur (M-S) bond strength of the catalyst [5-7], which is purportedly (and appealingly) consistent with the Sabatier principle, a theory that argues that intermediate catalytic bindings can optimize reactant adsorption, bond activation, and subsequent product desorption. However, such conclusions are premature without rigorous kinetic elucidation of HDS mechanisms and of the specific kinetic or thermodynamic parameters that govern the differences in observed reactivity among different catalytic surfaces. Our previous studies of thiophene HDS on well-defined SiO_2-supported monometallic Ru [8], Pt [9], and Re (Chapter Two) catalysts have suggested that reaction occurs on sulfur covered surfaces and require minority HDS sites as reaction intermediates, which are formed upon the removal of weakly-bound sulfur adatoms [10]. The extent of (strongly-bound) sulfur coverage necessary to sufficiently lower heats of sulfur adsorption (as a result of increased sulfur-sulfur repulsions) to facilitate formation of these HDS sites depends on the chemical properties of the different metal surfaces, resulting in different fractions of total exposed sites that are involved in actual turnovers.

In this current study, we reiterate the necessary conditions that eliminate transport artifacts and heat corruptions, which permit the interpretation of reaction rates of true kinetic origin, measured under differential conditions. We employ these strict conditions to our previous studies on Ru and Pt and find that they exhibit similar mechanistic features as those observed on Re. The isotropic nature of Ru/SiO_2 and Pt/SiO_2 allowed us to unequivocally observe that all products (i.e. tetrahydrothiophene (THT) and butene/butane (C_4)) are derived from a single type of site, avoiding the need to propose multiple types of sites for the different pathways [2,11] (i.e. hydrogenation and desulfurization). Such observations are reflected in our current analysis of product selectivities, which highlights the differences in both the stabilization and the molecularity of relevant transition states that lead to primary THT and C_4 products. Selectivity trends, as a function overall thiophene conversion, also indicated that secondary THT desulfurization steps proceed through dehydrogenation steps, possibly to reform the partially-hydrogenated transition state involved in cleaving the C-S bond. These behaviors appear analogous to other hydrogenolysis reactions that we have previously studied [12-15], which suggest that the formation of surface intermediates serve to activate the bond that undergoes scission (e.g. C-C, C-O), and provide further evidence of the role of metal sites in cleaving C-X bonds (X = S, C, O). We can compare rate parameters (on Ru, Pt, Re), from regression of kinetic data to similar functional forms of rate expressions, derived from (similar) sequences of elementary steps that persist on all metals studied, and find that their kinetic (numerator) rate

constants correlate to metal-sulfur (M-S) bond strengths. Such trends appear consistent with previous literature reports, and we argue that M-S bond energy influences the density of kinetically-accessible sites. Increased sulfur affinity does play a role in affecting HDS selectivity, by stabilizing the transition state that forms C_4 products over that that forms THT, leading to more facile C-S bond scission relative to ring saturation.

3.2 Methods

Protocols for the successful synthesis of monodispersed clusters of Ru [8], Pt [9], and Re (Chapter Two), details of their extensive characterization, and procedures for measuring rigorous HDS turnover rates have been reported in our previous works and are briefly summarized here.

3.2.1 Catalyst synthesis

Nanosized particles were deposited on inert SiO_2 support material (Cabosil, HS-5, 310 m^2 g^{-1}) that had been previously acid-washed and treated in dry air at 673-773 K (0.003 K s^{-1}) for 3-4 h. By exploiting the strong electrostatic adsorption between aqueous $Ru(NH_3)_6Cl_3$ (Aldrich, 98%) or $Pt(NH_3)_4(NO_3)_2$ (Alfa Aesar, 99.99%) and SiO_2, basic aqueous solutions of the metal precursors (final pH 11.2 and 9.2, respectively) were mixed with the support (200 cm^3 g^{-1} SiO_2) and stirred for 1 h in the presence of additional NaOH (EMD Chemicals Inc.) or $NH_3 \cdot H_2O$, respectively, at ambient temperature. The solids were then filtered, and in the case of Ru, washed with deionized water (17.9 M·Ω resistivity) to remove chlorine ions. The separated solids were then dried by keeping them in vacuum for >24 h, followed by subsequent treatment in flowing dry air (Praxair, 99.99%, 1.0 cm^3 g^{-1} s^{-1}) to 353-373 K for 5 h. For the synthesis of supported Re clusters, aqueous solutions of NH_4ReO_4 (Aldrich 99%+) were introduced to SiO_2 dropwise via incipient wetness impregnation methods. Stepwise impregnation was used with intervening drying steps in stagnant air at 353 K for >12 h in order to introduce high weight loadings of Re onto the support because of precursor solubility limits in water. After deposition, the materials were dried under vacuum for >12 h and subsequently treated in flowing dry air to 353 K for >12 h. These dried materials were then subjected to high treatments in dry air and subsequently in H_2 to synthesize a range of particle dispersions, as detailed in our previous reports. Samples were passivated after H_2 treatments by first cooling to ambient temperatures, under flowing H_2, before exposing them to low concentrations of O_2 (0.1-0.5% O_2/He, Praxair) for 2-6 h. Table 3.1 lists the samples referenced within this current study, along with their specific dry air and H_2 treatment conditions.

3.2.2 Catalyst characterization

Nominal metal contents were confirmed (within 15%) via inductively coupled plasma optical emission spectroscopy (ICP-OES, Galbraith Laboratories, Inc.). Surface dispersions were determined via chemisorption uptakes of hydrogen (for Ru, Pt) or oxygen (for Re) atoms on prepared samples, evacuated under vacuum after H_2 treatments at 673-773 K for 1 h. Isotherms collected over a range of H_2 and O_2 pressures (1-120 kPa) led to saturation uptakes of strongly-bound adsorbates, and surface dispersion was calculated assuming surface stoichiometries of 1:1 H/Ru_s, 1:1 H/Pt_s, and 0.4:1 O/Re_s. Fractional dispersions from chemisorption measurements are converted to particle sizes by assuming hemispherical clusters and bulk densities of the metal.

Sample powders were dispersed onto lacey carbon film on a 400 mesh copper grid (Ted Pella, Inc.) for transmission electron microscopy (TEM) analysis (JEOL 1200 EX at 80 kV or Philips 420 at 120 kV). Distributions of particle sizes were collected after measuring more than 300 clusters of Ru and Re, and surface-averaged particle sizes were calculated based on the equation, $\Sigma_i\ n_id_i^3/\ \Sigma_i\ n_id_i^2$, where n_i is the number of clusters exhibiting diameter d_i. Consistency between cluster sizes measured via both methods indicated clean, accessible surface sites prior to reaction.

The possibility of phase transformation to transition metal sulfides, under the levels of sulfur (i.e. H_2S) encountered during HDS, required rigorous determination of catalyst phase identity. Samples were exposed to S-chemical potentials prevalent during HDS reaction (3.0 MPa H_2, 3.0 kPa H_2S, 573-623 K) and cooled in flowing He to ambient temperature and pressure before running temperature program reduction (TPR) to measure S-content. S/M ratios were determined by monitoring H_2S evolution via mass spectrometry (Leybold Inficon, Transpector Series), whose signals were calibrated by known mixtures of H_2S/H_2/He; subunity values of S/M indicated that sulfidation was limited to the surface of the metal and that bulk phase transformation did not occur. Further characterization of these spent catalysts via X-ray absorption spectroscopy (XAS, SSRL, beamline 4-1) confirmed that the metal bulk properties of spent catalysts were retained.

3.2.3 *Reactor operation and HDS rate measurements*

After passivation steps (Section 3.2.1), powdered samples were mixed with additional (acid-washed and air-treated) SiO_2 (Cab-O-Sil, HS-5) to prepare intrapellet dilutions (SiO_2/catalyst=1-9) that were then pressed and sieved to retain aggregates of uniform size (0.125-0.18 mm). Interpellet dilutions with quartz (acid-washed, Fluka) of similar pellet size were performed to maintain similar catalyst bed mass (1.0 g) and to avoid heat effects that would corrupt the kinetic nature of measured rates and selectivities. These materials were loaded into stainless steel reactors, ensuring plug-flow hydrodynamics, and subjected to *in-situ* H_2 (Praxair, 99.999%) treatments at 673 K (Ru and Pt) or 773 K (Re) for 1 h prior to reaction.

After cooling the reactor to reaction temperature (623 K for Ru, 573 K for Pt and Re), H_2 (Praxair, 99.999%) and H_2S/H_2 (Praxair, certified mixtures) gases, metered with mass flow controllers (Parker, Series 201), were introduced to their desired set points, and unit pressure was controlled with a back pressure regulator (Mity Mite). Liquid solutions of thiophene (Alfa Aesar, 99%) and decane (Aldrich, 99+%), as a solvent and internal standard, were pressurized by a high pressure pump (Isco 500D) and volatilized upon injection into lines maintained at temperatures >433 K to avoid condensation. Analysis of effluent gases was performed by gas chromatography (Agilent 6890) equipped with a methyl silicone capillary column (HP-1, Agilent, 25 m x 0.32 mm x 0.52 μm) connected to a flame ionization detector (FID) and a Porapak Q packed column (Supelco, 1.82 m x 3.18 mm, 80-100 mesh) connected to a thermal conductivity detector (TCD).

Conversions were measured over a range of H_2 (1-3 MPa), thiophene (1-10 kPa), and H_2S (0.2-10 kPa) pressures and maintained below <15% by varying residence times (while keeping all partial pressures of inlet gaseous compounds constant) to encourage differential reactor conditions. Turnover rates for HDS are normalized by the number exposed metal atoms,

quantified via characterization probes that accurately measured total metal contents and surface dispersions (Section 3.2.2).

3.3   Results and Discussions

3.3.1   *Turnover rates of thiophene hydrodesulfurization on Ru and Pt*

Measuring turnover rates that reflect the intrinsic catalytic reactivity requires designed experiments that exploit differential reactor conditions. Such conditions are nontrivial to maintain in reactions (e.g. HDS) wherein reaction inhibitors are formed as byproducts (i.e. H_2S), resulting in axial concentration gradients as reactants are consumed across the catalyst bed. The equilibrated dissociations of H_2S and H_2 under relevant HDS conditions lead to sulfur coverages that are set by H_2S/H_2 ratios alone, indicating that any significant change in H_2S pressure (at nearly constant H_2 pressure) can lead to large differences in S-coverage of active surfaces within the bed [8,9]. Thus, product inhibitors must be co-fed at the inlet, in amounts greater than those that form from reactant conversion, to ensure that differences in their average concentrations are negligible across the catalyst bed; with such conditions met, measured rates reflect intrinsic reactivity, in the absence of severe reactant depletion.

Thiophene HDS on Ru and Pt proceeded via two major pathways: desulfurization (to form butadiene, butene, and butane) and hydrogenation (to form dihydrothiophene and tetrahydrothiophene), and the corresponding reaction networks are described in more detail within their respective reports [8,9]. Certain rates on Ru/SiO_2 clusters [8] were measured in the absence of inlet H_2S feed, thus, they suffered from severe product inhibition. While those reported rates were linearly extrapolated data to zero residence time, such approximations cannot eliminate the infinite-fold change in S-chemical potential that occurs as a result of incipient reactant conversion. Indeed, these turnover rates exhibited non-linear behaviors with residence time (Fig. 3.1, inset), which, by themselves, lead to ambiguities on how to linearly extrapolate data; "extrapolated" rates depend sensitively on the range of residence time over which the extrapolation is performed. Indeed, the decrease in rates over this range of residence time (0.14 to 0.09 mol thiophene (g-atom Ru_s s)$^{-1}$) cannot be attributed to reactant (thiophene) depletion (reactant conversion 4-10%), indicating the strong rate inhibitions were effected by increased S-chemical potential (set by H_2S/H_2 ratios). Instead, we can approximate H_2S/H_2 ratios at each residence time by (linearly) averaging H_2S/H_2 ratios across the catalyst bed, from estimating effluent H_2S pressures based on butene/butane (C_4) product concentrations (1:1 H_2S to C_4 molar ratio) (Fig. 3.1). At a given average H_2S/H_2 ratio, rates exhibit first-order dependences on H_2 pressure (Fig. 3.2), contradicting previously reported kinetic behaviors (i.e. sub-linear H_2 dependences) [8], which were based on (non-rigorous) linear extrapolations of rates (Fig. 3.2, open squares). We conclude that those data suffered from non-rigorous extrapolations of rates and misguided interpretations that suggested prevalent H-coverage of reactive Ru sites during HDS catalysis. Here, first-order H_2 dependences, observed when rates are plotted at similar (average) S-coverages (i.e. H_2S/H_2 ratios), instead indicate that H-species are not abundant on HDS surfaces; these trends are consistent with rates, measured with co-fed H_2S at the reactor inlet (Fig. 3.3), that exhibit first-order H_2 dependences. All previously reported HDS rates on Pt/SiO_2 [9] were rigorously measured at differential conditions (i.e. inlet H_2S co-feed and low thiophene conversion).

A positive dependence on H_2 pressure suggests the involvement of H-species in the kinetically-relevant step (Figs. 3.2, 3.3, and 3.4) of thiophene conversion. HDS rates on Pt exhibited sublinear dependences on H_2 pressure (Fig. 3.4), particularly at conditions of low thiophene pressure and low H_2S/H_2 ratios, suggesting that H-species can cover HDS sites on Pt surfaces. Rates on both Ru and Pt exhibited positive, sublinear dependences on thiophene pressure but were inhibited by H_2S/H_2 ratio (Figs. 3.5 and 3.6, respectively), similar to behaviors observed in SiO_2-supported Re/ReS_x catalysts (Chapter Two). These behaviors suggest that a thiophene-derived surface intermediate is involved in the formation of kinetically-relevant transition states on surfaces that can be covered by both thiophene- and H_2S-derived surface species. The prevalence of multiple species that can compete for surface sites on a "S-covered metal surface" appears to defy Langmuirian kinetics; such behaviors can be reconciled by considering that, similar to HDS on Re-based catalysts (Chapter Two), reaction occurs on minority HDS sites that occupy a small fraction of a metal surface that is otherwise nearly fully covered with strongly-bound S-atoms.

3.3.2 Elementary steps of thiophene HDS on Ru and Pt

HDS on supported transition metals occurs on surfaces nearly saturated with sulfur at relevant S-chemical potentials and temperatures under which bulk metal phases are expected to persist [8,9] (in the absence of any kinetic barriers to phase transformation). Work in the literature [16,17] have implicated the role of different hydrogens on either sulfhydryl ($*S^{\delta-}H^{\delta+}$) or hydride ($*H^{\delta-}$) surface species, with cationic and anionic character, respectively. These species are purportedly formed upon dissociation of H_2 and H_2S on sulfur-vacancy site pairs ($S*$—$*$) (i.e. ($H^{\delta+}S^{\delta-}*$—$H^{\delta+}*$) and ($H^{\delta+}S^{\delta-}*$—$H^{\delta+}S^{\delta-}*$), respectively). While selective hydrogenation or desulfurization routes have been attributed to the relative abundance of specific types of H-species [18,19], we find that neither S-inhibitions on rates (Figs. 3.5 and 3.6) nor selectivity trends (as discussed in Section 3.3.3) appear to require such distinctions in H-species; thus, we derive rate expressions based on reactions occurring on vacant sites ($*$) or site pairs ($*$—$*$).

We interpret total thiophene conversion rates, avoiding any inaccuracies in extrapolating product (THT and C_4) selectivities, in contrast to our previous attempts [8,9] at describing two parallel, independent reaction pathways, "direct desulfurization" and "hydrogenation," that form C_4 and THT, respectively. A sequence of elementary steps (Scheme 3.1) involving a kinetically-relevant H-addition step to a (equilibrated) partially-hydrogenated (monohydro)thiophene intermediate appear to describe all measured kinetic data; these steps also include quasi-equilibrated adsorption of reactants ($H*$, $T*$: thiophene*) and of products (H_2S*, $HS*$, $S*$), confirmed by isotopic H_2/D_2 and H_2S/D_2S scrambling at relevant HDS conditions [8,9]. Our previous reports [8,9] also indicated that rates (on both Ru and Pt) exhibited first-order dependences on H_2 pressure, while assuming H_2 dissociation on sulfur-vacancy site pairs ($S*$—$*$). There, we proposed that reactions occurred between reactant *pairs*, e.g. ($HS*$—$H*$) or ($HS*$—$HS*$) with ($S*$—$T*$), rather than between reactant *species*, e.g. $HS*$ or $H*$ with $T*$, and thus, first-order H_2 dependences were interpreted to describe a kinetically-relevant first H-addition step (i.e. without the equilibrated formation of monohydrothiophene intermediates). When elementary steps of adsorption and dissociation on ($S*$—$*$) site pairs are (properly) written (Eqs. 3.1-3.4), however, a kinetically-relevant first H-addition step would actually

require rates to exhibit half-order H_2 dependences, which is inconsistent with observed kinetic behaviors (Figs. 3.2-3.4).

$$H_2 + (*) + (S*) \leftrightarrow (H*) + (HS*) \tag{3.1}$$

$$H_2S + (*) + (S*) \leftrightarrow 2(HS*) \tag{3.2}$$

$$(HS*) + (*) \leftrightarrow (H*) + (S*) \tag{3.3}$$

$$T + (*) \leftrightarrow (T*) \tag{3.4}$$

Here, we propose that HDS occurs on minority HDS site pairs; however, the functional form of the derived rate expression is independent of whether reactions occur on (*—*) or (S*—*) pairs. The rate expression (Eq. 3.5) describes all kinetic data on Ru and Pt catalysts over a wide range of relevant HDS conditions (Fig. 3.7), suggesting that rates are limited by reactions between hydrogen (H*) and monohydrothiophene (MHT*) surface species (Scheme 3.1, step vii).

$$\frac{r}{[L]} = \frac{\alpha(H_2)(T)}{\left(1 + \beta(H_2)^{0.5} + \gamma(T) + \delta(T)(H_2)^{0.5} + \epsilon(H_2S) + \zeta\frac{(H_2S)}{(H_2)^{0.5}} + \eta\frac{(H_2S)}{(H_2)}\right)^2} \tag{3.5}$$

     (*)   (H*)   (T*)   (MHT*)   (H$_2$S*)   (HS*)   (S*)

, where $\alpha = k_0 K_{H_2} K_T K_{HT}$, $\beta = K_{H_2}^{0.5}$, $\gamma = K_T$, $\delta = K_T K_{H_2}^{0.5}$, $\epsilon = K_{H_2S}$, $\zeta = \frac{K_{H_2S} K_{HS}}{K_{H_2}^{0.5}}$, $\eta = \frac{K_S K_{H_2S} K_{HS}}{K_{H_2}} (= K_S')$

, T is thiophene, and [L] is the total number of HDS sites.

The presence of multiple species on HDS sites leads to pressure dependences (i.e. H_2, thiophene, H_2S) that appear on both the numerator and denominator of the rate expression (Eq. 3.5) and contribute to a degree of uncertainty during data regression. Statistical probes of regressed data on Pt (described in Section 3.8.1), which examined the limits of maximum and minimum numerator H_2 orders, confirm first-order H_2 dependences, and sensitivity analysis of parameters, which measured how sensitive rates were to their best fit values, suggest that (S*) is the most abundant among the H_2S-derived intermediates (i.e. ε=ζ=0, Eq. 3.5). While the prevalence of (MHT*) species could not be unambiguously ruled out on Pt surfaces, computational calculations (coupled-cluster single and double excitations (CCSD)) on the thermodynamics of gas phase, open-shell MHT radicals (Chapter Four, Table 4.2) indicate that the equilibrium constant for thiophene hydrogenation to MHT is ~10^{-8} at these temperatures and pressures; thus, unless the adsorption constant for MHT is significantly greater (e.g. >10^8) than that for thiophene, MHT is unlikely to compete for HDS sites (i.e. δ=0, Eq. 3.5). Ru-based catalysts exhibited first-order H_2 dependences over the entire range of H_2 pressures (Figs. 3.2 and 3.3) at constant H_2S/H_2 ratio, thereby indicating that other surface species whose concentrations would be influenced by changes in H_2 (i.e. (H*), (MHT*), (HS*)) or H_2S pressure (i.e. (H$_2$S*)) are not prevalent on HDS sites, suggesting that only (surface) terms associated with (T*) and (S*) are described by the rate expression (i.e. β=δ=ε=ζ=0, Eq. 3.5). The rate expressions derived for Ru and Pt are nearly identical in form, except that (H*) concentrations are measurable on the latter (i.e. β≠0). Such rate expressions can describe all kinetic data measured on Ru and Pt

clusters (Fig. 3.7) with three and four parameters, respectively, despite an order of magnitude difference in their absolute rates when normalized by exposed metal sites. Regressions of Ru and Pt data lead to very different rate parameter values, corresponding to the differences in their thermodynamic and kinetic properties (Table 3.2), which will be discussed in Section 3.3.5 under the context of how M-S bond energies can influence catalytic rates.

3.3.3   Primary and secondary reactions on Ru and Pt

Our kinetic studies (Section 3.3.2) have suggested that thiophene conversion occurs through a kinetically-relevant second H-addition step. The turnover is "completed" by desorption of HDS products (C_4 or THT) that are formed on the surface. Extracting mechanistic details regarding their formations requires careful analysis of selectivity data (Figs. 3.8 and 3.9) because they occur along a part of the reaction coordinate that is kinetically-silent. THT selectivity decreases as a function of thiophene conversion, at all HDS conditions, suggesting that secondary desulfurization reactions can convert THT to C_4. Similar to HDS reactions on Re-based catalysts (Chapter Two), selectivity appears to be a single-valued function of thiophene conversion, independent of thiophene pressures and H_2S/H_2 ratios over ranges that significantly influenced turnover rates (Figs. 3.5 and 3.6) and that affected the relative abundance of surface species (Eq. 3.5), therefore suggesting that all reactions occur on similar types of sites. Indeed, at constant H_2 pressure, selectivity values only changed as a result of reactant conversion, effected either by changing residence time or H_2S/H_2 ratio (which influences S-coverage of HDS sites), indicating that these reactive sites are isolated and uniform, therefore amenable to our Langmuirian treatment (Eq. 3.5, Scheme 3.1).

Fast secondary consumptions of THT observed in Ru (Fig. 3.8) do not enable linearization of selectivity data over the range of measured thiophene conversions; thus, measuring primary selectivity requires a deeper understanding of secondary reactions. Without a more careful treatment, analyses are prone to misinterpretation, leading us to propose that H_2S promoted primary hydrogenation pathways because we linearly extrapolated selectivities from non-overlapping low and high conversion ranges at high and low H_2S/H_2 ratios (e.g. 5.0×10^{-3} and 6.7×10^{-4}), respectively. Such techniques led to very different extrapolated THT selectivity values (e.g. 70% and 50%, respectively), at given H_2 and thiophene pressures (i.e. 3 MPa H_2, 2.5 kPa thiophene), despite that all data (Fig. 3.8) fall on a single selectivity curve and that, consequently, primary selectivities are actually independent of H_2S/H_2 ratio. We avoid such inaccuracies by interpreting these selectivity curves based on a simple reaction network of primary formations of C_4 and THT followed by secondary THT desulfurization to C_4 (Chapter Two, Scheme 2.1).

While selectivity trends appeared independent of thiophene and S-chemical potentials on both Ru and Pt clusters (Figs. 3.8 and 3.9), they were significantly influenced by H_2 pressure, affecting THT to C_4 concentration ratios (Figure 3.10, Pt data not shown); such effects reflect a role of H_2 in changing both primary selectivity and the rate of secondary reaction. We investigated these pronounced effects by proposing a set of elementary steps that occur after the kinetically-relevant formation of a (dihydro)thiophene intermediate, I* (Scheme 3.1, step vii), by introducing pseudo-first order reactions based on thiophene, I*, and THT, as detailed in Chapter Two, Section 2.3.5. Rate constants associated to these steps (i.e. k'_0 (Eq. 2.16), k'_1 (Eq. 2.9), k'_2

(Eq. 2.10), k'_3 (Eq. 2.11), Chapter Two) contain (numerator) H_2- and (denominator) surface species dependent terms that become nearly constant at given high (excess) H_2 pressures and low, differential conversions. An expression describing THT selectivity as a function of thiophene conversion, X, can be derived from solving a system of differential equations, detailed in Chapter Two, Eqs. 2.12-2.17,

$$S_{THT} = \frac{k'_1}{k'_1+k'_2} \cdot \left(1 - \frac{k'_3}{k'_0}\right)^{-1} \cdot \frac{\left\{(1-X)-(1-X)^{\frac{k'_3}{k'_0}}\right\}}{X} \tag{3.6}$$

, where k'_0, k'_1, k'_2, and k'_3 represent pseudo-rate constants for thiophene consumption, THT formation, C_4 formation, and THT secondary desulfurization, respectively.

Our previous works [8,9] assumed linear extrapolations of selectivity, which can be derived from a first-order Taylor approximation of Equation 3.6,

$$S_{THT} = \frac{k'_1}{k'_1+k'_2}\left(1 - \frac{k'_3}{k'_0} \cdot \frac{X}{2}\right) \tag{3.7}$$

Application of Equation 3.7, however, requires not only low conversions (X), but relatively slow secondary reaction, i.e. $\frac{k'_3}{k'_0} \cdot \frac{X}{2} \sim 0$. As a result of fast secondary reaction (i.e. high k'_3/k'_0) on S-covered Ru surfaces, linearization of selectivity data (Eq. 3.7) is invalid, even though conversions were near-differential and led to accurate measurements of thiophene conversion rates. Linear selectivity extrapolations deviated most significantly from accuracy at higher conversions, which were more typical during runs at low H_2S/H_2 ratios, causing a systematic underestimation of primary THT formation at such conditions and leading to (misguided) claims of a beneficial role of H_2S (and of $*S^{\delta-}H^{\delta+}$ species) in facilitating hydrogenation routes [8,9]. Instead, we can regress all selectivity data to the complete form of the THT selectivity function (Eq. 3.6).

THT to C_4 branching ratios were significantly affected by H_2 pressure (Fig. 3.10), even though all reactions occurred on similar types of sites; thus, the H_2 effect cannot be derived from any differences in surface coverages but rather from differences in the number of H-atoms (i.e. molecularity) involved in the formation of the two transition states. We can acquire values of k'_1/k'_2 from regression of selectivity data (Figs. 3.8 and 3.9) to Equation 3.6, which represents a direct ratio between the primary THT (i.e. r_1) and C_4 (i.e. r_2) formation rates,

$$\frac{k'_1}{k'_2} = \frac{r_1}{r_2} = \frac{k_1}{k_2} \cdot (H_2)^\lambda \tag{3.8}$$

The ratio of k'_1/k'_2 for both Ru and Pt exhibited half-order dependences on H_2 pressure (Fig. 3.11), although limited measured data at certain pressure conditions (e.g. 1.5 and 2.5 MPa H_2) required less rigorous extrapolation methods (Eq. 3.7). Despite these approximations, the general trend is preserved, and the resulting half-order H_2 dependences (λ=0.5, Eq. 3.8) suggest that the relevant transition state that forms THT involves one H-atom more than that that forms C_4. Actual regressed and approximated values of k'_1/k'_2 were greater on Pt (Fig. 3.11b) relative to Ru

(Fig. 3.11a), consistent with higher overall THT selectivities observed on Pt (Fig. 3.9). These selectivity trends are consistent with those observed on supported-Re clusters and ReS_x nanostructures (Chapter Two) and highlight the importance of ensuring rigorous assessment of selectivity data.

The rates of secondary THT reaction are also affected by H_2, exhibited by THT to C_4 concentration ratios that trend differently with conversion (Fig. 3.10). Values of k'_3/k'_0 ratios, extracted from regression of data to Eq. 3.6, reflect the ratio of secondary THT desulfurization to primary thiophene conversion rates,

$$\frac{k'_3}{k'_0} = \frac{r_3}{r} = \frac{k_3}{k_0} \cdot (H_2)^\delta \sim (H_2)^{z-1.0} \tag{3.9}$$

The dependence on H_2 (i.e. δ), in this case, reflects differences in the dependences between primary and secondary reactions; from our kinetic study (Section 3.3.2), thiophene conversion rates are first-order in H_2 pressure (i.e. kinetically-relevant second H-addition), thus, we can isolate the dependence (i.e. z) of secondary THT desulfurization. The k'_3/k'_0 ratio (Eq. 3.9) exhibited a negative H_2 dependence (δ=-1.8, Fig. 3.12) on Ru, indicating that secondary THT desulfurization rates decrease with increasing H_2 pressure (i.e. z=-0.8). A negative kinetic dependence on H_2 suggests that dehydrogenation steps must occur prior to the kinetically-relevant step to form C_4 products; sequential hydrogenations and dehydrogenations occur on HDS surfaces, both in primary reactions of thiophene and in the secondary desulfurization of THT, as depicted in Scheme 3.2. Kinetically viable H_2 dependences of k'_3 include $(H_2)^{-1}$ or $(H_2)^{-0.5}$, suggesting either the equilibrated formation of dihydrothiophene (DHT*) or trihydrothiophene (TrHT*) surface species, respectively; however, errors associated with regressions and experimental measurements of selectivity data have rendered a more ambiguous dependence (z=-0.8). We can reason, by considering previous kinetic conclusions, which of these two possibilities (z=-1 or -0.5) is more likely. Analysis of primary selectivity (Eq. 3.8, Fig. 3.11) suggests that one more H-atom is involved in the transition state that forms THT relative to that that forms C_4; thus, if THT were equilibrated with dihydrothiophene (DHT*, z=-1, δ=-2) on the surface, then the transition state that forms C_4 must involve one less H-atom, implying that monohydrothiophene (MHT*) must be the intermediate that undergoes C-S bond activation. Such a proposal, however, would be inconsistent with our kinetic study, which indicated that thiophene conversion is limited by a second H-addition. If THT were, instead, equilibrated with TrHT* (z=-0.5, δ=-1.5) on the surface, then this implies DHT* must be the intermediate that forms the transition state that cleaves the C-S bond. Such a pathway (Scheme 3.2) maintains consistency with thiophene HDS kinetics, and we observe that regression of k'_3/k'_0 data to $(H_2)^{-1.5}$ is within 95% confidence intervals (Fig. 3.12), confirming that such a reaction network is (also statistically) plausible.

The requisite formation of a partially-saturated thiophene intermediate for C-S bond activation appears similar to behaviors exhibited by C-C hydrogenolysis of substituted cyclo- and linear alkanes on H-covered metal surfaces [12,13,15,20]. During those reactions, adsorbed naphthenes and paraffins undergo dehydrogenation steps, forming an equilibrated "alkyl pool" of intermediates of varying degrees of unsaturation; one of those species, of a particular degree of unsaturation, can then activate the C-C bond, followed by fast hydrogenation and desorption

steps to form saturated product(s). Weakening C-C bonds (and by extension, C-S bonds) can be facilitated by increased coordination between carbon and the metal site (i.e. M-C bonds) by bond-order conservation arguments; such bond (i.e. M-C) formations can occur as a result of enthalpic and entropic gains from favorable M-C interactions and gas phase H_2 formation, respectively, that serve to compensate the enthalpic penalties associated with activating and cleaving C-H bonds. The intermediate responsible for bond activation is one that lowers the transition state barrier toward C-C (or C-S) bond scission relative to those in dehydrogenation and/or hydrogenation steps, allowing hydrogenolysis (or desulfurization) paths to compete. Our analysis of rates and selectivity on Ru and Pt suggest that dihydrothiophene (DHT*) species activate the C-S bond, similar to our previous proposals on Re and ReS_x (Chapter Two), despite differences in the kinetically-relevant H-addition step for thiophene conversion between Pt/Ru and Re-based catalysts. In contrast to cycloalkane ring-opening reactions, which exhibited equilibrium between aromatic molecules (e.g. toluene) and their corresponding saturated cyclic analogs (e.g. methylcyclohexane), thiophene and THT were not equilibrated under relevant HDS conditions; thus, under the context of C-S hydrogenolysis, THT formation is an "overhydrogenation mistake," for which the surface corrects by THT readsorption and subsequent dehydrogenation. Indeed, these mechanistic features are consistent with our proposals that C-S bonds are activated on DHT* intermediates, which can be formed from either direction, i.e. from thiophene via hydrogenation or from THT via dehydrogenation (Scheme 3.2).

3.3.4   *Consequences of M-S bond energy on HDS catalytic rates*

HDS occur on minority HDS sites formed upon desorption of weakly-bound S-atoms on S-covered metal surfaces, facilitated by sufficiently low heats of S-adsorption (Section 3.3.2 and Chapter Two, Section 2.3.4); these heats are achieved at high S-coverages as a result of increased S-S repulsive interactions. Such implications suggest that only a fraction of total exposed metal sites are available for turnovers and help explain the competitive, reversible adsorption of thiophene (T*), sulfur (S*), and hydrogen (H*, in Pt) species (Figs. 3.4-3.6) on a metal surface that is otherwise covered with strongly bound S-atoms [10,21]. This subtle distinction between whether reactions occur on metal sites or on HDS sites is important because it defines the site balance (i.e. [L]) used in derivations of the rate expression (Eq. 3.5). Reactions occur on reactive HDS sites, evident from poor correlations between regressed values of thiophene and S-adsorption constants (Table 3.2, K_T and K'_S) and theoretical *metal*-sulfur (M-S) bond energies (Section 3.8.2) at near monolayer S-coverages of Ru, Pt, and Re surfaces. Pt catalysts were most strongly inhibited by H_2S/H_2 ratios, despite exhibiting the lowest calculated M-S bond energy, suggesting that sulfur adsorption on kinetically-accessible HDS sites on Pt is the most facile. We speculate, however, that these behaviors may indicate that HDS sites on Pt suffer less from the effects of S-S repulsions, which could be, in turn, more severe on more densely packed S-covered surfaces of Ru and Re catalysts; but regardless of the explanation, it appears that M-S bond energy cannot alone describe the intrinsic (binding) properties of the HDS sites involved in actual catalytic turnovers.

The total number of HDS sites, [L], used in the site balance cannot be accurately measured by *ex-situ* characterization (i.e. chemisorption) on clean metal clusters. The inability to quantify these HDS sites directly affects the values of the regressed (numerator) kinetic rate parameter (i.e. α, Eq. 3.5). Indeed, the differences ($>10^2$) in measured turnover rates on Ru, Pt,

and Re, normalized by exposed metal sites, are largely accounted for by the values of α (Table 3.2, $k_0 K_{H2} K_T K_{MHT}$ or $k_0 K_{H2}^{0.5} K_T$). This numerator constant can be defined in terms of its corresponding collection of thermodynamic and kinetic rate constants; when rates are properly normalized, it reflects the (Gibbs) energy difference between the relevant transition state and gas phase reactants with (two) empty sites (Eq. 3.10, Pt and Ru; Eq. 3.11, Re).

$$\alpha_{Ru/Pt} = k_0 K_{H_2} K_T K_{MHT} = \exp\left(\frac{-\Delta G_{app}}{RT}\right) = \exp\left(\frac{-\left(G^{\ddagger}-\left(G_{H_2}+G_T+2G_*\right)\right)}{RT}\right) \qquad (3.10)$$

$$\alpha_{Re} = k_0 K_{H_2}^{0.5} K_T = \exp\left(\frac{-\Delta G_{app}}{RT}\right) = \exp\left(\frac{-\left(G^{\ddagger}-\left(\frac{1}{2}G_{H_2}+G_T+2G_*\right)\right)}{RT}\right) \qquad (3.11)$$

Gas phase energies (i.e. G_T and G_{H2}) are independent of the catalyst, although an additional term ($-1/2G_{H2}$) is included in the exponent of Equation 3.10 as a result of an equilibrated formation of surface MHT on Pt and Ru surfaces prior to the kinetically-relevant step. We exercise caution when directly comparing these energies because the structures of the transition states between Ru/Pt and Re are different; in particular, transition states on Pt and Ru are credited in transition state stabilization by an additional C-H bond formation. Qualitatively, the stability of any thiophene-derived transition state should increase on surfaces exhibiting stronger S-affinity, thus, we would have expected Re to exhibit the highest value of α, unless the structure of (more hydrogenated) transition states formed on Pt/Ru more than compensates for the stability afforded by increased surface coordination. Numerator rate constants, instead, increase with decreasing M-S bond energy, suggesting that either M-S bond energy fail to fully describe the coordinative nature of HDS sites or that characterization methods fail to estimate (even on a relative scale) the number of HDS sites present on the different metal surfaces.

Indeed, correlations between M-S binding energy and observed rates [5-7] are often reported, and our current study reveals similar trends with reaction rate constants (Fig. 3.13); the regressed numerator rate constants, α, decrease with increasing DFT-calculated M-S bond energy at near-monolayer sulfur coverages (Section 3.8.2). We argue that the values of these constants (Eqs. 3.10 and 3.11) cannot describe the intrinsic reaction barriers on these catalysts but instead trend with the density of kinetically-accessible HDS sites during catalysis; catalysts exhibiting stronger M-S bonds exhibit lower fractions of HDS sites, which can explain the lower regressed value of α for Re relative to Pt (Table 3.2). While we would prefer to develop descriptors that can correlate to the intrinsic chemical properties of reactive sites, we are unable to probe any effects they may have on rates (or reaction barriers) as a result of our inability to count the relevant number of sites that participate in turnovers.

Primary selectivity to THT and C_4 formations are also different among the catalysts studied, indicating that catalyst choice must be influencing the relative stabilities of their respective transition states. Both hydrogenation and desulfurization products are formed on similar types of sites (Section 3.3.3 and Chapter Two, Section 2.3.5); therefore, we can avoid any inaccuracies in HDS site counts by considering the ratios of (THT and C_4 formation) rates. Branching ratios (Eq. 3.8) exhibited similar H_2 dependences (λ=0.5) for all catalysts studied,

allowing us to compare regressed values of the coefficient of Equation 3.8, k_1/k_2, which reflects the true relative stabilities of transition states that form THT and C_4,

$$\frac{k_1}{k_2} = \frac{\exp\left(-\frac{\Delta G_{app,THT}}{RT}\right)}{\exp\left(-\frac{\Delta G_{app.C_4}}{RT}\right)} = \exp\left(-\frac{\left(\Delta G_{app.THT} - \Delta G_{app.C_4}\right)}{RT}\right) = \exp\left(-\frac{\left(G^{\ddagger}_{THT} + \frac{1}{2}G_{H_2} - G^{\ddagger}_{C_4}\right)}{RT}\right) \quad (3.12)$$

Gas phase energies (i.e. $1/2G_{H2}$) are independent of catalyst identity, therefore, selectivity differences must be a result of differences in the stability of the relevant transition states (i.e. ($G^{\ddagger}_{THT}$ - $G^{\ddagger}_{C4}$)). We propose that the transition state involved in cleaving the C-S bond should benefit from increased coordination of sulfur on HDS sites, which can weaken the C-S bond as a result of bond-order conservation. While the intermediate that undergoes C-S bond activation is similar (i.e. DHT*) on all catalysts (Section 3.3.3), its interaction with the metal appears to greatly influence the ease of bond scission (to form C_4) relative to hydrogenation (to form THT). Such an effect should lead to correlations between M-S bond strength and the selectivity toward C-S hydrogenolysis, but these M-S bond energies require referencing to other adsorbate-metal coordination in order to probe the extent of (disproportional) S-affinity on different transition metals. Here, we used metal-methylidyne (M-CH) binding energy as reference and assess the relative increase of M-S binding as a function of metal identity (Fig. 3.14). We find experimentally measured k_1/k_2 ratios increase with increasing differences between M-CH and M-S binding energies, calculated from DFT (Section 3.8.3). Such trends suggest that disproportional increases in M-S interactions (i.e. higher $|BE_{M-S}|$ values lower the values of $|BE_{M-CH}|-|BE_{M-S}|$) decrease barriers for C-S bond cleavage (i.e. lower k_1/k_2 values), supporting our proposals of the coordinative nature of DHT*-derived transition states on HDS sites.

3.4   Conclusions

Developing structure-function relationships obliges an understanding of the kinetic nature of reactions, which in turn requires that one evaluates the elementary steps of reactions. Such evaluations depend on measured rates of kinetic origin, necessitating reactor operations that are truly differential, particularly when the byproducts formed can act as strong reaction inhibitors. Fast secondary reactions of primary products can add complexities to the analysis of measured product distributions, rendering approximations that linearize selectivity as a function of reactant conversion inapplicable even over low (differential) ranges. We have applied these strict conditions and considerations in our studies of HDS on various monometallic catalysts.

Our studies have led to mechanistic insights, previously unattainable as a result of non-uniform surfaces and coverages, which indicate HDS should be more aptly referred as C-S hydrogenolysis, exhibiting behaviors analogous to bond activations in C-C hydrogenolysis in metal-catalyzed linear and isoalkane bond scission and cycloalkane ring opening. Formation of tetrahydrothiophene (i.e. via thiophene hydrogenation) results from an "over-hydrogenation mistake" stemming from an oversaturation of thiophene-derived intermediates on the surface; however, these same surfaces can correct this by product readsorption and dehydrogenation steps to reform the intermediate that sufficient weakens the C-S bond for cleavage.

Numerator rate constants of derived rate expressions, obtained through regression of kinetic data, decrease with increasing metal-sulfur (M-S) binding energies. While such trends are not inconsistent with observations reported in the extensive HDS literature, we argue that M-S binding energies describe the steady-state fractions of kinetically-accessible sites on surfaces covered with a dense layer of strongly-bound sulfur atoms during HDS catalysis, rather than describe any effects of catalyst properties on kinetically-relevant transition state stabilities. We find, however, that the increased relative sulfur affinity of metal sites does play a role in lowering the barrier towards C-S cleavage relative to that toward hydrogenation, effecting measurable changes in primary product selectivities among different metals. The development of such descriptors and an understanding of the coordinative nature of catalytic sites can facilitate better control and optimization of catalyst selection and process design for HDS applications.

3.5   Acknowledgements

Table 3.1: Synthesis treatment conditions for uniform clusters of SiO_2-supported Ru, Pt, and Re catalysts.

Catalyst (particle size[a])	Dry air treatment[b] temperature (K)/time (h)/ramp (K s^{-1})	H$_2$ treatment[c] temperature (K)/time (h)/ramp (K s^{-1})
Ru/SiO$_2$ (1.6 nm)	--	723 / 2 / 0.083 [d]
Pt/SiO$_2$ (4.8 nm)	823 / 5 / 0.05	673 / 1 / 0.033 [d]
Re/SiO$_2$ (6.9 nm)	573 / 3 / 0.033	773 / 2 / 0.05 [e]

[a] Particle sizes determined by (H$_2$ or O$_2$) chemisorption experiments and surface-averaged diameters of cluster size distributions measured from transmission electron microscopy.
[b] 99.99%, Praxair, 1.0 cm^3 g^{-1} s^{-1}.
[c] All H$_2$ treatments were followed by a passivation step in 0.1-0.5% O$_2$/He (Praxair); 0.05-1.0 cm^3 g^{-1} s^{-1} at ambient temperature for 2-6 h.
[d] 9% H$_2$/He, Praxair, 1.67 cm^3 g^{-1} s^{-1}.
[e] 99.999% H$_2$, Praxair, 1.0 cm^3 g^{-1} s^{-1}.

Table 3.2: Kinetic and thermodynamic parameters from regression of data to HDS rate expressions (Eq. 3.5 or Eq. 2.8) on S-covered, SiO$_2$-suppored clusters of Ru, Pt, and Re.

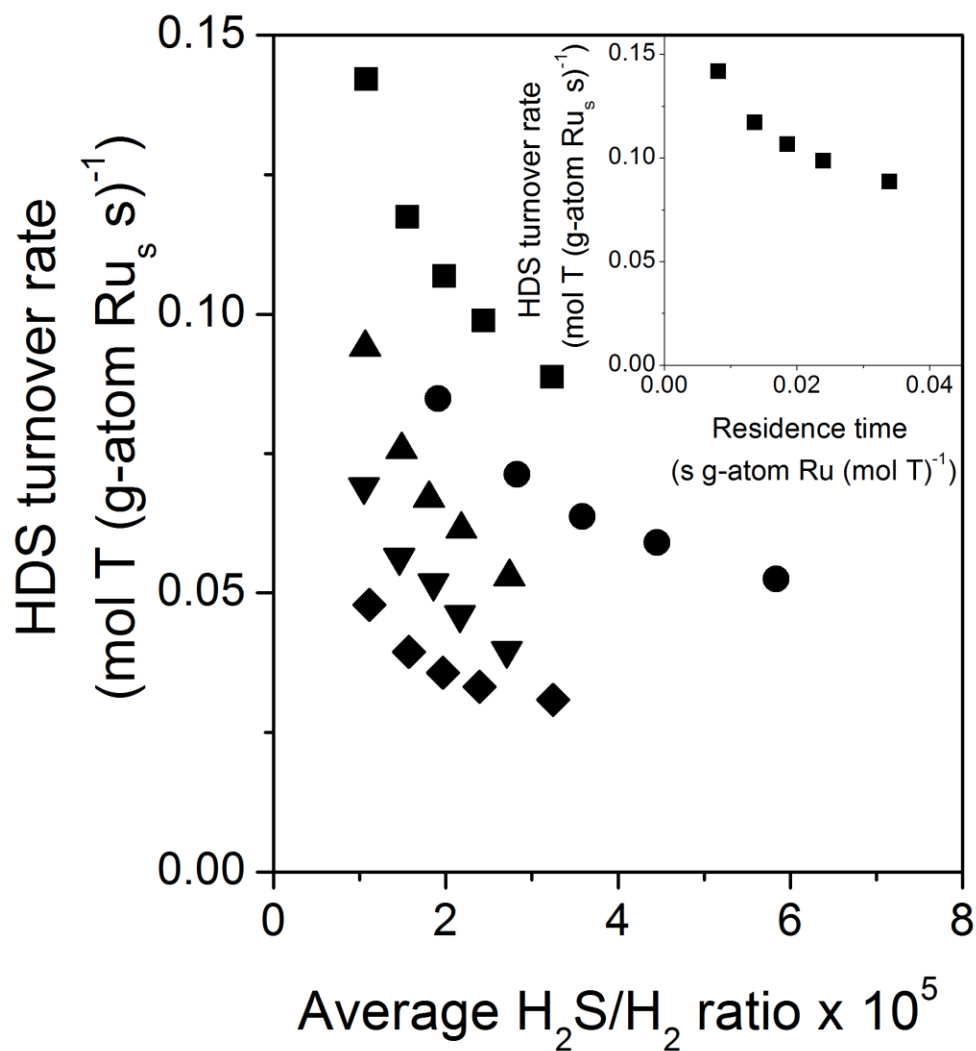| Rate parameter	Ru (1.7 nm, 623K)	Pt (4.8 nm, 573 K)	Re (6.9 nm, 573 K)
$k_0 K_{H2} K_T K_{HT}$ (mol g-atom^{-1} s^{-1} kPa^{-2})	2.0 ($\pm$0.6) x 10^{-5}	2.7 ($\pm$1.5) x 10^{-4}	--
$k_0 K_{H2}^{0.5} K_T$ (mol g-atom^{-1} s^{-1} kPa$^{-1.5}$)	--	--	2.2 ($\pm$0.4) x 10^{-6}
$K_{H2}^{0.5}$ (kPa$^{-0.5}$)	--	2.1 ($\pm$0.9) x 10^{-2}	--
K_T (kPa^{-1})	1.0 ($\pm$0.3) x 10^{-1}	1.5 ($\pm$0.5) x 10^{-1}	6.8 ($\pm$1.2) x 10^{-2}
K'_S	2.8 ($\pm$0.5) x 10^{2}	4.7 ($\pm$1.3) x 10^{3}	6.3 ($\pm$1.9) x 10^{2}

Figure 3.1: HDS turnover rates on Ru/SiO$_2$ as a function of average H$_2$S/H$_2$ ratio, estimated based on H$_2$S (i.e. butene/butane) concentration at reactor effluent, at 623 K, 2.5 kPa thiophene (T) and 1.0 MPa (◆), 1.5 MPa (▼), 2.0 MPa (▲), 2.5 MPa (●), and 3.0 MPa (■) H$_2$. Inset: HDS turnover rates on Ru/SiO$_2$ as a function of residence time at 623 K, 2.5 kPa thiophene, and 3.0 MPa H$_2$.
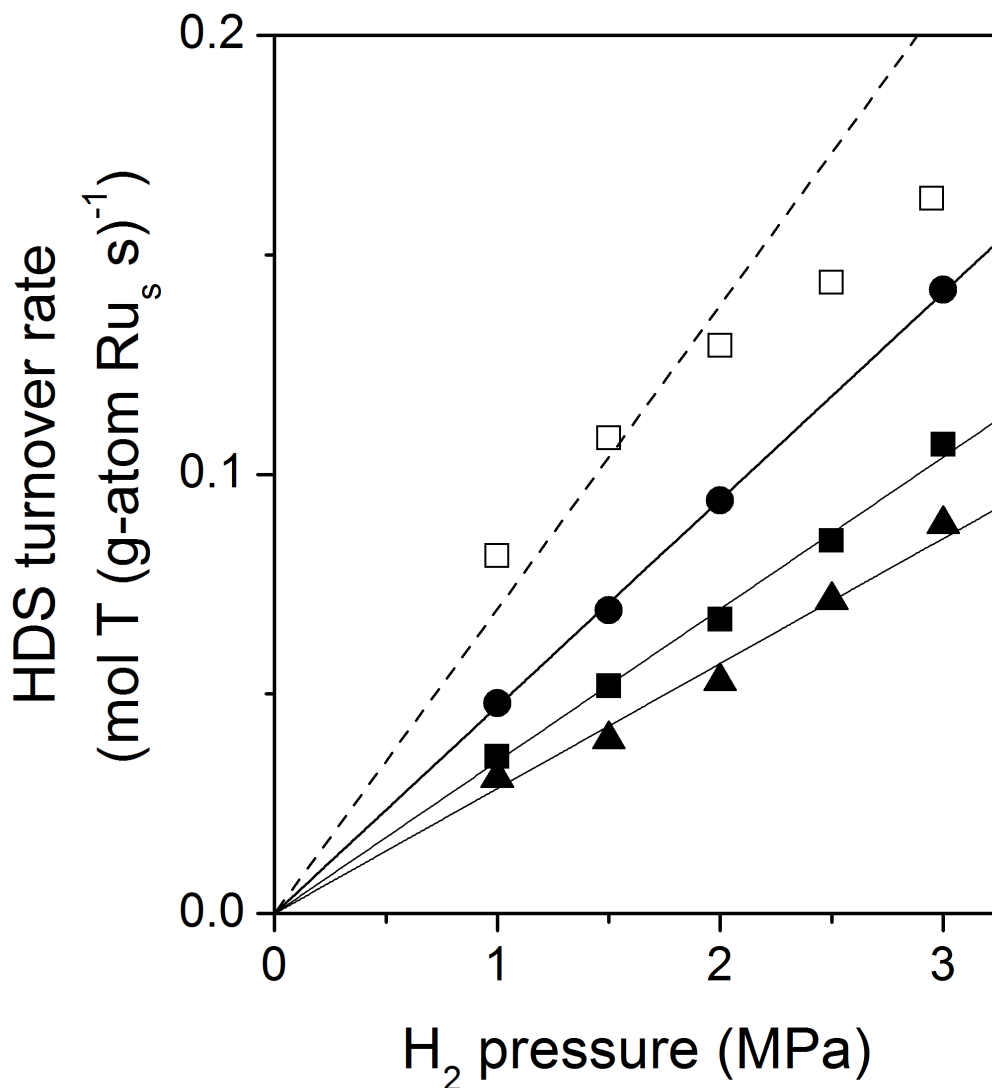
Figure 3.2: HDS turnover rates on Ru/SiO$_2$ as a function of H$_2$ pressure, at 623 K, 2.5 kPa thiophene (T) and 3 x 10^{-5} (▲), 2 x 10^{-5} (■), and 1 x 10^{-5} (●) average H$_2$S/H$_2$ ratios, estimated based on H$_2$S (i.e. butene/butane) concentration at reactor effluent. Previously reported rates (□), linearly extrapolated to zero residence time (from [8]), at 623 K and 2.5 kPa thiophene are included for comparison. Solid lines represent linear regression of data; dotted line represents linear regression of low H$_2$ pressure data (i.e. 1-2 MPa H$_2$) to highlight the negative deviations of extrapolated rates from first-order dependences at high H$_2$ pressures.

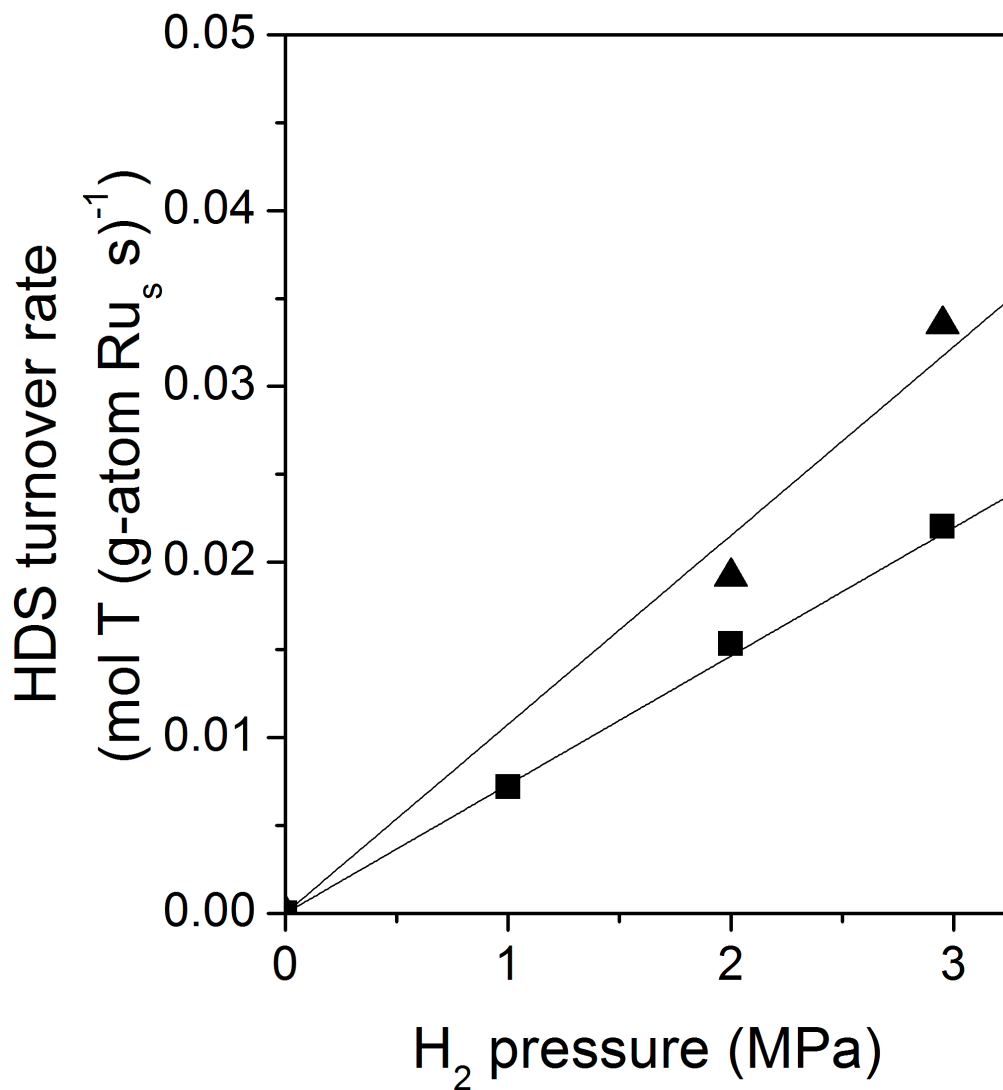**Figure 3.3**: HDS turnover rates on Ru/SiO$_2$ at 623 K as a function of H$_2$ pressure at 2.5 kPa thiophene (T) and 5 x 10^{-3}(■) and 3.3 x 10^{-3}(▲) H$_2$S/H$_2$ ratios. Lines represent linear regression of data.

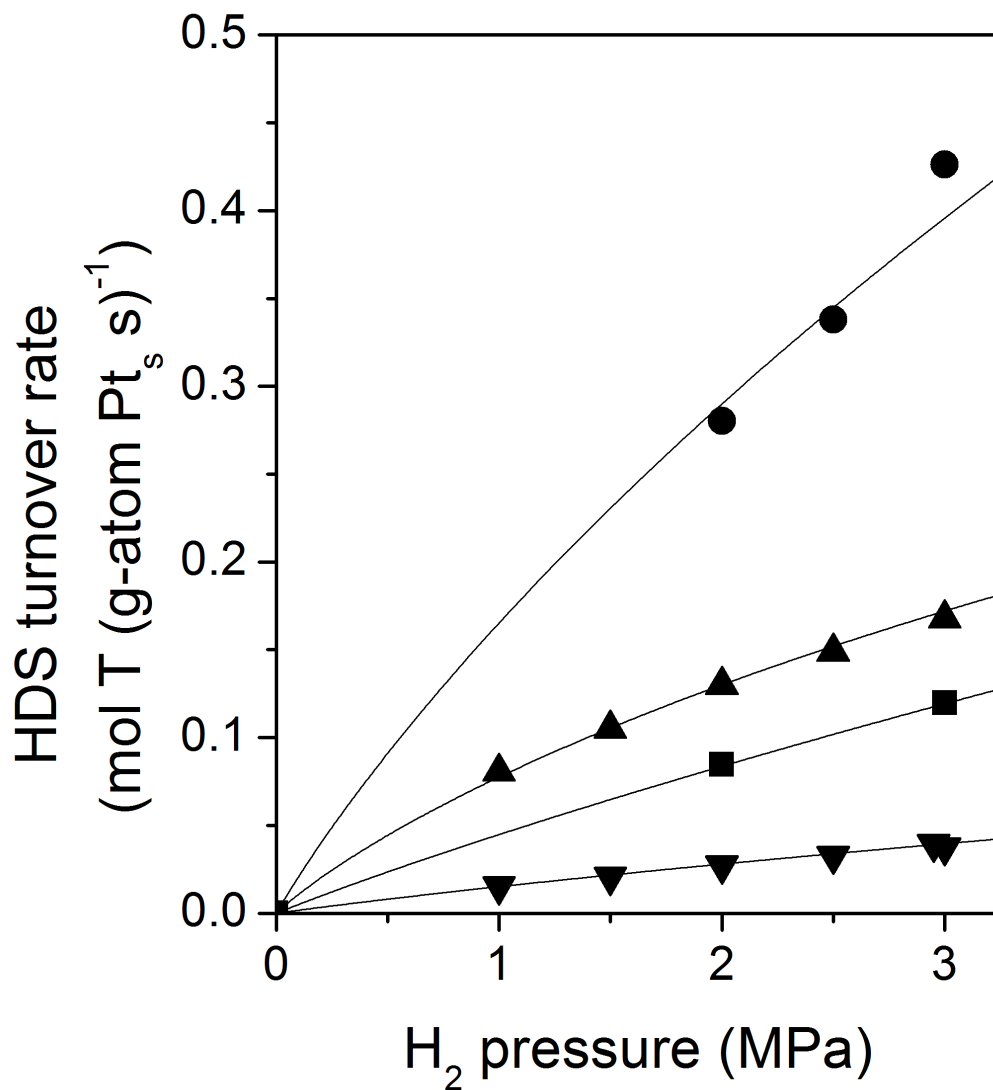**Figure 3.4**: HDS turnover rates on Pt/SiO$_2$ at 573 K as a function of H$_2$ pressure at 2.5 kPa thiophene (T) and 2 x 10^{-4} (▲) and 1 x 10^{-3} (▼) H$_2$S/H$_2$ ratios; and at 10.0 kPa thiophene and 2 x 10^{-4} (●) and 1 x 10^{-3} (■) H$_2$S/H$_2$ ratios. Curves represent regression of all measured data (on Pt) to the HDS rate expression (Eq. 3.5).
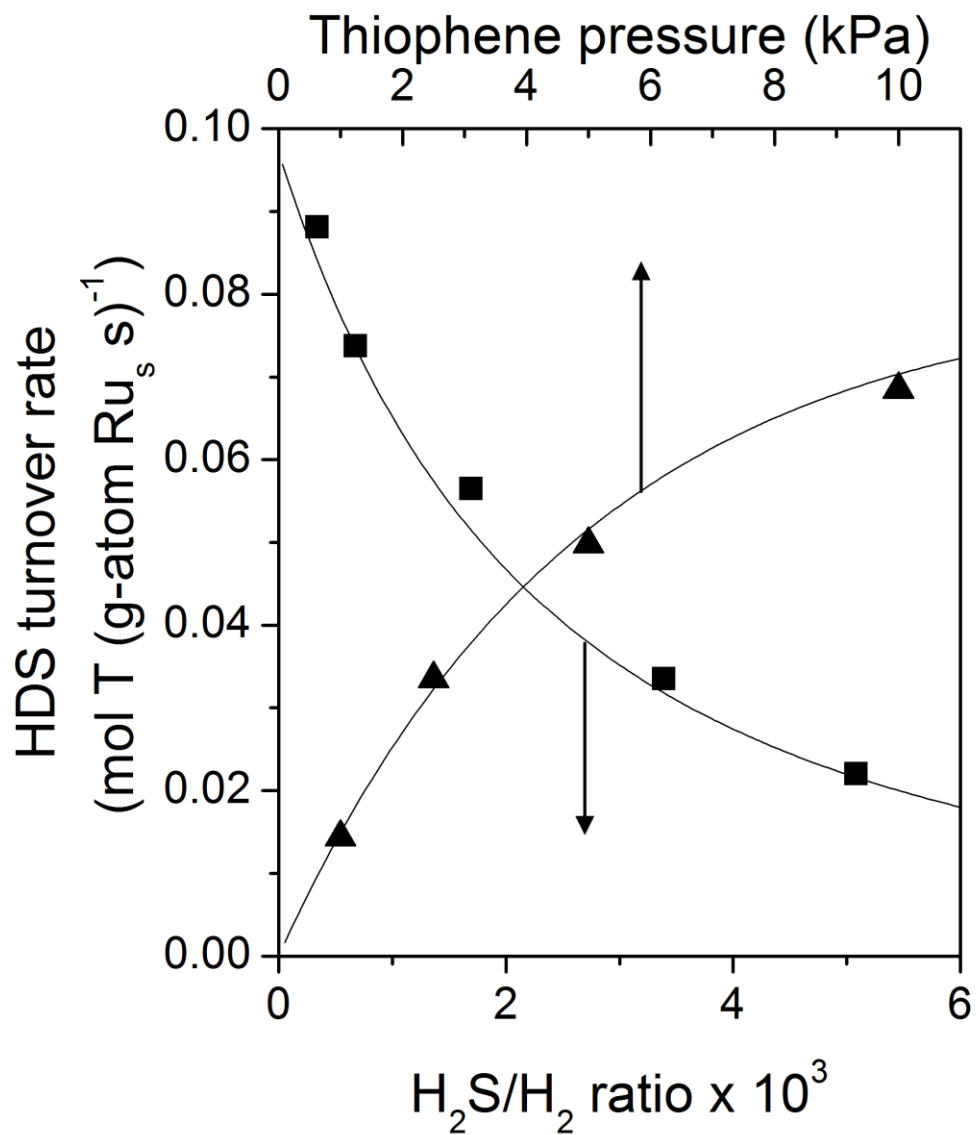
Figure 3.5: HDS turnover rates on Ru/SiO₂ at 623 K as a function of thiophene (T) pressure at 3.0 MPa H$_2$, 3.3 x 10^{-3} H$_2$S/H$_2$ ratio (▲) and as a function of H$_2$S/H$_2$ ratio at 2.5 kPa thiophene, 3.0 MPa H$_2$ (■). Curves represent regression of all measured data (on Ru) to the HDS rate expression (Eq. 3.5).
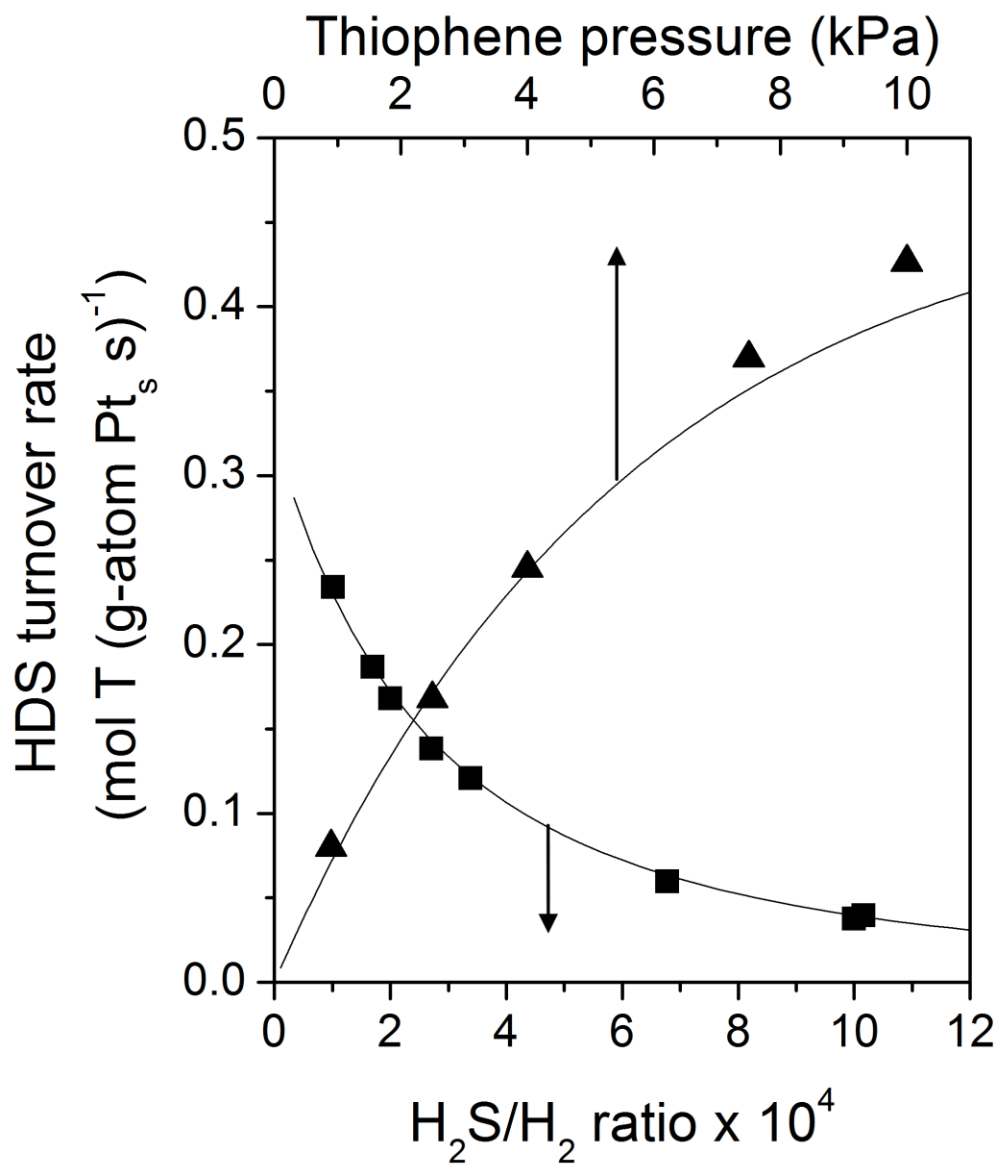
Figure 3.6: HDS turnover rates on Pt/SiO$_2$ at 573 K as a function of thiophene (T) pressure at 3.0 MPa H$_2$, 2 x 10^{-4} H$_2$S/H$_2$ ratio (▲) and as a function of H$_2$S/H$_2$ ratio at 2.5 kPa thiophene, 3.0 MPa H$_2$ (■). Curves represent regression of all measured data (on Pt) to the HDS rate expression (Eq. 3.5).
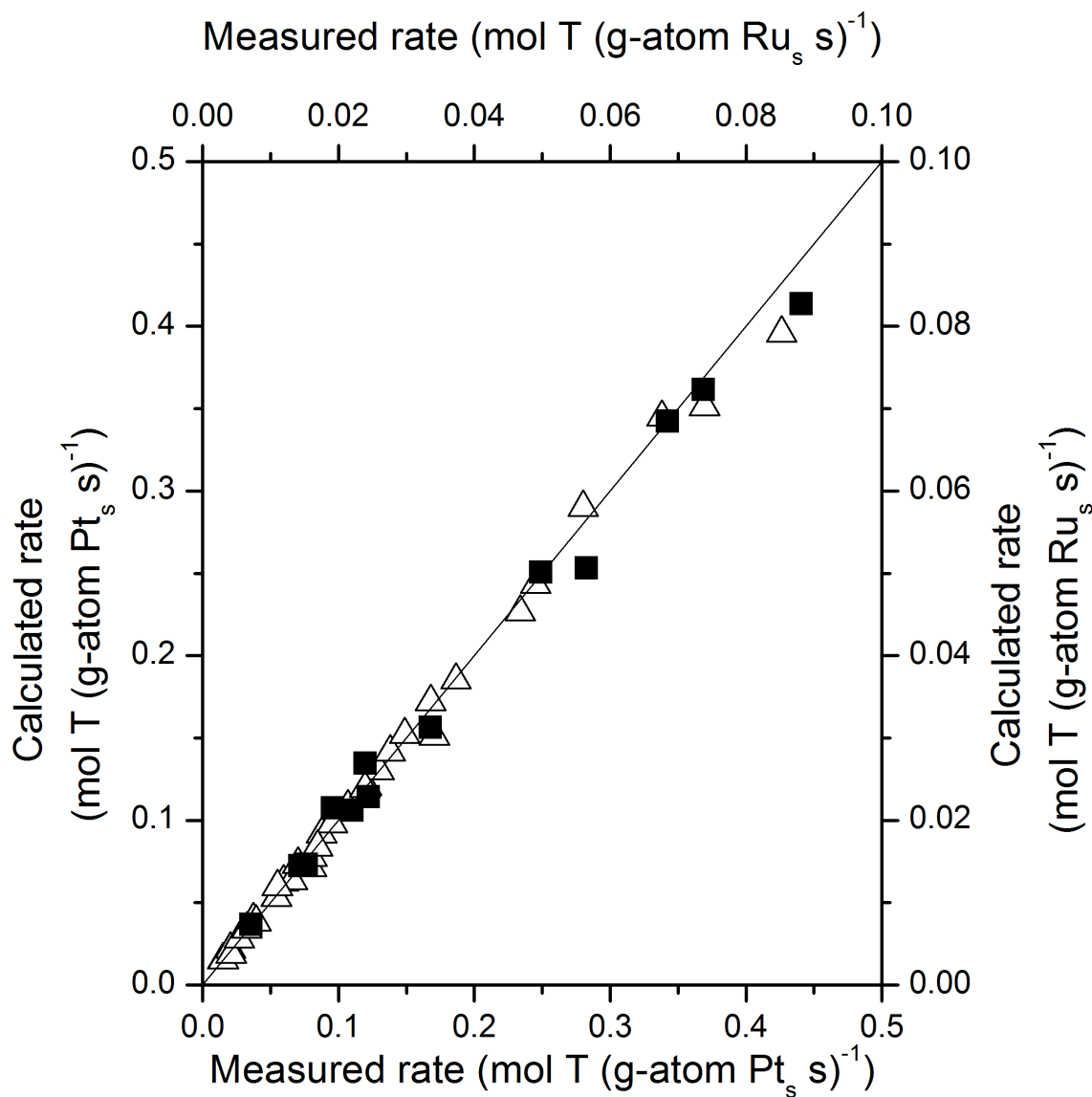
Figure 3.7: Parity plot of measured rates and rates calculated from the HDS rate expression (Eq. 3.5) for Pt/SiO$_2$ at 573 K ($\triangle$) and for Ru/SiO$_2$ at 623 K ($\blacksquare$) over a range of thiophene (T) (1-10 kPa), H$_2$ (1-3 MPa), and H$_2$S (0.2-10 kPa) pressures. Line reflects parity.
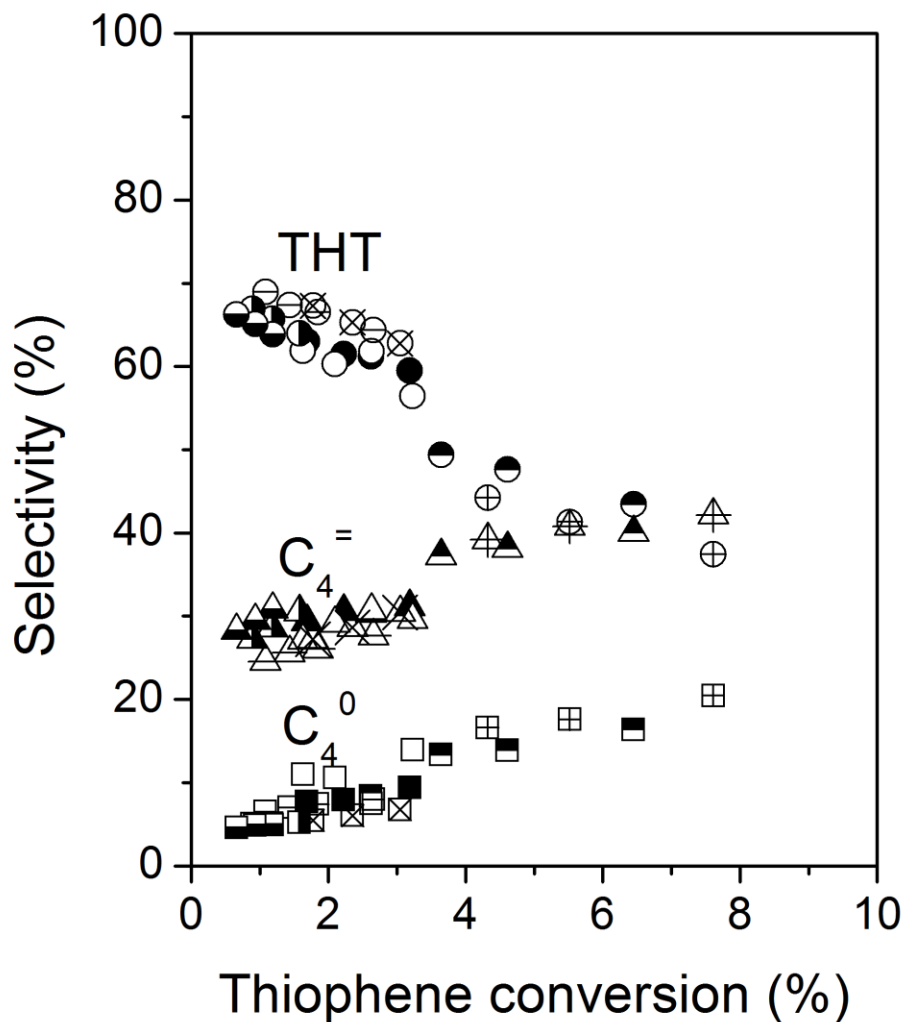
Figure 3.8: Selectivity to tetrahydrothiophene (THT, circles), butenes ($C_4^=$, triangles), and butane (C_4^0, squares) as a function of thiophene conversion for Ru/SiO_2 (623 K) at 3 MPa H_2, 2.5 kPa thiophene, and 3.3×10^{-4} (⊞), 6.7×10^{-4} (⊟), 1.7×10^{-3} (■), and 5.0×10^{-3} (⊟) H_2S/H_2 ratios; and at 3MPa H_2, 3.3×10^{-3} H_2S/H_2 ratio, and 1 kPa (⊠) 2.5 kPa (□), 5 kPa (◪), and 10 kPa (⬓) thiophene.
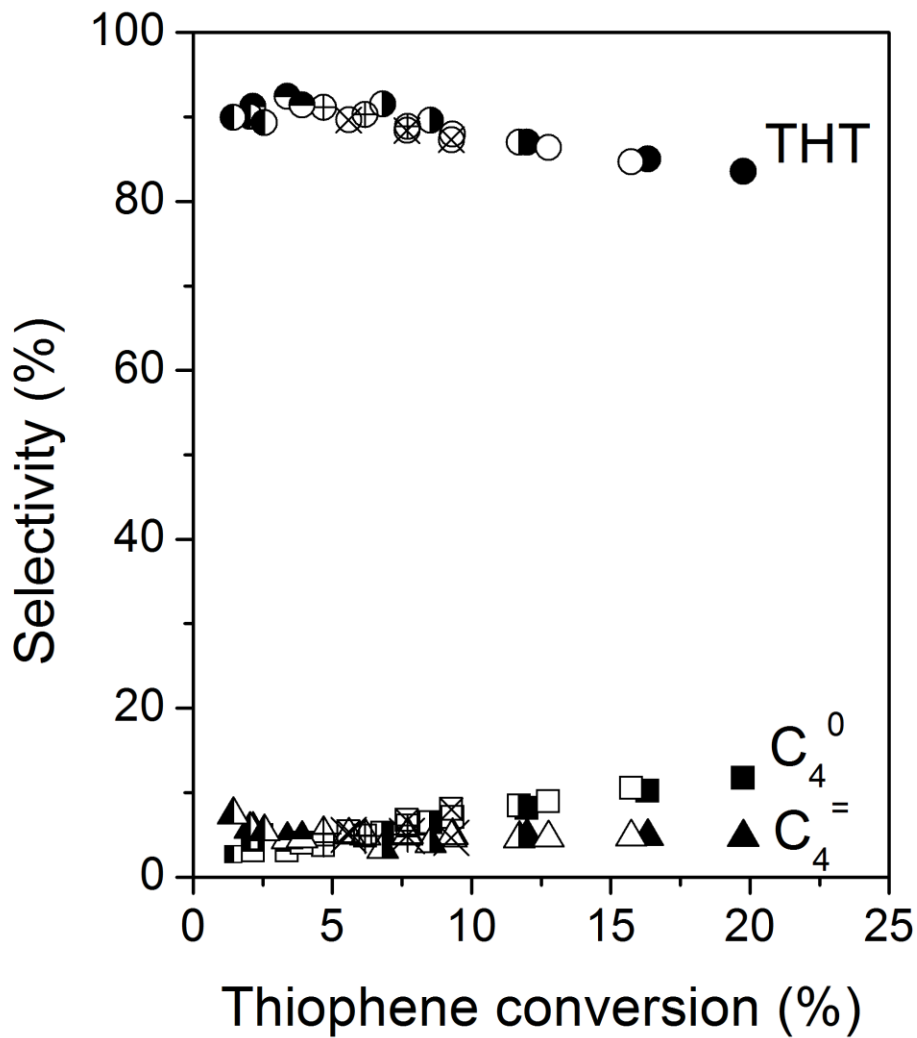
Figure 3.9: Selectivity to tetrahydrothiophene (THT, circles), butenes ($C_4^=$, triangles), and butane (C_4^0, squares) as a function of thiophene conversion for Pt/SiO$_2$ (573 K) at 2 MPa H$_2$, 2.5 kPa thiophene, and 1.5×10^{-4} (■), 2×10^{-4} (□), 3.3×10^{-4} (◧), 5.0×10^{-4} (⊞), and 1×10^{-3} (⊟) H$_2$S/H$_2$ ratios; and at 2 MPa H$_2$, 10 kPa thiophene, and 2×10^{-4} (⊠) and 1.5×10^{-3} (◪) H$_2$S/H$_2$ ratios.

Figure 3.10: THT to C_4 concentration ratio as a function of thiophene conversion at 3 MPa (●), 2 MPa (▲), and 1 MPa (■) H_2 pressures over a range of thiophene (1-10 kPa) and H_2S/H_2 ratios $((3.3\text{-}100) \times 10^{-4})$ for Ru/SiO_2 at 623 K. Lines are drawn to guide the eye.

Figure 3.11: Ratio of k'_1 to k'_2, representing rate constant ratios (Eq. 3.8) of pseudo-first order reactions for primary formation of THT and of C_4 products, respectively, derived from regression of selectivity data to the derived THT selectivity equation (Eq. 3.6) for (a) Ru/SiO_2 at 623 K and (b) Pt/SiO_2 at 573 K. Closed symbols represent values acquired through regression of the full form of the THT selectivity expression (Eq. 3.6), open symbols represent approximated values, derived from first-order approximations of THT selectivity (i.e. linear extrapolation). Solid curves reflect regression to half-order H_2 dependences; dotted curves represent corresponding upper and lower 95% confidence levels.
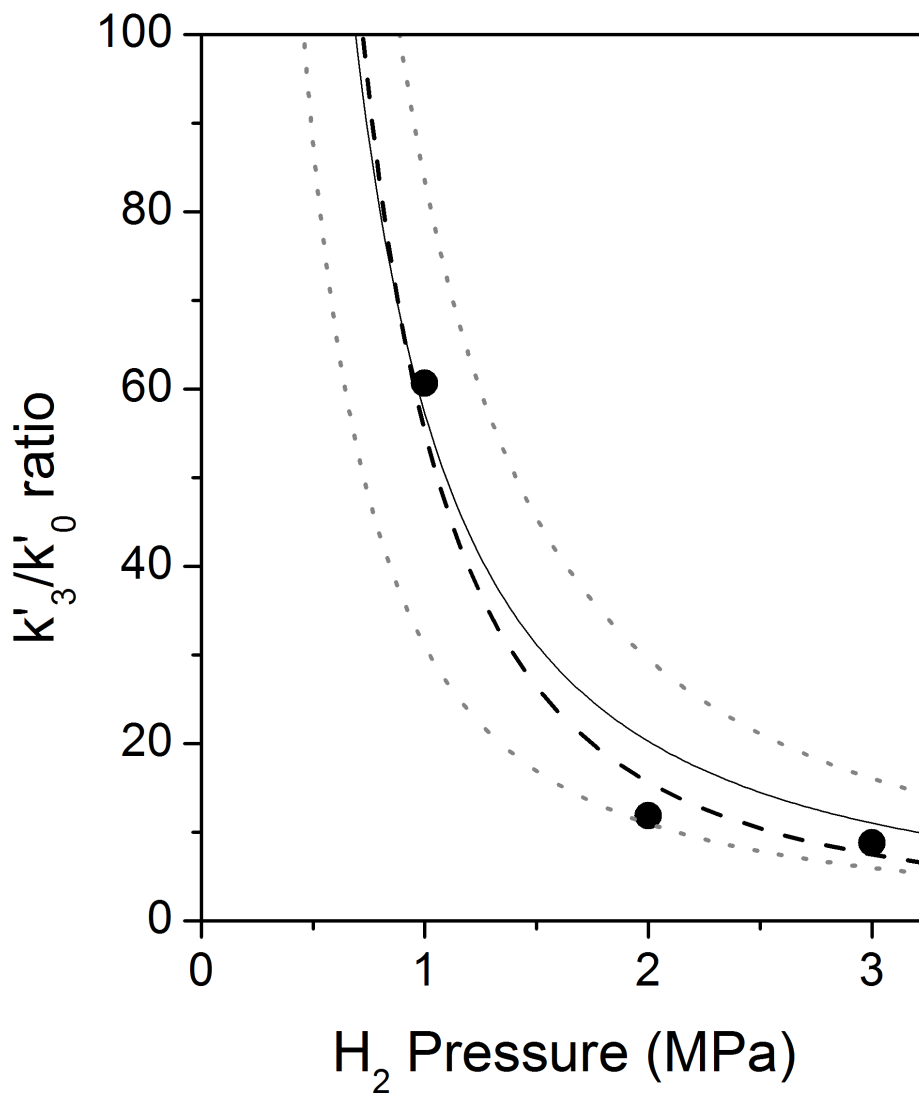
Figure 3.12: Ratio of k'_3 to k'_0, representing rate constant ratios (Eq. 3.9) of pseudo-first order reactions for secondary desulfurization of THT and of 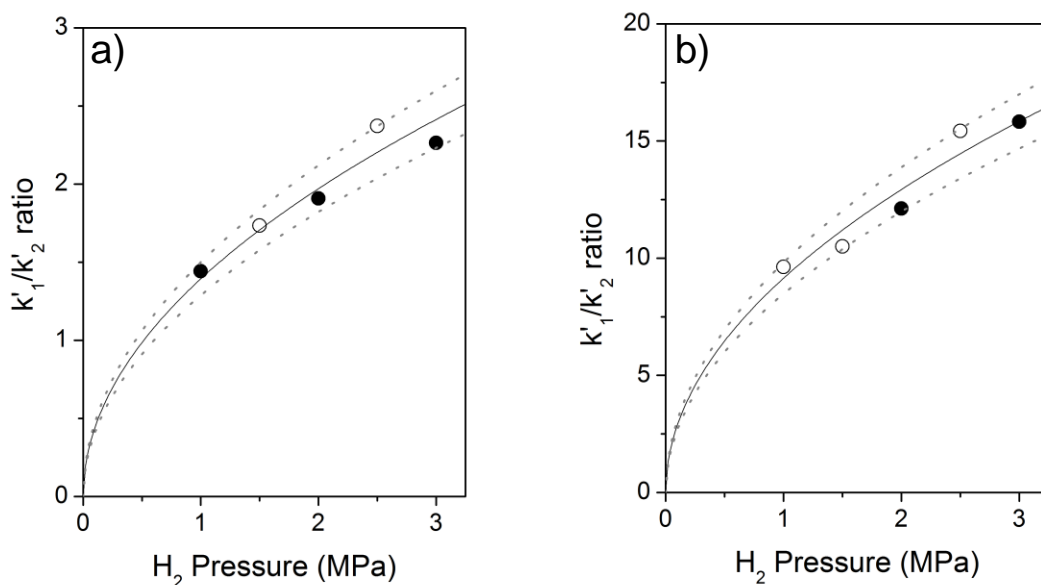primary thiophene conversion, respectively derived from regression of selectivity data to the derived THT selectivity equation (Eq. 3.6) for Ru/SiO_2 at 623 K. The dashed curve represents the best fit ($\delta = -1.8$) of the power law $\sim(H_2)^\delta$; the solid curve represents a kinetically viable dependence ($\delta = -1.5$) that can be supported from chemical analysis of the reaction network; dotted, grey curves represent 95% confidence intervals of the regression to $\sim(H_2)^{-1.5}$.
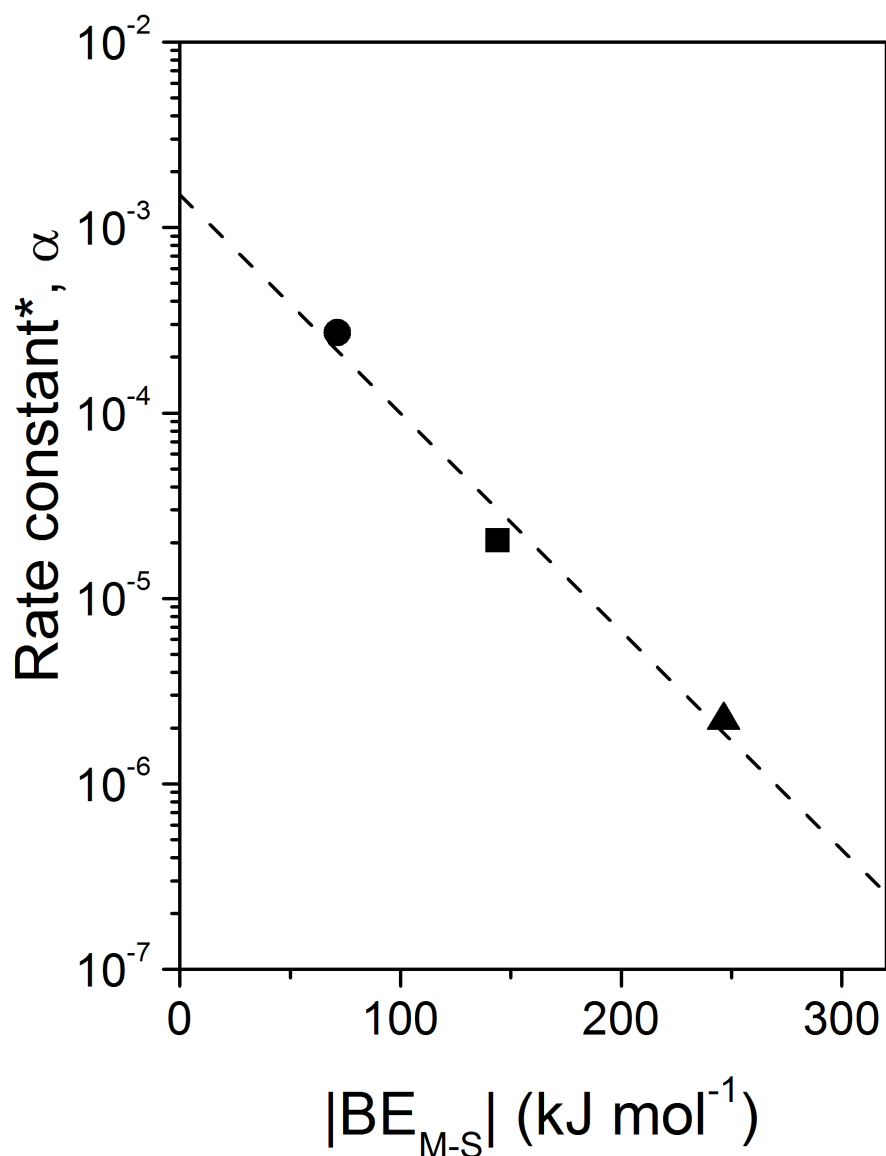
*Units are mol(g-atom s kPa^2)$^{-1}$ for Ru/Pt or mol(g-atom s kPa$^{1.5}$)$^{-1}$ for Re.

Figure 3.13: Regressed value of numerator rate parameter, α ($k_0 K_{H2} K_T K_{HT}$ or $k_0 K_{H2}{}^{0.5} K_T$, Table 3.2) from fitting all measured kinetic data to the functional form of the HDS rate expressions (Eq. 3.5 or Eq. 2.8, respectively) for supported Ru (■) at 623 K, and Pt (●) and Re (▲) at 573 K as a function of their sulfur binding energy ($|BE_{M-S}|$) at monolayer coverage, calculated from DFT. The dashed line serves to guide the eye.
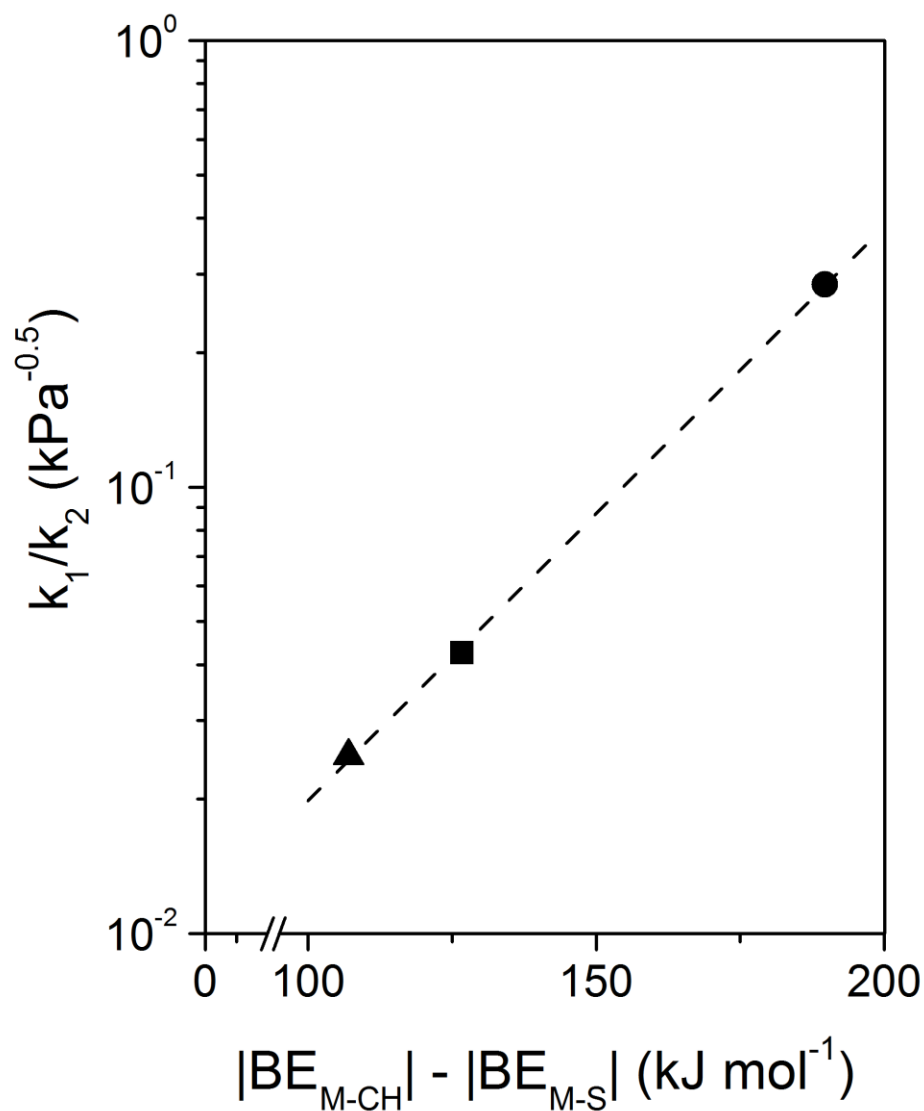
Figure 3.14: Ratio of rate constants, k_1/k_2 (Eq. 3.8), of primary formation of THT to that of C_4 as a function of the difference of binding energies ($|BE|$) between metal and carbon (i.e. methylidyne, M-CH) and metal and sulfur (M-S) adsorbates for SiO_2-supported Ru (■) at 623 K and Pt (●) and Re (▲) at 573 K. Binding energies are calculated from DFT at low coverages (1/9 and 1/4 monolayer, respectively). The dashed line serves to guide the eye.

3.6.3   Schemes

H_2	+	2*	$\xrightleftharpoons{K_{H2}}$	2 (H*)	(i)
H_2S	+	*	$\xrightleftharpoons{K_{H2S}}$	H_2S*	(ii)
H_2S*	+	*	$\xrightleftharpoons{K_{HS}}$	H* + HS*	(iii)
HS*	+	*	$\xrightleftharpoons{K_S}$	H* + S*	(iv)
T	+	*	$\xrightleftharpoons{K_T}$	T*	(v)
T*	+	H*	$\xrightleftharpoons{K_{HT}}$	MHT* + *	(vi)
MHT*	+	H*	$\xrightarrow{k_0}$	I*	(vii)
I*	+	nH*	$\xrightarrow{k_1}$	THT*	(viii)
I*	+	(n-1)H	$\xrightarrow{k_2}$	C_4*	(ix)
	C_4*		$\xrightleftharpoons{K_{C4}^{-1}}$	C_4 + *	(x)
	THT*		$\xrightleftharpoons{K_{THT}^{-1}}$	THT + *	(xi)
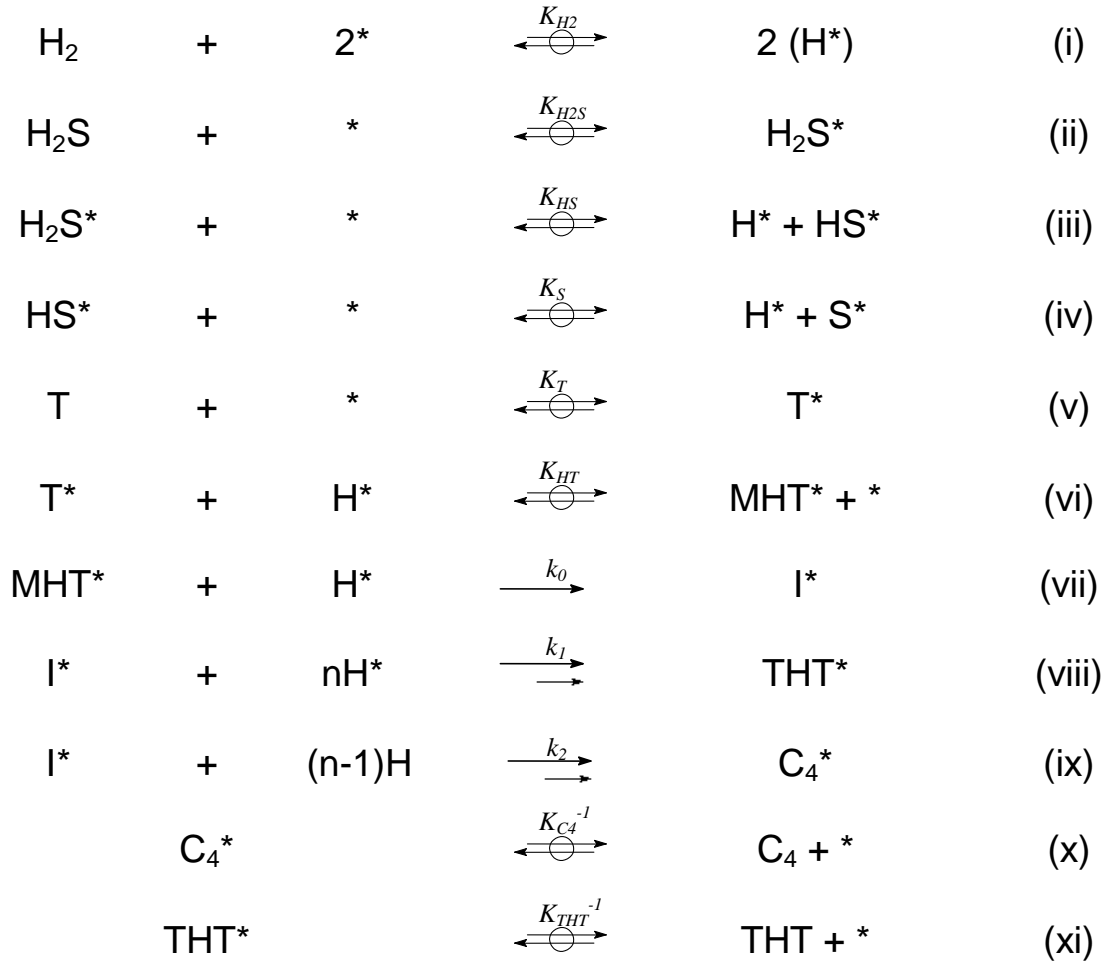
Scheme 3.1: Elementary steps for thiophene HDS on Ru and Pt catalysts. * is a vacant site; H*, H_2S*, HS*, S*, T*, MHT*, I* are hydrogen, hydrogen sulfide, sulfhydryl, sulfur, thiophene, monohydrothiophene, and dihydrothiophene surface species, respectively; $\xrightleftharpoons{}$ indicates a quasi-equilibrated step and $\longrightarrow$ represents a kinetically-relevant step; T, THT, and C_4 represent thiophene, tetrahydrothiophene and lumped butenes/butane (gas phase) species, respectively.
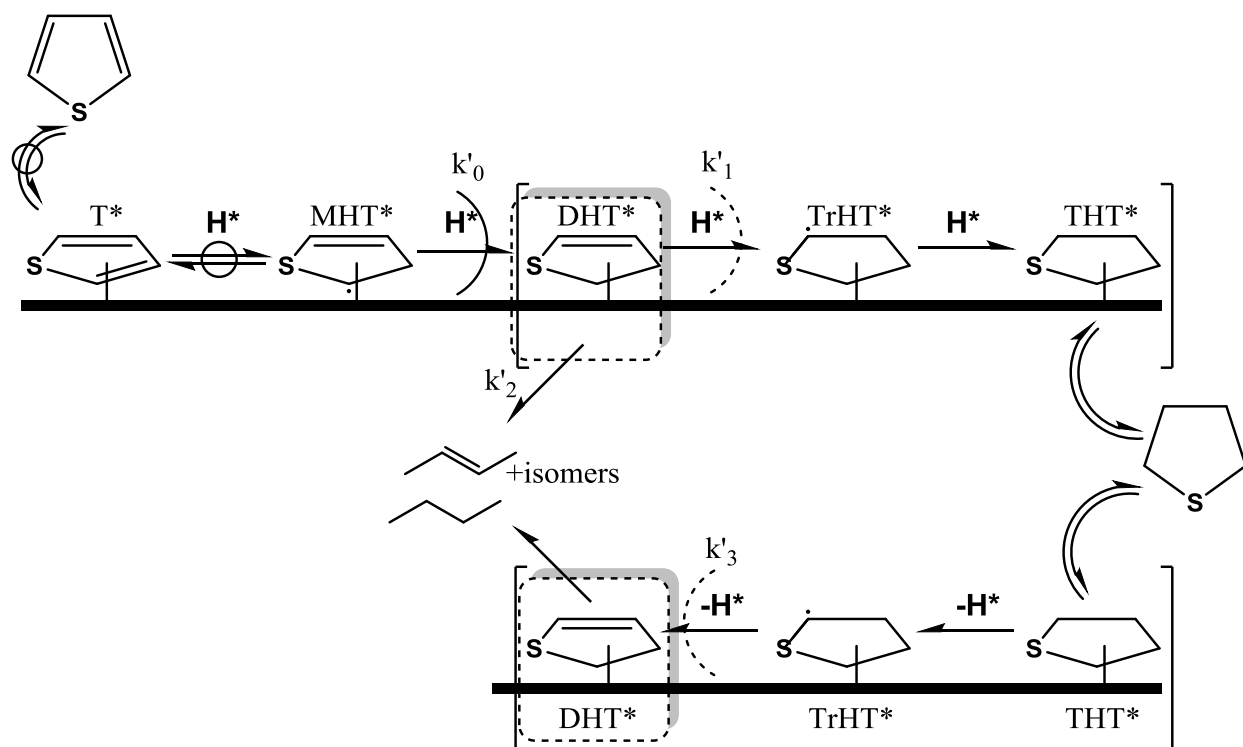
Scheme 3.2: Thiophene reactions on HDS sites, which are formed on sulfur-covered surfaces of Ru and Pt metal clusters. The rate of thiophene consumption is controlled by a kinetically-relevant, (second) hydrogen addition step to monohydrothiophene (MHT), denoted by the (pseudo-first-order) rate constant, k'_0. Subsequent surface species are kinetically-silent, but from analysis of selectivity data, the steps that limit the formation of THT and its secondary desulfurization is denoted by rate constants k'_1 and k'_3, respectively. Dihydrothiophene surface species (DHT) are implicated as the intermediate that undergoes C-S activation, leading to the eventual (C-S) bond cleavage and subsequent desorption as C_4 products.

3.7 References

1. Lauritsen, J. V.; Kibsgaard, J.; Olesen, G. H.; Moses, P. G.; Hinnemann, B.; Helveg, S.; Nørskov, J. K.; Clausen, B. S.; Topsøe, H.; Lægsgaard, E., et al. *J Catal*. **249** (2007) 220.
2. Borgna, A.; Hensen, E. J. M.; van Veen, J. A. R.; Niemantsverdriet, J. W. *J Catal*. **221** (2004) 541.
3. Cesano, F.; Bertarione, S.; Piovano, A.; Agostini, G.; Rahman, M. M.; Groppo, E.; Bonino, F.; Scarano, D.; Lamberti, C.; Bordiga, S., et al. *Catalysis Science & Technology*. **1** (2011) 123.
4. Prins, R.; De Beer, V. H. J.; Somorjai, G. A. *Catalysis Reviews*. **31** (1989) 1.
5. Pecoraro, T. A.; Chianelli, R. R. *J Catal*. **67** (1981) 430.
6. Hensen, E. J. M.; Brans, H. J. A.; Lardinois, G. M. H. J.; de Beer, V. H. J.; van Veen, J. A. R.; van Santen, R. A. *J Catal*. **192** (2000) 98.
7. Toulhoat, H.; Raybaud, P. *Journal of Catalysis*. **216** (2003) 63.
8. Wang, H. M.; Iglesia, E. *J Catal*. **273** (2010) 245.
9. Wang, H. M.; Iglesia, E. *Chemcatchem*. **3** (2011) 1166.
10. McCarty, J. G.; Sancier, K. M.; Wise, H. *J Catal*. **82** (1983) 92.
11. Kasztelan, S.; Guillaume, D. *Ind Eng Chem Res*. **34** (1995) 1500.
12. Flaherty, D. W.; Hibbitts, D. D.; Gürbüz, E. I.; Iglesia, E. *J Catal*. **311** (2014) 350.
13. Flaherty, D. W.; Hibbitts, D. D.; Iglesia, E. *J Am Chem Soc*. **136** (2014) 9664.
14. Flaherty, D. W.; Iglesia, E. *Journal of the American Chemical Society*. **135** (2013) 18586.
15. Flaherty, D. W.; Uzun, A.; Iglesia, E. *The Journal of Physical Chemistry C*. **119** (2015) 2597.
16. Berhault, G.; Lacroix, M.; Breysse, M.; Mauge, F.; Lavalley, J.-C.; Qu, L. *J. Catal.* **170** (1997) 37.
17. Berhault, G.; Lacroix, M.; Breysse, M.; Mauge, F.; Lavalley, J.-C.; Nie, H.; Qu, L. *J. Catal.* **178** (1998) 555.
18. Topsoe, N. Y.; Topsoe, H. *J Catal*. **139** (1993) 641.
19. Korányi, T. I.; Moreau, F.; Rozanov, V. V.; Rozanova, E. A. *Journal of Molecular Structure*. **410–411** (1997) 103.
20. Flaherty, D. W.; Iglesia, E. *J. Am. Chem. Soc*. **135** (2013) 18586.
21. McCarty, J. G.; Wise, H. *The Journal of Chemical Physics*. **74** (1981) 5877.

3.8 Supporting Information

3.8.1 *Parameter discrimination and sensitivity analysis*

For Ru and Pt systems, HDS rates were described by the following rate expression,

$$\frac{r}{[L]} = \frac{\alpha(H_2)^{x}(T)}{\left(1+\beta(H_2)^{0.5}+\gamma(T)+\delta(T)(H_2)^{0.5}+\epsilon(H_2S)+\zeta\frac{(H_2S)}{(H_2)^{0.5}}+\eta\frac{(H_2S)}{(H_2)}\right)^{2}} \tag{3.S1}$$

, from which regressions of measured kinetic data eliminated several denominator terms, simplifying the form of the rate law (Eq. 3.S2) without significant loss in the quality overall fits.

$$\frac{r}{[L]} = \frac{\alpha(H_2)^{1.0}(T)}{\left(1+\beta(H_2)^{0.5}+\gamma(T)+\eta\frac{(H_2S)}{(H_2)}\right)^2} \qquad (3.S2)$$

We unequivocally find that kinetic data are best described by first-order dependences on H_2 pressure (in the numerator), but we can probe the lower limit of H_2 order by regressing data to,

$$r_{y,min} = \frac{\alpha(H_2)^y(T)}{\left(1+\gamma(T)+\eta\frac{(H_2S)}{(H_2)}\right)^2} \qquad (3.S3)$$

Indeed, best fit values of y (Eq. 3.S3) were consistently greater than 0.5, suggesting that rates on Ru and Pt cannot be limited by a kinetically-relevant first H-addition step.

Regression of kinetic data to the functional forms of rate expressions, derived from a chemically plausible sequence of elementary steps, should be accompanied with statistical analysis to ensure that parameters are truly independent and measurable. This analysis permits a degree of parameter discrimination between various surface species, which may depend differently on the concentrations of various inlet feeds. We rely on sensitivity analysis of best fit parameter values to determine how strongly overall rates depend on them, which is particularly useful when evaluating the relative importance of various (denominator) surface species. This sensitivity is probed by evaluating the extent to which differences between predicted and measured rates, quantified by the sum of their squared residuals (Equation 3.S4), changes as a result of attenuations in the best fit value of each regressed rate parameter.

$$Sum\ of\ Squared\ Residuals\ (SSR) = \sum_i \left(r_{i,predicted} - r_{i,measured}\right)^2 \qquad (3.S4)$$

As described above, all kinetic data measured on Ru and Pt can be described by regression to rate expressions (Eq. 3.S1) simplified to include three (α, γ, ε) and four (α, β, γ, ε) parameters, respectively. We perform a sensitivity analysis on each of these parameters independently by evaluating a relative sum of squared residuals (Relative SSR, Eq. 3.S5) at different degrees of change to best fit parameter values (i.e. ±20%). Values of Relative SSR ranged from 2 to 20 when best fit parameter values were independently varied by 20%, suggesting that rates were strongly sensitive to these parameters.

$$Relative\ SSR = \frac{\partial(SSR)}{\partial(k_i)} \qquad (3.S5)$$

, where $\partial(SSR)$ is the change in SSR (defined in Eq. 3.S4) and $\partial(k_i)$ is the incremental change in the best fit value of a regressed parameter, k_i (e.g. α, β, γ, ε, Eq. 3.S2).
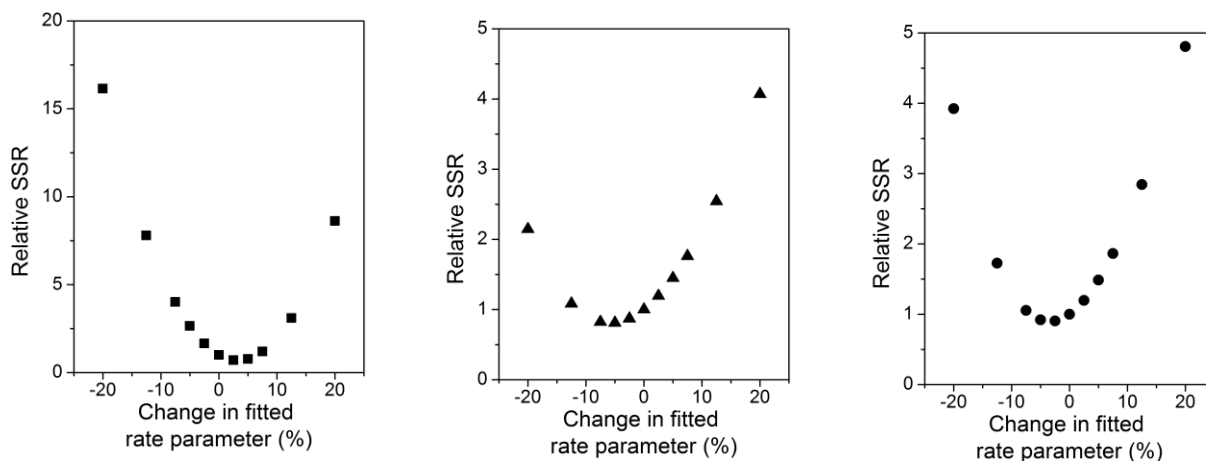
Figure 3.S1: Relative SSR as a function of percent changes in the best fit value of the regressed rate parameter: α (■), γ (▲), and ε (●) on Ru/SiO_2 (at 623 K).
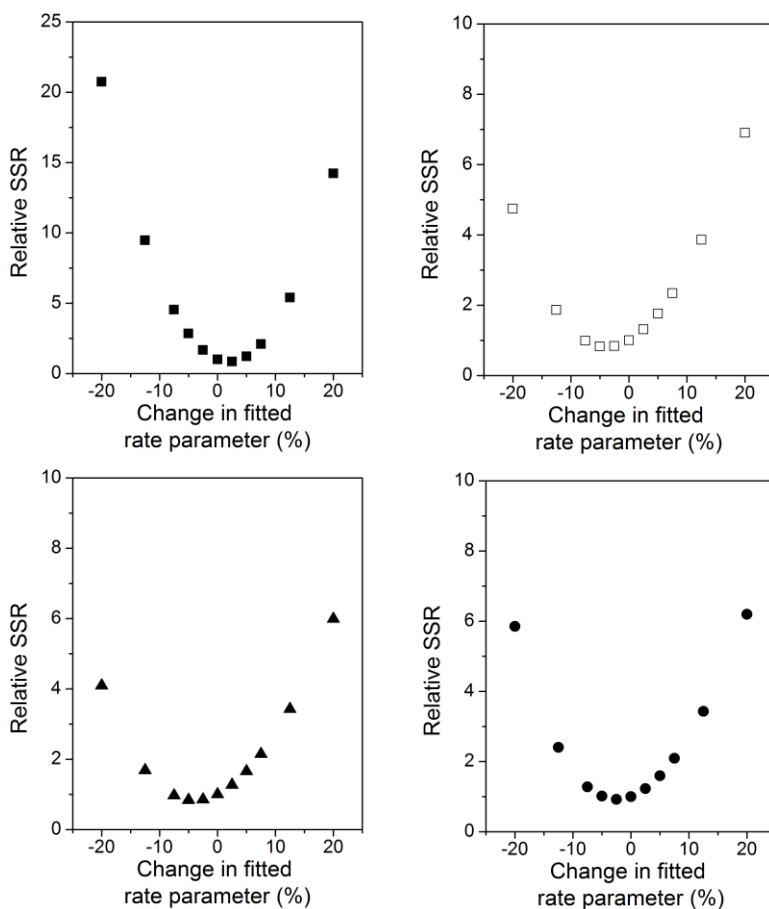

Figure 3.S2: Relative SSR as a function of percent changes in the best fit value of the regressed rate parameter: α (■), β (□), γ (▲), and ε (●) on Pt/SiO_2 (at 573 K).

3.8.2   Theoretical M-S binding energy at high coverages using density functional theory

Sulfur binding energies were calculated via density functional theory (DFT) on transition metal surfaces, expressed as the energy of formation of an adsorbed S-atom based on the following equation,

$$M\,(s) + \frac{1}{2}S_2(g) \;\leftrightarrow M - S \hspace{6cm} (3.S6)$$

Calculations were performed on 2x2 closed-packed surfaces, (111) or (0001) depending on whether the metal structure exhibits fcc or hcp crystal packing, with the top two layers relaxed and bottom two fixed. The structures were optimized using RPBE functional with PAW wavefunctions at 6x6x1 Brillouin sampling with convergence to below 0.05 eV Å^{-1}. Energies were obtained at 12x12x1 sampling with a 396 eV cutoff.

Table 3.S1: M-S binding energy of select transition metals at monolayer coverages

metal (crystal facet)	M-S binding energy (kJ mol^{-1})
Ni (111)	-33
Ru (0001)	**-144**
Rh (111)	-118
Pd (111)	-103
Re (0001)	**-246**
Ir (111)	-75
Pt (111)	**-72**

Hibbitts, David. *unpublished results*.

3.8.3   Theoretical M-X binding energy at low X-coverages using density functional theory

We propose (in Section 3.3.4) that increased sulfur affinity can shape product distributions by selectively stabilizing transition states that form desulfurization products. We can probe the specific metal coordination to sulfur (i.e. M-S bond strength) by referencing this energy to that between the (same) metal and a different (model) adsorbate. Commensurate changes in the adsorption of *all* adsorbates (as a function of metal identity) would lead to similar selectivity trends because, in such a scenario, transition states are equally stabilized or destabilized; thus, differences in product distribution require disproportionate increases in specific (i.e sulfur) adsorption properties. We explore the preferential S-affinity of different transition metals by referencing their M-S binding energies to their M-CH (metal-methylidyne) binding energies, calculated at similar S- or CH- coverages (1/4 and 1/9 fractional coverage, respectively).

Methods for calculating M-S binding energies are described in Section 3.8.2. M-CH binding energies are calculated on 4x4 unit cells of closed-packed surfaces, with the top two layers relaxed and bottom two fixed. Structures were optimized using RPBE-PAW at 3x3x1 Brillouin sampling with forces converged at 0.05 eV Å^{-1}. Energies were acquired at 6x6x1 sampling with 396 eV cutoff. Differences in the absolute values of M-CH and M-S binding energies (Table 3.S2, column 4) reflect the extent to which C-affinity to S-affinity differ on a

given metal. Each metal below exhibits a different |M-CH binding energy|-|M-S binding energy|, with Re exhibiting the lowest value and Pt exhibiting the highest, suggesting that the relative strength of Re-S referenced to Re-CH is greater than the relative strength of Pt-S referenced to Pt-CH.

Table 3.S2: M-S and M-CH binding energies of select transition metals at low coverages.

metal (crystal facet)	M-CH binding energy (kJ mol^{-1})	M-S binding energy (kJ mol^{-1})	|M-CH|-|M-S| [a] (kJ mol^{-1})
Ni (111)	-584	-463	120
Ru (0001)	-638	-511	**127**
Rh (111)	-616	-478	139
Pd (111)	-586	-420	165
Re (0001)	-630	-523	**107**
Ir (111)	-630	-460	170
Pt (111)	-625	-435	**190**

Hibbitts, David. *unpublished results*.

[a] Differences in the absolute values of binding energies, i.e. |M-CH binding energy|-|M-S binding energy|.

CHAPTER FOUR

Mechanistic Interpretation and Practical Consequences of Hydrogen Spillover in Hydrodesulfurization Catalysts

Abstract

Bifunctional cascade reactions exploit the use of two functions whose coupled reactivity is enhanced relative to that of each individual function. These functions communicate via active intermediates that are formed on one particular surface but that are readily consumed on a second, otherwise inactive, surface nearby; this cascade effect then leads to an overall increase in measured turnover rates, when normalized by the number of sites of the first function. These concepts are widely adopted to explain *hydrogen spillover* phenomenon, wherein functions that cannot dissociate molecular H_2 appear to contribute to overall rates of hydrogenation or reduction reactions when they are placed near domains that can activate H_2 and generate H-carrying species. While the transport of these active H-species to *non-dissociating* functions appears necessary, both the nature of these mobile H-species and mechanisms of their diffusion have been implausibly ascribed or neglected completely in the literature. Furthermore, the inconsistent observation of hydrogen spillover phenomena has led to debate over their requirements and their non-phenomenological existence. Our approach relies on rigorous measurements of thiophene hydrodesulfurization (HDS) rates on both monofunctional (i.e. SiO_2-supported monometallic catalysts) and bifunctional (i.e. physical mixtures of monofunctional catalysts and γ-Al_2O_3 materials) systems. We develop a transport-kinetic model that fully describes experimental observations, which indicate sole, selective enhancements of the hydrogenation product (i.e. tetrahydrothiophene). These enhancements exhibit asymptotic limits with increasing γ-Al_2O_3 content and become sensitive to changes in sulfur chemical potential, which influences sulfur coverages on metal surfaces although H_2 dissociation remains equilibrated at all relevant HDS conditions. Such behaviors are consistent with the formation of an unstable, partially-hydrogenated, thiophene-derived carrier capable of transporting active H-species from metal functions to γ-Al_2O_3, supported by kinetic pressure dependences that confirm spillover-mediated pathways are limited by metal chemistry. Maximum spillover effects are bound by such limits, but we can validate this synergy by using probes that can lower the magnitude of these enhancements, at commensurate γ-Al_2O_3-to-metal mixing ratios. We decreased the intimacy of mixing by physically increasing the distance between the functions by using different dilution techniques (i.e. from powdered mixtures of functions within single pellets (intrapellet dilution) to mixtures of separate pellets of each function (interpellet dilution)) and found that this indeed weakened the spillover effect, consistent with introducing greater diffusion lengths and transport constraints for the H-carriers. Alternatively, suppressing the formation of these molecular H-carriers, either in monofunctional reactions that limit all (sequential) hydrogenation steps or by selective exclusions of larger organosulfur compounds (i.e. thiophene) from accessing metal functions encapsulated within zeolite frameworks (e.g. LTA), led to a complete absence of any spillover effects. Such experimental evidence, combined with computational (coupled cluster single and double excitation) methods, strongly implicate monohydrothiophene (MHT) radical species as the identity of the H-carrier, challenging former attributions of mobile, atomic hydrogen as the spillover species.

4.1 Introduction

Spillover phenomena are ubiquitous in catalysis and involve the transport of active species, formed on one function, to another function that cannot form the active species or catalyze the reaction in isolation [1-6]. Spillover pathways have been proposed to mediate the transfer of atoms or small fragments of stable molecules, such as hydrogen [1-7], oxygen [2,8,9], methoxy (CH_3O) [2,10], and isocyanate (NCO) [2,11]. Among these, the spillover of hydrogen has received the most attention since its initial discovery, in which physical mixtures of WO_3 powders with Pt-containing porous solids formed H_xWO_3 bronzes under H_2 conditions at ambient temperature [7]. Activated hydrogen species, known to form on specific metal, oxide, or sulfide functions are proposed to transfer to an acceptor site, which, in most cases, resides well beyond atomic distances; these acceptors, such as particular oxides [7,12], sulfides [13,14], or adsorbed, unsaturated molecules [1-5] then undergo reduction. Spillover phenomena have also been implicated in increases of measured rate and capacities of hydrogen storage solids, such as carbonaceous solids [6,15] and metal organic frameworks [16], by physically mixing these materials with noble metal catalysts.

The occurrence of hydrogen spillover and its catalytic consequences seem incontrovertible, but the magnitude of catalytic enhancements and the nature and transport mechanism of mobile hydrogen species remain the subject of active dispute and of occasional implausible attributions. For instance, atomic hydrogen species formed on metal clusters have been proposed to mediate hydrogenation of unsaturated molecules on acid supports via their formation and transfer from metal sites present at distances much greater than molecular dimensions [2,17-27], but other studies have failed to detect spillover-mediated hydrogenation reactions for the same systems at similar conditions [28-31]. Evidence for spillover of atomic hydrogen from metals to reducible supports such as WO_3 seems unequivocal [7,12]; it appears to require the stabilization of positively charged hydrogen species by gaseous molecules with high proton affinity [32], suggesting that hydrogen atoms move as proton-electron pairs. While this route is plausible on reducible oxides, it is inaccessible when connecting surfaces are non-reducible insulators, and yet, spillover-mediated chemical reductions have been reported on non-reducible supports and the proposed mediators include highly unstable hydrogen atoms [2,4,5,17-27] and even bare protons [4] that lack the electrons required for charge balance and for chemical reduction events. The dubious nature of hydrogen atom transport across these non-reducible surfaces (e.g. SiO_2, γ-Al_2O_3, MgO) have been met with alternative explanations, among which the most popular implicates the presence of "impurity" species that are more easily desorbed from SiO_2 relative to γ-Al_2O_3 sites and that subsequently poison metal sites during catalyst pretreatment temperatures (e.g. 700 K) [33,34]; such proposals attribute the enhancements exhibited in catalyst dilutions with γ-Al_2O_3 to detrimental effects of SiO_2 diluents. These matters require the elimination of any purported contributions from unidentified "impurity" species, a clearer assessment of the nature of the active hydrogen species and of the means by which they diffuse, and a more definitive description of the mechanism by which these species form and transfer hydrogen to hydrogenate substrates adsorbed on sites that cannot themselves activate H_2.

We address here hydrogen spillover phenomena and their mechanism in the context of heteroatom removal from organosulfur compounds [35,36], for which acidic supports have been

implicated as promoters of hydrodesulfurization (HDS) catalysis on metals and sulfides [37-41]. Such effects are of practical interest because they provide a path for the removal of sulfur from molecules such as 4,6-dialkyldibenzothiophenes, for which steric constraints around the sulfur atom require sequential hydrogenation-desulfurization routes for sulfur removal [35,36,42,43]. Previous studies have claimed that a separate hydrogenation route on acid sites using spillover hydrogen species causes the synergistic effects of acidic supports, but without clear mechanistic attribution or specific discussions about the nature of the mobile hydrogen species [37-40].

Pt and Ru clusters dispersed on mesoporous SiO_2 gave higher thiophene HDS rates when mixed physically with γ-Al_2O_3, and rates initially increased before reaching a constant value with increasing γ-Al_2O_3-to-metal ratios in these mixtures. These trends reflect the involvement of mobile and very reactive hydrogen carriers present at very low pseudo-steady-state concentrations, formed in reversible steps on Pt or Ru clusters and transferred to non-vicinal γ-Al_2O_3 surfaces, where they hydrogenate adsorbed species. This current study of HDS pathways builds on advances made in previous reports [44,45] on the elementary steps and mechanistic features of monofunctional routes (Chapters Two and Three) to confirm the metal-derived nature and identity of these intermediates through rigorous interpretation of observed kinetic responses and their viability through computational methods. Consistency of our proposed pathways can be assessed on catalysts whose reaction mechanism precludes the formation of carriers that lead to productive hydrogen transfer events, for example monofunctional HDS on ReS_x/SiO_2, which exhibited an absence of any observable enhancements in rates over similar γ-Al_2O_3 mixing ratios. Such findings shed insights on the requirements for spillover and account for the lack of observable rate enhancements in certain hydrogenation reactions, on various catalysts, or under different operating conditions.

We further exploit recent developments [46,47] in the synthesis of encapsulated metal clusters, which are accessible to H_2 but in some cases not to the larger organic substrates (e.g. thiophene). These materials are used here to illustrate how hydrogen atoms diffuse only by attachment to molecular carriers, by forming unstable gaseous molecular intermediates that transfer hydrogen atoms to species adsorbed at distant acid sites. Indeed, metal clusters encapsulated within LTA zeolites, which are accessible to H_2 but not to thiophene, do not exhibit spillover-mediated HDS reactions when mixed with γ-Al_2O_3, indicating that thiophene-derived intermediates, present as unstable and very reactive partially-hydrogenated thiophene species, are required to transport the H_2-derived species required for hydrogenation at distant sites.

4.2   Methods

Synthetic protocols, materials characterization, and reactor operation for measuring HDS rates have been detailed extensively in our previous studies [44,45] and are briefly summarized in this section.

4.2.1   *Catalyst synthesis and characterization*

Supported Ru and Pt catalysts were synthesized via electrostatic adsorption methods on silica support materials (Cabosil, HS-5, 310 m^2 g^{-1}) that were previously acid washed and treated in flowing dry air at 673-773 K (0.003 K s^{-1}) for 3-4 h. Aqueous solutions of metal precursors,

Ru(NH$_3$)$_6$Cl$_3$ and Pt(NH$_3$)$_4$(NO$_3$)$_2$, were prepared in the presence of NaOH or NH$_3$·H$_2$O (final pH 11.2 and 9.2, respectively) and stirred with SiO$_2$ for 1 h. The solids were subsequently filtered, and, where necessary, additional washing steps with deionized water (17.9 MΩ·cm resistivity) were included to remove chlorine ions. The retentates were dried under vacuum at room temperature for >24 h and subsequently treated in flowing dry air (Praxair, 99.99%, 1.0 cm^3 g^{-1} s^{-1}) for 5 h at 353-373 K. After these drying steps, the catalysts were subsequently treated in high temperature air and/or H$_2$ treatments as detailed in Table 4.1 The effect of impurities that were either initially present on SiO$_2$ materials or introduced as a result of synthesis conditions was probed by synthesizing SiO$_2$-supported Pt catalysts via different synthetic routes and SiO$_2$ support sources. The other Pt/SiO$_2$ sample was prepared via incipient wetness impregnation of SiO$_2$ (Davison Chemical, Davisil Grade 646) with aqueous H$_2$PtCl$_6$·(H$_2$O)$_6$ (Aldrich), dried in ambient air at 383 K for >8 h and subsequently treated in flowing dry air (Praxair, 99.99%) to 823 K (0.033 K s^{-1}) for 3 h and then to 923 K (0.033 K s^{-1}) for 5 h. After high temperature air treatment, this sample was cooled to ambient temperatures and subsequently treated in H$_2$ (Praxair, 99.99%) to 573 K for 2 h. All metal catalysts were passivated in low O$_2$/He (0.1-1.0%, Praxair, certified mixture) at ambient temperatures for 2-6 h.

ReS$_x$ nanostructures were prepared by incipient wetness impregnation of acid-washed, air-treated SiO$_2$ (Cabosil, HS-5, 310 m^2 g^{-1}) with aqueous NH$_4$ReO$_4$ (Aldrich) precursors. Samples were dried under vacuum for >12 h prior to treatment in flowing dry air (Praxair, 99.99%) at 353 K overnight and then at 573 K (0.033 K s^{-1}) for 3 h. *In-situ* sulfidation of these materials was performed by flowing 5% H$_2$S/balance He (Praxair, certified mixture) at 773 K (0.05 K s^{-1}) for 2 h, under atmospheric pressure.

Encapsulated metal particles within zeolite frameworks were used to probe the effects of selective reactant exclusion based on molecular size relative to metal clusters dispersed on unconfined, mesoporous SiO$_2$ supports. Metal encapsulation within LTA (SiO$_2$/Al$_2$O$_3$ = 2) and FAU (SiO$_2$/Al$_2$O$_3$ = 2.3) frameworks were achieved during hydrothermal zeolite crystallization and post-synthetic ion-exchange, respectively. Crystallization from aluminosilicate gels in the presence of [Pt(NH$_3$)$_4$]$^{2+}$ led to successful Pt encapsulation, confirmed by selective reactions of ethene and isobutene hydrogenation and protection of ethene hydrogenation from thiophene poisons that indicated that >80% of Pt surface atoms resided within LTA crystals. Ion-exchange of FAU zeolites with aqueous Pt(NH$_3$)$_4$(NO$_3$)$_2$ solutions led to successful metal encapsulation, following previously reported protocols. These samples were treated in 9% H$_2$/He (Praxair, certified mixture) at 673 K (0.033 K s^{-1}) for 1 h, followed by passivation in 0.5% O$_2$/He (Praxair, certified mixture) at ambient temperatures for 6 h. Detailed characterization of these materials is included in Section 4.8.1.

Catalyst samples were further mixed with SiO$_2$ (in *intrapellet* dilutions) to avoid concentration gradients, pressed, and then sieved to retain aggregates of different size ranges (0.16 mm average diameter). These aggregates were then physically mixed (in *interpellet* dilutions) with quartz (Fluka, acid purified), of similar pellet size to avoid heat corruptions across catalyst beds during reaction. Similar types of dilutions (*intrapellet* and *interpellet*) were performed between samples and γ-Al$_2$O$_3$ (Sasol, SBa-200, 192 m^2 g^{-1}), previously treated under dry air at 673 K (0.033 K s^{-1}) for at least 3 h, over a range of γ-Al$_2$O$_3$-to-metal ratios, defined as β (m^2 γ-Al$_2$O$_3$ (g-atom surface metal) $^{-1}$), to study bifunctional catalysis. The consequences of

mixing intimacy and site proximity were probed by mixing of different sized pellet aggregates within interpellet dilutions (0.10 to 0.16 mm average diameters) and through intimate mixtures within intrapellet dilutions.

Fractions of accessible metal surfaces were determined via H_2 chemisorption for catalysts (i.e Ru, Pt) whose bulk properties remained metallic during HDS reactions, as reported previously [44,45]. Chemisorption uptakes were determined using an Autosorb-1 titration apparatus (Quantachrome) on samples pretreated *in-situ* to 673 K (0.083 K s^{-1}) in H_2 (Praxair 99.999%, 0.2 cm^3 s^{-1} g^{-1}) for 1 h and evacuated for 1 h prior to cooling to analysis temperature (313 K) under vacuum. Uptake stoichiometries of 1:1 H-atom to surface metal atom ratios were assumed in calculating surface dispersion from measuring irreversibly (i.e. strong) bound, dissociated hydrogen, measured from pressure differentials as a result of H_2 uptakes over a range of exposure to H_2 pressure (6-120 kPa). Particle sizes are estimated from dispersion values, assuming hemispherical clusters and corresponding bulk metal densities, and are reported in Table 4.1 (column 1). As a result of the layered morphologies of ReS_x, the fraction of exposed surfaces cannot be measured from chemisorption uptakes, whose values are sensitive to pretreatment conditions prior to measurement and thus do not reflect true surface dispersions (see Section 2.3.2). The number of exposed sites are also ambiguous to measure from transmission electron micrographs (TEM); thus, we assumed full dispersion (i.e. 1.0) in order to report consistent, lower-bound estimate of rates in this study. Both characterization probes and kinetic evidence on ReS_x/SiO_2 (Chapter Two) have suggested structural stability during HDS catalysis for over 100 h of reaction time.

4.2.2   Reaction rate measurements and computational methods

HDS rates were measured on packed beds that contained intrapellet mixtures (in SiO_2 or in γ-Al_2O_3) within interpellet mixtures (with quartz or with γ-Al_2O_3). These catalyst beds were loaded into stainless steel, tubular reactors in plug flow configurations. Prior to rate measurements, catalysts were treated in pure H_2 (Praxair, 99.999%) to 673 K (0.033 K s^{-1}) for 1 h or 573 K (0.025 K s^{-1}) for 2 h, except in the case of ReS_x materials, where samples were subjected to an *in-situ* sulfidation treatment (in 5% H_2S/He) at 773 K (0.05 K s^{-1}) for 2 h. After these treatments, inlet gases were metered with mass flow controllers (Parker, Series 201) and the reactor unit was pressurized with a back pressure regulator (Mity Mite) equipped with a Teflon diaphragm (Freudenberg Oil and Gas) to desired set points. Liquid solutions of thiophene (Aldrich 99%) dissolved in n-decane (Aldrich 99+%), which served as both a solvent and internal standard, were injected with a high pressure syringe pump (Isco 500D) and volatilized upon entry into reactor lines, heated to >453 K to prevent condensation. Reactor effluents were analyzed with on-stream gas chromatography (Agilent, 6890), equipped with a methyl silicone capillary column (Agilent, HP-1, 25 m x 0.32 mm x 0.52 µm) connected to a flame ionization detector and a Porapak Q packed column (Supelco, 1.82 m x 3.18 mm) connected to a thermal conductivity detector.

Conversions were measured over a range of H_2 (1-3 MPa), thiophene (2.5-10 kPa), and H_2S (0.5-3 kPa) pressures and varied by changing the residence time while maintaining constant partial pressures. Differential reactor conditions (i.e. thiophene conversions < 15%) were maintained by adjusting residence times and catalyst loading amounts. All reported turnover

rates, including those diluted with γ-Al$_2$O$_3$, were normalized per surface g-atom of metal, based on measured dispersion values from chemisorption uptakes, except ReS$_x$, for which rates were normalized per total g-atom of Re.

Computational methods were used to probe thermodynamic equilibria of partially-saturated thiophene molecules and radicals in order to evaluate their equilibrium gas phase concentrations under catalytic conditions. Calculations were performed using Gaussian [48] at coupled cluster single and double excitation (CCSD) level of theory [49] and aug-cc-pvDZ basis sets for all atoms. Convergence conditions for energies and forces on atoms were $< 1 \times 10^{-6}$ Ha and $< 4.6 \times 10^{-3}$ Ha/bohr, respectively. Vibrational frequencies were calculated at these settings and used to estimate enthalpies and entropies at 573 K, 3.0 MPa H$_2$, and 2.5 kPa thiophene.

4.3 Results and Discussions

4.3.1 *Thiophene HDS rates on Pt/SiO$_2$ and its mixtures with γ-Al$_2$O$_3$*

Thiophene HDS has been studied extensively on SiO$_2$-supported Ru [45], Pt [44], and Re/ReS$_x$ (Chapters Two and Three) systems. Non-reducible support materials (e.g. SiO$_2$, Al$_2$O$_3$) facilitate the formation of well-dispersed metal clusters during synthesis, while avoiding any purported electronic effects derived from metal-support interactions. Their seemingly "inert" nature is evidenced by negligible HDS reactivity when they alone are exposed to relevant reaction conditions that otherwise lead to appreciable rates in the presence of transition metal catalysts.

Intrapellet dilutions of catalysts with SiO$_2$ (1-9 SiO$_2$/catalyst, by mass) and interpellet dilutions of those catalyst pellets with quartz (200-400 quartz/catalyst, by mass) did not lead to any significant differences in measured rates, confirming the absence of heat or transport effects and indicating that the addition of SiO$_2$ and quartz does not enhance (via any spillover-mediated pathways) or inhibit (via catalyst poisoning by residual "impurities" present on diluents) HDS rates. In contrast, mixtures of the same catalyst diluted instead with γ-Al$_2$O$_3$ led to measurable enhancements in the rate of tetrahydrothiophene (THT) formation (Fig. 4.1) at dilution ratios equivalent and lower than those with SiO$_2$ and quartz, respectively (1-9 γ-Al$_2$O$_3$/catalyst intrapellet dilutions and 9-100 γ-Al$_2$O$_3$/catalyst interpellet dilutions). We define a mixing parameter, β (m^2 γ-Al$_2$O$_3$ (g-atom surface metal)$^{-1}$), and observe an effect of mixing preparation (i.e. intrapellet and interpellet dilutions) on the magnitude of spillover-mediated rates at constant β; these enhancements also depend on the distance between the two functions (measured by aggregate radius, R, within interpellet dilutions) at constant values of β. Rates increase (e.g. 1.4 to 2.9 mol (g-atom Pt$_s$ s)$^{-1}$ at β =2.5 $\times$ 10^8 m^2 γ-Al$_2$O$_3$ (g-atom Pt$_s$)$^{-1}$ and 1.9 to 2.1 mol (g-atom Pt$_s$ s)$^{-1}$ at 28 $\times$ 10^8 m^2 γ-Al$_2$O$_3$ (g-atom Pt$_s$)$^{-1}$) with a decrease in the interfunctional distance, R (50 to <10 μm and 80 to 50 μm, respectively), measured from the radius of the pellets (interpellet dilution) or estimated by powder crystallite sizes (intrapellet dilution), thus implicating the importance of site proximity in facilitating spillover-mediated routes.

The addition of γ-Al$_2$O$_3$ did not lead to products that were different from those formed on monofunctional (i.e Pt/SiO$_2$) systems [50] (Scheme 4.1), but instead led to specific enhancements of the hydrogenation product, tetrahydrothiophene (THT) at all H$_2$S/H$_2$ ratios
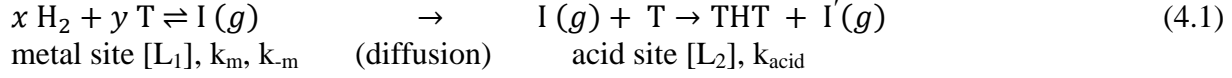
(Fig. 4.2); butene/butane formation rates remained constant, as a result of slow secondary THT desulfurization exhibited on Pt catalysts as shown in Chapter Three (Fig. 3.9). Increases in THT formation rates, at β values that gave the maximum enhancements in Figure 4.1 (i.e. 2.5 x 10^8 m^2 γ-Al$_2$O$_3$ (g-atom Pt$_s$)$^{-1}$), were equally sensitive to S-chemical potentials (set by H$_2$S/H$_2$ ratio) as monofunctional rates. Thus, ratios of THT formation rates on γ-Al$_2$O$_3$-diluted (i.e. bifunctional rates, $r_{bif,THT}$) and on SiO$_2$-diluted ($r_{metal,THT}$) catalysts were constant (~1.8, Fig. 4.2, inset) across the range of H$_2$S/H$_2$ ratios, indicating that spillover-mediated pathways can *sense* the number of HDS sites that remain accessible at a given sulfur coverage. Such behaviors contradict proposed spillover mechanisms that involve the diffusion of atomic H-species because dissociation of H$_2$ remains equilibrated under these HDS conditions and at higher S-chemical potentials (3.3 x 10^{-4} H$_2$S/H$_2$) [44]. If spillover were facilitated by the movement of atomic H-species, then $r_{bif,THT}$/$r_{metal,THT}$ ratio should have increased with increasing H$_2$S/H$_2$ because constant surface concentrations of H-species would have led to similar H-transfer rates (i.e. $r_{bif,THT}$) at a given H$_2$ pressure, assuming negligible changes in the diffusivity of atomic H-species with varying H$_2$S pressure (0.03 to 0.06 kPa). Spillover-mediated rates that decrease with increasing S-coverages on metal surfaces (that equilibrate H$_2$ dissociation), therefore, dispel conventional proposals of surface or gas phase diffusion of atomic H·, H$^+$, or H$^-$ species; such H-transport would pose formidable barriers on the order of M-H bond energies (250-260 kJ mol^{-1}, M=Pt [51]) because both SiO$_2$ and γ-Al$_2$O$_3$ surfaces lack H-binding sites, as expected from their closed (valence) shell. While defects on insulating supports could, in principal, provide binding sites of intermediate adsorption energies, an interconnected network of these defects would have to extend over molecular distances in order to justify surface-diffusion of H· or (H$^+$-e$^-$) pairs as a plausible mechanism.

4.3.2 *Spillover pathways of active hydrogen species*

Bifunctional enhancements in hydrogenation rates are widely reported [1-6] and unequivocally require the involvement of H-species. The surfaces of secondary functions (e.g. γ-Al$_2$O$_3$) cannot themselves dissociate H$_2$ and consequently exhibit low hydrogenating ability; thus, the functions known to activate H$_2$ (most often a noble metal) are implicated as the source of hydrogen within bifunctional systems. Acid functions can act instead as binding sites for olefinic or aromatic molecules such as thiophene, which can adsorb on Brønsted [52,53] or Lewis [54,55] acid sites and become an acceptor of H-species (by undergoing hydrogenation). While such cascading effects are chemically reasonable, the mechanism by which these H-carriers are transported to unsaturated molecules remain a subject of active debate.

As we briefly described in Section 4.3.1, mechanisms that implicate atomic-H transport for spillover are kinetically inconsistent with thermodynamically-controlled, equilibrated formation of H-species at relevant HDS conditions [44], which should have led to constant spillover-mediated rates at a given H$_2$ pressure. Instead, spillover-mediated rates exhibited similar inhibition as monofunctional rates with increasing H$_2$S/H$_2$ ratio (Fig. 4.2), suggesting the involvement of a H-carrying species whose formation is kinetically-limited by the same HDS surfaces that limit monofunctional reactions. These H-carriers must also form from reactions between surface thiophene and hydrogen species only, without any positive contributions from H$_2$S or H$_2$S-derived species, which would have otherwise reduced the sensitivity of spillover-mediated rates to H$_2$S/H$_2$ ratio, relative to that of monofunctional rates. We propose, therefore,

that spillover (Scheme 4.2) involves a molecular H-carrier, I, formed on metal HDS sites, L_1, that subsequently diffuses in the gas phase to thiophene molecules bound on acid (γ-Al_2O_3) sites, L_2, and undergoes H-transfer, as described by the following expression,

$$x\,H_2 + y\,T \rightleftharpoons I\,(g) \qquad \rightarrow \qquad I\,(g) + T \rightarrow THT + I'(g) \qquad\qquad (4.1)$$

metal site $[L_1]$, k_m, k_{-m} (diffusion)   acid site $[L_2]$, k_{acid}

, where T and THT represents thiophene and tetrahydrothiophene, respectively, k_m and k_{-m} are rate constants for the forward and reverse steps on metal sites, and k_{acid} is the rate constant for the irreversible hydrogenation reaction step on acid sites.

Based on this chemical path, the rate of the spillover-mediated pathway, r_{acid}, can be described as,

$$r_{acid} = k_{acid} \cdot (I) \cdot K_{T,acid}(T) \cdot \left(1 + K_{T,acid}(T)\right)^{-1} \cdot [L_2] \qquad\qquad (4.2)$$

, where $K_{T,acid}$ represents the equilibrium constant for thiophene adsorption on L_2.

The major products of reaction are THT and C_4, but at certain conditions, low concentrations of dihydrothiophene (DHT) were detected [44]. The absence of any appreciable concentrations of other species (within analytical detection limits) suggest that H-carriers, if they exist, are consumed at rates commensurate to those of their formation, allowing us to apply the pseudo-steady-state hypothesis (PSSH) on the intermediate, I, whose concentration can be described,

$$(I) = \frac{k_m\left[K_{H_2}^{0.5}(H_2)\right]^x \left[K_{T,metal}(T)\right]^y (MASI)^{-2}\cdot[L_1]}{k_{-m}\cdot(MASI)^{-2}\cdot[L_1] \;+\; k_{acid}\cdot K_{T,acid}(T)\cdot\left(1+K_{T,acid}(T)\right)^{-1}\cdot[L_2]} \qquad\qquad (4.3)$$

, where $K_{T,metal}$ represents the equilibrium constant for thiophene adsorption on metal sites and (MASI) (Eq. 4.4) reflects a summation of most abundant surface intermediates on metal functions (L_1), which is detailed in Chapter Three (Section 3.3.2),

$$(MASI) = \left(1 + \gamma(H_2)^{0.5} + \delta(T) + \epsilon\frac{(H_2S)}{(H_2)}\right) = \frac{1}{(*)}\cdot\left((*) + (H*) + (T*) + (S*)\right) \qquad\qquad (4.4)$$

, where (*), (H*), (T*), and (S*) represent vacant site, H-atom species, thiophene species, and S-atom species, respectively, and γ, δ, ϵ represent equilibrium constants associated to the equilibrated formation of those surface species (Chapter Three, Scheme 3.1).

Substitution of (I) (Eq. 4.3) into spillover-mediated rate equation (Eq. 4.2) yields,

$$r_{acid} = \frac{k_{acid}\cdot k_m\left[K_{H_2}^{0.5}(H_2)\right]^x \left[K_{T,metal}(T)\right]^y (MASI)^{-2}\cdot K_{T,acid}(T)\cdot\left(1+K_{T,acid}(T)\right)^{-1}\cdot[L_1]\cdot[L_2]}{k_{-m}\cdot(MASI)^{-2}\cdot[L_1] \;+\; k_{acid}\cdot K_{T,acid}(T)\cdot\left(1+K_{T,acid}(T)\right)^{-1}\cdot[L_2]} \qquad\qquad (4.5)$$

Reported turnover rates are normalized per metal site ($[L_1]$), thus, after substituting in the mixing ratio, $\beta = [L_2]/[L_1]$, we can express spillover-mediated rates as,

$$\frac{r_{acid}}{[L_1]} = \frac{k_{acid} \cdot k_m \left[K_{H_2}^{0.5}(H_2)\right]^x \left[K_{T,metal}(T)\right]^y (MASI)^{-2} \cdot K_{T,acid}(T) \cdot \left(1 + K_{T,acid}(T)\right)^{-1} \cdot \beta}{k_{-m} \cdot (MASI)^{-2} + k_{acid} \cdot K_{T,acid}(T) \cdot \left(1 + K_{T,acid}(T)\right)^{-1} \cdot \beta} \tag{4.6}$$

The functional form of this rate expression can describe the observed kinetic behaviors with β (Fig. 4.3) because it predicts enhancements will increase proportionally with acid-to-metal ratios before reaching an asymptotic limit. Similar asymptotic features persist at different S-chemical potentials and on different Pt/SiO_2 samples (and cluster sizes), despite differences in the magnitude of their rates. At low β values, reaction rates are limited by the concentration of acid sites (Eq. 4.7), and formation of the H-carrier, I, is equilibrated (i.e. $k_m/k_{-m}=K_m$, equilibrium constant).

$$\frac{r_{acid}}{[L_1]} = k_{acid} \cdot \frac{k_m}{k_{-m}} \cdot \left[K_{H_2}^{0.5}(H_2)\right]^x \left[K_{T,metal}(T)\right]^y \cdot K_{T,acid}(T) \cdot \left(1 + K_{T,acid}(T)\right)^{-1} \cdot \beta \tag{4.7}$$

Rates that are independent of β (i.e. asymptote) reflect a regime wherein H-carriers are scavenged by nearby acid sites, causing rate enhancements to become independent of acid site density (i.e. at high β) and, instead, limited by the H-carrier formation kinetics on the metal function (Eq. 4.8).

$$\frac{r_{acid}}{[L_1]} = k_m \left[K_{H_2}^{0.5}(H_2)\right]^x \left[K_{T,metal}(T)\right]^y (MASI)^{-2} \tag{4.8}$$

Asymptotic limits of r_{acid} are reached (Fig. 4.3) at higher β values (0.6 x 10^8 m^2 γ-Al_2O_3 (g-atom Pt_s)$^{-1}$) under conditions without inlet H_2S feed compared to those with appreciable inlet H_2S/H_2 ratios (≥0.3 x 10^{-3}, β < 0.3 x 10^8 m^2 γ-Al_2O_3 (g-atom Pt_s)$^{-1}$). These behaviors are consistent with the spillover-mediated rate expression (Eq. 4.6), as higher S-chemical potentials (i.e. H_2S/H_2) increase the value of (MASI) (Eq. 4.4) and concomitantly decrease the first term of the denominator of Equation 4.6 (i.e. $k_{-m}(MASI)^{-2}$). The increase in sulfur coverage decreases the number of accessible HDS sites, $[L_1]$, and effectively increases the acid-to-(accessible) metal ratio, shifting the metal-limiting regime to dominate at lower physical β values.

Maximum enhancement factors, defined as the ratio of asymptotic rates (i.e. at high β) measured on γ-Al_2O_3-diluted samples (bifunctional) to rates measured on SiO_2-diluted (monofunctional) samples, appear similar (ranging from 1.8 to 2.4) across different Pt samples and S-chemical potentials, casting doubt on the role of γ-Al_2O_3 as an impurity trapping agent [28,33] in our present study. Significant catalyst deactivation during these experiments was not observed, and negative effects from increasing SiO_2 (Cabosil)/catalyst dilution ratios were absent; thus, impurities (at β =0) must originate from the conditions of synthesis. If we assume that these impurities exist, their removal by γ-Al_2O_3 trapping appears complete at high β, because rates did not further increase with increasing γ-Al_2O_3 content. Thus, the relative difference between the "clean" rates and SiO_2-diluted rates implies that impurities consistently poison half of all available metal sites, despite marked differences in catalyst synthesis preparations (Section 4.2.1 and Table 4.1), metal precursors ($Pt(NH_3)_4(NO_3)_2$ or $H_2PtCl_6 \cdot (H_2O)_6$), SiO_2 support sources (Cabosil HS-5, 310 m^2g^{-1} or Davisil Grade 646, 300 m^2 g^{-1}), and resulting Pt cluster sizes. We

avoid such pathological implications by concluding that the behaviors observed with β (Fig. 4.3) are unlikely the result of any impurity cleaning abilities attributed to γ-Al$_2$O$_3$.

4.3.3 *Effects of site proximity and diffusion of molecular H-carriers*

The upper limit in spillover-mediated rates (as a function of β) suggests that H-carriers are low in concentration because they are unable to diffuse to reactants adsorbed on more distant acid sites either as a result of their scavenging, in which the rate of their generation cannot compete with the rate of their consumption (on more proximal sites), or of transport limitations that lower their effective concentrations across even greater diffusion distances. Indeed, reaching this limiting regime depends not only on the physical ratio of acid sites to metal sites (i.e. β), but also on the intimacy of their mixing (e.g. interpellet or intrapellet), which directly influences the effective diffusion length, R, between these two domains; we estimate R by aggregate diameters (R = (pellet diameter)/2) when functions are in separate pellets (interpellet dilution) or by the size of the crystallites themselves when functions are mixed in powdered forms and pressed within a single pellet (intrapellet dilution). These diffusion lengths (or domain sizes) appear to influence the onset of maximum rate enhancement (with respect to β), reflecting the strong effects of site proximity and the involvement of reaction mediators that may be subjected to diffusional constraints.

Transport restrictions can lead to severe concentration gradients across functional domains. In our proposed spillover mechanism, such limitations (for I) are likely to be present across the acid domain, as concentrations of H-carriers are no longer supplied once they leave metal domains. These effects are accounted by including an effectiveness factor to the spillover-mediated rate expression (Eq. 4.2), η (ranging from 0 to 1), that reflects the extent to which observed rates deviate from intrinsic kinetic rates as result of diffusion control,

$$r_{acid,observed} = \eta \cdot k_{acid} \cdot (I) \cdot K_{T,acid}(T) \cdot \left(1 + K_{T,acid}(T)\right)^{-1} \cdot [L_2] \tag{4.9}$$

, and consequently,

$$\frac{r_{acid}}{[L_1]} = \frac{\eta \cdot k_{acid} \cdot k_m \left[K_{H_2}^{0.5}(H_2)\right]^x \left[K_{T,metal}(T)\right]^y (MASI)^{-2} \cdot K_{T,acid}(T) \cdot \left(1 + K_{T,acid}(T)\right)^{-1} \cdot \beta}{k_{-m} \cdot (MASI)^{-2} + \eta \cdot k_{acid} \cdot K_{T,acid}(T) \cdot \left(1 + K_{T,acid}(T)\right)^{-1} \cdot \beta} \tag{4.10}$$

, where η, derived for spherical particles, is defined,

$$\eta = \frac{1}{\phi}\left[\frac{1}{\tanh(3\phi)} - \frac{1}{3\phi}\right] \tag{4.11}$$

, where φ is the Thiele modulus, which represents the ratio of the maximum reaction rate to the maximum diffusion rate (for first-order reaction within the acid domain),

$$\phi^2 = \left(\frac{R}{3}\right)^2 \cdot \frac{\rho_{acid} S_{acid}}{D_{eff}} \cdot \frac{k_{acid} K_{T,acid}(T)}{1 + K_{T,acid}(T)} \tag{4.12}$$

, where ρ$_{acid}$, and S$_{acid}$ are the density and surface area of γ-Al$_2$O$_3$ aggregates, respectively, and D$_{eff}$ is the effective diffusivity of the H-carrier.

Several parameters in Equation 4.12 are constant at given reaction conditions, including ρ_{acid} and S_{acid}, which are physical and chemical properties of γ-Al_2O_3; D_{eff}, which is a physical property of the H-carrier and its diffusive medium; and k_{acid} and $K_{T,acid}$, which are kinetic and thermodynamic rate constants. Thus, at any particular HDS condition and catalyst loading, the Thiele modulus is only governed by the (acid) function domain size (i.e. R). Furthermore, in the limit of significant diffusion limitations (i.e. $\phi \gg 1$), the effectiveness factor becomes inversely proportional to the Thiele modulus, $\eta \sim \phi^{-1}$, which allows us to simplify Equation 4.10 to

$$\frac{r_{acid}}{[L_1]} = \frac{a \cdot R^{-1} \cdot \beta}{b \ + \ c \cdot R^{-1} \cdot \beta} \tag{4.13}$$

, where

$$a = k_{acid} \cdot k_m \left[K_{H_2}^{0.5}(H_2)\right]^x \left[K_{T,metal}(T)\right]^y (MASI)^{-2} \cdot \sqrt{k_{acid} \cdot K_{T,acid}(T) \cdot \left(1 + K_{T,acid}(T)\right)^{-1}} \cdot 3 \cdot \sqrt{\frac{D_{eff}}{\rho_{acid}S_{acid}}}$$

$$b = k_{-m} \cdot (MASI)^{-2}$$

$$c = \sqrt{k_{acid} \cdot K_{T,acid}(T) \cdot \left(1 + K_{T,acid}(T)\right)^{-1}} \cdot 3 \cdot \sqrt{\frac{D_{eff}}{\rho_{acid}S_{acid}}}$$

Decreasing domain sizes (i.e. decreasing R) serves to minimize the concentration gradients of I across acid functions, which leads to higher measured rates (Eq. 4.13). Indeed, THT formation rates increase (1.9 to 2.1 mol (g-atom Pt_s s)$^{-1}$) as pellet sizes decrease (from 2xR = 160 to 100 μm, at constant β =28 x 10^8 m^2 (g-atom Pt_s)$^{-1}$), and they increase even more significantly (1.4 to 2.9 mol (g-atom Pt_s s)$^{-1}$) when functions are mixed and pressed within the same pellet (from 2xR = 160 μm to <20 μm, at constant β =2.5 x 10^8 m^2 (g-atom Pt_s)$^{-1}$) (Fig. 4.1). The pronounced effects of reducing R (e.g. from 160 to <10 μm), which alone increased spillover-mediated rates alone (calculated by subtracting monofunctional rates) more than 20-fold (0.07 to 1.57 mol (g-atom Pt_s s)$^{-1}$ at β =2.5 x 10^8 m^2 γ-Al_2O_3 (g-atom Pt_s)$^{-1}$), support the effect that increasing proximity has toward reducing diffusion limitations. While increasing β has already been demonstrated (Fig. 4.3) as an effective method of overcoming the constraints imposed by sizeable diffusion lengths, the interplay between site ratio and domain size (i.e. β/R) is what (Eq. 4.13), in fact, determines whether bifunctional systems are under the regime wherein rates are limited by metal chemistry to form the H-carrier, I (Eq. 4.8). Thus, at sufficiently high β/R, increasing proximity (i.e. decreasing R) will not benefit spillover pathways, even though it could, in principal, continue to minimize concentration gradients within acid domains.

The asymptotic values of spillover-enhanced rates reflect their maximum limit, and increasing acid-to-metal ratios, acid-metal proximity, or the reactivity of the acid function (i.e. k_{acid}) cannot increase spillover-mediated rates at those (high) β/R values because rates are limited by metal chemistry (of H-carrier formation). This "metal-limiting" regime is validated by rates of both monofunctional (at β =0) and bifunctional systems (at β =0.2 x 10^8 and 2.3 x 10^8 m^2 γ-Al_2O_3 (g-atom Pt_s)$^{-1}$) that are similarly inhibited by H_2S/H_2 ratio (Fig. 4.4). Changes in S-chemical potentials (set by H_2S/H_2 ratio) should only affect HDS surfaces (Fig. 4.4), therefore suggesting that spillover-mediated rates must *sense* the full effect of metal surface coverages and that concentrations of I are limited by (and not equilibrated on) metal sites.

Both monofunctional and bifunctional (β =0.2 x 10^8 m^2 γ-Al_2O_3 (g-atom Pt_s)$^{-1}$) systems exhibit sublinear dependences on thiophene pressure (Fig. 4.5), consistent with both the presence

of thiophene species as abundant species on HDS surfaces and their involvement in spillover-mediated pathways. Moreover, the sensitivities toward thiophene are similar on both systems as well, even at different sulfur-coverages (i.e. H_2S/H_2 ratios), evident from ratios of bifunctional (r_{bif}) to monofunctional (r_{metal}) rates that remain constant as a function of thiophene pressure ($r_{bif}/r_{metal}\sim2.1$; Fig. 4.5, inset). Such behaviors are consistent with reactivities (of both spillover-mediated and monofunctional routes) that are controlled by the same (metal) function.

4.3.4 Identity of H-carrier, I, in spillover-mediated pathways

Our proposed mechanism requires the formation of *molecular* H-carriers from metal-catalyzed reactions of thiophene molecules with hydrogen species. These requirements can be probed by selectively excluding thiophene from metal surfaces by encapsulating metal sites within zeolite frameworks that restrict reactant access based on molecular size. We examine whether these bifunctional synergies require access of *both* hydrogen *and* thiophene to metal sites by exploiting recent efforts in the synthesis of Pt clusters, encapsulated within zeolites [46,47] that are exchanged with Na^+ to eliminate any effects from hydroxyl groups, which have been implicated in facilitating proton diffusion [2].

Pt clusters within LTA, in the absence of γ-Al_2O_3, exhibited low reactivity relative to those within FAU frameworks (Fig. 4.6), suggesting that the zeolite aperture size of the former (0.41 nm) selectively excluded thiophene molecules (0.46 nm kinetic diameter) from accessing active metal sites, while the windows of FAU (0.71 nm) permitted diffusion of reactant molecules through its cages. Pt clusters of similar sizes (1.5 and 1.4 nm within NaLTA and NaFAU, respectively) were present in both frameworks, indicating that cluster size effects cannot account for the large differences in measured HDS rates. Discrepancies in measured rates between unconfined Pt/SiO_2 clusters (2.4 nm) and Pt-NaFAU are consistent with reported particle size trends [44] and reflect the structure sensitive nature of this reaction on Pt catalysts.

Addition of γ-Al_2O_3 led to a ~2 fold increase in rates, including those on Pt-NaLTA, which derives its reactivity from small fractions of Pt residing in extra framework locations (~20%, Section 2.8.1) as a result of less than perfect encapsulation. The uninhibited diffusion of H_2 (0.29 nm kinetic diameter) through LTA apertures, and its resulting dissociation on encapsulated Pt particles, demonstrated by equilibrated H_2/D_2 exchange [44], confirm H-carriers cannot be formed from H_2 alone but require assistance (or derivation) from larger organosulfur compounds. Such findings indicate that H_2 dissociation is a necessary but *insufficient* condition to facilitate spillover phenomena, providing compelling evidence that molecular carriers are responsible for H-transport between functions that, in this case, are separated beyond physical contact, given that most Pt clusters reside within the intrazeolite locations of FAU cages (Scheme 4.3).

The molecular identity of H-carriers can be investigated via kinetic probes. Similar kinetic dependences on thiophene pressure and H_2S/H_2 ratio (Figs. 4.4 and 4.5) were observed for both monofunctional and bifunctional systems (at β values that exhibited asymptotic rate enhancements), despite differences in their absolute rates. Specific dependences on thiophene (Fig. 4.5) not only suggest that both rates (monofunctional and spillover-mediated) are limited by metal surfaces but also that a single thiophene molecule is involved in the kinetically-relevant

steps of both pathways (i.e. y=1 in Eq. 4.1), consistent with first-order thiophene dependences that also describe monofunctional HDS rates (r_{metal}, z=1, Eq. 4.14) on Pt clusters (as we detailed in Chapter Three).

$$\frac{r_{metal}}{[L_1]} = \frac{\alpha(T)(H_2)^z}{\left(1+\gamma(H_2)^{0.5}+\delta(T)+\epsilon\frac{(H_2S)}{(H_2)}\right)^2}$$

(4.14)

Kinetic rate dependences on H_2 pressure, in particular, can shed mechanistic insights on the formation of partially-hydrogenated, thiophene-derived H-carrier implicated in spillover-mediated routes. Linear H_2 dependences of rates observed on the monofunctional system (Fig. 4.7a) are consistent with the rate expression derived for thiophene HDS on Pt systems (Eq. 4.14, z=1, Chapter Three) and reflect a kinetically-relevant second H-addition step on surfaces exhibiting negligible concentrations of H* species (i.e. γ=0, Eq. 4.14). In contrast, rates exhibited sublinear dependences on H_2 pressure on catalysts mixed with γ-Al$_2$O$_3$ (intrapellet dilution, β =(0.2-2.3) x 10^8 m^2 γ-Al$_2$O$_3$ (g-atom Pt)$^{-1}$) (Fig. 4.7b), implying the presence of multiple mechanisms that involve differences in the molecularities (i.e. H-contents) of their respective kinetically-relevant transition states. Such apparent differences in the kinetic response toward H_2 pressure argue against any impurity trapping abilities of γ-Al$_2$O$_3$, without invoking different mechanisms that would have to exist on "impurity-free" metal sites. Thus, the overall H_2 dependence, assuming monofunctional reactions remain unaffected by the presence of γ-Al$_2$O$_3$, results from the sum of multiple pathways, which happen to exhibit different sensitivities to H_2 pressure, allowing us to differentiate between these separate routes; such differences in H_2 dependences persist even at different H$_2$S/H$_2$ ratios (0.3 x 10^{-3} and 1.0 x 10^{-3}, Fig. 4.7), despite commensurate inhibition of overall rates on both systems at high S-chemical potentials, as a result of increased sulfur coverages of reactive HDS metal sites.

We have already detailed compelling evidence that spillover-mediated rates are limited by metal sites, L_1 (Figs. 4.3, 4.4, and 4.5), at sufficiently high acid-to-metal ratios (i.e. intrapellet $\beta \geq$ 0.2 x 10^8 m^2 γ-Al$_2$O$_3$ (g-atom Pt$_s$)$^{-1}$). Spillover-mediated rates (r_{acid}), calculated from subtraction of monofunctional rates (i.e. SiO$_2$-diluted catalysts, r_{metal}) from bifunctional rates (i.e. γ-Al$_2$O$_3$-diluted, r_{bif}), decrease with H$_2$S/H$_2$ ratio (0.3 x 10^{-3} to 1.0 x 10^{-3}) (Fig. 4.8) at given thiophene and H_2 pressures, arguing, once again, that r_{acid} is limited by metal chemistry because equilibrated formation of I would have otherwise led to similar rates over a range of H$_2$S/H$_2$ ratios. Similar H_2 dependences persist, however, independent of H$_2$S/H$_2$ ratio, with power law fits indicating $r_{acid} \sim$(H$_2$)$^{0.45}$ and $\sim$(H$_2$)$^{0.52}$ at 0.3 x 10^{-3} and 1.0 x 10^{-3} H$_2$S/H$_2$ ratios, respectively. A kinetic half-order H_2 dependence (within errors of measurement) indicates that the barrier to form the spillover H-carrier involves a kinetically-relevant, first H-addition step (Eq. 4.8, x=0.5).

These kinetic behaviors suggest that the formation of the H-carrier is limited by the first H-addition, without necessarily implicating monohydrothiophene (MHT) radicals as the species themselves. Their possibility as the responsible intermediate, however, remains attractive, in light of previous HDS studies on monofunctional Pt clusters (Chapter Three) that indicate MHT* species are equilibrated on the surface (Scheme 4.4b), prior to a subsequent kinetically-relevant H-addition step. The requisite *unstable* nature of I does suggest that either MHT or trihydrothiophene (TrHT) radicals are the most likely candidates, with their calculated (CCSD) equilibrium pressures well below the limit of analytical detection at typical HDS conditions (e.g.

3.0 MPa H_2, 2.5 kPa thiophene). Negligible changes in rate occurred when the pressure of the internal standard, n-decane, was varied or when dimethylcyclohexane was introduced at the feed, suggesting that stable, saturated alkanes and cycloalkanes are not hydrogen donors (Section 4.8.2).

Low equilibrium concentrations alone are insufficient to implicate radical (i.e. MHT and TrHT) species as the H-carrier; they must also exhibit some degree of thermodynamic stability capable of maintaining sufficient gas phase concentrations in order to facilitate enough collisions with $\gamma\text{-}Al_2O_3$ surfaces to justify the magnitude of spillover-mediated rates observed. We have calculated gas phase enthalpies and free energies using CCSD methods [49] to accurately predict thermodynamic equilibria (Table 4.2) between partially-hydrogenated thiophene species and starting reactants (thiophene and H_2). The resulting values indicate radical species (i.e. MHT, TrHT) exhibit much higher Gibbs free energies (77 to 133 kJ mol^{-1}) relative to the stable (i.e. DHT, THT) species (-8 to 11 kJ mol^{-1}). Within MHT radicals, the delocalization of an unpaired electron (i.e. 2-monohydrothiophene, Scheme 4.5) across double bonds (i.e. resonance) appears to play an effective role in increasing its stability (Gibbs energy: 87 kJ mol^{-1}, Table 4.2) relative to that of its isomer (i.e. 3-monohydrothiophene, Gibbs energy: 133 kJ mol^{-1}, Table 4.2), which cannot delocalize its electron. Relative stabilizations between TrHT isomers are more modest because both molecules lack the ability to resonate through double bonds; the radical with its unpaired electron α to the sulfur heteroatom (i.e. 2,3,4-trihydrothiophene, Gibbs energy: 77 kJ mol^{-1}) is more stable compared the isomer with the electron at the β position (i.e. 2,3,5-trihydrothiophene, Gibbs energy: 96 kJ mol^{-1}).

Equilibrium conversions were calculated at typical reaction conditions (573 K, 3.0 MPa H_2, 2.5 kPa thiophene), based on computationally-calculated equilibrium constants, and subsequently used to estimate equilibrium pressures of partially-saturated thiophene molecules (Table 4.2, column 4), based on the following equilibrated reaction,

$$\frac{i}{2} H_2(g) + T\ (g) \rightleftharpoons H_iT\ (g) \tag{4.15}$$

, where i represents the number of hydrogen species added to thiophene.

As expected, stable species (i.e. DHT and THT) exhibit high equilibrium concentrations (1.9 and 2.5 kPa, respectively), indicating 75 to 100% conversion under thermodynamically-controlled conditions. However, the most stable radical species, 2-monohydrothiophene and 2,3,4-trihydrothiophene species, exhibited maximum concentrations of 1.6 x 10^{-4} and 3.7 x 10^{-2} Pa, respectively.

We can probe whether these concentrations are sufficient to facilitate spillover-mediated pathways by estimating their collision frequencies (F) with surfaces (Table 4.2, column 5), based on kinetic theory of gases,

$$F = \frac{P}{\sqrt{2 \cdot \pi \cdot m \cdot k_B \cdot T}} \tag{4.16}$$

, where P and m are the pressure and mass of the colliding molecule, respectively, k_B is the Boltzmann constant, and T is the temperature of the system.

While the calculated collision frequency of TrHT radicals (2.3×10^{-5} mol m^{-2} s^{-1}) is greater than that of MHT radicals (1.0×10^{-7} mol m^{-2} s^{-1}), it is unlikely that TrHT is equilibrated with thiophene given measurable kinetic barriers to form DHT exist, based on our kinetic data (Eq. 4.14, z=1, Chapter Three). We probe whether MHT concentrations are sufficient to account for the observed spillover effects by examining whether the collision frequency, which serves as an estimate of the rate of supplying H-carriers to γ-Al$_2$O$_3$ surfaces, is greater than measured spillover-mediated reaction rates. These rates, which must be normalized by the $[L_2]$ surface, can only be estimated under regimes "limited" by the acid (i.e. at low β, $r_{acid} = c\beta$, Eq. 4.7),

$$\frac{r_{acid}}{[L_1] \cdot \beta} = \frac{r_{acid}}{[L_2]} = c \ (constant) \tag{4.17}$$

We can measure rates that exhibit first-order β dependence on Pt clusters, at low β values (<0.6 m^2 γ-Al$_2$O$_3$ (mol Pt$_s$)$^{-1}$) under conditions without inlet H$_2$S (Fig. 4.3); this leads to a normalized rate of 2.3×10^{-8} mol (m^2 γ-Al$_2$O$_3$ s)$^{-1}$; such kinetic rates are nearly a magnitude lower than the collision frequencies calculated for MHT species, suggesting their plausible identity as molecular H-carriers.

We implicate MHT as the sole H-carrier identity because any involvement of radical species (i.e. TrHT) formed after the kinetically-relevant monofunctional H-addition step cannot lead to observable rate enhancement; the formation rate of a TrHT-derived H-carrier would be set by the kinetically-relevant step along the reaction coordinate of sequential hydrogenations in Horiuti-Polanyi-type mechanisms [56]. Even if these more highly saturated species (i.e. DHT, TrHT, TrHT) could carry active H-species to γ-Al$_2$O$_3$ sites, measured rates would become insensitive to whether a metal or acid function completes the turnover because reactants must (first) cross the reaction barrier that limits monofunctional product formation.

The nature of H-carrier identity and requirements for its formation are demonstrated by probing the presence or absence of spillover-mediated enhancements on hydrogenation reactions that either include or preclude the formation of H-carrier species prior to the kinetically-relevant step of monofunctional reactions. Mechanistic features of HDS on Ru (Chapter Three) resemble those observed on Pt; they both exhibit a kinetically-relevant second H-addition step (i.e. z = 1, Eq. 4.14). In contrast, the first hydrogen addition controls HDS reactivity on ReS$_x$ nanostructures (i.e. z=0.5, Eq. 4.14, Chapter Two), thereby preventing the possibility of forming partially-hydrogenated species via routes that can avoid crossing monofunctional energy barriers (Scheme 4.4a).

The effects of intrapellet γ-Al$_2$O$_3$ dilutions for different catalysts must be evaluated at commensurate mixing ratios that compensate for the dissimilarities in HDS reactivity of different metal sites, $[L_1]$. We can account for differences in intrinsic metal activity by defining a corrected mixing ratio, β' (Eq. 4.18), which normalizes β by monofunctional turnover rates (measured at $\beta =0$) to recognize that what actually matters in these comparisons is the relative chemical reactivities, not their relative physical densities, of the two functions.

$$\beta' = \beta \cdot \frac{1}{r_{metal}/[L_1]} = \frac{[L_2]}{[L_1]} \cdot \frac{[L_1]}{r_{metal}} = \frac{[L_2]}{r_{metal}} \ [=]m^2 \ Al_2O_3 \ (mol \ thiophene \ s^{-1})^{-1} \tag{4.18}$$

Indeed, Ru/SiO$_2$ catalysts (Fig. 4.9), which share similar monofunctional HDS elementary steps as Pt/SiO$_2$, exhibited measurable rate enhancements (0.09 to 0.2 mol (g-atom Ru$_s$ s)$^{-1}$) when mixed with γ-Al$_2$O$_3$ (intrapellet dilutions), over the same range of β′ as that for Pt/SiO$_2$. Such rate enhancements, however, are not observed on ReS$_x$, over a range of comparable intrapellet dilutions (β′= 0 to 15 x 10^8 m^2 γ-Al$_2$O$_3$ ((mol thiophene) s^{-1})$^{-1}$) because thiophene enters a pool of partially-hydrogenated intermediates after a kinetically-relevant first H-addition step. The absence of measurable enhancement persists even at lower H$_2$ pressures (i.e. 1 MPa H$_2$, Fig. 4.9, open circles), conditions at which enhancement factors were found to be even more pronounced on Pt/SiO$_2$ (Fig. 4.7, enhancement factors of 2.7 and 2.1-2.2 at 1 MPa and 3 MPa H$_2$, respectively) as a result of increased selectivity toward spillover-mediated pathways at lower H$_2$ pressures. These observations suggest that MHT radicals are the H-carriers, whose role in spillover pathways is productive only in systems wherein their formations are either independent of or occur before the kinetically-relevant step along the monofunctional reaction coordinate (Scheme 4.4).

4.4   Conclusions

We have presented detailed descriptions of the nature of hydrogen spillover mechanisms and derived kinetic-transport models for hydrogenation reactions that occur at locations beyond molecular distances from functions that can form active H-species. These proposals are consistent with kinetic and computational evidence, implicating the formation of a reactant-derived, molecular H-carrier species on metal sites. The observed effects of proximity are consistent with the need of such species, unstable and low in concentration, to diffuse to acid sites; their effective concentrations are lowered as diffusion distances between the two functions become larger, leading to weaker promotional effects. Synergies between these two functions are maximized when transport constraints are minimized and spillover-mediated routes become limited by the metal ability to catalyze the formation of these H-carriers, consistent with rates that increase with γ-Al$_2$O$_3$-to-catalyst ratios before reaching constant (asymptotic) values. We can suppress the concentrations of these H-carriers by encapsulating metal clusters within zeolite frameworks (i.e. Pt-NaLTA) that prevent the access of thiophene molecules while allowing H$_2$ molecules to enter and egress through their apertures. Such interventions prevent the promoting effect of γ-Al$_2$O$_3$ in these zeolite systems, suggesting the involvement of organosulfur-derived molecular carriers (that require access of reactants to metal sites) and challenging previous claims over the role of atomic H-species in spillover mechanisms.

The absence of observed bifunctional promotion in rates on catalysts (e.g. ReS$_x$/SiO$_2$) whose monofunctional HDS rates are limited by the first H-addition is consistent with provisions that hydrogen must be supplied to molecular reactants (i.e. thiophene) in steps prior to the kinetically-relevant step in monofunctional reactions, in order to form H-carriers that can facilitate productive (i.e. rate enhancing) spillover events. These requirements are further supported by kinetic pressure dependences of spillover-mediated rates on Pt that suggest the formation of H-carriers is limited by a first H-addition step, which is a plausible condition given that the second hydrogen addition step is kinetically-relevant on Pt surfaces. Such open-shell, singly-hydrogenated thiophene species (monohydrothiophene) can exist at reasonable gas phase concentrations, as predicted by computational methods, and subsequently transport active H-species to reactants adsorbed on γ-Al$_2$O$_3$ functions via H-transfer events.

4.5   Acknowledgements

4.6 Tables, Figures, and Schemes

4.6.1 Tables

Table 4.1: Synthesis treatment conditions for SiO$_2$-supported Ru, Pt, and ReS$_x$ catalysts.

Catalyst <particle size[a]>	SiO$_2$ source	Aqueous precursor	Dry air treatment[c] temp.(K)/time(h)/ramp(K s^{-1})	H$_2$ treatment[e] temp.(K)/ time(h)/ ramp(K s^{-1})
Ru/SiO$_2$ <1.4 nm>	Cabosil HS-5	Ru(NH$_3$)$_6$Cl$_3$	--[d]	673 / 1 / 0.033
Pt/SiO$_2$ <2.4 nm>	Cabosil HS-5	Pt(NH$_3$)$_4$(NO$_3$)$_2$	773 / 5 / 0.05	673 / 1 / 0.033
Pt/SiO$_2$ <5.4 nm>	Davisil 646	H$_2$PtCl$_6$·(H$_2$O)$_6$	923 / 5 / 0.033	573 / 2 / 0.033
ReS$_x$/SiO$_2$[b]	Cabosil HS-5	NH$_4$ReO$_4$	573 / 3 / 0.033	--[f]

[a] Particle sizes determined from chemisorption uptake experiments, assuming hemispherical clusters and the bulk density of the metal.
[b] Particle sizes were not measurable on layered morphologies, full dispersion (100%) assumed for rate normalization.
[c] Flowing dry air (Praxair, 99.99%), 1.0 cm^3 g^{-1} s^{-1}.
[d] Ru samples were directly treated in H$_2$ after drying steps.
[e] 9% H$_2$/He, Praxair, 1.67 cm^3 g^{-1} s^{-1}. All H$_2$ treatments were followed by a passivation step in 0.1-1.0% O$_2$/He (Praxair), 0.05-1.0 cm^3 g^{-1} s^{-1} at ambient temperature for 2-6 h.
[f] Samples were not treated in H$_2$ after high temperature treatments in air. Instead, direct sulfidation of samples occurred *in-situ* at 773 K (0.05 K s^{-1}) for 2 h in flowing 5% H$_2$S/He (Praxair, certified mixture), prior to catalytic reactions.

Table 4.2: Calculated enthalpies and free energies from coupled cluster single and double excitation (CCSD) methods and derived equilibrium pressures and collision frequencies for partially-hydrogenated thiophene molecules at typical reaction conditions.

(Partially) hydrogenated thiophene molecule[a]	Enthalpy[c] (kJ mol^{-1})	Gibbs free energy[c] (kJ mol^{-1})	Equilibrium pressure[d] (Pa)	Collision frequency[e] (mol m^{-2} s^{-1})
2-monohydrothiophene[b]	58.8	87.0	1.6×10^{-4}	1.0×10^{-7}
3-monohydrothiophene[b]	99.4	133.4	9.5×10^{-9}	6.0×10^{-12}
2,3-dihydrothiophene	-63.0	10.9	1.9×10^{3}	1.2
2,5-dihydrothiophene	-64.5	5.8	2.2×10^{3}	1.4
2,3,4-trihydrothiophene[b]	-27.1	77.3	3.7×10^{-2}	2.3×10^{-5}
2,3,5-trihydrothiophene[b]	-5.1	95.7	7.8×10^{-4}	4.9×10^{-7}
Tetrahydrothiophene	-177.5	-8.4	2.5×10^{3}	1.5

[a] Corresponding structures of partially-hydrogenated molecules are depicted in Scheme 4.5.
[b] Open shell, radical species.
[c] Calculated at 573 K, 1 bar pressure based on the equilibrated gas phase reactions of thiophene (T) hydrogenation, referenced to gas phase thiophene based on the following stoichiometric balance (Deshlahra, Prashant. *unpublished results*),

$$T + \frac{x}{2} H_2 \leftrightarrow H_x T \, .$$
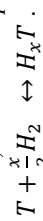
[d] Equilibrium pressures based on equilibrium conversion of 2.5 kPa thiophene, 3 MPa H$_2$, at 573 K.
[e] Collision frequency with surface based on kinetic theory of gases at 573 K and equilibrium pressures of the corresponding colliding molecule.
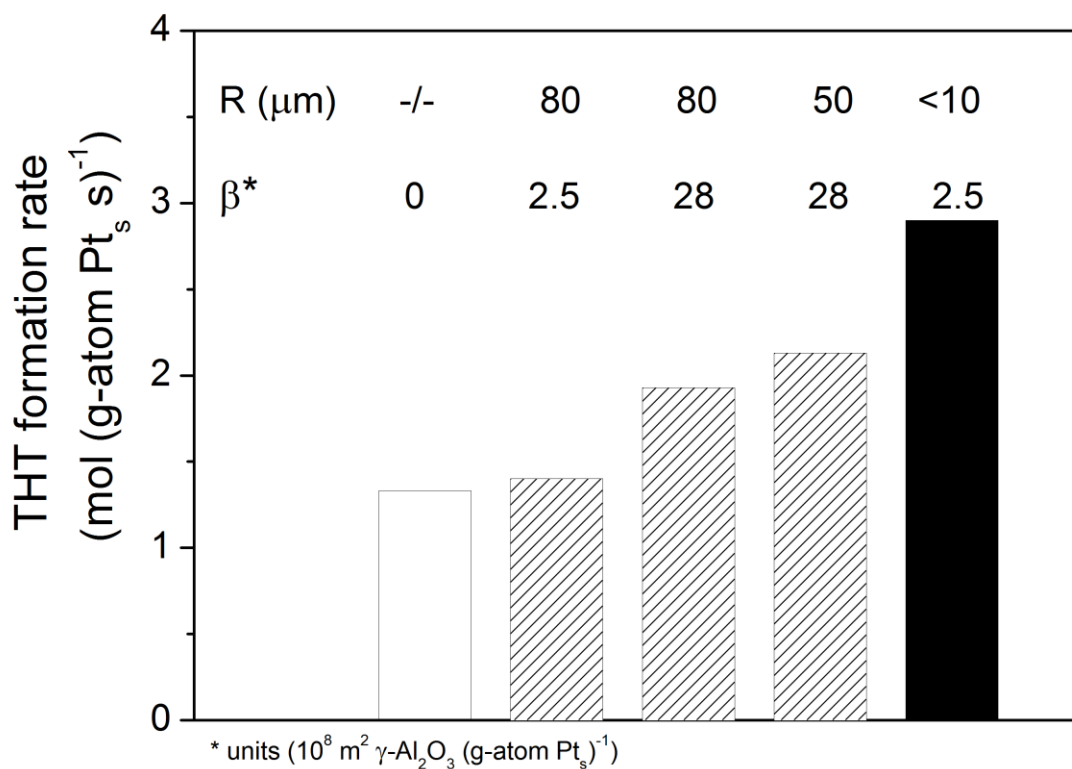
Figure 4.1: Formation rate of tetrahydrothiophene (THT) at 3 MPa H_2, 2.5 kPa thiophene, 573 K on Pt/SiO_2 diluted with γ-Al_2O_3 at various mixing ratios, β (10^8 m^2 γ-Al_2O_3 (g-atom Pt_s)$^{-1}$). Proximity between metal and acid functions can be described by the characteristic diffusion length, R (μm), which represents the distance between the two functions, estimated by the diameters of pellet aggregates within interpellet dilutions or of powder crystallite sizes within intrapellet dilutions. Bar style denotes the mixing technique with γ-Al_2O_3: undiluted (unshaded), interpellet dilution (hatched), and intrapellet dilution (shaded).
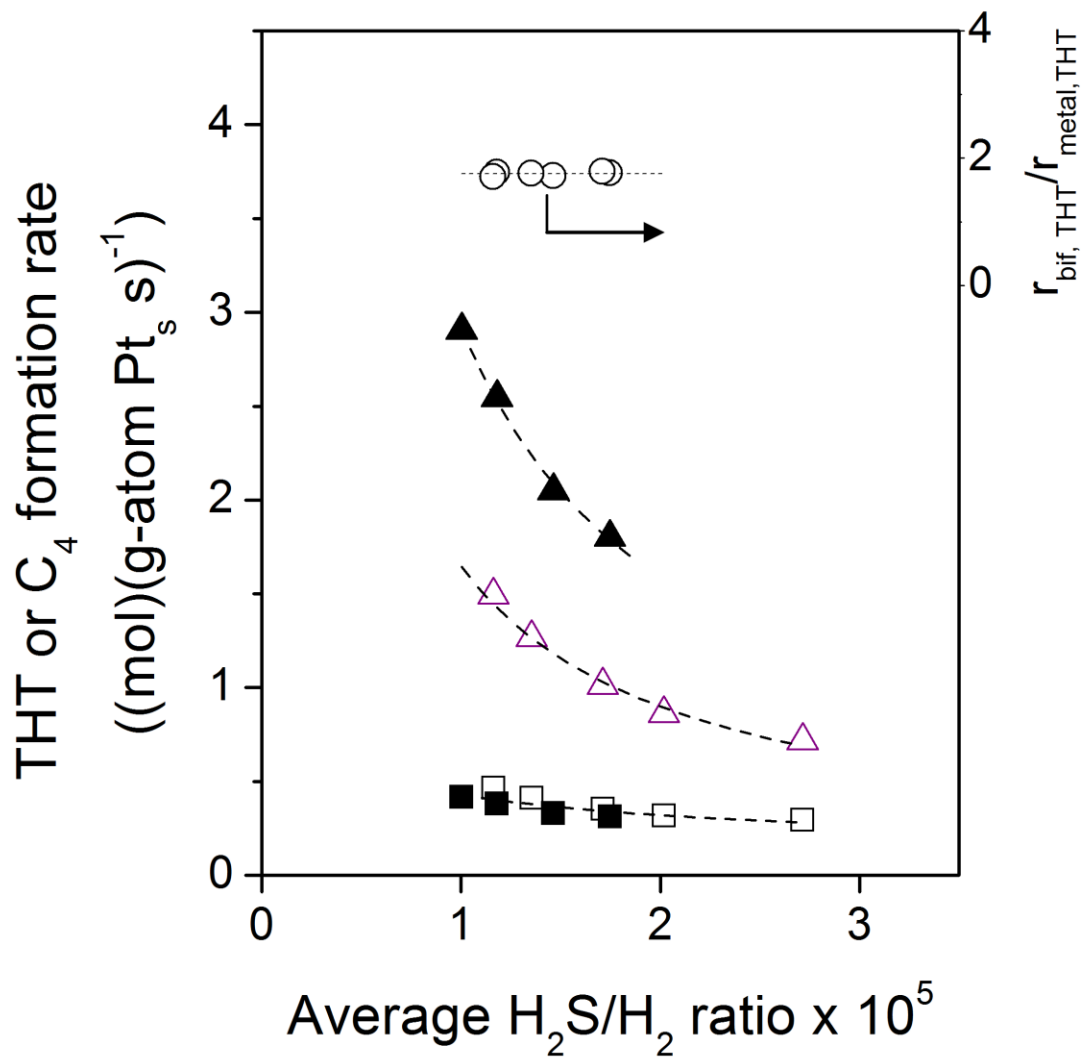
Figure 4.2: Formation rate of tetrahydrothiophene (THT) (▲,△) or butenes/butane (C_4) (■,□) products at 3 MPa H_2, 2.5 kPa thiophene, 573 K as a function of H_2S/H_2 ratios, linearly-averaged across the catalyst bed from measured H_2S at the reactor effluent on Pt/SiO_2, diluted (intrapellet) with SiO_2 (open symbols) or with γ-Al_2O_3 at β = 2.5 x 10^8 m^2 γ-Al_2O_3 (g-atom Pt_s)$^{-1}$ (closed symbols). Inset: ratio of THT formation rates on γ-Al_2O_3-diluted samples (r_{bif}) to those on SiO_2-diluted (r_{metal}) samples (○) as a function of averaged H_2S/H_2 ratios. Dotted curves serve to guide the eye.
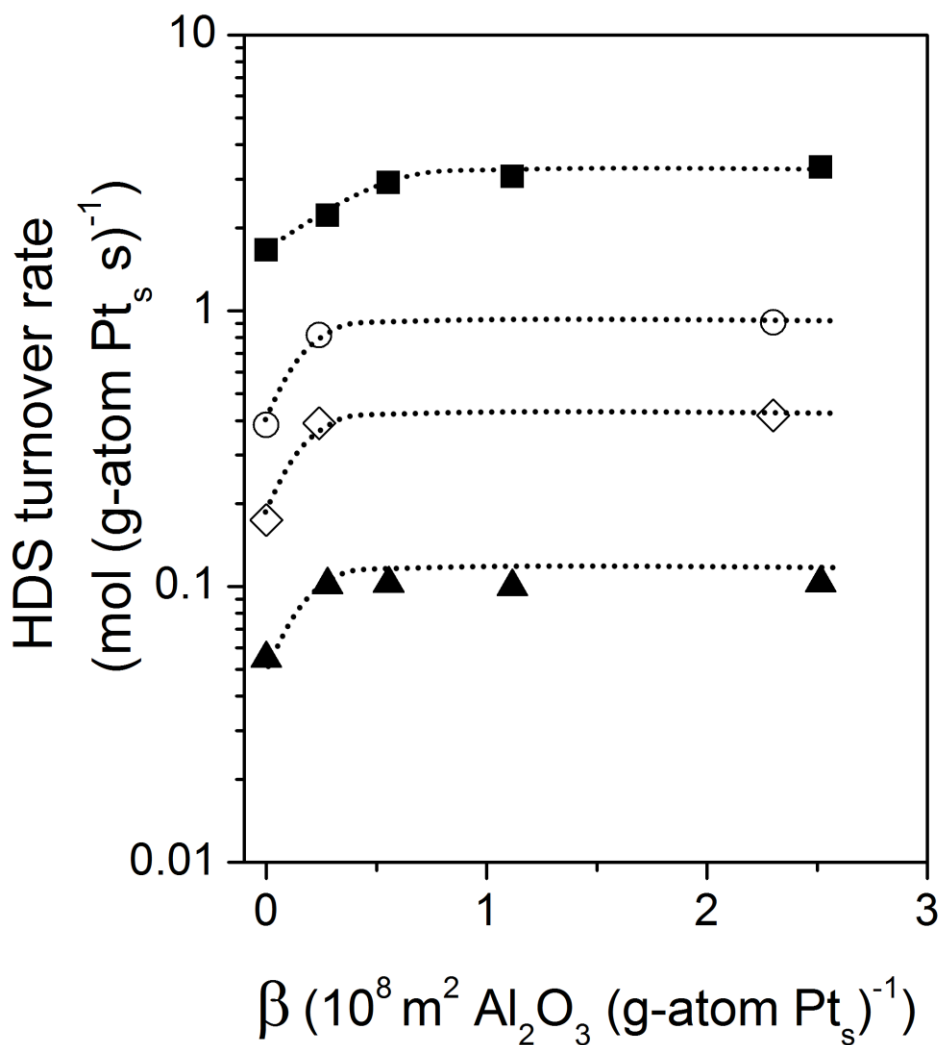
Figure 4.3: HDS turnover rates of thiophene consumption on 2.4 nm (closed symbols) and 5.4 nm (open symbols) sized clusters of Pt/SiO$_2$ at 3 MPa H$_2$, 2.5 kPa thiophene, and 0 (no inlet) (■), 0.3 x 10^{-3} (○), 1.0 x 10^{-3} (◇), and 1.7 x 10^{-3} (▲) H$_2$S/H$_2$ ratios as a function of acid-to-metal mixing ratios, β, at constant R (<50 μm, intrapellet dilutions). Dotted curves serve to guide the eye.
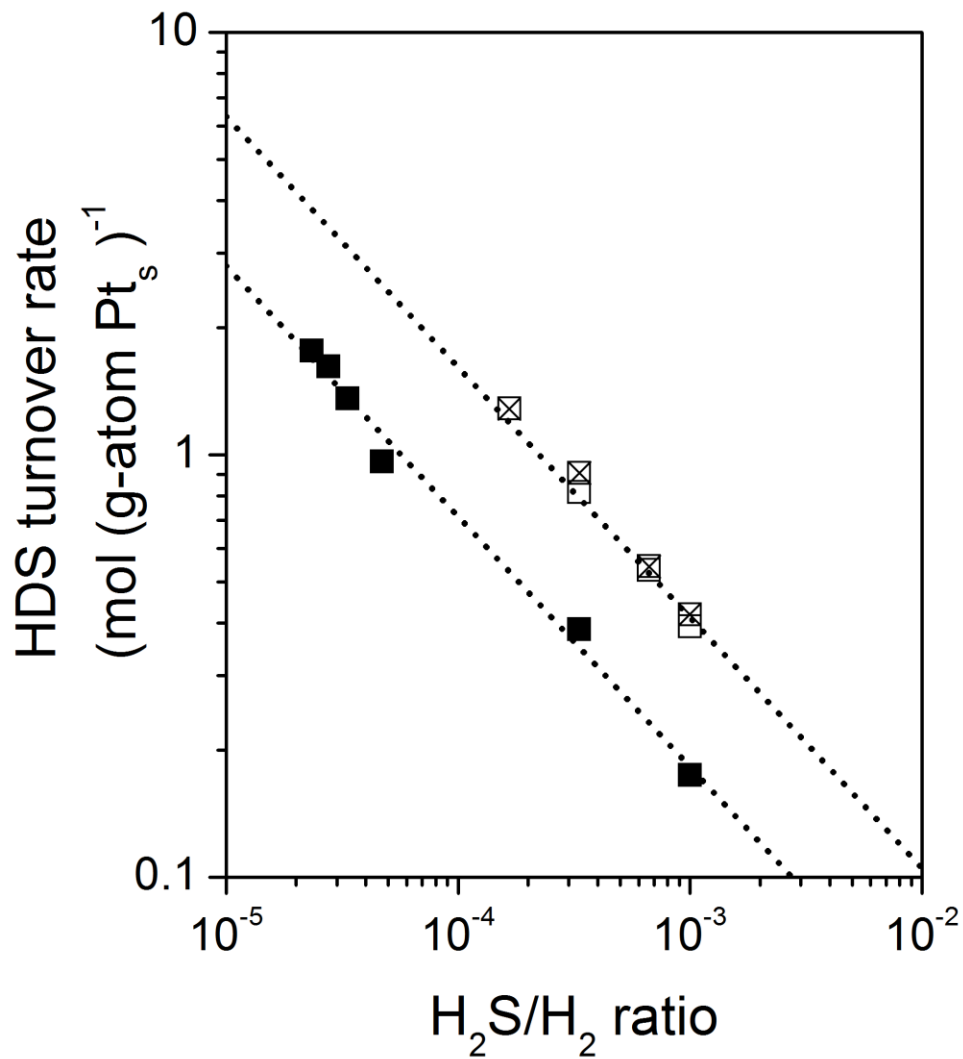
Figure 4.4: HDS turnover rate of thiophene consumption as a function of H_2S/H_2 ratio at 3.0 MPa H_2, 2.5 kPa thiophene, on Pt/SiO_2 (5.4 nm) diluted with SiO_2 (β =0, monofunctional) (■) or mixed with γ-Al_2O_3 (intrapellet dilutions) at β =0.2 x 10^8 m^2 γ-Al_2O_3 (g-atom Pt_s)$^{-1}$ (□) and 2.3 x 10^8 m^2 γ-Al_2O_3 (g-atom Pt_s)$^{-1}$ (⊠). Dotted lines serve to guide the eye.
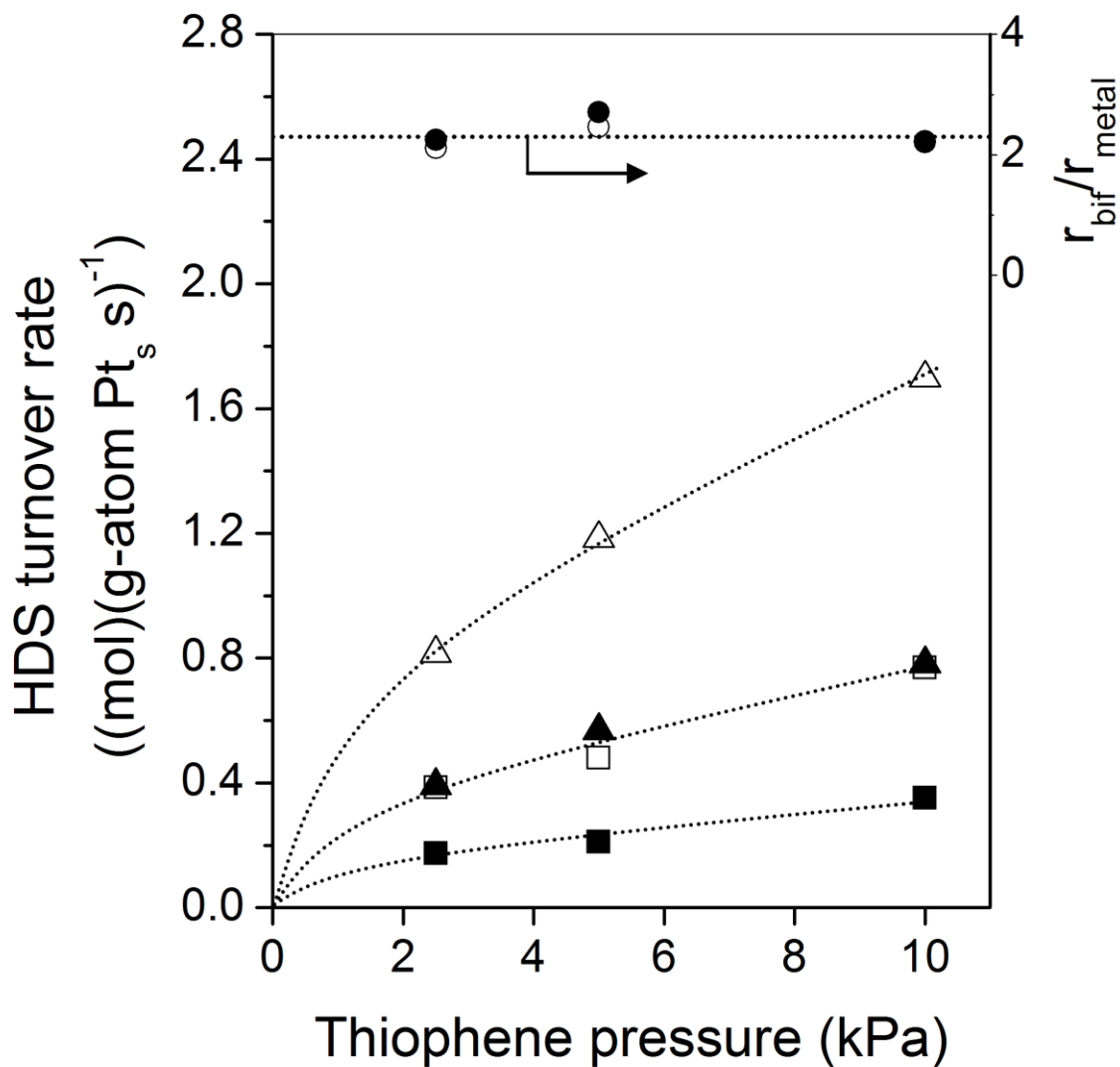
Figure 4.5: HDS turnover rates of thiophene consumption as a function of thiophene pressure on Pt/SiO$_2$ (5.4 nm) in intrapellet dilutions with SiO$_2$ (β =0, squares: $\square$,$\blacksquare$) or with γ-Al$_2$O$_3$ (β =0.2 x 10^8 m^2 γ-Al$_2$O$_3$ (g-atom Pt$_s$)$^{-1}$, triangles: $\triangle$,$\blacktriangle$) at 3.0 MPa H$_2$ and 0.3 x 10^{-3} H$_2$S/H$_2$ (open symbols) and 1.0 x 10^{-3} H$_2$S/H$_2$ (closed symbols) as a function of thiophene pressure. Inset: ratio of rates on catalyst diluted with γ-Al$_2$O$_3$ (r$_{bif}$) to those on catalyst diluted with SiO$_2$ (r$_{metal}$) at 3.0 MPa H$_2$ and 0.3 x 10^{-3} H$_2$S/H$_2$ ($\circ$) and 0.3 x 10^{-3} H$_2$S/H$_2$ ($\bullet$). Dotted curves serve to guide the eye.
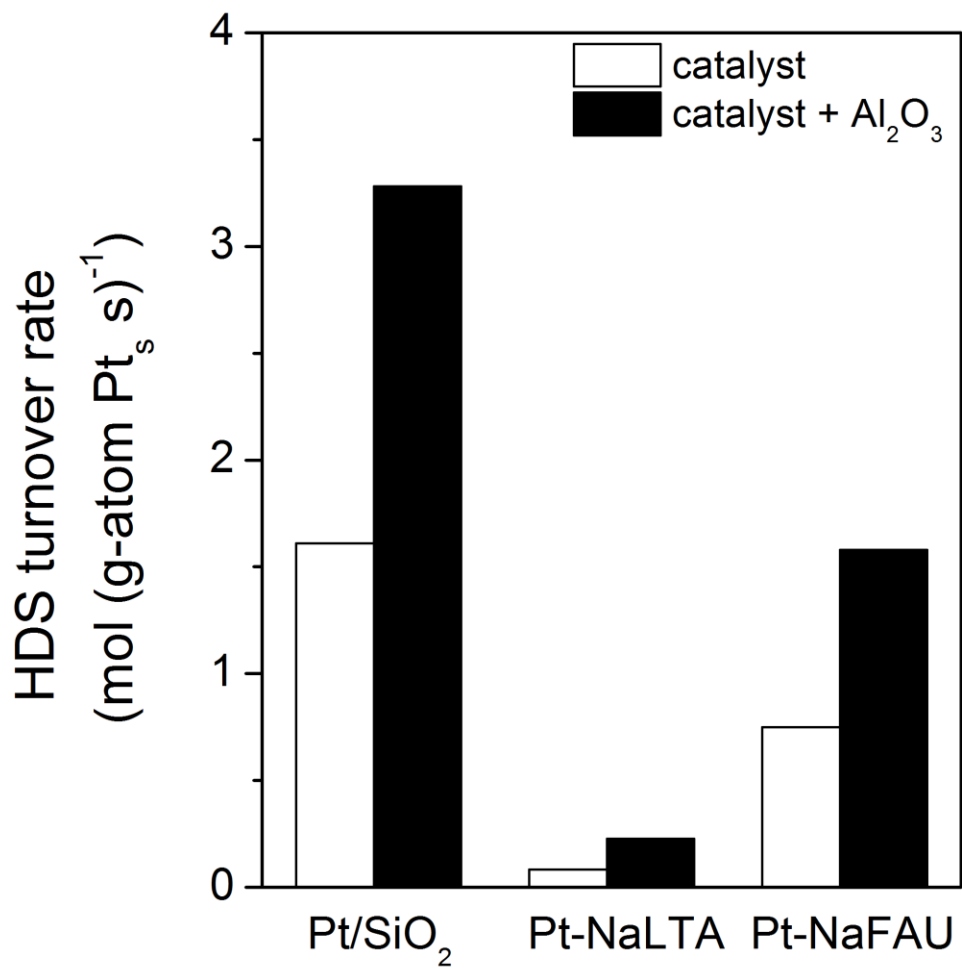
Figure 4.6: HDS turnover rates of thiophene consumption, per surface Pt atom, on Pt/SiO$_2$, Pt-NaLTA, and Pt-NaFAU (unshaded bars) and their corresponding mixtures (interpellet dilutions) with γ-Al$_2$O$_3$ (shaded bars) at 2.5 kPa thiophene, 3.0 MPa H$_2$, and 573 K.
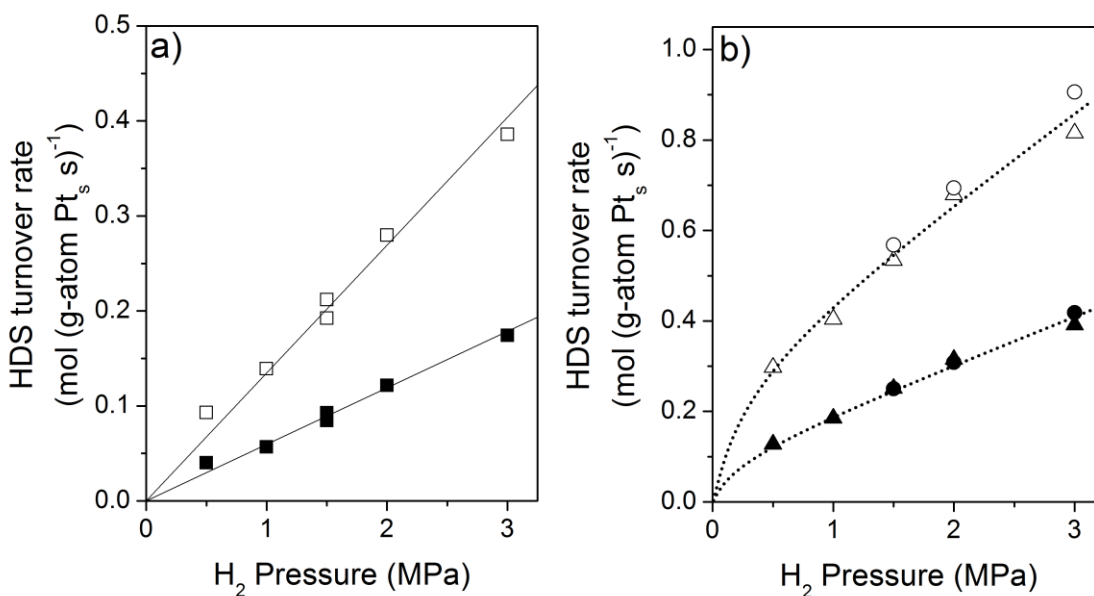
Figure 4.7: HDS turnover rates of thiophene consumption at 573 K, 2.5 kPa thiophene, 0.3 x 10^{-3} H$_2$S/H$_2$ (open symbols) and 1.0 x 10^{-3} H$_2$S/H$_2$ (closed symbols) on Pt/SiO$_2$ at (a) β =0 (squares: □,■) and at (b) β =0.2 x 10^8 m^2 γ-Al$_2$O$_3$ (g-atom Pt$_s$)$^{-1}$ (triangles: Δ,▲) and at 2.3 x 10^8 m^2 γ-Al$_2$O$_3$ (g-atom Pt$_s$)$^{-1}$ (circles: ○, ●) as a function of H$_2$ pressure. Solid lines indicate linear fits to data; dotted curves serve to guide the eye.
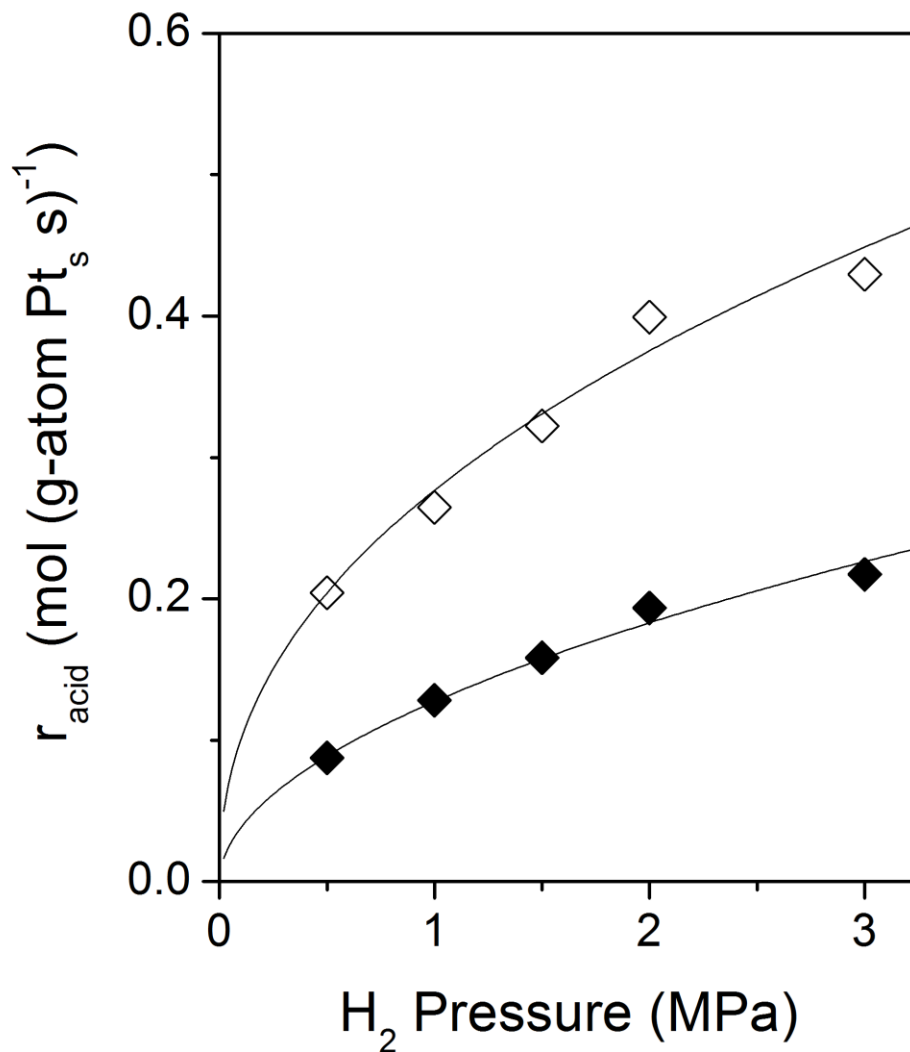
Figure 4.8: Spillover-mediated rates ($\beta = 0.2 \times 10^8$ m^2 γ-Al$_2$O$_3$ (g-atom Pt$_s$)$^{-1}$), r$_{acid}$, normalized by the number of surface metal sites (i.e. difference of rates on γ-Al$_2$O$_3$-diluted and those on SiO$_2$-diluted samples, r$_{bif}$-r$_{metal}$) at 573 K, 2.5 kPa thiophene, and 0.3×10^{-3} H$_2$S/H$_2$ ($\diamond$) and 1.0×10^{-3} H$_2$S/H$_2$ ($\blacklozenge$) as a function of H$_2$ pressure. Curves represent best fits of the data.
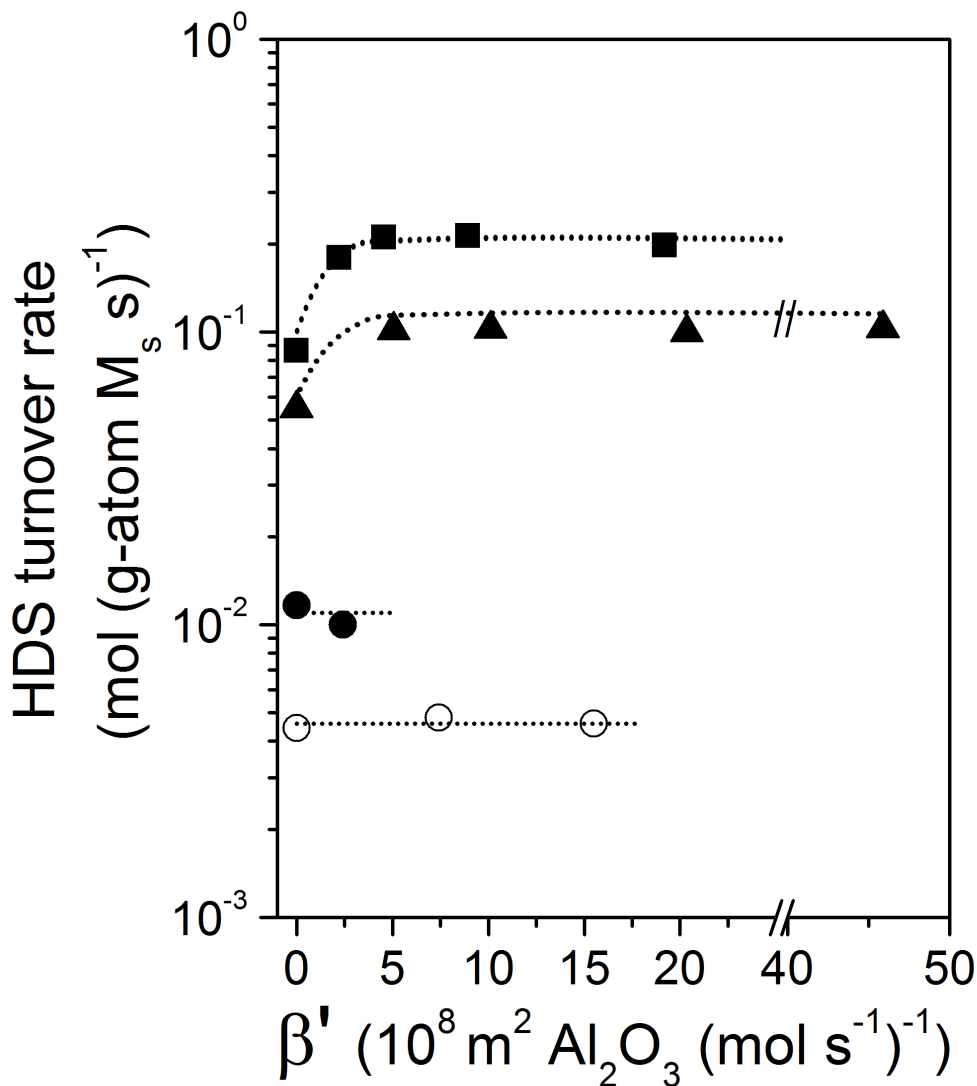
Figure 4.9: Turnover rate of thiophene consumption as a function of β', corrected intrapellet mixing ratio, that scales the surface area of acid function by the reactivity per metal site (i.e. monofunctional rate), on Pt/SiO$_2$ at 3 MPa H$_2$, 2.5 kPa thiophene, 1.7 x 10^{-3} H$_2$S/H$_2$ (▲); Ru/SiO$_2$ at 3 MPa H$_2$, 2.5 kPa thiophene, 2.0 x 10^{-5} (averaged) H$_2$S/H$_2$ (■); and ReS$_x$/SiO$_2$ at 3 MPa H$_2$, 2.5 kPa thiophene, 3x10^{-4} H$_2$S/H$_2$ (●) and at 1 MPa H$_2$, 2.5 kPa thiophene, and 5.0 x 10^{-4} H$_2$S/H$_2$ (○). Dotted curves serve to guide the eye.
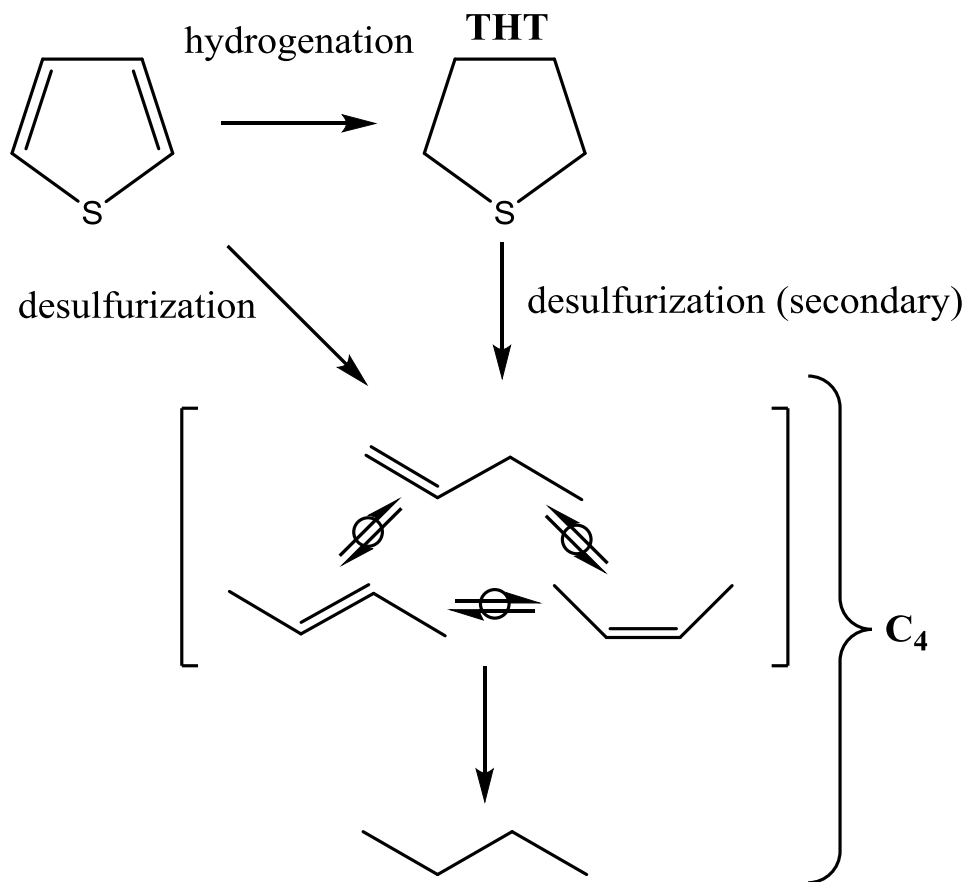
**Scheme 4.1**: Proposed reaction network for thiophene HDS, which undergoes two primary routes, hydrogenation to THT and desulfurization to C_4. THT can undergo secondary desulfurization as a result of product readsorption and reaction. All products are formed on similar types of surface sites and the isomers of C_4 olefins are experimentally detected to form in

an equilibrated mixture, as depicted above with   .
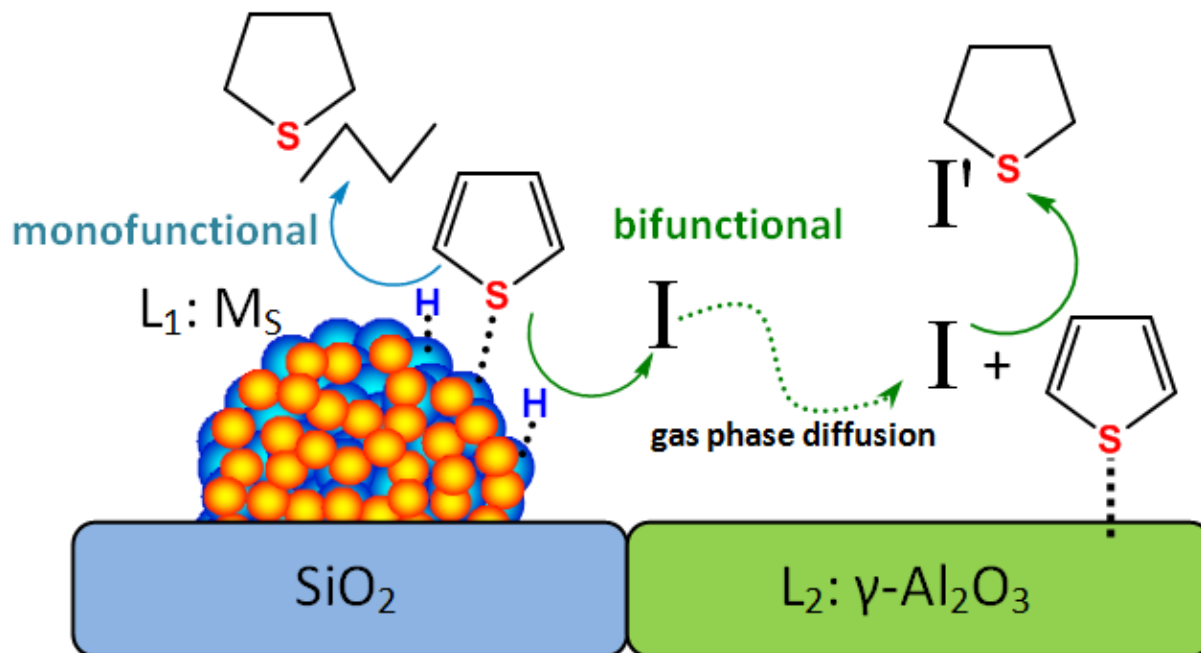
Scheme 4.2: Proposed mechanism for spillover-mediated routes. Monofunctional HDS occurs on metal sites, L_1, which can dissociate H_2 molecules, to form tetrahydrothiophene (THT) and C_4 products. Formation of a molecular H-carrier (i.e. partially-hydrogenated thiophene species), I, diffuses (in the gas phase) and reacts with thiophene molecules adsorbed on γ-Al_2O_3 sites, L_2, which cannot dissociate H_2 molecules, located beyond molecular distances from L_1.
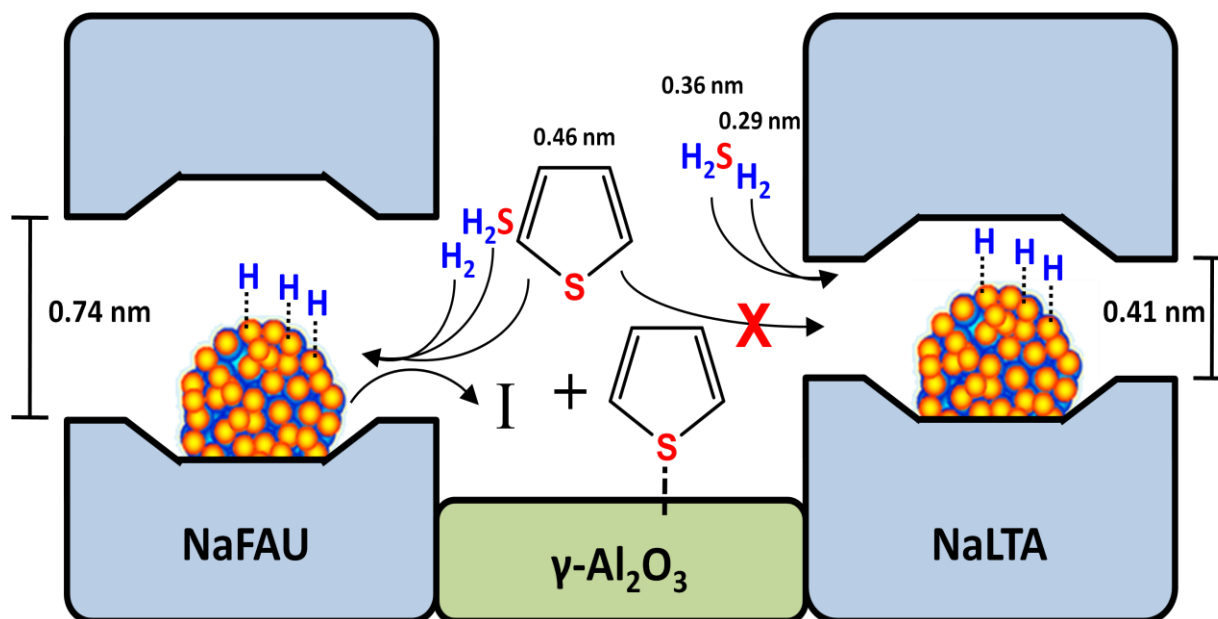
Scheme 4.3: Proposed HDS spillover-mediated mechanism on Pt-encapsulated in Na-exchanged zeolites, FAU and LTA, intimately mixed with γ-Al$_2$O$_3$. Partially-hydrogenated, thiophene-derived molecular H-carriers, I, can be formed only on Pt within NaFAU because zeolite apertures sizes (0.74 nm) allow the diffusion of thiophene (0.46 nm) to access metal sites. Such carriers cannot be formed on Pt within NaLTA (aperture size 0.41 nm), despite uninhibited access of H$_2$ (0.29 nm) and H$_2$S (0.36 nm) to metal clusters that can dissociate H$_2$ and form active H-species, as a result of specific size-selective exclusions of thiophene molecules.
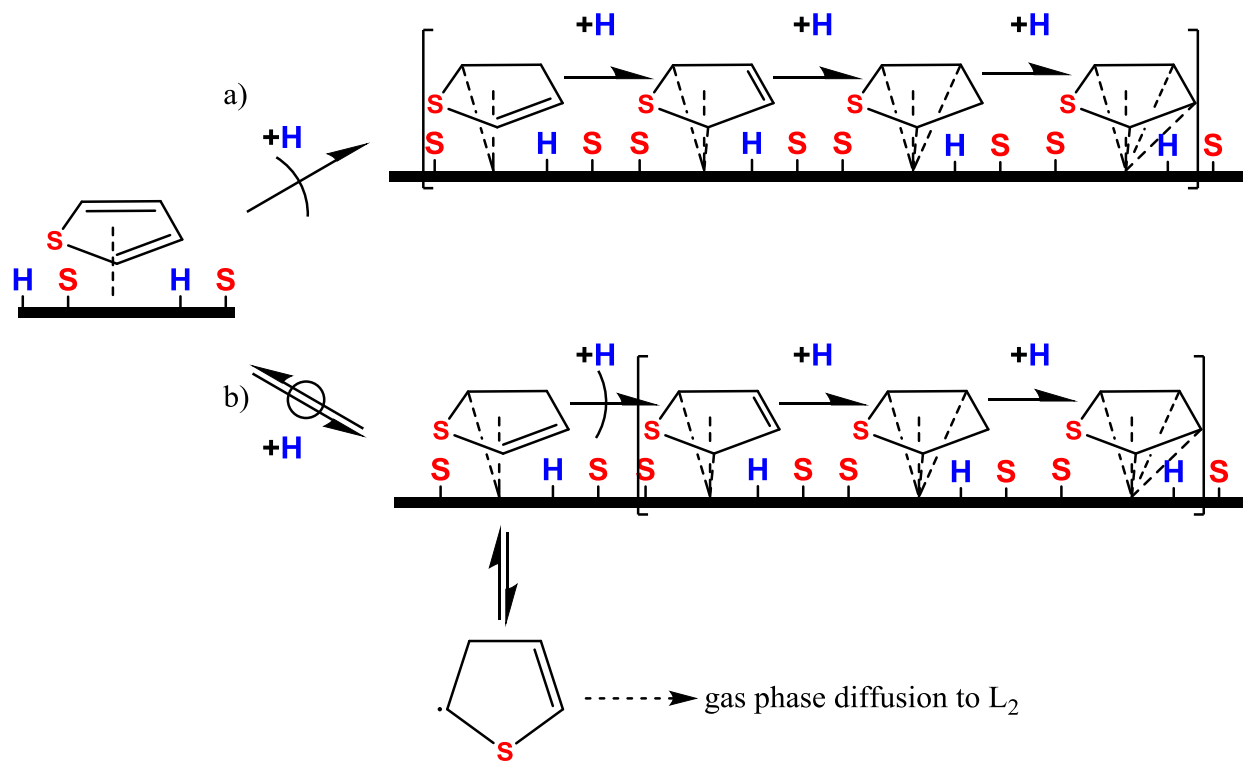
Scheme 4.4: Sequential hydrogenation events on metal HDS sites (L_1) on catalysts for which the molecularity of the kinetically-relevant transition state for thiophene consumption involves a) one more hydrogen species (i.e. on Re or ReS_x) or b) two more hydrogen species (i.e on Pt or Ru) relative to the stoichiometry of thiophene. Reaction counters, depicted with right parenthesis,), indicate the kinetically-relevant H-addition step for the two mechanisms. HDS reactions that are limited by a second H-addition (b) lead to surface-equilibrated formation of monohydrothiophene species, which can desorb (as the H-carrier) and diffuse to a secondary function, L_2 (i.e. γ-Al_2O_3). Desorption and diffusion of partially-hydrogenated molecules may occur in (a), but they cannot lead to additional rate enhancements because all partially-saturated cyclic molecules form after the kinetically-relevant first H-addition step.
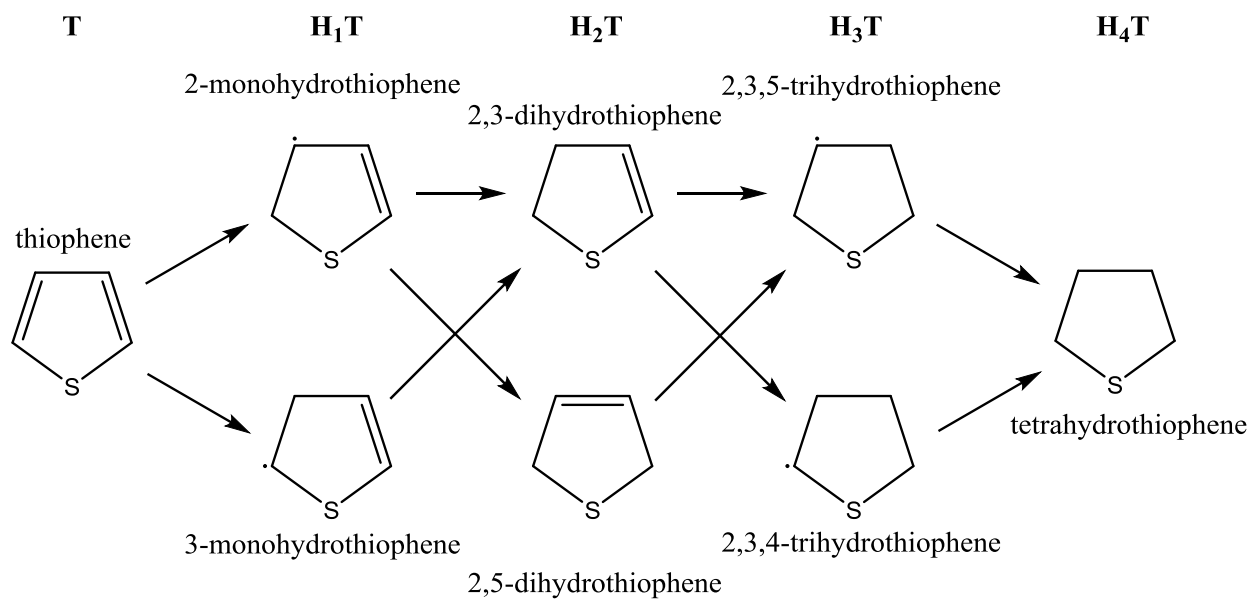
Scheme 4.5: Nomenclature for partially-hydrogenated thiophene molecules and radical species. H_iT labels indicate the number of hydrogen species (i.e. i) added to thiophene.

4.7 References

1. Boudart, M. In *Advances in Catalysis*; D.D. Eley, H. P., Paul, B. W., Eds.; Academic Press: 1969; Vol. Volume 20, p 153.
2. Conner, W. C., Jr.; Falconer, J. L. *Chem. Rev. (Washington, D. C.)*. **95** (1995) 759.
3. Conner, W. C., Jr.; Pajonk, G. M.; Teichner, S. J. *Adv. Catal.* **34** (1986) 1.
4. Roland, U.; Braunschweig, T.; Roessner, F. *J. Mol. Catal. A: Chem.* **127** (1997) 61.
5. Sermon, P. A.; Bond, G. C. *Catal. Rev.* **8** (1973) 211.
6. Wang, L.; Yang, R. T. *Energy Environ. Sci.* **1** (2008) 268.
7. Khoobiar, S. *J. Phys. Chem.* **68** (1964) 411.
8. Keulks, G. W. *J. Catal.* **19** (1970) 232.
9. Weng, L. T.; Delmon, B. *Appl. Catal., A*. **81** (1992) 141.
10. Sen, B.; Falconer, J. L.; Mao, T. F.; Yu, M.; Flesner, R. L. *J. Catal.* **126** (1990) 465.
11. Solymosi, F.; Volgyesi, L.; Sarkany, J. *J. Catal.* **54** (1978) 336.
12. Benson, J. E.; Kohn, H. W.; Boudart, M. *J. Catal.* **5** (1966) 307.
13. Song, C.; Ma, X. *Appl. Catal., B*. **41** (2003) 207.
14. Delmon, B.; Froment, G. F. *Catal. Rev. - Sci. Eng.* **38** (1996) 69.
15. Lueking, A. D.; Yang, R. T. *Appl. Catal., A*. **265** (2004) 259.
16. Niquille-Röthlisberger, A.; Prins, R. *J Catal*. **242** (2006) 207.
17. Srinivas, S. T.; Rao, P. K. *J. Catal.* **148** (1994) 470.
18. Sinfelt, J. H.; Lucchesi, P. J. *J. Am. Chem. Soc.* **85** (1963) 3365.
19. Sancier, K. M. *J. Catal.* **20** (1971) 106.
20. Antonucci, P.; Nguyen, v. T.; Giordano, N.; Maggiore, R. *J. Catal.* **75** (1982) 140.
21. Ceckiewicz, S.; Delmon, B. *J. Catal.* **108** (1987) 294.
22. Lin, S. D.; Vannice, M. A. *J. Catal.* **143** (1993) 554.
23. Ohgoshi, S.; Nakamura, I.; Wakushima, Y. *Stud. Surf. Sci. Catal.* **77** (1993) 289.
24. Simon, L. J.; van Ommen, J. G.; Jentys, A.; Lercher, J. A. *J. Catal.* **203** (2001) 434.
25. Yang, H.; Chen, H.; Chen, J.; Omotoso, O.; Ring, Z. *J. Catal.* **243** (2006) 36.
26. Chen, H.; Yang, H.; Omotoso, O.; Ding, L.; Briker, Y.; Zheng, Y.; Ring, Z. *Appl. Catal., A*. **358** (2009) 103.
27. Baeza, P.; Ureta-Zanartu, M. S.; Escalona, N.; Ojeda, J.; Gil-Llambias, F. J.; Delmon, B. *Appl. Catal., A*. **274** (2004) 303.
28. Vannice, M. A.; Neikam, W. C. *J. Catal.* **23** (1971) 401.
29. Baumgarten, E.; Wagner, R.; Lentes-Wagner, C. *J. Catal.* **104** (1987) 307.
30. Frohlich, G.; Sachtler, W. M. H. *J. Chem. Soc., Faraday Trans.* **94** (1998) 1339.
31. Miller, J. T.; Pei, S. *Appl. Catal., A*. **168** (1998) 1.
32. Levy, R. B.; Boudart, M. *J. Catal.* **32** (1974) 304.
33. Schlatter, J. C.; Boudart, M. *J Catal*. **24** (1972) 482.
34. Briggs, D.; Dewing, J. *J Catal*. **28** (1973) 338.
35. *Catalysis Science and Technology*; H. Topsøe, B. S. C., F.E. Massoth in: J.R. Anderson, M. Boudart Ed.; Springer-Verlag: New York, 1996; Vol. 11.
36. Song, C. S. *Catal Today*. **86** (2003) 211.

37.   Welters, W. J. J.; de Beer, V. H. J.; van Santen, R. A. *Appl. Catal., A*. **119** (1994) 253.

38.   Robinson, W. R. A. M.; van Veen, J. A. R.; de Beer, V. H. J.; van Santen, R. A. *Fuel Process. Technol.* **61** (1999) 103.

39.   Sugioka, M.; Andalaluna, L.; Morishita, S.; Kurosaka, T. *Catal. Today*. **39** (1997) 61.

40.   Li, X.; Wang, A.; Sun, Z.; Li, C.; Ren, J.; Zhao, B.; Wang, Y.; Chen, Y.; Hu, Y. *Appl. Catal., A*. **254** (2003) 319.

41.   Niquille-Roethlisberger, A.; Prins, R. *Catal. Today*. **123** (2007) 198.

42.   Prins, R.; Egorova, M.; Roethlisberger, A.; Zhao, Y.; Sivasankar, N.; Kukula, P. *Catal. Today*. **111** (2006) 84.

43.   Wang, H.; Prins, R. *J. Catal.* **264** (2009) 31.

44.   Wang, H.-M.; Iglesia, E. *ChemCatChem*. **3** (2011) 1166.

45.   Wang, H.-M.; Iglesia, E. *J. Catal.* **273** (2010) 245.

46.   Zhan, B.-Z.; White, M. A.; Sham, T.-K.; Pincock, J. A.; Doucet, R. J.; Rao, K. V. R.; Robertson, K. N.; Cameron, T. S. *J Am Chem Soc*. **125** (2003) 2195.

47.   Wu, Z.; Goel, S.; Choi, M.; Iglesia, E. *J Catal*. **311** (2014) 458.

48.   Frisch, M. J.; Trucks, G. W.; Schlegel, H. B.; Scuseria, G. E.; Robb, M. A.; Cheeseman, J. R.; Scalmani, G.; Barone, V.; Mennucci, B.; Petersson, G. A., et al.; Gaussian, Inc.: Wallingford, CT, USA, 2009.

49.   Peterson, K.; Feller, D.; Dixon, D. *Theor Chem Acc*. **131** (2012) 1.

50.   Wang, H.-M.; Iglesia, E. *ChemCatChem*. **3** (2011) 1166.

51.   Garcia-Araez, N. *The Journal of Physical Chemistry C*. **115** (2011) 501.

52.   Chica, A.; Strohmaier, K.; Iglesia, E. *Langmuir*. **20** (2004) 10982.

53.   Welters, W. J. J.; de Beer, V. H. J.; van Santen, R. A. *Applied Catalysis A: General*. **119** (1994) 253.

54.   Sarbak, Z. *Applied Catalysis A: General*. **159** (1997) 147.

55.   Jeevanandam, P.; Klabunde, K. J.; Tetzler, S. H. *Microporous and Mesoporous Materials*. **79** (2005) 101.

56.   Morin, C.; Simon, D.; Sautet, P. *Surface Science*. **600** (2006) 1339.

4.8   Supporting Information

4.8.1   *Characterization of Pt-NaLTA and Pt-NaFAU catalysts*

Approximately 80% of the Pt atoms are present within the micropores of LTA, as evidenced from the degree of inhibition of ethene hydrogenation by thiophene poisons and differences in the rates of hydrogenation of ethene and isobutene (Table 4.S1). While ethene hydrogenation turnover rates were similar on Pt-NaLTA (0.42 nm aperture size) and unconfined Pt/SiO_2, the rate on Pt-NaLTA catalyst decreased by 20% when thiophene (0.46 nm kinetic diameter) was co-fed, whereas the rate on Pt/SiO_2 decreased to almost zero. Relative turnover rates for hydrogenation of ethene (0.39 nm) and isobutene (0.50 nm) ($TOR_{ethane}/TOR_{isobutene}$ in Table 4.S1) on Pt-NaLTA is approximately 7-fold greater than that on Pt/SiO_2. These results indicate that ~80% of Pt is located inside the LTA cage [38,42].

Table 4.S1: Catalytic properties of Pt-NaLTA (0.76 wt.% Pt, 0.75 dispersion) and Pt/SiO$_2$ (0.30 wt.% Pt, 0.98 dispersion) in the hydrogenation of ethene (kinetic diameter, 0.38 nm) and isobutene (0.50 nm)[a].

Catalyst	TOR$_{ethene}$		TOR$_{isobutene}$	TOR$_{ethene}$/ TOR$_{isobutene}$
	0 kPa thiophene	0.1 kPa thiophene (% decrease)		
Pt-NaLTA	0.81	0.65 (20%)	0.051	15.9
Pt/SiO$_2$	1.26	0.00056 (99%)	0.61	2.1

[a] Conditions: 1.5 kPa alkenes, 5 kPa H$_2$ at 294 K, with/without 0.1 kPa thiophene; TOR in mol (g-atom Pt$_s$ s)$^{-1}$.

About 90% of the Pt atoms were present within Na-FAU zeolite (0.74 nm aperture size), evidenced by differences in the hydrogenation rate of toluene (0.59 nm kinetic diameter) and 1,3,5-triisopropylbenzene (TIPB, 0.85 nm kinetic diameter). Toluene hydrogenation turnover rates were similar on Pt-NaFAU and Pt/SiO$_2$ and the relative turnover rates for hydrogenation of toluene (0.59 nm kinetic diameter) and TIPB (0.85 nm kinetic diameter) (TOR$_T$/TOR$_{TIPB}$ in Table 4.S2) of Pt-NaFAU is approximately 8-fold greater than that of Pt/SiO$_2$, indicating that ~90% of Pt is located inside the FAU cage [38].

Table 4.S2: Catalytic properties of Pt-NaFAU (0.42 wt.% Pt, 0.78 dispersion) and Pt/SiO$_2$ (0.30 wt.% Pt, 0.98 dispersion) in the hydrogenation of toluene (T; kinetic diameter, 0.59 nm) and 1,3,5-triisopropylbenzene (TIPB; 0.85 nm).

Catalyst	TOR$_T$[a]	TOR$_{TIPB}$[b]	TOR$_T$/TOR$_{TIPB}$
Pt-NaFAU	1.6	0.2	8.0
Pt/SiO$_2$	1.7	1.7	1.0

[a] Conditions: 111 kPa toluene, 2.75 MPa H$_2$, 423 K; TOR in mol (g-atom Pt$_s$ s)$^{-1}$
[b] Conditions: 6.72 kPa TIPB, 2.96 MPa H$_2$, 473 K; TOR in mol (g-atom Pt$_s$ s)$^{-1}$

Figure 4.S1 shows the infrared spectra of Pt-NaLTA and Pt-NaFAU, and of Pt-HFAU for comparison. Infrared spectra were collected using a Nicolet NEXUS 670 infrared spectrometer equipped with a Hg-Cd-Te (MCT) detector. Data was collected with 2 cm^{-1} resolution in the 4000-400 cm^{-1} range. Self-supporting wafers were sealed within a quartz vacuum infrared cell equipped with NaCl windows. Samples were treated in flowing dry air (1.67 cm^3 s^{-1}, zero grade, Praxair) by heating to 723 K (0.033 K s^{-1}), holding for 2 h, and then evacuating for at least 2 h at 723 K (using a diffusion pump) before cooling to 303 K in vacuum and analytical measurement. OH bands (3400~3700 cm^{-1}) were observed on Pt-HFAU, consistent with the abundance of OH groups expected in the Brønsted acid form of Pt/HFAU. The OH stretching region exhibited five bands corresponding to supercages (~3630 cm^{-1}), extra-framework Al species (~3600 cm^{-1}), sodalite cages (~3554 cm^{-1}), hexagonal prisms (~3520 cm^{-1}), and silanols (~3670 cm^{-1}) [Okumura, K. et al. *Molecules* **16** (2011) 38]. In contrast, there were no detectable bands in the 3200-3600 cm^{-1} range for Pt-NaLTA or Pt-NaFAU, indicating the absence of OH groups and of Brønsted acid sites in Na-exchanged samples.
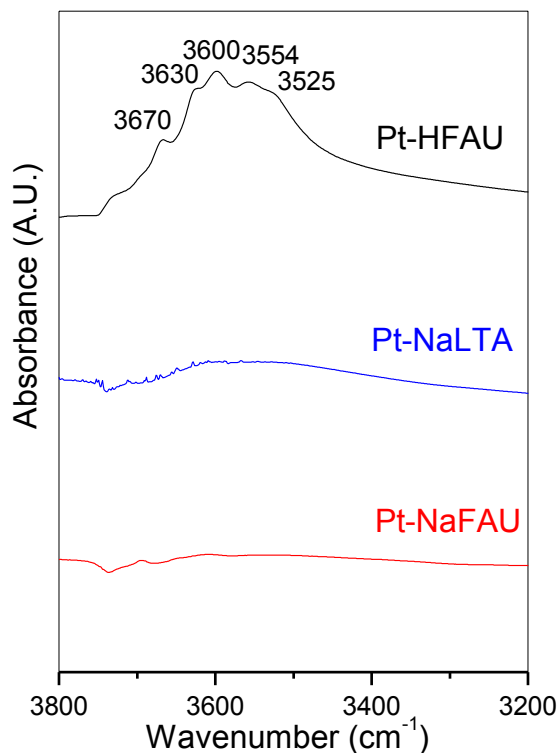
Figure 4.S1: Infrared spectra of the Pt-NaLTA and Pt-NaFAU catalyst and a Pt-HFAU sample for comparison.

4.8.2 *Linear alkanes and cycloalkanes are not spillover hydrogen carriers*

Table 4.S3 shows the thiophene HDS turnover rates on bifunctional catalysts (i.e. Pt/SiO_2 diluted with γ-Al_2O_3) with different co-feed concentrations of decane, intended as a thiophene (reactant) solvent. Increasing the partial pressure of decane from 50 to 100 kPa did not lead to any changes in turnover rate, indicating that decane is not involved in the spillover process. Addition of dimethylcyclohexane, a potentially more reactive hydrogen transfer species, also did not yield any appreciable differences in rates, thereby suggesting that even cycloalkanes are not involved in the spillover process as an active hydrogen carrier. Such findings are consistent with spillover mechanisms that implicate *unstable* carriers, which apparently are not introduced or formed from these hydrocarbons. Thermodynamics (at these high hydrogen chemical potentials) and preferential (competitive) adsorption of sulfur-containing compounds on these catalytic surfaces disfavors the dehydrogenation of these hydrocarbons, thus any partially-hydrogenated species that could otherwise act as H-carriers cannot be formed from hexane or dimethylcyclohexane.

Table 4.S3: Thiophene HDS turnover rates on $Pt/SiO_2 + \gamma\text{-}Al_2O_3$ in the presence of decane and dimethylcyclohexane.

Catalyst	Condition	Thiophene HDS TOR[b] $(mol\ (g\text{-}atom\ Pt_s\ s)^{-1})$
$Pt/SiO_2 + \gamma\text{-}Al_2O_3$[a]	50 kPa decane	3.28
	100 kPa decane	3.26
	50 kPa decane + 10 kPa dimethylcyclohexane	3.27

[a] mixing ratio (intrapellet dilution) of $\gamma\text{-}Al_2O_3$ and Pt/SiO_2 (β) $= 2.52 \times 10^8\ m^2\ \gamma\text{-}Al_2O_3$ surface $(g\text{-}atom\ Pt_s)^{-1}$.
[b] at 573 K, 3.0 MPa H_2, and 2.5 kPa thiophene.